Template Directed Synthesis of Porphyrin Nanorings

Melanie Claire O'Sullivan

Keble College
University of Oxford

A thesis submitted in partial fulfilment of the requirements for the degree of *Doctor of Philosophy*

Trinity 2011

Table of Contents

Chapter 2

Chapter 3

Chapter 4

Chapter 5

Publications

Papers

M. C. O'Sullivan, J. K. Sprafke, D. V. Kondratuk, C. Rinfray, T. D. W. Claridge, A. Saywell, M. O. Blunt, J. N. O'Shea, P. H. Beton, M. Malfois, H. L. Anderson, "Vernier templating and synthesis of a 12-porphyrin nano-ring", *Nature* **2011**, *469*, 72–75.

Highlighted in: "Supramolecular chemistry: Bigger and better synthesis", *Nature* **2011**, *469*, 39–41; "Macrocycles: Templating triumph", *Nature Chem.* **2011**, *3*, 186–187; *C&EN* News of the Week (January 2011); *Chemistry World* (February 2011); *Science News* (January 2011) and *Chemistry & Industry* (January 2011).

Lectures

M. C. O'Sullivan, J. K. Sprafke, H. L. Anderson, "Vernier template directed synthesis of giant nanorings", 240th ACS National Meeting, Boston, MA, United States, August 2010.

M. C. O'Sullivan, H. L. Anderson, "Towards fully conjugated large porphyrin nanorings", COST D31/0003 Working Group Meeting, Institute of Chemical Research of Catalonia (ICIQ), Tarragona, Spain, November 2008.

Posters

M. C. O'Sullivan, J. K. Sprafke, H. L. Anderson, "Classical and Vernier templated synthesis of a [12]porphyrin nanoring", Pfizer Organic Chemistry Poster Symposium, University of Oxford, October 2010.

M. C. O'Sullivan, H. J. Hogben, H. L. Anderson, "Ligand binding of cyclic porphyrin hexamer", RSC Supramolecular and Macrocycles Meeting, University of Cambridge, December 2009.

M. C. O'Sullivan, H. J. Hogben, H. L. Anderson, "Ligand binding of cyclic porphyrin hexamer", ISNA13 13th International Symposium on Novel Aromatic Compounds, Luxembourg, July 2009.

Summary

This thesis describes supramolecular approaches to porphyrin nanorings. Cyclic porphyrin arrays resemble natural light harvesting systems, and it is of interest to probe the photophysical effects of bending the porphyrin aromatic π-system.

A general overview of the synthesis and photophysical properties of porphyrins and their arrays is carried out in *Chapter 1*. The electronic structure of porphyrins is examined, and how conformational effects in oligomers, such as inter-porphyrin torsional angle and backbone bending influence the π-conjugation pathway. The structures of light harvesting complexes are discussed.

Chapter 2 describes the design and synthesis of a complementary 12-armed template designed to coordinate linear porphyrin oligomers in the correct conformation for cyclisation to give a cyclic porphyrin dodecamer.

Chapter 3 demonstrates two approaches to a cyclic porphyrin dodecamer ring. Firstly, a classical templating approach using the 12-armed template is described. The limitations of this approach in the quest for larger nanorings are discussed. Vernier templating, which utilises a mismatch in the number of binding sites between a ligand and its receptor is introduced as a general strategy to the synthesis of large nanorings. This is demonstrated by the synthesis of cyclic dodecamer from a linear porphyrin tetramer and a hexadentate template *via* a figure-of-eight intermediate.

The general utility of the Vernier method to large nanorings is explored in *Chapter 4* with steps towards the synthesis of a cyclic tetracosamer, consisting of 24 porphyrin subunits. In preliminary experiments, an improved route to the cyclic porphyrin octamer is described.

Finally, the photophysical properties of the nanoring series are explored in *Chapter 5* as a function of size and conformation. Femtosecond photoluminescence spectroscopy shows that even in cyclic dodecamer, exciton delocalisation over the entire porphyrin backbone occurs on a sub-picosecond timescale, and parallels are drawn with the dynamics of natural light harvesting complexes.

Acknowledgements

Firstly I would like to thank Harry for giving me the opportunity to work on such a fantastic project, and for providing guidance and encouragement over the three years.

Thanks to Dr. Barbara Odell and Dr. Tim Claridge for all their help and advice with NMR. Thank you to Wilson Chen, Chaw-Keong Yong and Dr. Laura Herz who carried out all the PL anisotropy and have patiently answered all my physic-sy questions. Johannes Sprafke is thanked for fluorescence measurements, SAXS and NMR data, as well as Figures 3.38–3.41 used in Chapter 3. Thank you also to our collaborators: Marc Malfois at Diamond Light Source for the SAXS experiments, Peter Beton and his group in Nottingham for the STM images. Colin Sparrow and James McCullagh at Oxford, and Mark Wyatt at the EPSRC MS Service in Swansea are thanked for all their help with MALDI-MS.

A particular thank you goes to Prof. Stephen Faulkner for the pastoral support over the three years; I am incredibly grateful for all your help.

I am appreciative to all the members of the HLA group past and present who have made the lab a great place to be. In particular, my lab supervisor in the early days, Karl Thorley, who enlightened me to the most efficient method for covering a Kugelrohr with dipyrro. Thank you goes to Dmitry Kondratuk who has provided fantastic ideas and suggestions, porphyrin oligomers and enthusiasm. My two indispensible summer students Miquel Planells and Corentin Rinfray who kept me constantly supplied with starting materials. Simon Chambers is mostly accredited with plundering my chemical stocks and glassware, but repaid his debt with great chat. Louisa and James R are thanked profusely for all their help with HPLC. Miłosz, Jon, Matthew and James W in particular have been incredible friends and are thanked for all the laughs and beers. A massive thank you goes to all the people who have willingly (!) read these manuscripts and given me brilliant feedback. Igor, good luck with the whistling.

A special thanks goes to the Oxford-based folk who have kept me sane. Karis, for being a brilliant housemate, mountain, cycling, and sailor buddy: I will never leave you alone in a tent again. My two welfare ~~tea~~ whisky regulars, Bronnie and Jenn for all the great chats, chocolates and 'Phoebe Specials' that fuelled the write-up. My main lady Ali, for all our big gay dates and jubblyjubblies. Thanks to Tom, Blue Nun is no longer the sign of a classy night in. Abi, Raffi,

Mollers, and Tessa, you are wonderful people and made Keble awesome. Simon, you are still the best date I ever had (sorry Gus).

To all my friends outside of Oxford, in particular: Kevin Hands (and the sadly late John Silver)- I promised to share the Nobel prize with you, but failing any cure for 'pig AIDS' I dedicate at least one chapter for inventing a far more efficient method of punting. My Hinckley girls Michelle, Katie and Keira, thanks for all our brilliant weekends away. Dexter, although we've not seen each other as much as we'd both like, I'm glad we've always been there for the important stuff, and congratulations on becoming a father. Steve, Becky and Barney-chan, thanks for keeping the Daiwa-love™ alive and genki.

Finally, a huge thank you to my two favourite boys, Dad and Gus, who have always been on the end of a phone/train journey/cycle ride/corridor for a laugh or a cry. You have both been rocks and I wouldn't be at this point if it hadn't been for your support. Love you both!

Abbreviations

Ac	Acetyl
aq	Aqueous
Ar	Aryl
ATP	Adenosine triphosphate
BBO	*β*-Barium borate
BChl	Bacteriochlorophyll
BINOL	1,1'-Bi-2,2'-napthol
BIPIP	4,4'-bipiperidine
BIPY	4,4'-bipyridine
Bphe	Bacteriopheophytins
Bu	Butyl
Chl	Chlorophyll
cod	1,5-Cyclooctadiene
COSY	Correlation spectroscopy
CPP	Cyclic paraphenylenes
CPPA	Cyclic paraphenylacetylenes
CSD	Cambridge Structural Database
d	Doublet
d	Days
DABCO	1,4-diazabicyclo[2.2.2]octane
dba	Dibenzylideneacetone
DCTB	Trans-2-[3-(4-*tert*-butylphenyl)-2-methyl-2-propenylidene] malononitrile
DDQ	2,3-dichloro-5,6-dicyanobenzoquinone
DFT	Density functional theory
DIBAL	Diisobutylaluminium hydride
DME	Dimethoxyethane
DMF	Dimethylformamide
DMSO	Dimethylsulfoxide
DNA	Deoxyribonucleic acid
DOSY	Diffusion-ordered spectroscopy
dppf	1,1'- bis(diphenylphosphino) ferrocene
EEH	Excitation energy hopping
EET	Excitation energy transfer
EM	Effective molarity
EPSRC	Engineering and Physical Sciences Research Council
ES	Electrospray
ESI	Electrospray ionisation

Et	Ethyl
EtOH	Ethanol
FRET	Förster resonance energy transfer
FT	Fourier transform
GPC	Gel permeation chromatography
h	Hours
HOMO	Highest occupied molecular orbital
HPLC	High performance liquid chromatography
HSQC	Heteronuclear single quantum coherence
i-	*iso-*
IC	Internal conversion
IR	Infrared
ISC	Intersystem crossing
LD-FTMS	Laser desorption Fourier transform mass spectrometry
LH	Light harvesting
LUMO	Lowest unoccupied molecular orbital
m	Multiplet
m-	*meta-*
m.p.	Melting point
MALDI	Matrix-assisted laser desorption ionisation
Me	Methyl
MeOH	Methanol
min	Minutes
MM	Molecular mechanics
MO	Molecular orbital
MS	Mass spectrometry
NMR	Nuclear magnetic resonance
NOE	Nuclear Overhauser effect
NOESY	Nuclear Overhauser effect spectroscopy
o-	*ortho-*
ORTEP	Oak Ridge Thermal-Ellipsoid Plot
p-	*para-*
PCC	Pyridinium chlorochromate
PDF	Pair-distribution function
Ph	Phenyl
PL	Photoluminescence
PLE	Photoluminescence excitation
PMT	Photomultiplier tube
ppm	Parts per million
Pr	Propyl
PS	Photosystem
Py	Pyridine
rac-	Racemic

RC	Reaction centre
RNA	Ribonucleic acid
ROESY	Rotating frame nuclear Overhauser effect spectroscopy
Rps.	*Rhodopseudomonas*
rt	Room temperature
s	Singlet
SAXS	Small-angle X-ray scattering
SEC	Size-exclusion chromatography
STM	Scanning tunnelling microscopy
t	Triplet
t-/tert-	*tertiary-*
TA	Transient absorption
TAA	Transient absorption anisotropy
TBAF	Tetrabutyl ammonium fluoride
TCSPC	Time-correlated single photon counting
TFA	Trifluoroacetic acid
THF	Tetrahydrofuran
THS	Trihexylsilyl
TLC	Thin layer chromatography
TMEDA	Tetramethylethylenediamine
TMS	Trimethylsilyl
TMV	Tobacco mosaic virus
ToF	Time of flight
Ts	Tosyl
UC	Upconversion
UV	Ultraviolet
Vis	Visible
YAG	Yttrium aluminium garnet

Chapter One
Introduction

This chapter sets out to describe the synthesis and photophysical properties of porphyrins and their arrays. First the basic structure and nomenclature of the porphyrin will be discussed. The electronic structure of porphyrins is examined, and how conformational effects in oligomers, such as inter-porphyrin torsional angle and bending effects influence the π-conjugation pathway and thus the absorption and emission properties. A review on porphyrin oligomer linker units is carried out. Finally, the importance of porphyrin derivatives in photosynthesis is highlighted, with a discussion of the structure of light harvesting complexes.

1.1 Porphyrins

1.1.1 Structure and Nomenclature

Porphyrins are large, heterocyclic aromatic compounds which consist of four pyrrole units linked by methine bridges (–CH=) through their α-carbons. Porphyrins are intensely coloured, with the word deriving from the Greek word *porphura*, meaning 'purple'. They possess a total of 22 π electrons; but only 18 π electrons can be involved in any one delocalisation pathway (Figure 1.1a), allowing porphyrins to be regarded as a bridged diaza[18]annulene structure.[1] This obeys Hückel's $4n+2$ rule for aromaticity.

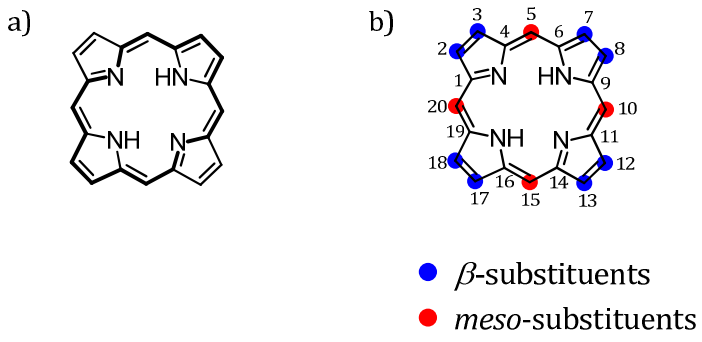

Figure 1.1 a) The bold bonds indicate the 18 π electron delocalisation pathway responsible for the aromaticity of porphyrins; b) Numbering and nomenclature for naming porphyrins.

The simplest porphyrin, known as porphin, has no substituents on the periphery of the macrocycle. Porphin can be easily functionalised; substituents on the methine carbons (carbons 5, 10, 15 and 20) are known as *meso*-substituents; those on the β-positions of the pyrrole units are known as β-substituents (Figure 1.1b).[2] The nitrogens pointing toward the centre of the macrocycle can ligate to various metals. The strength of this coordination increases with electronegativity and charge of the metal ion, and depends on the ionic radius.[3] Zinc forms stable complexes with porphyrins, and the resulting complex can reversibly bind another ligand, such as pyridine, perpendicular to the plane of the ring.

Pyridine, therefore, can be used to disrupt π-stacking of porphyrins to prevent aggregation,[4] or multi-pyridyl molecules can be used to bind many porphyrins into supramolecular structures, which will be discussed in depth later.

1.1.2 Synthesis

The synthesis of 5,10,15,20-tetraaryl substituted porphyrins was first reported by Adler in 1967,[5] and later developed by Lindsey.[6] Pyrrole **1** was condensed with an aromatic aldehyde **2** under acidic conditions. The resulting porphyrinogen **3**, formed under equilibrium conditions, was then irreversibly oxidised to the corresponding porphyrin **4** in 46% yield (Scheme 1.1). It was found the yield of porphyrin was highest when the condensation reaction was carried out at concentrations of 10^{-2} M.

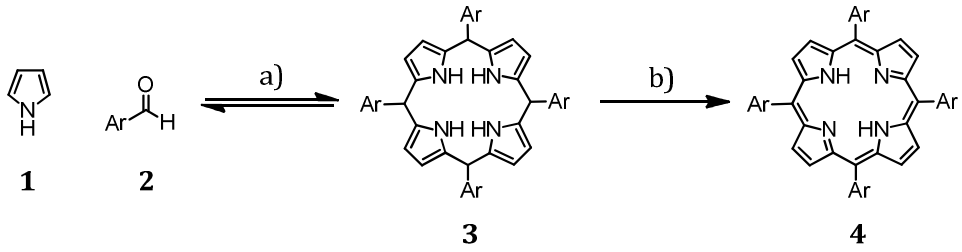

Scheme 1.1 Lindsey's synthesis of a 5,10,15,20-tetraarylporphyrin: a) BF_3 or TFA; b) *p*-chloranil, 46%.

Gunter[7] and Lawrence[8] reported the synthesis of 5,15-diarylporphyrins **6** in 73–92% yields using equimolar ratios of a dipyrromethane derivative **5** and an aromatic aldehyde under acidic conditions (Scheme 1.2).

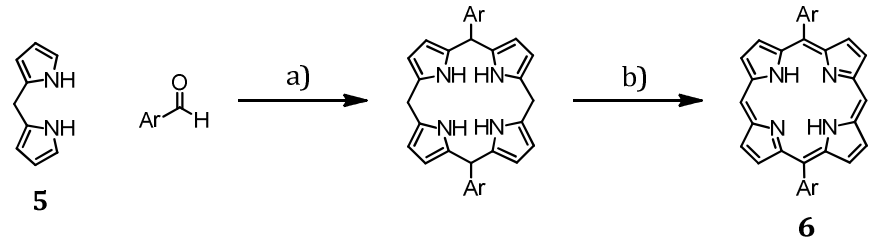

Scheme 1.2 Synthesis of a 5,15-diarylporphyrin as reported by Lawrence:[8] a) TFA, CH_2Cl_2; b) *p*-chloranil.

Dipyrromethane **5** can be readily synthesised by acid-catalysed condensation of pyrrole with an aldehyde.[9] If formaldehyde is used to form dipyrromethane, the resulting porphyrin will be unsubstituted at two *meso*-positions; these positions can be later functionalised selectively by electrophilic aromatic substitution. Due to the higher electron density at the *meso*-positions, *meso*-substitution generally occurs faster than at the free *β*-positions.[10][11]

1.1.3 Optoelectronic properties

The UV-vis absorption spectra of porphyrins consist of an intense transition between 380 – 420 nm (Soret, or B band) and a weaker transition at lower energies (Q band).[12] The Q band arises from a transition from the ground state to the first singlet excited state (S_0–S_1), and the B band from a transition from the ground state to the second singlet excited state (S_0–S_2). The absorption spectra of metalloporphyrins are largely similar regardless of the coordinated metal ion,[13] indicating that absorption in the visible region of the spectrum is due to π–π* transitions.

The Gouterman four orbital model can be used to describe these transitions.[14] The HOMO of an unsubstituted metalloporphyrin monomer with D_{4h} symmetry consists of two orbitals, a_{1u} and a_{2u}, which are close together in energy. The LUMO consists of two orbitals $e_{g(x)}$ and $e_{g(y)}$, which are degenerate due to the porphyrin symmetry. Instead of producing two coincident absorption bands due to $a_{1u} \rightarrow e_g$ and $a_{2u} \rightarrow e_g$ transitions, the transitions interact with one

another in a process of configurational interaction. Constructive interference of the transitions results in the high intensity B band; destructive interference gives the weaker Q band (Figure 1.2). In phthalocyanines, the energies of the a_{1u} and a_{2u} π orbitals are further apart in energy,[15] so configurational interaction is significantly reduced. As a result, the Q and B bands in the spectra of phthalocyanines are approximately the same intensity.[16]

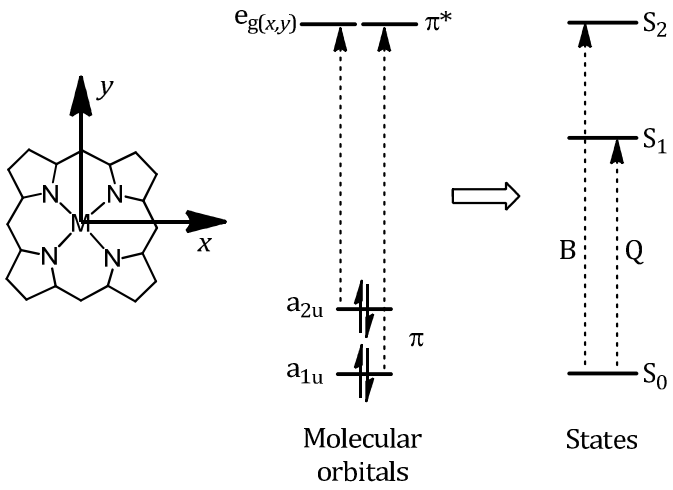

Figure 1.2 Configurational interaction of the $a_{1u}e_g$ and $a_{2u}e_g$ transitions leads to the B and Q bands seen in the absorption spectra of D_{4h} symmetric porphyrin monomers.

1.1.4 Fundamentals of energy transfer

The processes which occur in a molecule after photoexcitation can be summarised in a Jablonski diagram (Figure 1.3).[17][18]

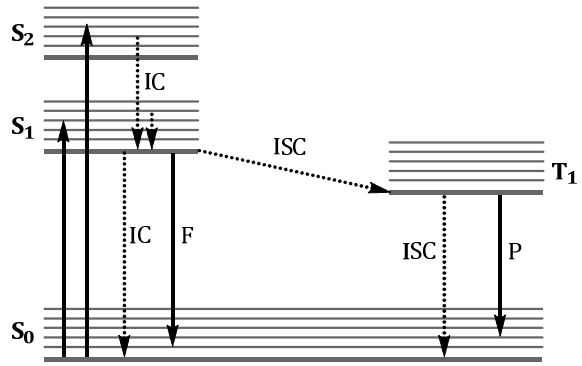

Figure 1.3 A Jablonski diagram showing the absorption and emission pathways following radiative excitation. IC = internal conversion; F = fluorescence; ISC = intersystem crossing; P = phosphorescence. Solid arrows represent radiative pathways; dotted arrows represent non-radiative processes.

When a photon of electromagnetic radiation is absorbed, an electron is promoted from the ground state S_0 to a singlet excited state (S_1, S_2, S_3… S_N). Relaxation from higher excited states to S_1 can occur *via* internal conversion on a femtosecond timescale. Further non-radiative relaxation can subsequently occur to the ground state. Emission of a photon from a singlet excited state to the ground state is called fluorescence, and occurs on a pico- or nanosecond timescale. Alternatively, the excited electron can undergo a 'spin-flip' to a triplet excited state in a process called intersystem crossing. As in the singlet state, the triplet state can decay without emitting radiation, or by releasing a photon, which is termed phosphorescence. As this is a spin-forbidden process, phosphorescence has a significantly longer lifetime, on the order of 10^{-6}–10^{-3} seconds for porphyrins. Finally, both the singlet and excited state can relax by energy or electron transfer to another chromophore.

1.1.5 Excitation energy transfer

Excitation energy transfer (EET) is a radiationless process where an excited donor molecule relaxes to the ground state, promoting an acceptor chromophore to an excited state. A number of mechanisms have been proposed to explain EET processes. Resonance transfer, first

proposed by Förster,[19] describes long range energy transfer where the separation of the donor and acceptor greatly exceeds the sum of their van der Waals radii. The mechanism relies on the interaction between the transition dipole moments of the chromophores. The rate constant for Förster energy transfer $k_{D^*\rightarrow A}$ can be calculated[20][21]

$$k_{D^*\rightarrow A}^{Förster} = \tau_D{}^{-1}\left(\frac{R_F}{R}\right)^6 \qquad \text{Eq. 1}$$

where R is the donor-acceptor separation distance; τ_D is the mean lifetime of the donor excited state, and R_F is the Förster radius, which can be expressed as a function of the overlap integral of the donor emission $F_D(\upsilon)$ and acceptor absorption $F_A(\upsilon)$ spectra:

$$R_F{}^6 \propto \kappa^2 \int_0^\infty F_D(\upsilon) F_A(\upsilon) \frac{d\upsilon}{\upsilon^4} \qquad \text{Eq. 2}$$

κ is a constant which factors in the relative orientation of the donor and acceptor transition dipole moments, and is usually assumed to be $2/3$ for a random distribution of chromophores, however can vary from 0 (for perpendicular arrangements) to 4 (for parallel arrangements). For fully allowed transitions (where $\varepsilon_A \sim 10^4$) with significant spectral overlap, Förster energy transfer can occur up to distances of 10 nm.

The exchange energy mechanism was described by Dexter.[22] Energy transfer in this case is dependent on the spatial overlap between donor and acceptor wavefunctions, and so is a short-range interaction. The rate constant for Dexter energy transfer $k_{D^*\rightarrow A}$ can be calculated[21]

$$k_{D^*\rightarrow A}^{Dexter} = \frac{2\pi}{\hbar} Z^2 \int f_D(\upsilon) f_A(\upsilon)\, d\upsilon \qquad \text{Eq. 3}$$

where

$$Z^2 = K^2 e^{\frac{-2R}{L}} \quad \text{Eq. 4}$$

K is a constant with dimensions of energy; L is the effective average Bohr radius; $f_D(\upsilon)$ is the donor emission spectrum, $f_A(\upsilon)$ is the acceptor absorption spectrum and R is the donor-acceptor separation distance.

1.2 Molecular wires

Conjugated polymers act like organic semiconductors, with the occupied π orbitals being the valence band and the unoccupied π* orbitals acting as the conduction band. Progress towards miniaturisation of current silicon technology to achieve faster processing times and lower power consumption has a finite limit. Conjugated polymers can be envisaged as molecular wires for nanoscale electronics, and provide a potential solution to the limits of traditional inorganic semiconductors.

Polymers offer several advantages. Synthetic modification of the polymer structure or morphology can allow tuning of emission wavelength, electron affinity and ionisation potential.[23] Traditional inorganic semiconductors require expensive high temperature or high vacuum processes in device fabrication. Polymers on the other hand, can be self-assembled from solution using spin casting, dip coating, or most recently, inkjet printing[24] to create structures with high charge-carrier mobilities.[25][26] The flexibility of polymers, relative to solid-state inorganic materials, allows deposition on a wide range of substrates, allowing the creation of flexible electronic devices. This has seen conjugated polymers being used in electroluminescent devices,[27][28][29][30] transistors[31][32][33] and photovoltaic[34][35] applications.

The strong optical oscillator strength, polarisability and ability to tune the properties of porphyrins either by coordination chemistry or peripheral substitution makes them ideal for creating low band-gap materials. In order to act as molecular wires, porphyrin polymers must be able to transport charge over long distances. The wires therefore, must be fully π-conjugated to enable strong electronic communication between chromophores. In the following section, the effect of backbone linkers on the π-conjugation of porphyrin wires will be discussed.

1.2.1 Butadiyne-linked porphyrin oligomers

The first example of alkyne-linked porphyrin dimers was reported in 1978 with the synthesis of a *meso*-*meso* butadiyne linked porphyrin dimer **7** (Figure 1.4).[36][37]

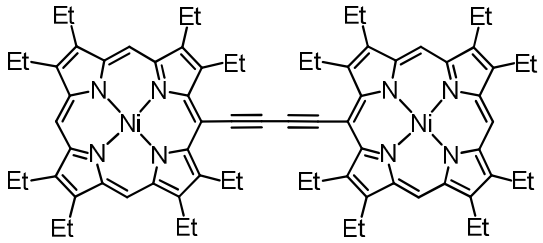

7

Figure 1.4 Arnold's butadiyne linked porphyrin dimer.

The unusual properties of these molecules was not recognised until 1994 with papers by Therien[38] and Anderson,[4] which reported the synthesis and properties of alkyne-linked porphyrin oligomers **8**–**9** and **10**, respectively (Figure 1.5).

a)

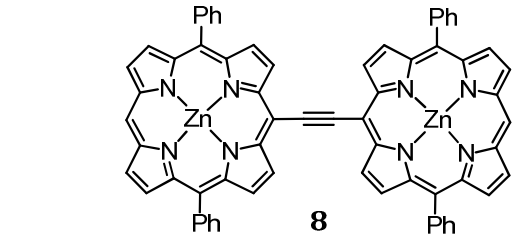

8

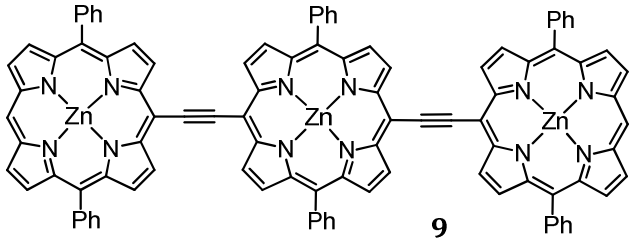

9

b)

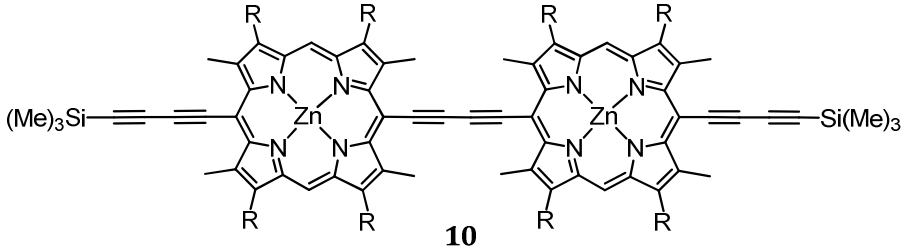

10

Figure 1.5 a) Therien's ethyne *meso-meso* linked porphyrin dimer **8** and trimer **9**. b) Anderson's butadiyne linked porphyrin dimer **10**; R = isodecyl ester.

Therien used a single ethyne linker to link porphyrins at the *meso*-positions. Both dimer **8** and trimer **9** showed split B bands and red-shifted, intensified Q bands relative to reference monomers,[a] with the dimer showing a wavelength absorption maximum of 683 nm, and the trimer at 802 nm. This indicated an approximate coplanar arrangement of porphyrins with a strong ground state electronic interaction (see Section 1.2.2).

Anderson's butadiyne-linked porphyrin dimer showed greater electronic communication between porphyrins with a Q band centred at 703 nm. The Soret band showed strong excitonic splitting of 76 nm, far greater than the 10 nm predicted by theory. Point dipole theory assumes

[a] (5,15-diphenylporphinato)zinc has a Q band centred at 540 nm.

no electronic interaction between chromophores; the much larger splitting shows that the two chromophore wavefunctions overlap on the central butadiyne.

The absorption spectrum of porphyrin trimer **9** showed a 1903 cm^{-1} mode vibronically coupled to the electronic excitation. This was assigned to a –C≡C– stretch, which typically lies at 2150 cm^{-1}. The red shifting of this vibration is frequently seen in acetylenes bonded to conjugated organic molecules, suggesting significant cumulenic character of the alkyne bridge (Figure 1.6).

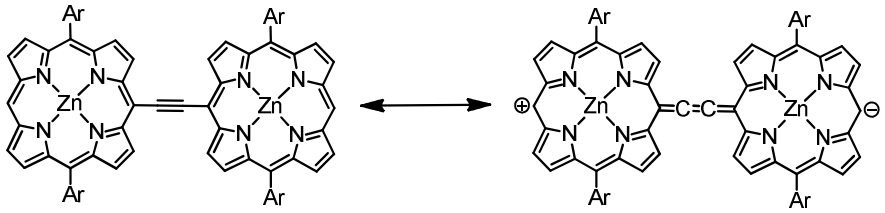

Figure 1.6 Resonance structures of a *meso-meso* ethyne linked porphyrin dimer, showing aromatic structure (*left*) and cumulenic structure (*right*).

To reduce the HOMO-LUMO gap further, various pro-quinoidal spacers were inserted into the butadiyne bridges to stabilise this cumulenic structure. Insertion of a 9,10-anthrylene spacer (Figure 1.7a) red shifted emission by 71 nm.[39] Introduction of a benzobis(thiadiazole) (Figure 1.7b) gave a strong increase in π-conjugation, with the Q band shifting to 1006 nm.[40]

a)

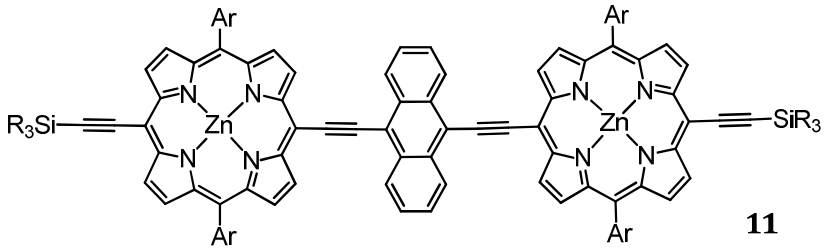

b)

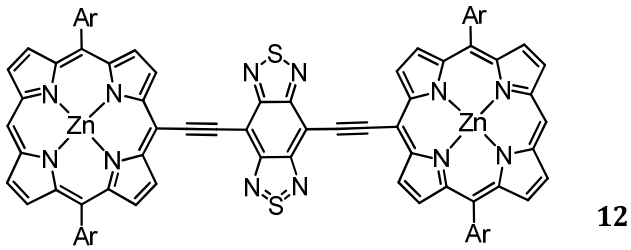

Figure 1.7 a) Anderson's 9,10-anthrylene stabilised porphyrin dimer **11**; R = *n*-hexyl, Ar = 3,5-di(*tert*-butyl)phenyl. b) Therien's benzobis(thiadiazole) stabilised porphyrin dimer **12**.

Meso-aryl linkers have been extensively explored as bridge units for porphyrin oligomers, including paraphenylene,[41][42] biphenyl,[43][44] naphthyl,[45] and anthracenyl[42][43][44][45][46] groups. However, due to the steric clash between the aryl bridge and *β*-pyrrole protons, the aryl groups are held approximately orthogonal to the plane of the porphyrin: a search of the Cambridge Crystallographic Database[47] for *meso*-aryl *β*-unsubstituted Zn(II), Cu(II), Ni(II) or free base porphyrins shows the mean porphyrin-aryl plane angle is 73°. As a result, *meso*-aryl bridged porphyrin oligomers are not π-conjugated.

Alkene linkers usually provide better electronic communication between chromophores than the corresponding alkyne[48] because of poor sp-sp^2 orbital overlap in the latter.[49] In the case of porphyrins however, the steric clash between alkene and *β*-pyrrole protons causes the bridge to twist 45° out of the porphyrin plane,[50] resulting in only partial π-conjugation.

Azo groups have been explored as an isoelectronic alternative to alkenes.[51] Although the crystal structure of nickel porphyrin dimer **Ni-13** showed a 37° deviation from planarity, the azo linker was shown to be a superior electronic bridge, with the absorption Q band for the

zinc porphyrin **Zn-13** at 841 nm.[52] However, difficulties in extending the synthesis to longer oligomers limit the azo group as a porphyrin linker.

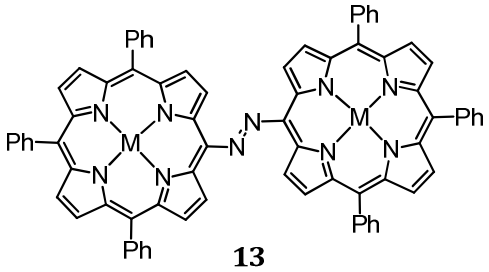

Figure 1.8 Arnold's azo-bridged porphyrin dimer **13**; M = Ni, Zn.

Meso-meso directly linked porphyrin oligomers up to the 128-mer have been synthesised by Osuka *et al*.[53][54][55] Despite the remarkable length of these oligomers, only modest changes in Q band absorption wavelength and fluorescence are observed relative to the monomer due to the orthogonal arrangement of adjacent porphyrins. The porphyrins can be planarised by introduction of bonds between adjacent *β*-positions to give triply *meso-meso*, *β-β*, *β'-β'* linked porphyrin tapes **14·*N*** (Figure 1.9).

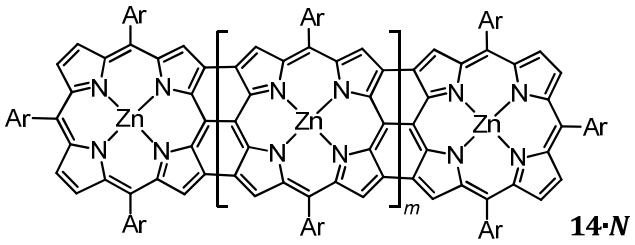

Figure 1.9 Osuka's *meso-meso*, *β-β*, *β'-β'* triply fused porphyrin tapes **14·*N***; *m* = 0 – 10.

Oligomers up to the dodecamer were synthesised.[56] The absorption spectrum of fused porphyrin dimer **14·2** showed the Q band shifted to 1068 nm,[57] and the dodecamer maximum absorption peaking in the infrared at 2857 nm. This extreme reduction of the HOMO-LUMO

gap on fusion makes the triply fused porphyrin tapes the most π-conjugated molecular wires to date.

1.2.2 Torsional effects

The crystal structure of butadiyne-linked porphyrin dimer shows that in the solid state the two porphyrin macrocycles prefer to lay coplanar, with an average deviation from planarity of ± 0.391 Å (Figure 1.10).[58] In solution however, there is a balance between rotational freedom and maximum π-conjugation.

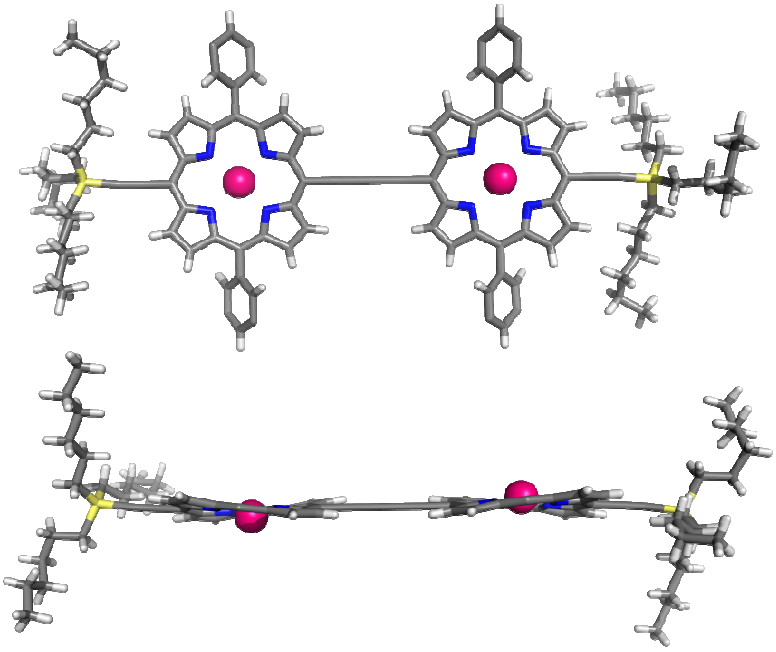

Figure 1.10 Crystal structure showing face on (*top*) and edge on (*bottom*) views of a *meso-meso* butadiyne linked porphyrin dimer ***l*-P2**.[58] Coordinating pyridine and selected ^{t}Bu and aryl side chains are omitted for clarity.

Extending the π-system from a porphyrin monomer ***l*-P1** to a porphyrin dimer ***l*-P2** results in splitting and broadening of the B band and significant red-shifting of the Q band. Kasha used a point-dipole coupling theory to account for the shape of the absorption spectra.[59] The B band

consists of two components, B_x and B_y, which are equivalent in the porphyrin monomer due to symmetry. In the dimer, the *x* and *y* directions are no longer equivalent, removing the degeneracy of the e_g π* orbitals. If the *x*-axis is placed along the long axis of the molecule,[60] then two different transition dipole couplings are possible. Transition dipoles aligned on the *y*-axis are parallel to one another, as shown in Figure 1.11. If the transition dipoles on the individual monomer units are coupled in opposite directions, this leads to a stabilisation in energy. However, the sum of the two dipole moments is 0, so this transition is not allowed. If the two transition dipoles are in the same direction, this leads to an increase in the energy of the excited state, with a sum vector of 2μ (where μ is the transition dipole moment of an individual monomer subunit). This leads to a blue-shifting of the B_y transition.

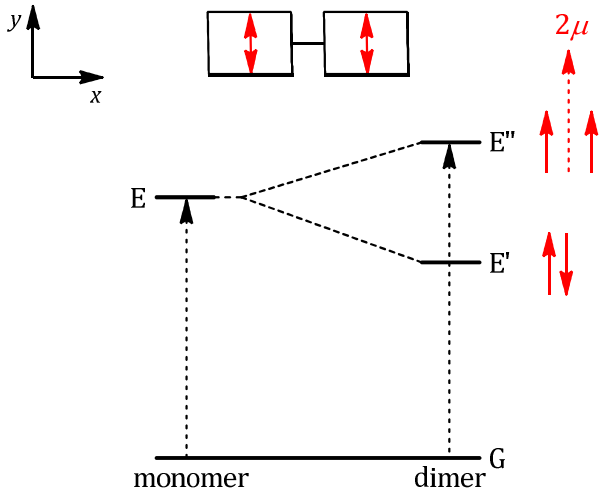

Figure 1.11 Parallel transition dipoles aligned on the *y*-axis leads to a blue shift of absorption.

Similarly, if the transition dipoles are in-line with the *x*-axis (Figure 1.12), only the transition where the individual dipole moments are arranged head-to-tail is allowed. This is an attractive interaction when considered electrostatically, and the B_x component is red shifted relative to the monomer.

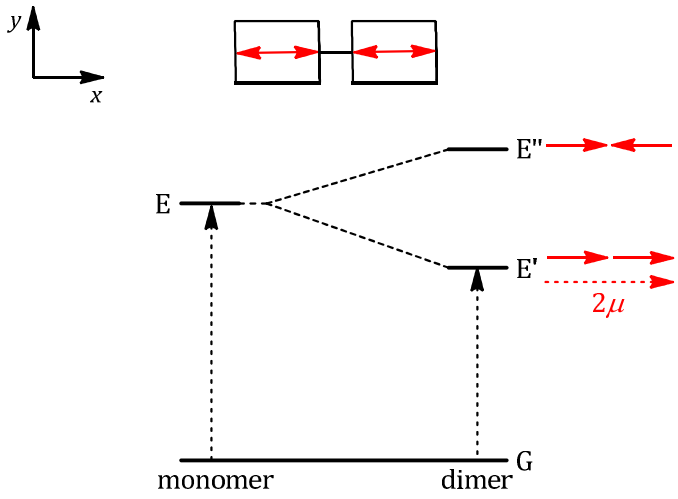

Figure 1.12 Parallel transition dipoles aligned on the *x*-axis leads to a red shift of absorption.

According to the point-dipole approximation, the exciton coupling ΔE can be estimated using Equation 5.

$$\Delta E = E'' - E' = \frac{2|\mu_u \mu_v|}{r_{uv}^3}(\cos\alpha + 3\ \cos^2\theta) \qquad \text{Eq. 5}$$

where μ_u *and* μ_v are the transition dipole moments for the singlet-singlet transitions of chromophores *u* and *v*, r_{uv} is the centre-to-centre distance, α is the torsional angle about the molecular axis and θ is the angle between the polarised axes of the component units (Figure 1.13).

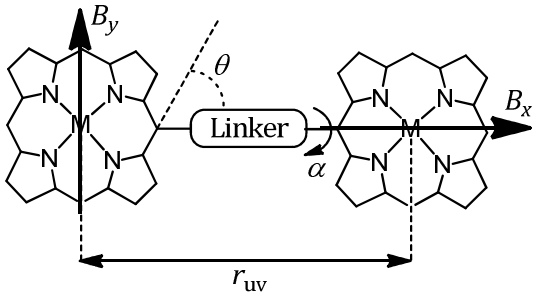

Figure 1.13 Porphyrin dimer showing the parameters α, θ, and r_{uv}.

From Equation 5, the exciton coupling strength is inversely proportional to the distance between the monomer subunits cubed, and proportional to the square of the transition dipole moment. This means the greater the absorption of the individual subunits, the greater the exciton coupling strength.

The oscillator strength f is related to the square of the transition dipole moment μ by:[61]

$$f = \frac{8\pi m_e \upsilon}{3he^2}\mu^2 \qquad \text{Eq. 6}$$

where m_e is the mass of an electron, υ is the energy in wavenumbers, h is Planck's constant and e is the elementary charge.

The extinction coefficient ε can be related to the oscillator strength f by[13]

$$f = 4.33 \times 10^{-9} \int \varepsilon \, d\upsilon \qquad \text{Eq. 7}$$

The maximum exciton coupling will occur at α = 0°; at α = 90°, the dimer acts as two isolated monomers (Figure 1.14a). The Q band of a porphyrin oligomer therefore reflects the distribution of torsional conformations: coplanar subunits reduce the HOMO-LUMO gap,

causing a red-shift in absorption (Figure 1.14b). The Q bands of higher oligomers are broader and more Gaussian as they are a superposition of many conformations.[4][62]

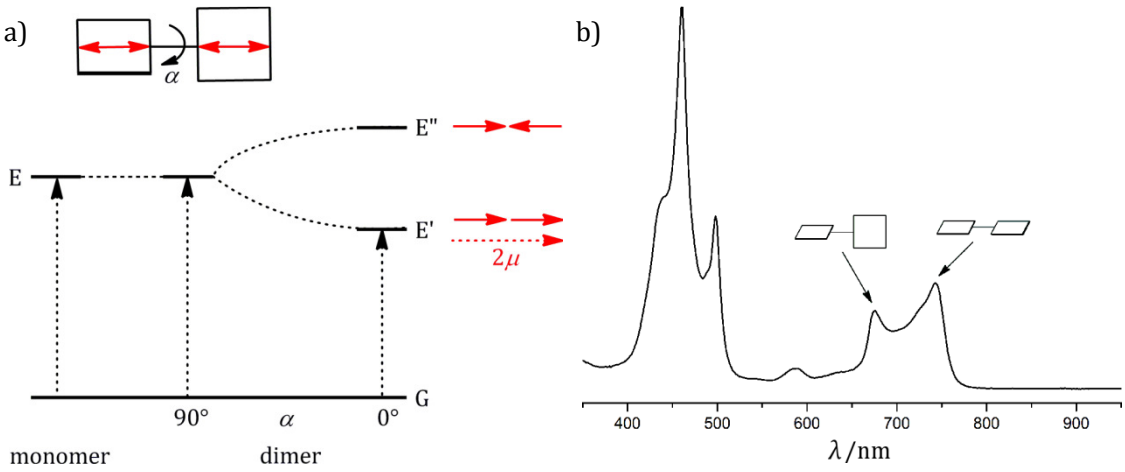

Figure 1.14 a) The effect of changing α on the exciton coupling strength ΔE. b) An absorption spectrum of a porphyrin dimer: coplanar arrangement of monomer sub-units leads to red-shifting of the Q-band.

The Q band also increases in intensity relative to the B band with increasing oligomer length (Figure 1.15). In the dimer, approximate density functional theory (DFT) shows the lowest energy excited state lies 7000 cm^{-1} below a state of the same symmetry.[63] This reduces the configurational interaction, so the Q band intensity increases, analogous to that seen for phthalocyanines.

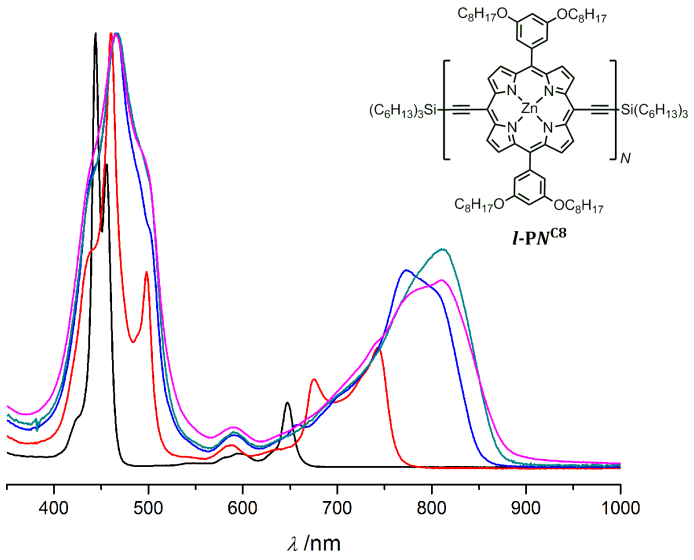

***l*-PN^{C8}**

Figure 1.15 The normalised absorption spectra of the butadiyne-linked porphyrin series ***l*-PN^{C8}**: porphyrin monomer ***l*-P1^{C8}** (*black*), dimer ***l*-P2^{C8}** (*red*), tetramer ***l*-P4^{C8}** (*blue*), hexamer ***l*-P6^{C8}** (*green*) and octamer ***l*-P8^{C8}** (*pink*). The Q band is red-shifted and more intense with increasing oligomer length.

The broad Q band of the butadiyne-linked dimer shows that, in the ground state, the two porphyrin units adopt a wide range of conformations. Approximate DFT studies by Stranger indicated barrierless rotation between dihedral angles of 0–60°, with a significant energy barrier arising at angles greater than this.[63] The 59 kJ mol^{-1} energy difference calculated between coplanar and perpendicular geometries suggested free rotation about the alkyne linker was not possible at room temperature. However, studies by Anderson using variable temperature time-correlated single photon counting (TCSPC) estimated the activation enthalpy for rotation to be ~8.4 kJ mol^{-1} in Me-THF.[62] This figure was in agreement for that previously reported.[64][65] Calculations to a BLYP/6-31G(d) level of theory also showed a very low (2.9 kJ mol^{-1}) barrier to rotation in the ground state. This energy difference increased dramatically to 16.4 kJ mol^{-1} in the excited state reflecting the enhanced cumulenic character of the molecule. The potential energy peaked at 90°, showing the excited state has strong preference for planarity (Figure 1.16). This finding was supported experimentally by Therien,

where a 30–35 ps transient red shift of emission was assigned to planarisation of the S_1 excited state, with a subsequent increase in π-conjugation.[66]

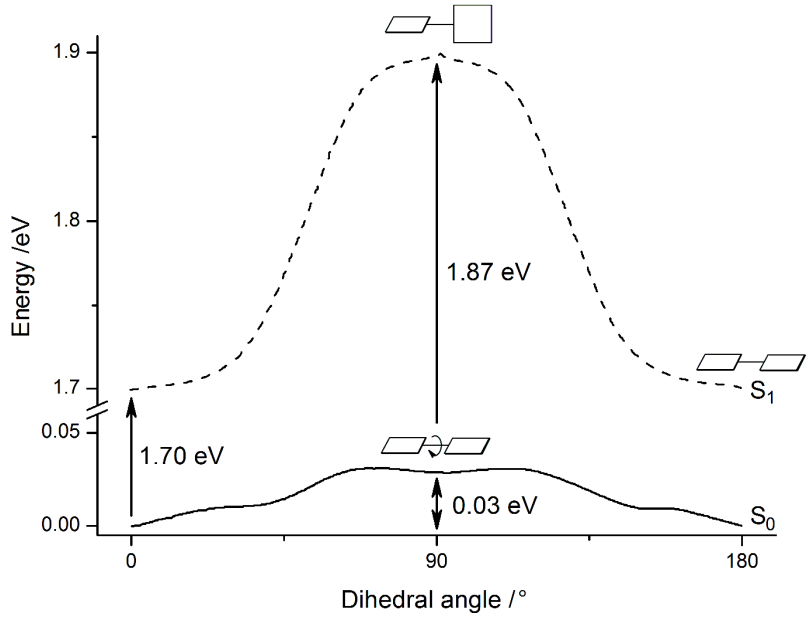

Figure 1.16 S_0 and S_1 potential energy surfaces plotted as a function of dihedral angle for a butadiyne-linked porphyrin dimer.

Strategies for restricting torsional motion of the conjugated polymer substituents have been explored to enhance effective conjugation length. Formation of rigid rod multi-stranded complexes *via* aggregation has shown to cause a red shift in the absorption of poly(thiophenes).[67][68] Titration of porphyrin oligomers ***l*-P2**–***l*-P6** with a diamine ligand such as 1,4-diazabicyclo[2.2.2]octane (DABCO),[4][69] 4,4'-bipiperidine (BIPIP),[4] or 4,4'-bipyridine (BIPY)[4][69] leads to all-or-nothing formation of ladder complex $\mathbf{(}\boldsymbol{l}\mathbf{\text{-}PN)_2{\cdot}L_N}$ (Scheme 1.3). Torsional freedom was shown to still exist for dimer complex $\mathbf{(}\boldsymbol{l}\mathbf{\text{-}P2)_2{\cdot}DABCO_2}$, however, oligomers ***l*-P3**–***l*-P6** showed further splitting of the B band and a red-shift of the Q band on complexation, showing complete planarisation of the porphyrin substituents.

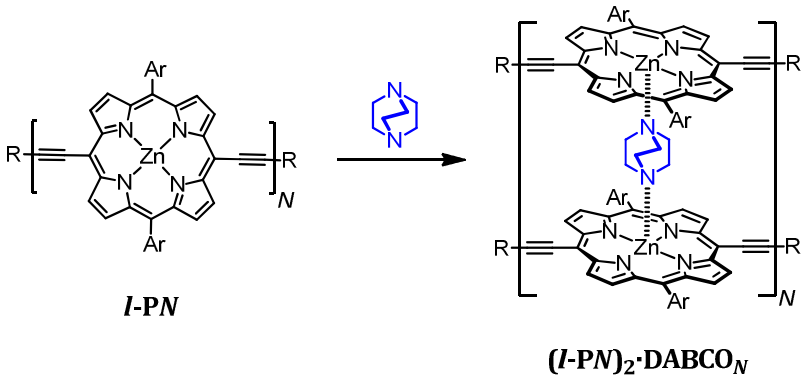

l*-P*N

(*l*-P*N*)$_2$·DABCO$_N$

Scheme 1.3 All-or-nothing formation of porphyrin ladder **(*l*-P*N*)$_2$·DABCO$_N$** by titration of butadiyne-linked porphyrin oligomer ***l*-P*N*** with DABCO; Ar = 3,5-di(*tert*-butyl)phenyl; R = trihexylsilyl.

Similar changes in the absorption spectrum are seen on titrating porphyrin dimer ***l*-P2^{C8}** with the dipyridyl pyrrole ligand **15** to form a 1:1 complex (Figure 1.17).

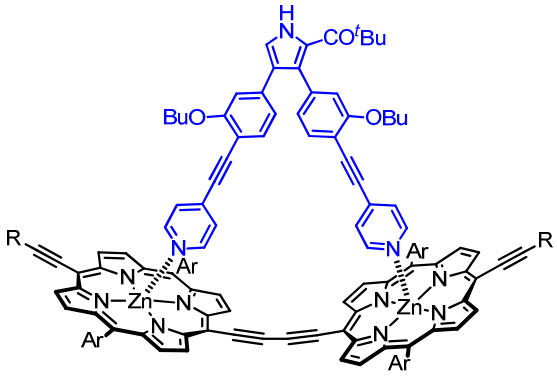

***l*-P2^{C8}·15**

Figure 1.17 Planarised butadiyne-linked porphyrin dimer ***l*-P2^{C8}** coordinated to dipyridyl pyrrole ligand **15**, to give complex ***l*-P2^{C8}·15**; Ar = 3,5-di(octyloxy)phenyl.

The pyridyl groups of the ligand **15** bind strongly to the porphyrin zinc centres, with a binding constant of K_b = 10^7–10^8 M^{-1} (Chapter 2), forcing the porphyrin substituents to planarise.[62]

1.2.3 Bending effects

Acetylenes display a surprising degree of flexibility: infrared and Raman spectroscopy measurements have estimated the average bending force constant for an alkyne C≡C–C at ~0.9–1.3 eV/radian^2;[64][70] three times lower than that of the corresponding C–C–C bonds.[71] NMR studies on alkyne-linked porphyrins **16** and **17** (Figure 1.18) in solution measured an average bending of 26° for the ethyne linker, and 31° for the butadiyne linker.[64] Electron diffraction and NMR studies of cyclooctyne have revealed a C–C≡C–C bending angle of 26°.[72]

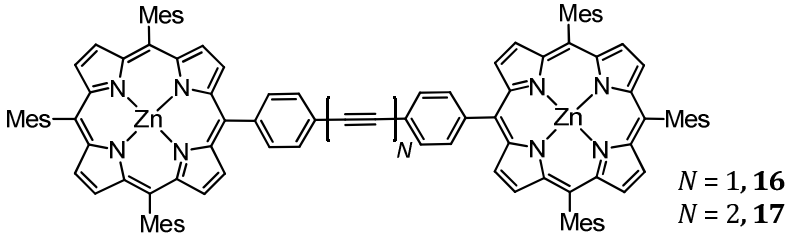

Figure 1.18 Diphenylethyne linked porphyrin dimer (*N* = 1, **16**) and diphenylbutadiyne linked porphyrin dimer (*N* = 2, **17**).

Kuhn developed a classical method based on a model by Calvin and Lewis[73] for calculating how the band gap of polyenes evolves with increasing chain length.[74] The formal double bonds of the polymer are regarded as *N* identical oscillators each vibrating with frequency E_0

$$E_0 = h\sqrt{\frac{k_0}{4\pi 2\mu_0}} \qquad \text{Eq. 8}$$

where k_0 and μ_0 are the force constant and reduced mass of the isolated oscillator, respectively.

If *N* double bonds are coupled with a force constant *k'*, then the lowest energy transition *E*, can be described

$$E = E_0\sqrt{1 + 2\frac{k'}{k_0}\cos\frac{\pi}{N+1}} \qquad \text{Eq. 9}$$

The effect of bending on the optical band gap of porphyrin oligomers was investigated by Hoffmann.[75]

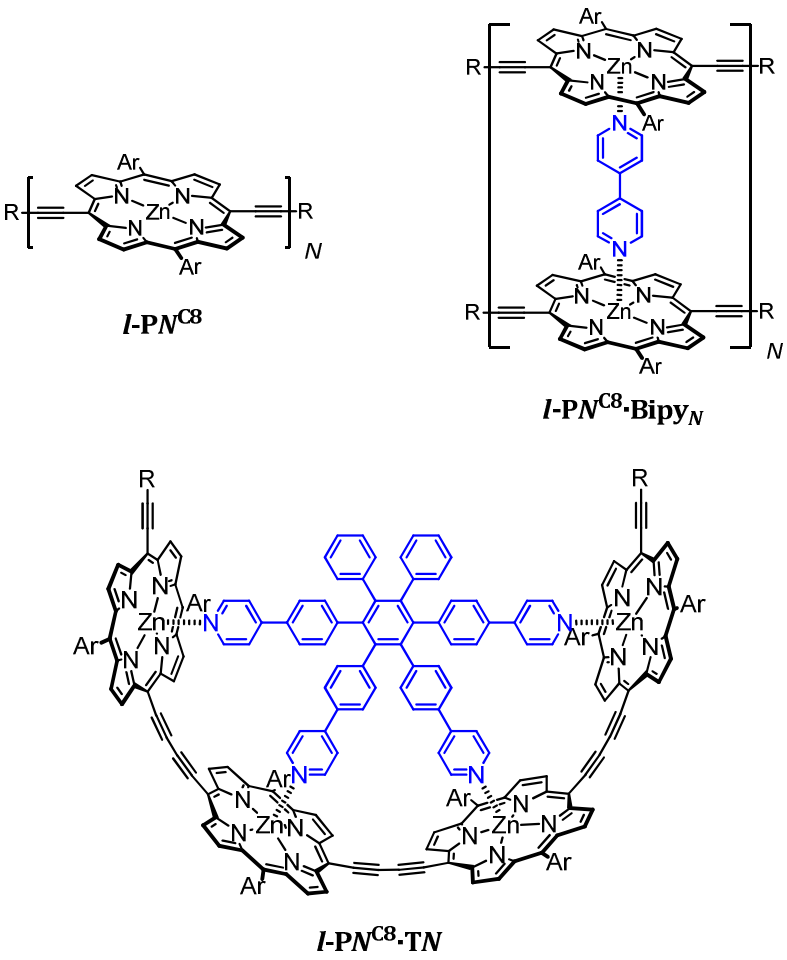

Figure 1.19 Anderson's porphyrin oligomers as the single strand ***l*-P*N*^{C8}**, the double stranded ladder complex ***l*-P*N*^{C8}·Bipy$_N$**, and as a bent oligomer around a radial template ***l*-P*N*^{C8}·T*N***; Ar = 3,5-di(octyloxy)phenyl, R = trihexylsilyl.

The band gap of single stranded, double stranded ladder complexes, and radial template-bound bent oligomers of increasing length (Figure 1.19) were plotted against reciprocal chain

length (Figure 1.20). Fitting the data to the Kuhn equation (Equation 8) gave predicted band gaps for the infinite polymer as 1.51 eV for the single strand, 1.42 eV for the ladder complex, and 1.32 eV for the bent strand.

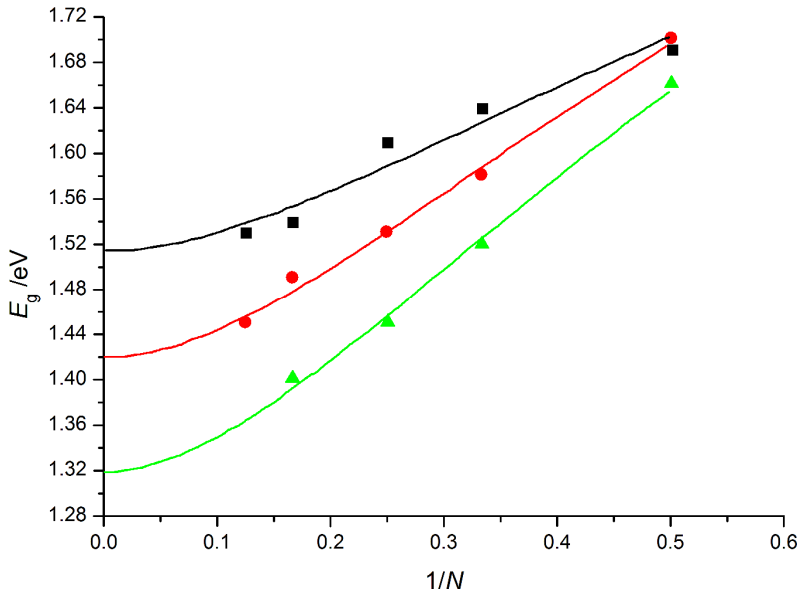

Figure 1.20 The HOMO-LUMO gap, obtained from ground state absorption spectra as a function of reciprocal chain length, for single strand oligomers (*black squares*), double stranded bipyridine ladder complexes (*red circles),* and bent oligomers around a radial template (*green triangles*). The data were fit to the Kuhn equation.

Unexpectedly, the bent polymer exhibited the lowest energy transition, showing that π-conjugation is enhanced on bending the aromatic system. This enhancement of electronic communication between chromophores cannot be solely attributed to planarisation of the porphyrin subunits: the lowest energy absorption of the bent dimer is 16 nm more red-shifted than the corresponding dimer-ladder.

1.3 Porphyrins in nature

1.3.1 Photosynthesis

Photosynthesis is a process whereby photosynthetic organisms fix solar energy into a chemically useful form. The initial "light" stages of this process occur in protein-pigment complexes embedded in the photosynthetic membrane of the cell. These protein pigment complexes known as photosystems (PS) consist of two major components: the light harvesting (LH) complex and the reaction centre (RC). The role of the LH is to capture incident solar radiation and efficiently funnel it to the RC, where the resulting charge separation powers the production of ATP, and ultimately reduces atmospheric carbon dioxide to complex sugars.

The LH complex is comprised of a protein scaffold that supports a mixture of chlorophyll and carotenoid pigments, which absorb solar radiation and transfer this energy by Förster resonance energy transfer to the RC. Chlorophylls are more saturated derivatives of a porphyrin. Plant chlorophylls have one double bond missing giving stereochemistry at two *β*-pyrrole positions and are called *chlorins*; in bacteriochlorophyll (BChl), two double bonds are missing giving stereochemistry at four sites (Figure 1.21).[76] Although the stereocentres impact on their biological properties, the 18 π electron delocalisation pathway of porphyrins is conserved, so their optical and photophysical properties are similar.

a) b)

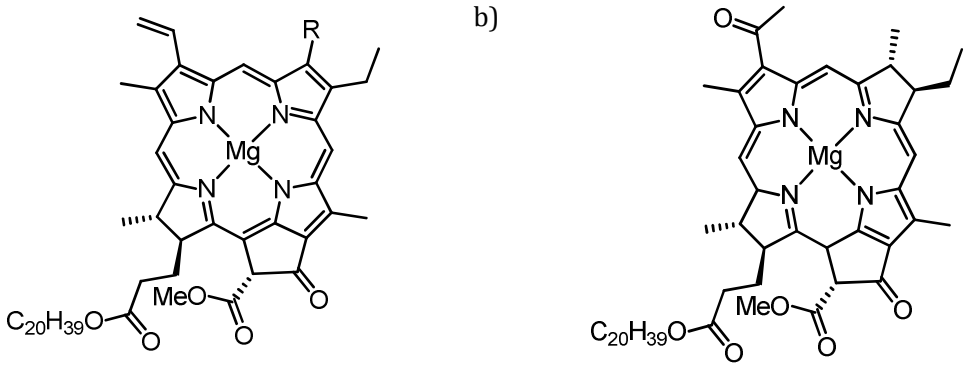

Figure 1.21 a) The general structure of chlorophyll. In chlorophyll *a*, R = Me; in chlorophyll *b*, R = CHO. b) Structure of bacteriochlorophyll *a*.

There are two distinct light harvesting systems, LH1 and LH2. In bacteria, LH1 is always present as a 1:1 complex with the RC. The expression of LH2 is regulated by light intensity: under low light conditions, the ratio of LH2 to LH1 is high;[77] in some species which occupy high intensity light environments, LH2 may be completely absent.[78]

Photosynthesis in purple bacteria begins with the absorption of a photon by LH2. The crystal structure of LH2 in *Rps. acidophila*, shown in Figure 1.22, is built up of two concentric rings of bacteriochlorophyll *a* (BChl *a*) molecules.[79]

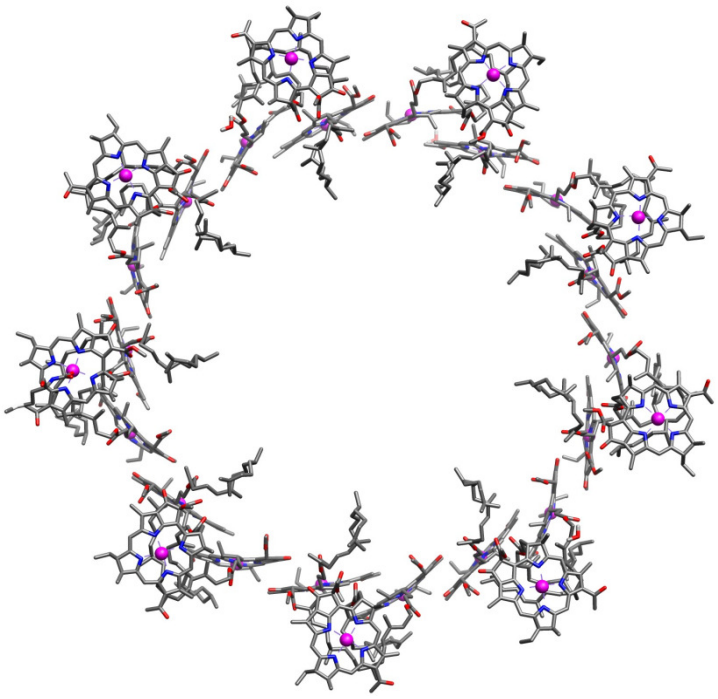

Figure 1.22 Crystal structure of LH2 from *Rhodopseudomonas acidophila* to 2 Å resolution. The structure consists of eighteen closely overlapping B850 molecules in the outer ring (Mg–Mg distance of 8.7 Å and 9.7 Å), and 9 monomeric B800 molecules (Mg–Mg distance of 21 Å) in the inner ring.

The inner ring consists of nine monomeric BChl *a* molecules lying planar to the membrane surface, with a Mg–Mg distance between adjacent chromophores of 21 Å. The central five-coordinate magnesium ion of the BChl *a* ligates to a methionine residue on the protein scaffold providing structural stability. These pigments have a λ_{max} of 800 nm, therefore are termed B800. The outer ring lies 16.5 Å above the B800 ring and comprises of 18 BChl *a* molecules lying perpendicular to the photosynthetic membrane. These pigments are in van der Waals contact with one another, but with alternating Mg–Mg distances of 8.7 Å and 9.7 Å can be considered as 9 closely associated dimers. The absorption maximum for these BChl *a* molecules comes at 850 nm, so these bacteriochlorins are termed B850.

The different absorption maxima of the chemically identical B800 and B850 reflect their different environments. Factors such as environment polarity, macrocycle deformation and ligands effect red shifting of the Q_y transition from 770 nm of the "free" bacteriochlorin,[80] however quantum mechanical calculations have shown aggregation to be the major cause of the 50 nm discrepancy.[81] On going from two independent BChl *a* monomers to a closely associated dimer, the first singlet excited states mix to give two exciton bands, one of higher and one of lower energy. The resulting red shift increases with the size of the aggregate, thus the 18-mer outer ring of LH2 has a red shift of 50 nm compared to that of the monomeric outer ring.

The photon absorbed by the outer B800 ring of LH2 is transferred to the lower energy B850 inner ring. The excitation energy is then transferred to the second photosynthetic system, LH1. The crystal structure of LH1 from *Rps*. *palustris* revealed 30 BChl *a* molecules arranged in an open ring configuration of diameter 110 Å by 95 Å (Figure 1.23).[82][83] These BChl *a* molecules have a λ_{max} of 875 nm, and it has been suggested that the larger size of the aggregate accounts for the further red shifting exhibited in these pigments.

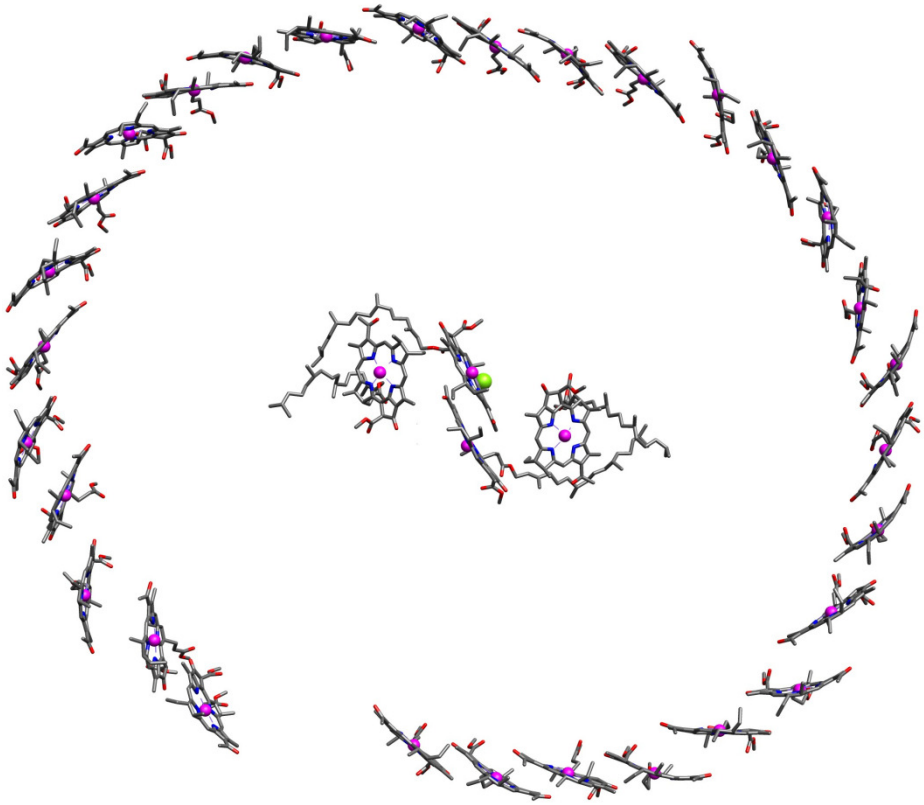

Figure 1.23 Crystal structure of the reaction centre-light harvesting complex 1 (RC-LH1) from *Rhodopseudomonas palustris* at 4.8 Å resolution. Due to the resolution limit, the orientation and position of the bacteriochlorophylls are of low accuracy.

The reaction centre is situated in the centre of LH1 (Figure 1.23). The energy captured by the antenna system funnels down an energy gradient to a closely associated BChl *a* dimer within the RC, exciting a single electron. This electron is shared over the dimer, also known as the "special pair". A series of electron transfers follow, hopping first to the bacteriopheophytins (Bphe), a free base bacteriochlorin, a process facilitated by a neighbouring BChl *a* molecule, and finally reducing a quinone.[84] The quinone shuttles out of the LH complex through the gap in the antenna ring (Figure 1.23) to continue the "dark" portion of the photosynthetic reaction.

1.4 Conclusions

An overview of the synthesis and photophysical properties of porphyrins and their oligomers has been carried out. In particular, methods of optimising electronic communication between porphyrin subunits by control of oligomer linker and inter-porphyrin torsional angle have been discussed with a view towards molecular wires. Single stranded butadiyne-linked porphyrin oligomers show strong π-conjugation, and this optical gap can be tuned by formation of supramolecular complexes. Acetylenes are surprisingly flexible, and butadiyne-linked porphyrin oligomers can be bent around a radial pyridyl-terminated template. These complexes have a smaller HOMO-LUMO gap relative to the corresponding double-stranded ladder complex or single stranded oligomer, showing that π-conjugation is enhanced on bending the aromatic system. Finally, light harvesting complexes found in photosynthetic bacteria were introduced as cyclic arrays of bacteriochlorins, and their photophysical properties were briefly discussed.

Chapter Two
Synthesis of a [12]template

This chapter begins by defining a molecular template and the thermodynamics which govern self-assembly. In continuation of the porphyrin nanoring series, a cyclic dodecamer ***c-P12*** *target is identified. As before, a complementary multidentate template is required to coordinate linear oligomers in the correct conformation for cyclisation. Molecular modelling shows 12-dentate template* ***T12*** *to have the correct dimensions for the cavity of* ***c-P12****; moreover, the template appears synthetically accessible from known compounds. Coupling conditions to construct the template are explored through the use of model systems. After 15 steps,* ***T12*** *is accessed and purification of the poorly soluble, highly polar target compound is discussed. Characterisation by NMR, MALDI-MS and GPC confirms the structure and purity of the template.*

2.1 Defining a template

Examples of molecular templates in nature are numerous, the most well-known being DNA. Watson and Crick in 1953 recognised the significance of base-pairing on DNA's ability to self-replicate.[85] One strand of DNA acts as a template for the formation of the complementary strand in replication, and for RNA in transcription. Chemists aim to mimic the complexity of biological systems through the use of rationally designed templates.

Busch provided the following definition:[86]

"A chemical template organises an assembly of atoms, with respect to one or more geometric loci, in order to achieve a particular linking of atoms."

This assembly can be mediated by metal-ligand interactions,[87] π-π stacking interactions,[88] or hydrogen bonding.[89][90] Generally, after the template has directed the formation of the product, it is removed to yield the template-free product. However, some templates operate by covalent bonds, in which case the template becomes an integral part of the final structure.[91]

2.1.1 Kinetic and thermodynamic templates

Templates can be classed as either thermodynamic or kinetic templates.[92][93][94] Thermodynamic templates operate under reversible reaction conditions. In the absence of the template, the desired product may form in addition to other products which are all in equilibrium with one another. A thermodynamic template binds preferentially to one species in solution, shifting the position of equilibrium in the favour of one product. An excellent example of this was demonstrated by Lehn,[95] where complexation of a tris-2,2'-bipyridine ligand in the presence of iron(II) sulfate gave hexanuclear complex **19**, with the sulfate ion enclosed in the centre of the cavity. Ion exchange to chloride under identical reaction conditions generated the pentanuclear complex **18**, this time with the chloride encapsulated in

the centre (Scheme 2.1). Screening of a variety of ions showed the hexanuclear complex **19** formed preferentially in the presence of large anions (BF_4^-, SO_4^{2-}, SiF_6^{2-}), whereas smaller anions, such as Cl^-, gave the pentanuclear complex **18**.

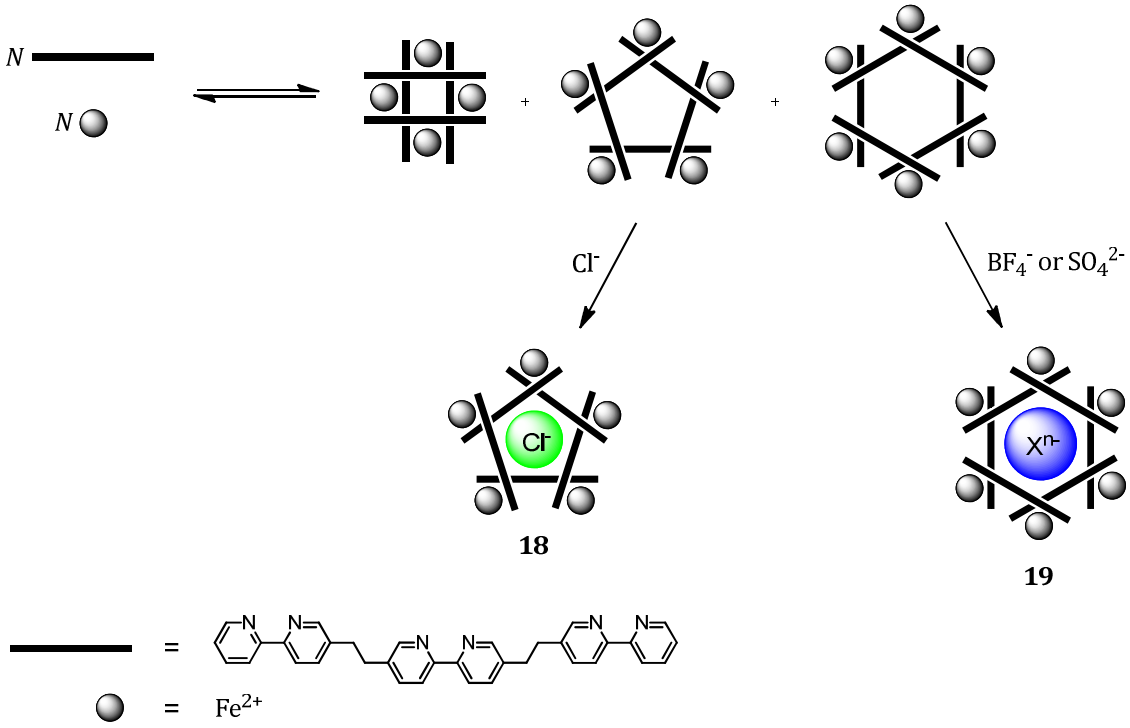

Scheme 2.1 Anions act like a thermodynamic template in the formation of polynuclear iron(II) complexes with tris-2,2'-bipyridine to selectively form one product.

The instability of a template-free product under reaction conditions provides the clearest indication of a thermodynamic template. Condensation of phthalonitrile **20** in the presence of $UOCl_2$ yields superphthalocyanine **21**. The preferred pentagonal bipyramidal coordination geometry and long U–N bond length (2.5–2.6 Å)[96] of a uranyl (UO_2) ion templates the formation of this unusual macrocycle.[97] Similarly, condensation in the presence of tricoordinate boron trifluoride gives the contracted macrocycle subphthalocyanine **22** (Scheme 2.2).[98] Removal of the central uranyl or boron atom by transmetalation or addition

of TFA sees a spontaneous transformation to the normal phthalocyanine **23**,[99] showing that they are acting as a thermodynamic template.

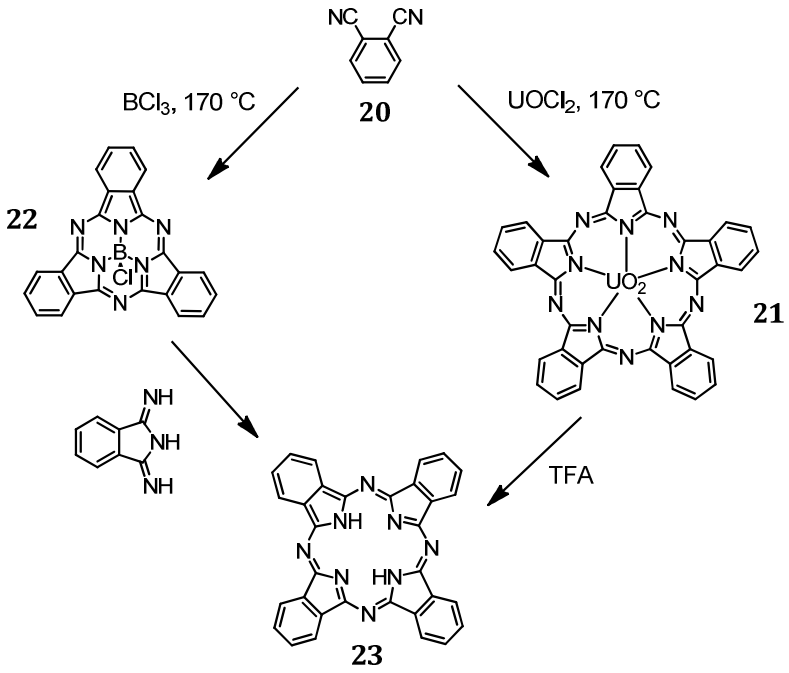

Scheme 2.2 Boron and uranyl ions direct the formation of subphthalocyanine **22** and superphthalocyanine **21**, respectively. Removal of the template results in spontaneous formation of free base phthalocyanine **23**.

Unlike thermodynamic templates which only have to stabilise the product, kinetic templates need to stabilise all the transition states leading to the product. Kinetic templates function by binding a species such that their reactive groups are held in a specific orientation and geometry to direct formation of a single product, and operate under irreversible conditions. Alkali metal cations act as kinetic templates in the synthesis of crown ethers.[100] The oxygen atoms of the oligo(ethylene glycol) chain coordinate around a potassium ion, lowering the entropy of activation $\Delta S^{\ddagger}$, and increasing the effective molarity (*EM*) of the reactive tosyl group (Section 2.3.2). This favours intramolecular cyclisation over intermolecular polymerisation, resulting in a yield of 93% for 18-crown-6 (Scheme 2.3).

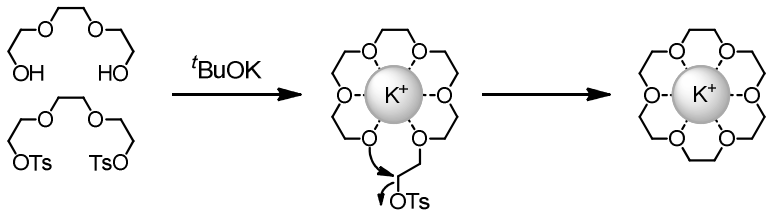

Scheme 2.3 Synthesis of 18-crown-6 is templated by a potassium metal ion.

2.1.2 Positive and negative templates

While positive templates increase the rate of formation of a product by holding the reactive groups in close proximity to one another, negative templates favour formation of a product by specifically disfavouring competitive reactions. Cyclic porphyrin dimer **25** can be synthesised from monomer **24** in the absence of template in 20–25% yield (Scheme 2.4).[101] The first step in this reaction is the dimerisation of monomer **24** to give the linear dimer ***l*-25.** In the absence of the ligand **Bipy**, intermolecular oligomerisation is favoured at moderate concentrations, and a low yield of the cyclic product results. In the presence of the ligand, the zinc centres of the linear dimer ***l*-25** coordinate to the pyridyl groups. This brings the reactive ends close together, favouring intramolecular cyclisation. In this way, **Bipy** acts as a positive template and the yield of cyclic porphyrin dimer ***c*-25** is increased dramatically to 72%. An effective molarity (see Section 2.3.2) of 34 M for **Bipy** indicates the good complementarity for the cavity of ***c*-25**.

Introduction of the tridentate template tripyridyltriazine **Py_3T** to the cyclic trimer reaction (Scheme 2.4) has a more modest impact on the yield, increasing from 34% for the untemplated reaction to 50%. The lower effective molarity of the template for the cavity of the cyclic trimer ***c*-26** (*EM* = 1 M), suggests that the template is slightly too small.

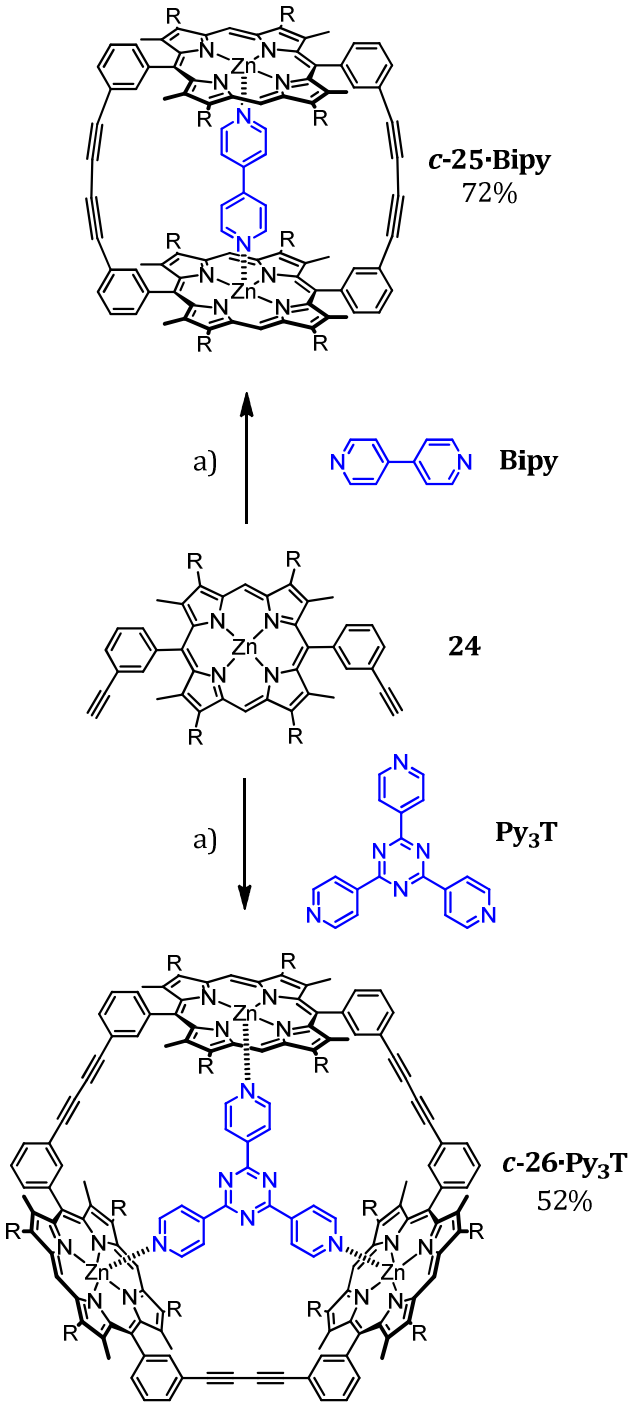

Scheme 2.4 Template directed synthesis of cyclic porphyrin dimer ***c*-25·Bipy** and trimer ***c*-26·Py$_3$T**: a) CuCl, TMEDA, CH_2Cl_2, air. R = CH_2CH_2COOMe.

In the trimerisation reaction, the intermediate linear dimer is coordinated by **Py$_3$T**, which holds the reactive ends away from one another, preventing intramolecular cyclisation. The competing formation of cyclic dimer is completely suppressed; therefore **Py$_3$T** acts as a negative template. 2,6-Dipyridylpyridine has the same geometry as **Py$_3$T** but lacks a third coordination site; cyclisation in the presence of this ligand gives a similar product distribution, showing that **Py$_3$T** as a template does not accelerate formation of the cyclic trimer ***c*-26**, but rather suppresses cyclic dimer formation.

2.2 Supramolecular self-assembly

2.2.1 Thermodynamics of porphyrin binding

As mentioned in Chapter 1, zinc porphyrins can reversibly bind an axial ligand to become five coordinate (Figure 2.1).

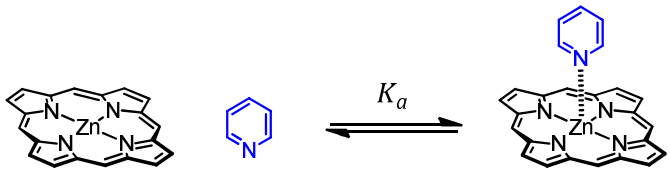

Figure 2.1 Zinc porphyrins can bind a fifth ligand reversibly in the axial position. The strength of this binding interaction can be quantified by the association constant, K_a.

Although examples of six fold coordination involving N and O ligands have been reported,[102][103][104] these are limited to the solid state; there is no concrete evidence of formation in solution. Porphyrins can bind to a variety of heteroatoms, but nitrogen is by far the most common ligating element utilised in the supramolecular complexes of Zn(II) porphyrins.

The strength of the binding interaction is quantified by the association constant K_a, which can be defined as

$$K_a = \frac{[\mathbf{PL}]}{[\mathbf{P}][\mathbf{L}]} \qquad \text{Eq. 10}$$

where **P** is porphyrin, **L** is ligand, and **PL** is the porphyrin–ligand complex.

The magnitude of K_a is affected by solvent, reaction temperature, the donating properties of the ligand, and steric hindrance. Binding constants in toluene are an order of magnitude larger than in chloroform, due to the higher dielectric constant of the latter, and its ability to solvate the ligand by acting as a hydrogen-bond donor.[105] Temperature decreases the strength of binding.[106]

The strength of association constants roughly correlates with the pK_a of the amine, which is a measure of the ligand's σ-donor properties.[107] As can be seen in Figure 2.2, the association constant K_a increases 4-cyanopyridine < pyridine < 4-aminopyridine,[108] reflecting the increased availability of the pyridine nitrogen lone pair.[109] Imidazoles exhibit anomalously high binding constants to zinc porphyrins, of an order of magnitude higher than a substituted pyridine of comparable pK_a. The increased Zn–N bond order results from π-backbonding onto the imidazole nitrogen.

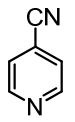

1.1×10^2 [a]

6.2×10^2 [a]

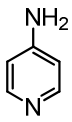

3.3×10^3 [a]

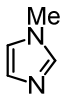

1.5×10^4 [b]

Figure 2.2 Association constants, K_a (M^{-1}) for zinc porphyrin–amine interactions. [a] Determined using UV-vis titrations with zinc tetraphenylporphine in $CHCl_3$ at 298 K.**[109]** [b] Determined by ^1H NMR titrations in $CDCl_3$ with zinc tetraphenylporphine at 293 K.**[110]**

The effect of steric hindrance on the association constant for zinc porphyrin interactions can be seen in Figure 2.3. Increasing steric bulk from primary → secondary → tertiary amine, the K_a decreases from 10^4 M^{-1} to 10^1 M^{-1}. Cyclic amines remove the effect of steric interference, and the association constants for piperidine and DABCO are correspondingly high.[111][103]

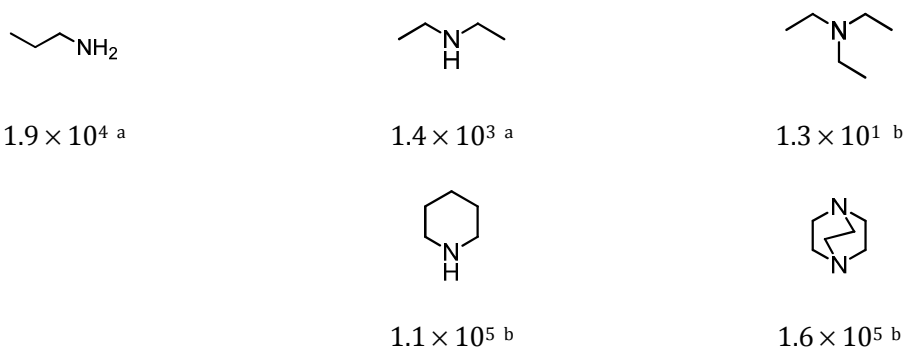

Figure 2.3 Association constants, K_a (M^{-1}) for zinc porphyrin–amine interactions. [a] Determined using UV-vis titrations with [*meso*-tetrakis(*p*-methylphenyl)porphyrinato]zinc(II) in toluene at 298 K. [b] Determined using UV-vis titrations with zinc tetraphenylporphine in benzene at 298 K.

In soft metal-ligand interactions such as the interactions between zinc porphyrins and amines, thermodynamic stabilities may not reflect kinetic parameters. Despite high association constants of $\sim 10^3$ M^{-1}, ligand exchange for pyridines occurs on a 10^5 s^{-1} timescale. Only in multi-pyridyl binding events, where cooperativity increases the binding strength to values greater than 10^6 M^{-1} (see Section 2.3), will the off-rate be slow enough to resolve free and bound species on the NMR timescale.[112][113]

2.3 Cooperativity

The binding of a monodentate ligand **B** to a monovalent receptor **A** is shown in Figure 2.4.

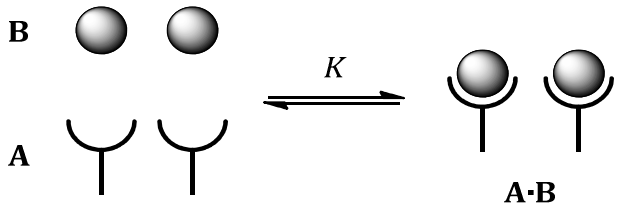

Figure 2.4 The binding of a monodentate ligand **B** to a monovalent receptor **A** to give complex **A·B** is a non-cooperative process.

The microscopic binding constant, *K*, for this process can defined simply as

$$K = \frac{[\mathbf{A} \cdot \mathbf{B}]}{[\mathbf{A}][\mathbf{B}]} \qquad \text{Eq. 11}$$

The binding of one ligand to one receptor does not influence any other binding event occurring in the system, so we describe this as *non-cooperative* binding. Progressing to a divalent receptor or bidentate ligand, the strength of a binding event can be influenced by the preceding interaction. This is a result of cooperativity, and there are two types: allosteric, and chelative.

2.3.1 Allosteric cooperativity

Figure 2.5 shows the interaction of a divalent receptor **AA** with two identical monodentate ligands **B**, with microscopic association constants K_1 and K_2 relating the three species.[114]

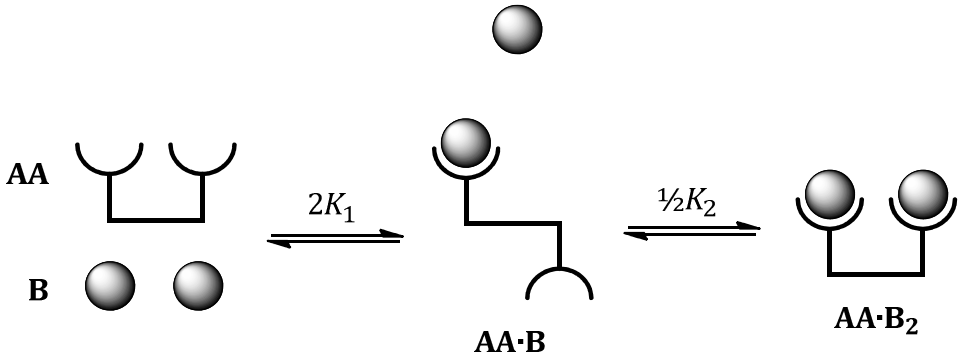

Figure 2.5 The stepwise binding of a monodentate ligand **B** to a divalent receptor **AA** to form **AA·B$_2$**. The system exhibits allosteric cooperativity if $K_1 \neq K_2$. 2 and ½ are statistical factors which account for the degeneracy of the complexes due to symmetry.[115]

K_1 and K_2 can be described by[116]

$$K_1 = \frac{[\mathbf{AA \cdot B}]}{[\mathbf{AA}][\mathbf{B}]} \qquad \text{Eq. 12}$$

and

$$K_2 = \frac{[\mathbf{AA \cdot B_2}]}{[\mathbf{AA \cdot B}][\mathbf{B}]} \qquad \text{Eq. 13}$$

The allosteric cooperativity factor α can be defined as

$$\alpha = \frac{K_2}{K_1} \qquad \text{Eq. 14}$$

If α is unity, the system shows no allosteric cooperativity, and the microscopic constants K_1 and K_2 are the same as that for the reference single site receptor–ligand interaction, K. Where $\alpha > 1$, the system displays positive cooperativity, and interactions in the fully bound state **AA·B$_2$** are more attractive than in the intermediate complex **AA·B**. When the value of α is much larger

than 1, the system exhibits 'all-or-nothing' behaviour, where the intermediate bound state is never significantly populated.

The system shows negative cooperativity when $\alpha < 1$. In this case the first binding event disfavours subsequent binding events, and so even at high concentrations of **B** the fully bound state **AA·B$_2$** is never fully populated. Negative cooperativity can often be attributed to steric repulsion between the two bound ligands.

One of the most commonly cited examples of allosteric cooperativity is the binding of oxygen to haemoglobin.[117] Haemoglobin can bind up to four molecules of dioxygen, with the binding affinity for each event increasing due to conformational changes in the protein structure. Other factors can cause positive or negative allosteric cooperativity, including long range electrostatic interactions between ligands,[118] or electronic polarisation of the receptor.[119]

2.3.2 Chelative cooperativity and effective molarity

Chelative cooperativity, unlike allosteric cooperativity, can only be positive and can still operate when the microscopic binding constant K for each binding event is equal. Consider a system where a bidentate ligand **BB** binds to a divalent receptor **AA** (Figure 2.6).[116]

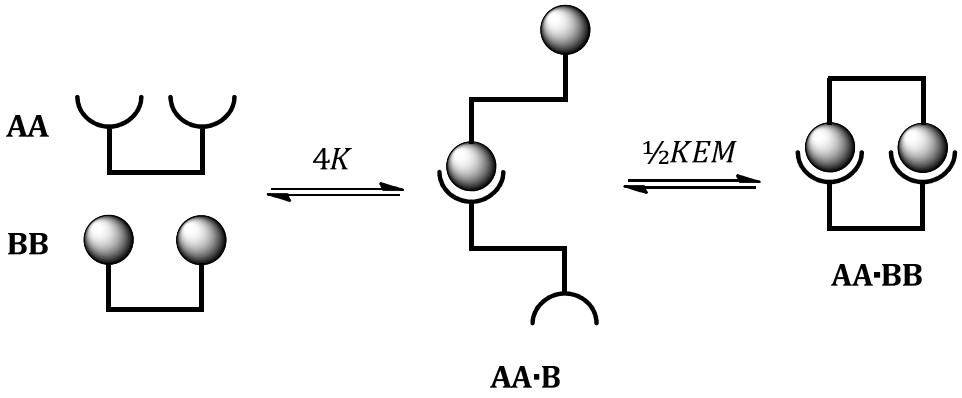

Figure 2.6 The stepwise binding of a bidentate ligand **BB** to a divalent receptor **AA**. The product *K EM* determines the extent to which the cyclic complex **AA·BB** is populated, and defines the cooperativity of the system.

The preference of the system towards forming the cyclic complex **AA·BB** is quantified by the product *K EM*, where *EM* is the effective molarity. When *K EM* >> 1, the cyclic complex **AA·BB** is more stable than the partially bound, open complex **AA·B**, and the system exhibits an "all-or-nothing" population of the cyclic complex. Dissociation back to the unbound ligand and receptor occurs only when $2[\mathbf{BB}]_0 > EM$, and so effective molarity defines the concentration at which intermolecular interactions begin to compete with intramolecular ones.

Effective molarity can be described thermodynamically:[120]

$$EM = \exp\left[\frac{-\Delta H^{\circ}_{intra} + \Delta H^{\circ}_{inter}}{RT}\right] \cdot \exp\left[\frac{\Delta S^{\circ}_{intra} - \Delta S^{\circ}_{inter}}{R}\right] \qquad \text{Eq. 15}$$

where ΔH°_{intra}, ΔH°_{inter}, ΔS°_{intra} and ΔS°_{inter} are the enthalpy and entropy changes of the intramolecular and intermolecular interactions, R is the gas constant, and T is absolute temperature. Equation 15 can be written in a simpler manner, describing it as the product of the enthalpic EM_{H} and entropic contributions EM_{S} to the effective molarity:

$$EM = EM_H \times EM_S \quad \text{Eq. 16}$$

In Equation 15, the enthalpic term ($-\Delta H^\circ_{intra} + \Delta H^\circ_{inter}$) quantifies the strain energy of the ring. If the ring has no strain, then EM_H = 1, and effective molarity is solely determined by the entropic contribution, EM_S. As EM_H is temperature dependant, if the experimentally determined effective molarity is found to be independent of temperature,[121] the cyclic assembly has no strain associated with its formation.

EM_S defines the loss of torsional entropy on cyclisation, and is a function of the number of skeletal bonds in the linear precursor, *r*. In covalent systems, the entropy cost of cyclisation at low *r* has been estimated at 5.6 kJ mol^{-1} per rotor, showing most torsional entropy is lost on cyclisation.[122] At high *r*, the rings retain a degree of flexibility and so cyclisation pays a smaller entropic penalty.

The effective molarity of non-covalent systems shows a weaker dependence on chain length, consistent with a random walk encounter of end groups model.[123]

$$EM \approx 10r^{-3/2} \quad \text{Eq. 17}$$

In contrast with covalent systems, the relationship described in Equation 17 extends to low values of *r*.

For a strain free cyclic complex, the maximum effective molarity, EM_{max} can be described by[113]

$$EM_{max} = \exp\left[\frac{\Delta S^{trans} + \Delta S^{vib}_{\mathbf{AA\cdot BB}} - 2\Delta S^{vib}_{\mathbf{AA\cdot B}}}{R}\right] \quad \text{Eq. 18}$$

where ΔS^{trans} is the rotational and translational entropy of the free ligand **BB** in solution (190 ± 20 J K^{-1} mol^{-1}), and $\Delta S^{vib}_{\mathbf{AA\cdot BB}}$ and $\Delta S^{vib}_{\mathbf{AA\cdot B}}$ are the vibrational entropies gained on formation of

the **AA·BB** and **AA·B** complexes, respectively. As the vibrational enthalpies of **AA·BB** and **AA·B** are likely to be similar, Equation 18 can be simplified to:

$$EM_{max} = \exp\left[\frac{\Delta S_{\mathbf{AA{\cdot}BB}}}{R}\right] \qquad \text{Eq. 19}$$

where

$$\Delta S_{\mathbf{AA{\cdot}BB}} = \Delta S^{vib}_{\mathbf{AA{\cdot}B}} - \Delta S^{trans} \qquad \text{Eq. 20}$$

Page and Jencks calculated the maximum theoretical effective molarity possible to be of the order of 10^8 M.[122][124] This value applied to the formation of covalent bonds; in the case of non-covalent interactions, the bonds are weaker and so vibrate at lower frequencies. This acts to increase the entropy of the self-assembled system. Ercolani calculated the EM_{max} of amine coordinated zinc porphyrin assemblies to be on the order of 10^3 M.[125] Using values of 40–50 J K^{-1} mol^{-1} for the entropy of forming a zinc porphyrin-pyridine complex,[106][126] Sanders *et al*. calculated a value of 100–400 M for the maximum effective molarity.[113]

With the exception of porphyrin ladders,[4][69] perfectly strainless systems do not occur, so experimentally determined effective molarities are considerably lower. The highest effective molarities observed are therefore seen in systems which are pre-organised to fit together. This eliminates strain caused by bending a rigid system, and minimises the loss of entropy due to torsional and conformational restrictions imposed on binding. This was best demonstrated in the binding of hexadentate template **T6** to cyclic porphyrin hexamer ***c*-P6**, which demonstrated a statistically corrected *EM* of 210 M, in contrast to the complexation of the linear analogue ***l*-dP6** with an *EM* of just 0.03 M (see following section).[127][128]

2.3.3 Template-directed synthesis of cyclic porphyrin hexamer and octamer

The strained cyclic porphyrin hexamer ***c*-P6** can be accessed by oxidative coupling[129] of linear porphyrin dimer ***l*-dP2** in the presence of template **T6** (Scheme 2.5).[128] Template **T6** has an N–N calculated distance of 20.1 Å, which, assuming a Zn–N bond length of 2.14 Å,[130] is ideal to fit in the cavity of the cyclic hexamer with a calculated inner dimension of 24.2 Å.

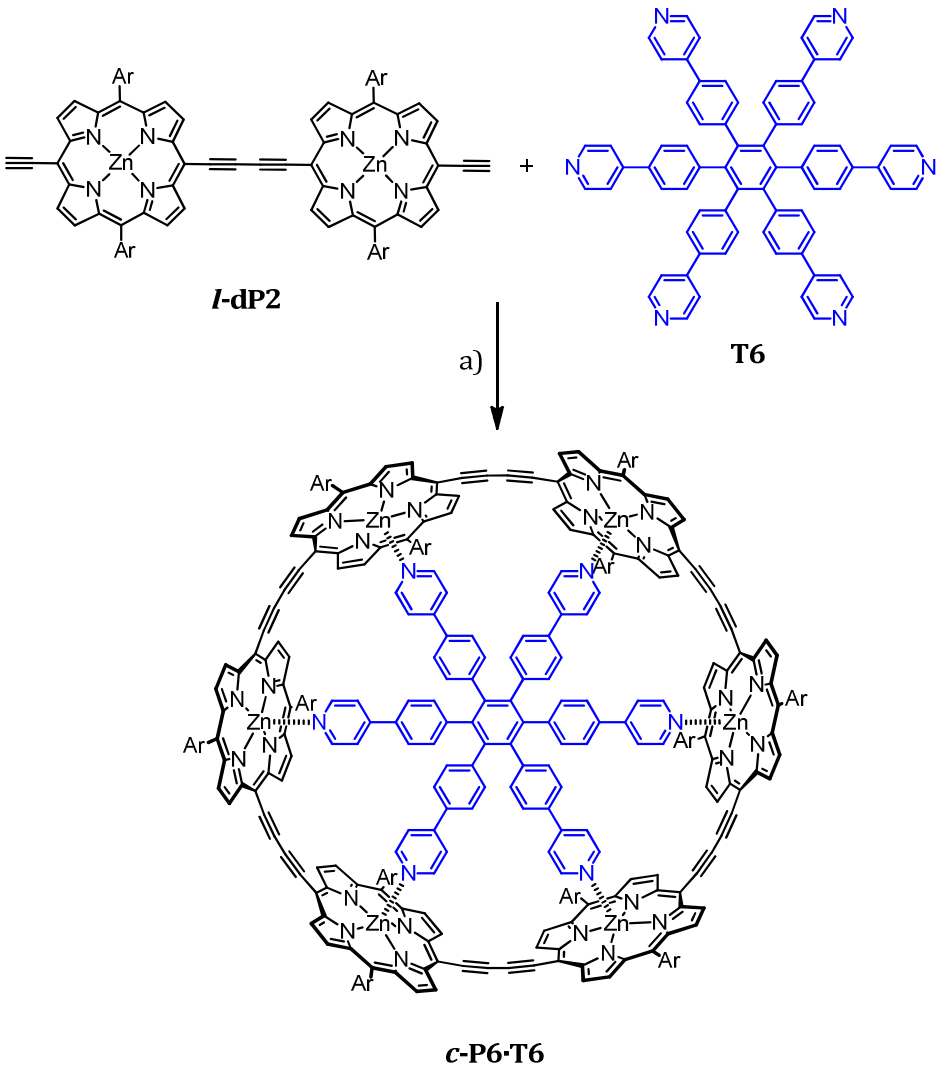

Scheme 2.5 Synthesis of cyclic porphyrin hexamer-template complex ***c*-P6·T6** from linear porphyrin dimer ***l*-dP2** and hexadentate template **T6**: a) $Pd(PPh_3)_2Cl_2$, CuI, I_2, $^iPr_2NH$, air, 60 °C. Ar = 3,5-di(*tert*-butyl)phenyl, yield 44%; Ar = 3,5-di(octyloxy)phenyl, yield 33%.

The template coordinates the porphyrin dimer, bringing the terminal acetylenes in close spatial proximity for reaction. In the presence of the template, ***c*-P6·T6** was obtained in 44% yield; in the absence, only polymeric products were isolated. The complex ***c*-P6·T6** remained intact even when dissolved in neat pyridine ([pyridine] = 12.4 M); a large excess of a more strongly coordinating amine such as quinuclidine or DABCO was required. The high concentration of the competitive monodentate ligand needed for knock-out ([quinuclidine] > 0.4 M) reflects the complementarity of the template for the cavity of ***c*-P6**.

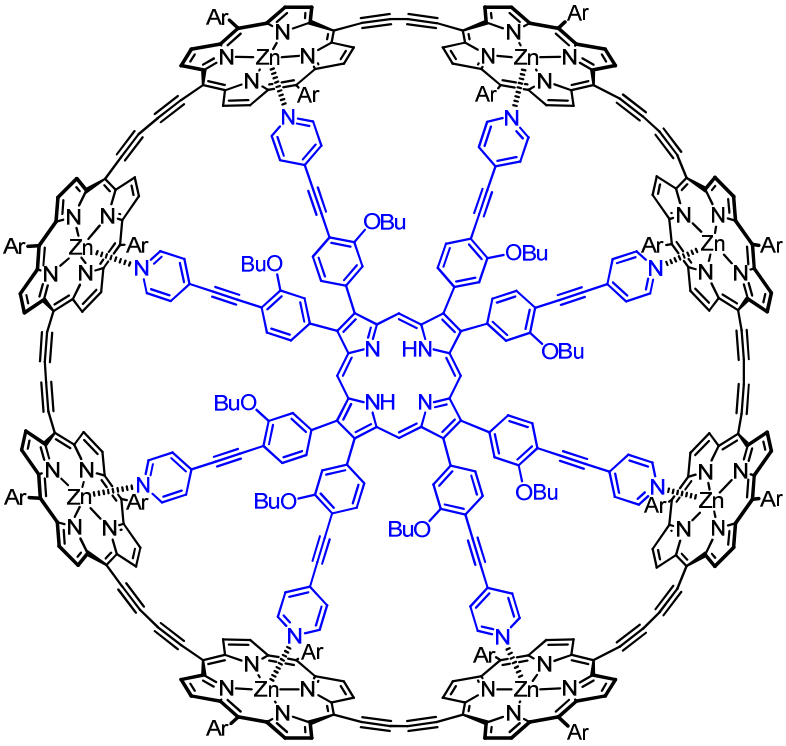

***c*-P8^{C8}·T8**

Figure 2.7 Cyclic porphyrin octamer-template complex ***c*-P8^{C8}·T8**. Ar = 3,5-di(octyloxy)phenyl.

Cyclic porphyrin octamer ***c*-P8^{C8}** (Figure 2.7) was synthesised in a similar manner.[131] Linear porphyrin octamer ***l*-dP8^{C8}** was oxidatively coupled under the same conditions in the presence of template **T8**, to give the cyclic product in 14% isolated yield. UV-Vis titrations gave a value

for the effective molarity of 5.4 M for the cyclic ***c*-P8^{C8}·T8** complex, in contrast to 0.28 M for linear ***l*-dP8^{C8}·T8**, reflecting the preorganisation of the ***c*-P8^{C8}** cavity for the template. The weaker *EM* meant that **T8** could be removed from ***c*-P8^{C8}** by addition of an excess of pyridine, unlike for the cyclic hexamer.

2.4 Results and Discussion

2.4.1 Modelling a dodecadentate template

In continuation of the series of porphyrin nanorings developed by the group, the new target of the cyclic dodecamer ***c*-P12** was selected (Figure 2.8). As in the synthesis of the cyclic hexamer ***c*-P6** and octamer ***c*-P8^{C8}**, the key step in the synthesis of the strained nanoring would be the design of a complementary template of the correct dimensions and geometry to hold the linear oligomers in a suitable position for cyclisation.

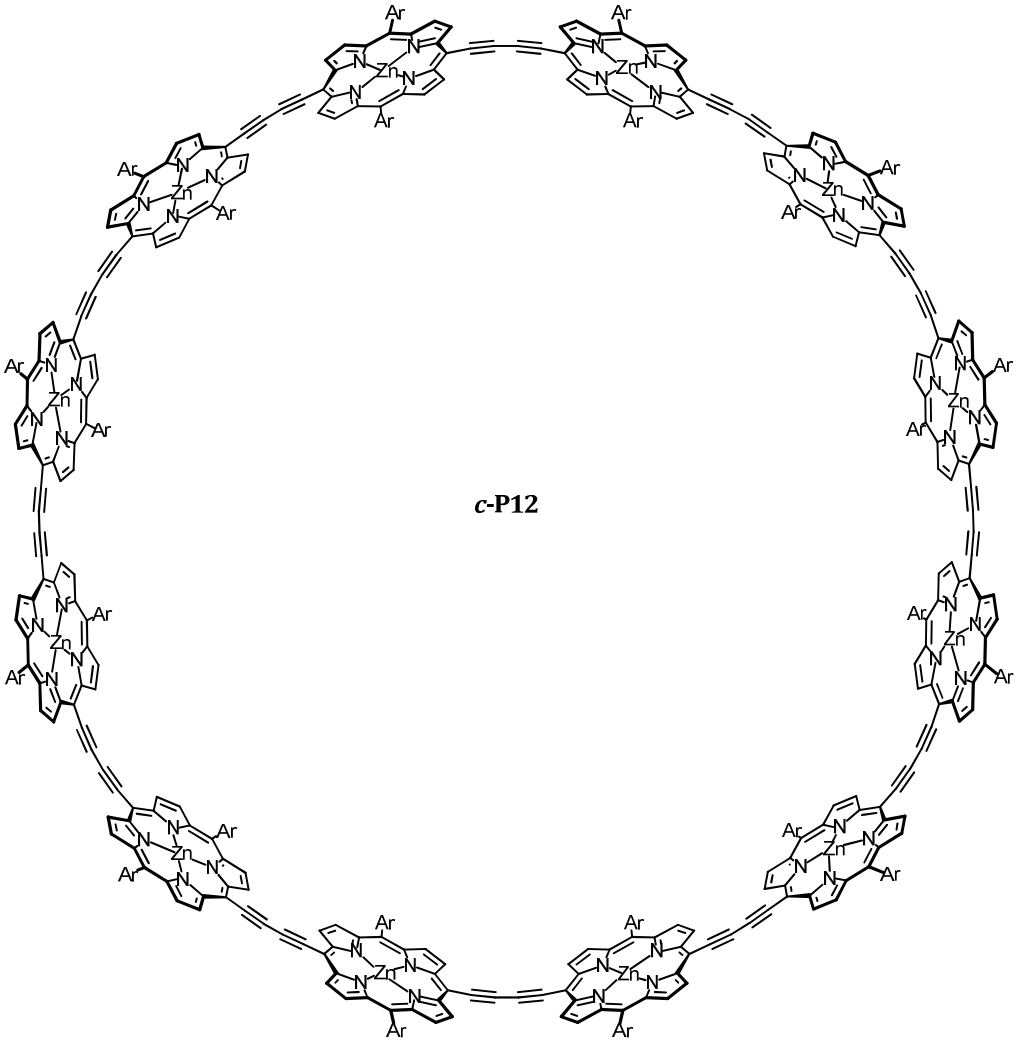

Figure 2.8 Cyclic porphyrin dodecamer target ***c*-P12**.

The main difficulty in the design of the template was finding a suitable molecule which would provide the required 12-fold symmetry. In the case of the cyclic hexamer template **T6**, the six fold symmetry originated from the central benzene; in the cyclic octamer template **T8**, the near D_{8h} symmetry was achieved by *β*-pyrrole substitution of a free base porphyrin.

With no suitable starting point, the best way to achieve twelve evenly spaced pyridyl terminated arms would be to have a 6-fold symmetry core, dividing each of these into two at an intermediate point to give a dendritric-like structure. A series of templates were explored,

and it was found template **T12** (Figure 2.9) was the most suitable candidate, both in dimensions, and synthetic accessibility.

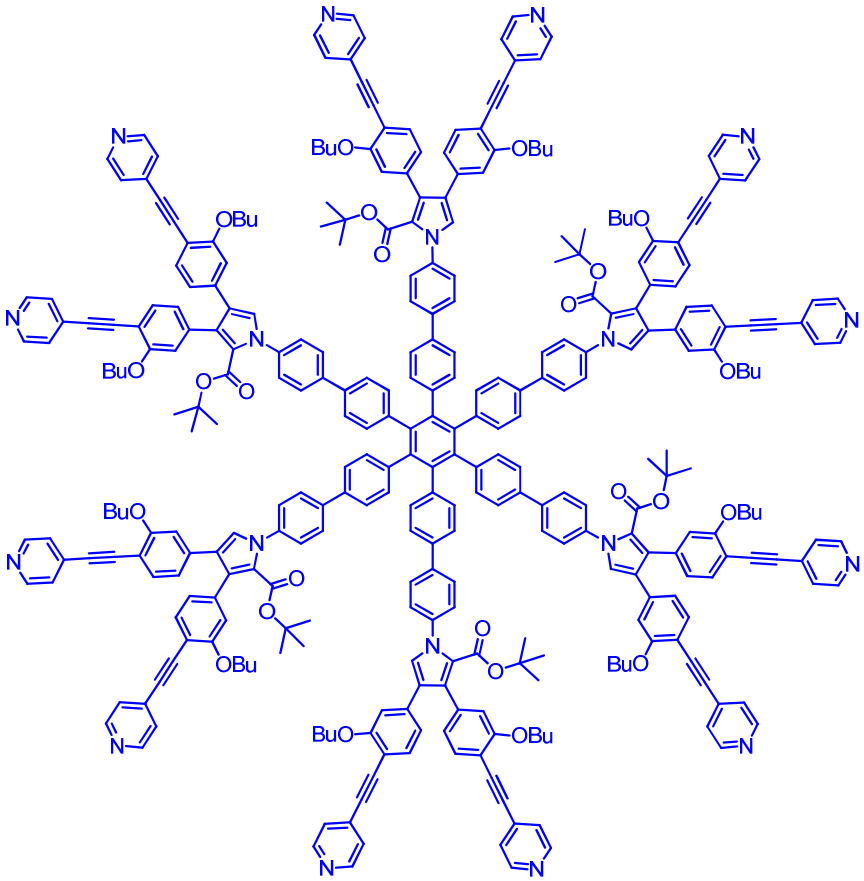

T12

Figure 2.9 Target dodecadentate template **T12**.

Cyclic dodecamer ***c*-P12** and various template candidates were modelled in Hyperchem™ using an MM+ forcefield.[132] The free cyclic porphyrin dodecamer ***c*-P12** has an optimised zinc-zinc distance (the distance between opposing zinc atoms) of 48.6 Å. A search of the Cambridge Structural Database (CSD) gives a mean zinc-nitrogen bond length of 2.157 Å,[133] and an out of plane displacement (the distance the central zinc atom sits out of the porphyrin plane) of 0.3 Å,[134] giving an ideal template diameter for the cavity of ***c*-P12** of 44.3 Å. Dodecadentate template **T12** has a calculated nitrogen-nitrogen distance (the distance between opposing

pyridyl arms) of 44.7 Å, 0.4 Å larger than the optimal size (Figure 2.10a). Putting this discrepancy into perspective, using the same MM+ forcefield, cyclic octamer template **T8** is 1.86 Å larger than the calculated optimum diameter, yet the binding to the cyclic porphyrin octamer ***c*-P8^{C8}** has an exceptionally high association constant of 1.3×10^{37} M^{-1}. The slight discrepancy in template size from the ideal can be overcome by distortions to the structure. Recently, the crystal structure of ***c*-P6·T6** showed that the hexamer ring adopts a chair-like conformation, with alternate butadiyne links lying above and below the mean plane of the six zinc atoms, to compensate for the hexadentate template **T6** being slightly too small.[135] Similarly, while modelling other, less suitable **T12** candidates, large templates were seen to bend the ring into a pringle-like conformation.

The synthetic strategy to ***c*-P12** was foreseen as binding porphyrin tetramers ***l*-dP4** to template **T12** and oxidative coupling of the terminal acetylenes. Binding smaller oligomers would permit too much flexibility in the template; larger oligomers require a lot of synthetic effort and are more difficult to purify. Modelling of the intermediate template-tetramer complex (Figure 2.10b) showed that the terminal acetylenes of the bound tetramers were held in close proximity to one another, at an average distance of 4.2 Å.

a)

b)

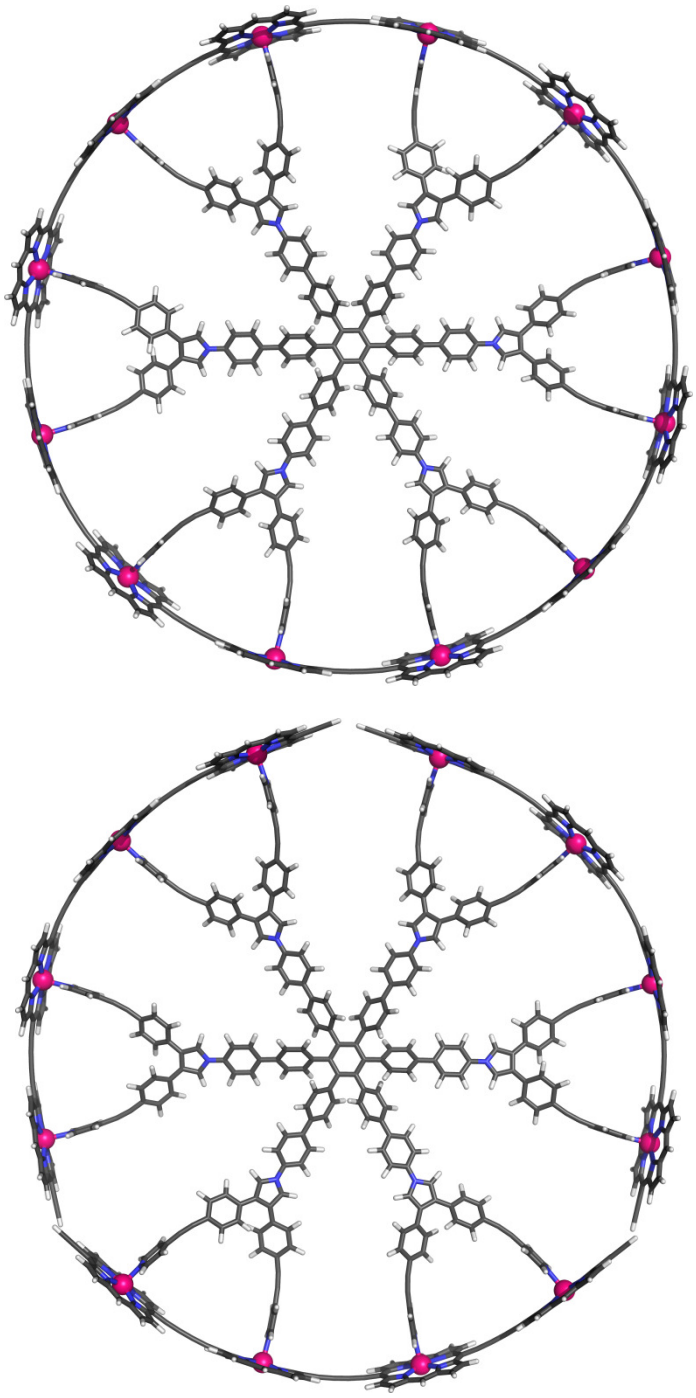

Figure 2.10 Optimised geometries calculated in Hyperchem™ using an MM+ forcefield: a) Template **T12** binding cyclic porphyrin dodecamer ***c*-P12**; b) template **T12** binding three linear butadiyne-linked porphyrin tetramers ***l*-dP4**. Porphyrin *meso*-aryl, *n*-butyloxy and *tert*-butyl ester groups are omitted from the model to simplify the calculation.

2.4.2 Retrosynthetic analysis of **T12**

A retrosynthetic analysis of template **T12** (Scheme 2.6) suggested an initial disconnection to give pyrrole **15** and "iodohexacore" **27**, corresponding to a Buchwald-type coupling[136] in the forward direction. This approach would simplify the route to the template immensely, as both iodohexacore **27**[137][138] and pyrrole **15** are known compounds, the latter being an intermediate in the synthesis of octadentate template **T8**.[131]

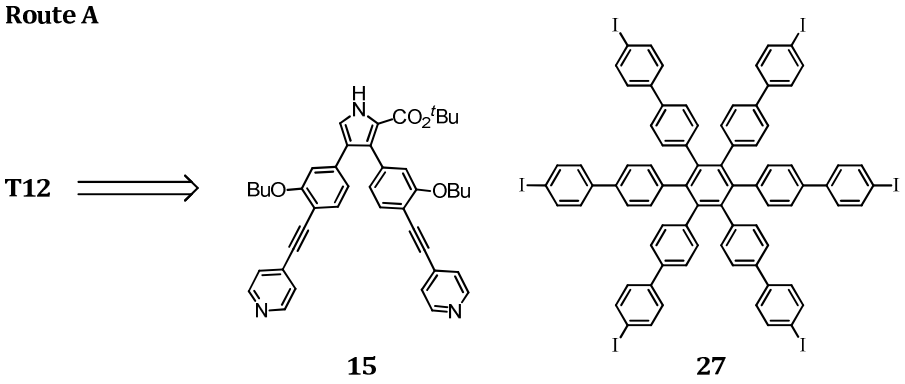

Scheme 2.6 Retrosynthetic analysis of template **T12**.

The synthetic pathway could thus be broken down in two ways. The first route (Route A, Scheme 2.6) would involve direct coupling of pyrrole **15** onto the iodohexacore. Although literature report yields of up to > 99% for the coupling of pyrroles with aryl iodides,[139][140][141][142] the six-fold coupling of sterically hindered **15** and subsequent purification was seen as potentially challenging.

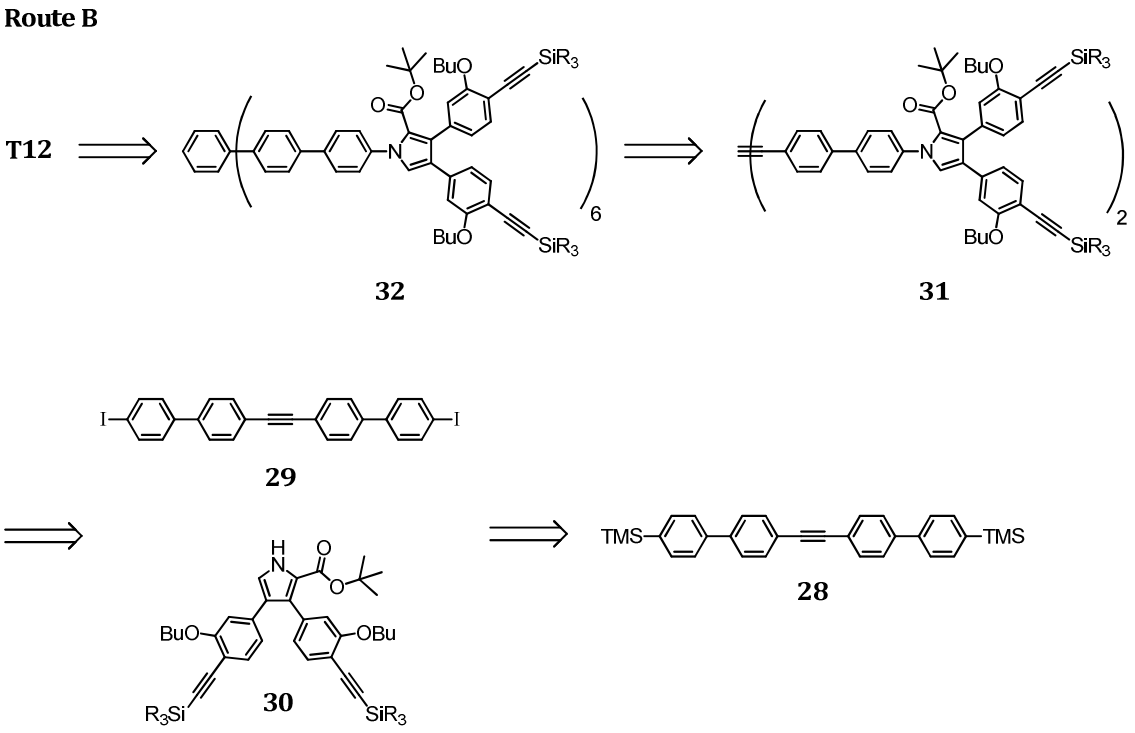

Scheme 2.7 Retrosynthetic analysis of template **T12** *via* a cobalt catalysed cyclotrimerisation step.

The second route, Route B (Scheme 2.7), would involve coupling of the pyrrole to a bis(4-iodobiphenyl)acetylene derivative **29**, followed by a cobalt cyclotrimerisation.[143] The iodinated biphenyl acetylene **29** appeared to be accessible from the TMS-derivative **28**, an intermediate in the synthesis of iodohexacore **27**. However, in the synthesis of the hexadentate template **T6**, it was found that the cobalt catalyst was incompatible with the pyridyl functionality, presumably because coordination of the pyridyl groups served to deactivate the catalyst.[75] For this reason, if pursuing this route, it would be necessary to carry out the trimerisation prior to attaching the pyridyl groups; potentially using the silicon protected precursor to dipyridyl pyrrole **15**, **30** (R = Me). This route would require a 12-fold Sonogashira step to give template **T12** from **32**, although with an excess of iodopyridine this may be achievable. A drawback to Route B would be potential regioselectivity issues in the

cyclotrimerisation step with the acetylene on the pyrrole moiety. For this reason, Route A was pursued first.

2.4.3 Synthesis of **T12** precursors dipyridyl pyrrole **15** and iodohexacore **27**

The synthesis of known compound iodohexacore **27** using published methods was efficient.[137][138] A double elimination of HBr from 1,2-dibromoethane derivative **33** using sodium ethoxide gave alkyne **34** in 73% yield.[144] Suzuki coupling with commercially available 4-trimethylsilylphenyl boronic acid gave **28** in 85% yield. The published procedure reported an 81% yield using 7 mol% of the cobalt carbonyl catalyst,[138] however when attempted only starting material was recovered. An alternate procedure, using the same catalyst at a higher loading of 35 mol%,[143] yielded the TMS-hexacore **35** in 80% yield. Finally, iodination with iodine monochloride gave the iodohexacore **27** in 85% yield (Scheme 2.8).

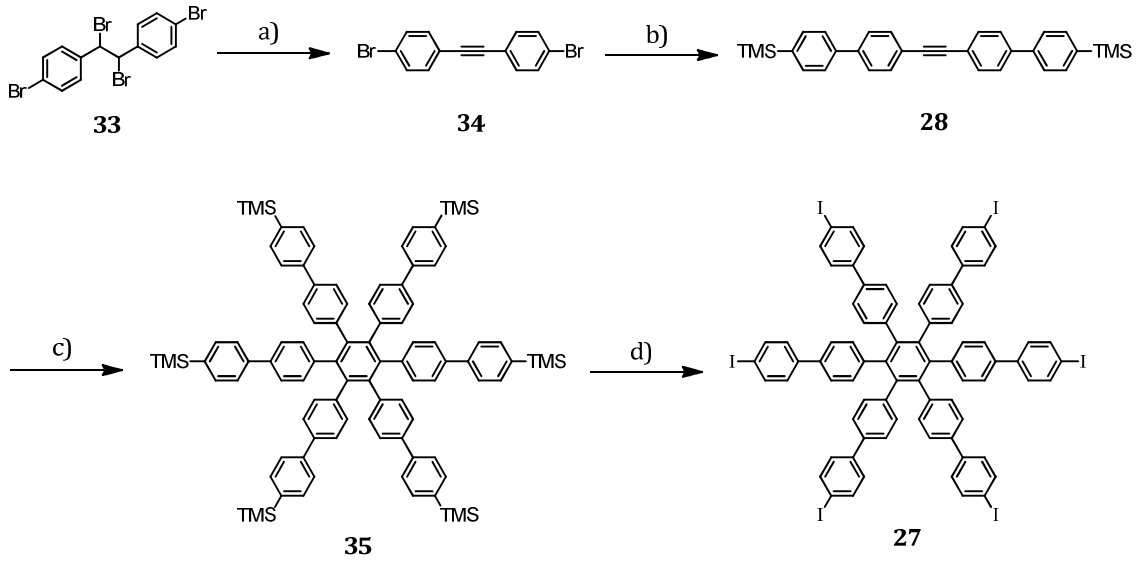

Scheme 2.8 Synthesis of iodohexacore **27**: a) EtONa, EtOH, 80 °C, 73%; b) 4-(Trimethylsilyl)phenylboronic acid, $Pd(PPh_3)_4$, K_2CO_3, toluene, EtOH, 50 °C, 85%; c) $[Co(CO)_8]$, 1,4-dioxane, 125 °C, 80%; d) ICl, CH_2Cl_2, rt, 85%.

For the synthesis of dipyridyl pyrrole **15**, a similar procedure to that used in the synthesis of octadentate template **T8** was used,[145][131] and is outlined in Scheme 2.9.

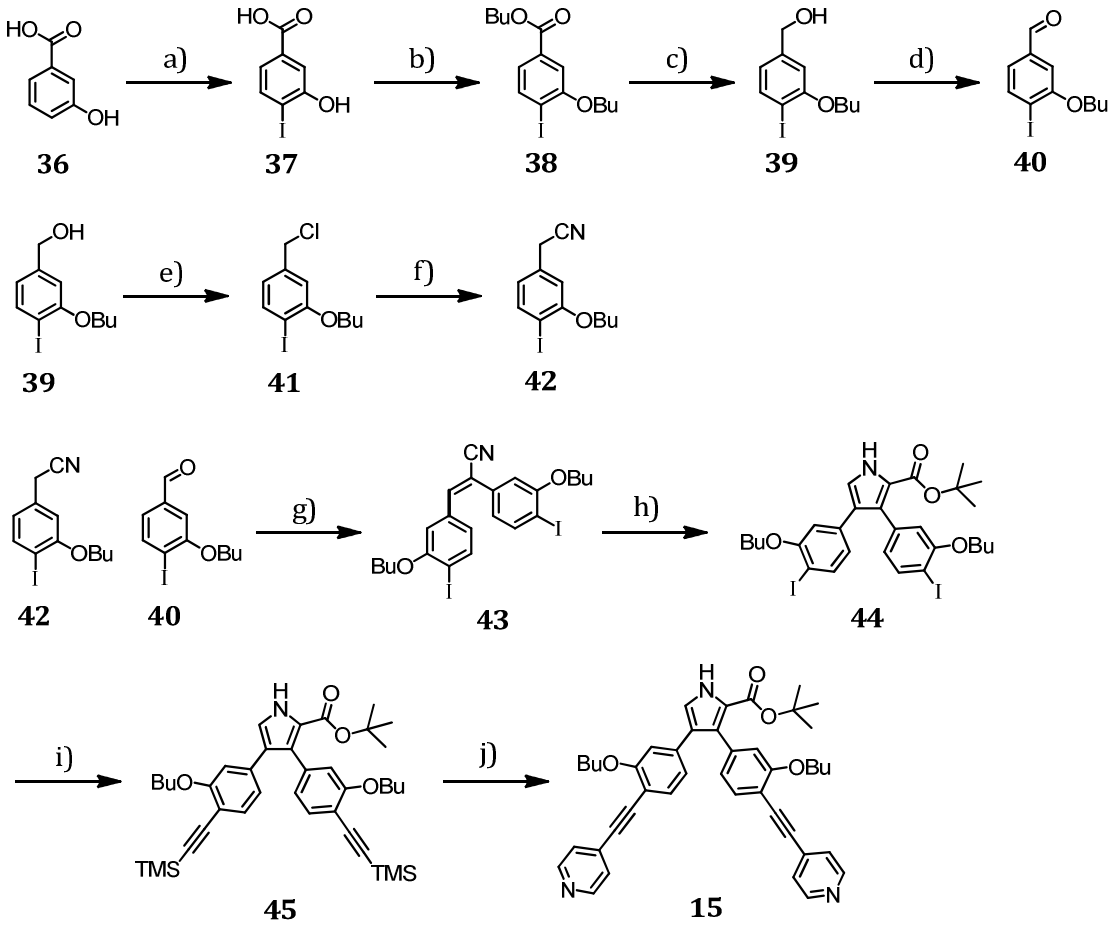

Scheme 2.9 Synthesis of dipyridyl pyrrole **15**: a) KI, I_2, NH_3, H_2O, 50 °C, 71%; b) ^{n}BuBr, K_2CO_3, 18-crown-6, acetone, 60 °C, 99%; c) DIBAL, toluene, –78 °C, 74%; d) PCC, CH_2Cl_2, rt, 99%; e) $SOCl_2$, CH_2Cl_2, rt, 77%; f) NaCN, DMSO, rt, 89%; g) EtONa, EtOH, rt, 80%; h) *Tert*-butylisocyanoacetate, KO^{t}Bu, THF, 0 °C → 50 °C, 95%; i) $Pd_2(dba)_3$, PPh_3, CuI, NEt_3, TMS-acetylene, rt, 90%; j) TBAF, $Pd_2(dba)_3$, PPh_3, CuI, 4-iodopyridine, toluene, THF, NEt_3, rt, 97%.

3-Hydroxybenzoic acid **36** was iodinated with KI_3 in water to give the 4-iodo species **37** in 30% yield.[146] The low yield of this step was attributed to the low solubility of iodine in water at room temperature; heating the reaction to 50 °C improved the yield to 71%. Alkylation and

esterification with *n*-butyl bromide gave **38** in 99%.[147] Reduction with DIBAL gave the corresponding alcohol **39** in 74% yield.

At this point the synthetic routes diverged: alcohol **39** was oxidised to the aldehyde **40** using pyridinium chlorochromate (PCC) in 99% yield. The remaining alcohol was converted to the chloride **41** in 77% yield using thionyl chloride, then reaction with sodium cyanide in DMSO[148] gave the nitrile **42** in 89%.

Stilbene **43** was afforded in 80% yield by condensation of aldehyde **40** and nitrile **42** in the presence of sodium ethoxide.[149] A reaction with *tert*-butylisocyanoacetate in a Barton-Zard reaction[150] gave pyrrole **44** in 95% yield. A Sonogashira coupling with trimethylsilylacetylene afforded pyrrole **45** in 90% yield.

In the originally reported route, Wilson used commercially available 4-bromopyridyl hydrochloride salt to attach terminal pyridyl moieties to the deprotected acetylenes, giving a yield over the deprotection-coupling step of 62%.[145][131] Due to the increased reactivity of aryl iodides over the respective bromides, it was predicted that this yield could be increased if 4-iodopyridine **48** was used. 4-Iodopyridine was synthesised using a simple Sandmeyer reaction in 31% yield; by reacting 4-aminopyridine **46** at low temperatures with sodium nitrite, and quenching with potassium iodide (Scheme 2.10).[151][152] The crude product could be purified by sublimation.

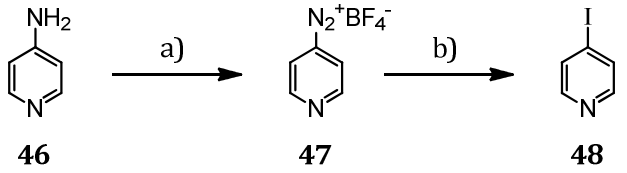

Scheme 2.10 Synthesis of 4-iodopyridine **48**: a) $NaNO_2$, HBF_4 (48% aq. soln.), –10 °C; b) potassium iodide, acetone/water, rt, 31% over two steps.

4-Iodopyridine was reacted under the conditions used by Wilson, giving an improved yield of the target pyrrole **15** in 87% yield. However the deprotection and subsequent Sonogashira reactions were time consuming, and the terminal acetylenes of deprotected dipyridyl pyrrole **49** made the compound unstable. Louisa Esdaile, a postdoctoral researcher in the group, had developed a one-pot deprotection-coupling step for the synthesis of *meso*-substituted 4-(phenylethynyl)pyridine porphyrins, where the terminal acetylenes were too unstable to be isolated.[153] Applying these conditions to TMS-acetylene pyrrole **49** gave the dipyridyl pyrrole **15** in 97% isolated yield after 3 h (Scheme 2.11).

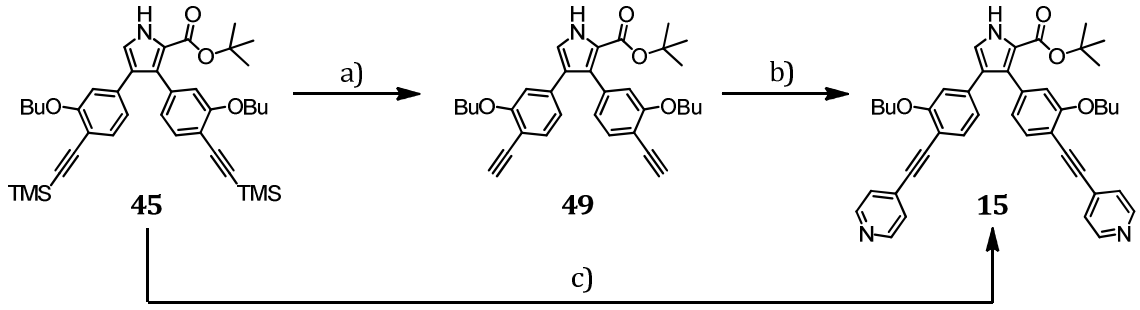

Scheme 2.11 Original (a–b)[131][145] and new (c) route to dipyridyl pyrrole **15**: a) TBAF, CH_2Cl_2, rt; b) $Pd_2(dba)_3$, PPh_3, CuI, 4-bromopyridine hydrochloride, piperidine, rt, 62% over two steps; c) TBAF, $Pd_2(dba)_3$, PPh_3, CuI, 4-iodopyridine, toluene, THF, NEt_3, rt, 97%.

2.4.4 Coupling strategies

In order to find and optimise suitable coupling conditions to connect pyrrole **15** to iodohexacore **27**, it was decided to synthesise a model pyrrole to conserve stocks of **15**. Commercially available phenyl acetonitrile **51** was condensed with benzaldehyde **50** to give the corresponding stilbene **52** in 72% yield. A Barton-Zard reaction using *tert*-butylisocyanoacetate gave pyrrole **53** in 63% yield (Scheme 2.12).[b]

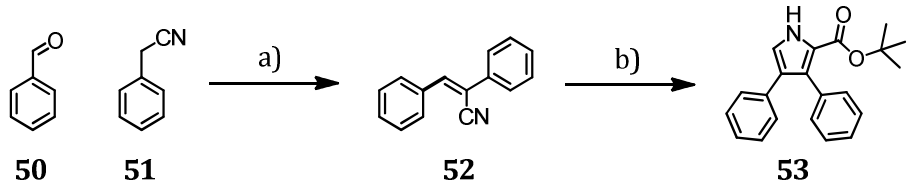

Scheme 2.12 Synthesis of model pyrrole **53**: a) EtONa, EtOH, rt, 72%; b) KO^{t}Bu, THF, 50 °C, 63%.

In collaboration with Corentin Rinfray, a summer student in the group, a series of coupling conditions were screened using pyrrole **53** and iodobenzene as a model system. The reactions were monitored by analytical HPLC. The optimised method used a gradient solvent ramp of heptane and dichloromethane (60:40 → 0:100 over 16 min) and was calibrated using pure samples of pyrrole **53** and the *N*-phenyl derivative **54**.

The results from screening the conditions are summarised in Table 2.1. To mimic the reaction conditions for coupling to iodohexacore **27**, an excess of pyrrole **53** was used in the reactions (3:2 pyrrole to iodobenzene), as an excess would be required in the **T12** synthesis to ensure 6-fold coupling.

[b] The crystal structure of **53** can be found in the Appendix.

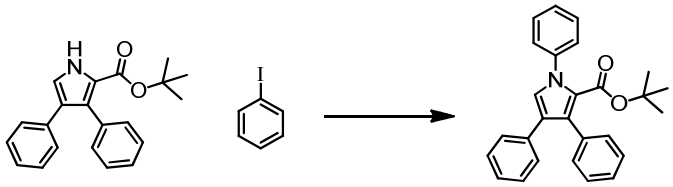

53 **54**

Entry	Reaction conditions	Yield of 54 after 3 days (HPLC) /%
1	$FeCl_3$, CuO, *rac*-BINOL, Cs_2CO_3, DMF, 110 °C [154]	17
2	Cu_2O, Cs_2CO_3, DMF, 110 °C [155]	9
3	CuI, K_3PO_4, *N*,*N*'-dimethylethylenediamine, toluene, 110 °C [141]	85
4	Cu(0), Cs_2CO_3, acetonitrile, 82 °C [156]	0
5	CuI, $^nBu_4NBr$ NaOH, toluene, 110 °C	0

Table 2.1 Yields from the conditions screened for the coupling of model pyrrole **53** with iodobenzene, obtained by analytical HPLC. For all conditions, 1.5 equivalents of pyrrole **53** was reacted with 1 equivalent of iodobenzene.

Methodology reported by Chan employs sodium hydroxide as a base, with Aliquot 100 (tetrabutylammonium bromide) as a phase transfer reagent (Entry 5).[142] HPLC analysis showed consumption of **53** and growth of another peak with a different retention time to that of **54**. The product was isolated and determined to be the carboxylic acid derivative of **53**, showing the *tert*-butyl ester was sensitive to the presence of nucleophilic hydroxide.

The best conditions were those reported by Buchwald *et al.*, which utilised a copper iodide/*N,N'*-dimethylethylenediamine system in the presence of potassium phosphate, reporting yields of up to 96% for sterically hindered 2-substituted pyrroles with aromatic iodides.[141] Analytical HPLC showed 85% conversion of **53** after 3 days (Entry 3), with TLC

showing complete consumption of iodobenzene. Workup of the reaction gave *N*-phenyl pyrrole **54** in 46% isolated yield.

The same paper had reported superior yields using *trans*-*N*,*N*'-dimethylcyclohexane-1,2-diamine as a ligand. However, in our hands, no reaction was observed after two days with this ligand.

The conditions in Entry 3 were applied to the coupling of model pyrrole **53** with iodohexacore **27**. Iodohexacore **27** was reacted with an excess of the pyrrole using high catalyst loadings to reduce the incidence of partially substituted side products; obtaining the hexasubstituted template model **55** in 44% yield (Scheme 2.13).

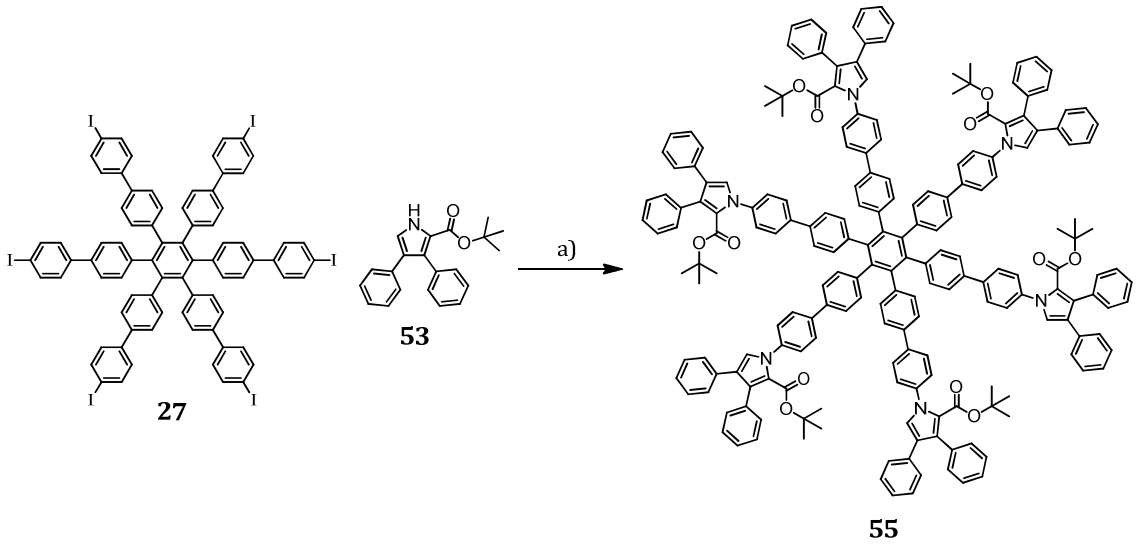

Scheme 2.13 Synthesis of hexasubstituted template model **55**: a) *N,N'*-dimethylethylenediamine, CuI, K_3PO_4, toluene, 110 °C, 44%.

The simplicity of the NMR spectrum, with one singlet denoting the presence of the 2-position proton and one signal for six *tert*-butyl groups, confirmed the D_{6h} symmetry of the model template (Figure 2.11). Irradiating the 2-pyrrole proton revealed an NOE with the adjacent phenyl proton, confirming *N*-arylation.

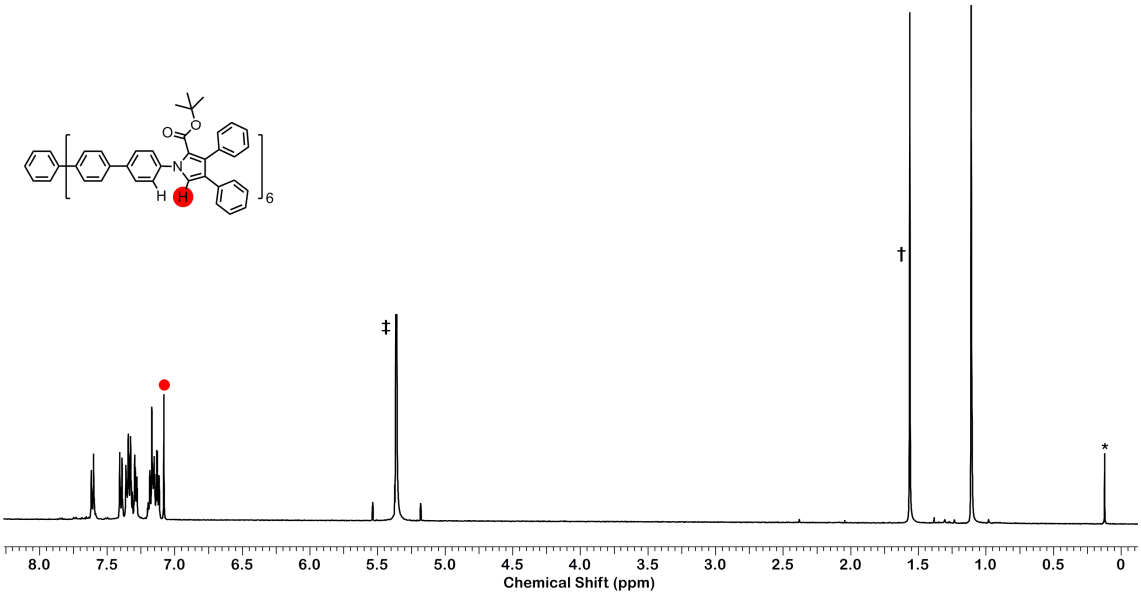

Figure 2.11 ^{1}H NMR (500 MHz, CD_2Cl_2, 298 K) of model template **55**, showing a single singlet for the 2-pyrrolic proton (marked red). ‡ indicates residual solvent; † indicates water; * indicates grease.

2.4.5 Synthesis and purification of **T12**

The conditions used for the coupling of model pyrrole **53** to iodohexacore **27** were applied to the synthesis of **T12** (Scheme 2.14). To minimise partially substituted side products, a large excess of pyrrole **15** and high catalyst loadings were used.

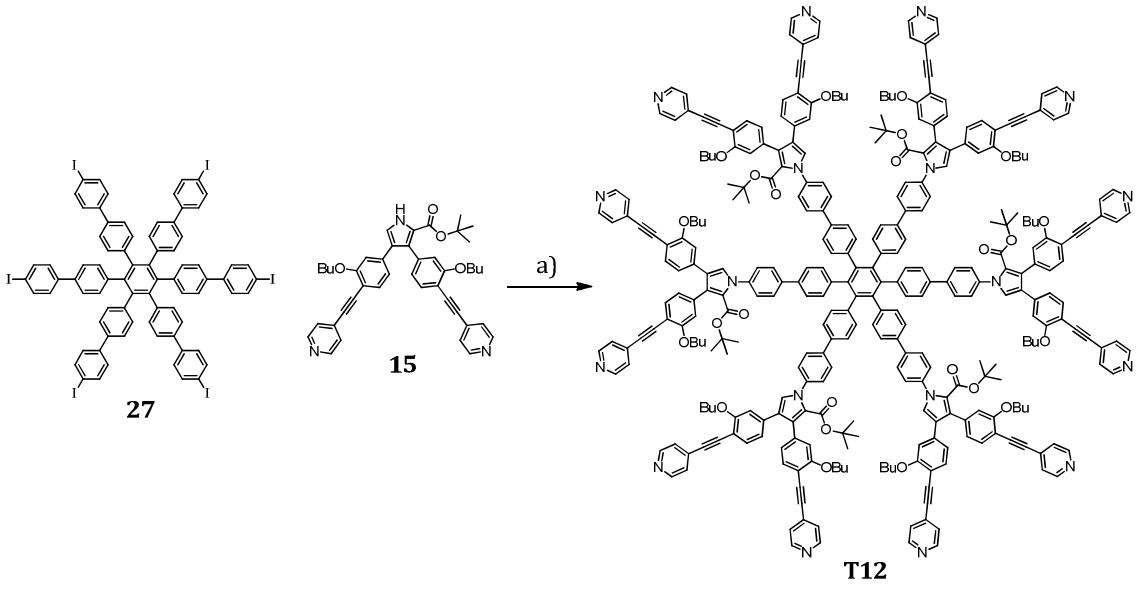

Scheme 2.14 Synthesis of template **T12**: a) *N,N'*-dimethylethylenediamine, CuI, K_3PO_4, toluene, 110 °C, 3 d.

After 3 days, complete consumption of the iodohexacore **27** and appearance of a highly fluorescent baseline spot could be seen by TLC. Mobile phases containing up to 15% methanol failed to move the spot off the baseline. The reaction could therefore not be worked up by passing down a silica column. For this reason, the copper catalyst was removed by an aqueous ammonium chloride wash, and the excess starting pyrrole **15** was removed by passing down a size-exclusion column, eluted with THF. Attempts to check the purity of the baseline spot, using reverse phase chromatography, PEWA/MEWA[c] mobile phases on silica, normal and reverse phase HPLC, and GPC were all unsuccessful. Cyanopropyl "cyano" columns have the highest polarity for a reverse phase HPLC column and can be used either in reverse or normal phase, depending on the choice of the mobile phase.[157] Using readily available and structurally similar octadentate template **T8**, a HPLC method for the cyano-column was developed. The optimum method used a gradient of heptane, dichloromethane, and pyridine

[c] PEWA is a mixture of propan-2-ol, ethyl acetate, water and acetic acid. MEWA replaces propan-2-ol with methanol. Both are useful for separation of highly polar molecules.

(60:35:5 → 25:70:5 over 12 min) as the mobile phase. Injection of the crude reaction mixture gave well resolved peaks (Figure 2.12a).

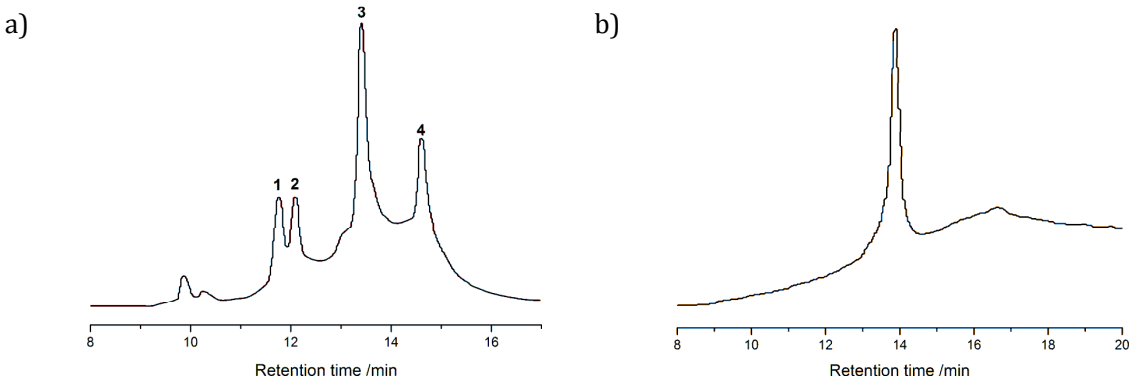

Figure 2.12 a) HPLC trace of crude reaction mixture in the synthesis of **T12**; b) purified **T12**.

Separation of these peaks by preparative HPLC and identification by MALDI-MS assigned the peaks as target **T12** (Peak 4, yield 3%), penta-substituted iodohexacore (Peak 3, yield 2%), and two structural isomers of tetra-substituted iodohexacore (Peak 1 and 2, total 3% yield). It became apparent that **T12** was sparingly soluble under the HPLC conditions, evidenced by an increasingly noisy background and drifting retention times. This accounts for the exceptionally low yields of **T12**. Alternative separation conditions were investigated, but conditions in which **T12** was soluble gave no separation. Injection concentrations were therefore kept very low, and several HPLC cycles were required to obtain a sufficient purity of **T12**.

The poor solubility of the template could be partially attributed to the large number of pyridyl end-groups. An alternate route to the template by coupling TMS-protected pyrrole **45** to iodohexacore **27** was considered, as the more hydrophobic end-groups might allow for easier separation by HPLC. However, despite the high yield for converting TMS-pyrrole **45** to dipyridyl pyrrole **15**, it was predicted that purification of **T12** from a 12-fold Sonogashira coupling would encounter more difficulties than for the 6-fold *N*-arylation. For a molecule of such high molecular weight, the polarity difference between an 11-substituted and 12-

substituted template would be less exaggerated, whilst simultaneously suffering the same solubility issues. Furthermore, the similarity of the ^{1}H NMR spectra for **T12** and its partially substituted products from the *N*-arylation reaction meant that it would difficult to establish the purity of **T12** from a 12-fold Sonogashira coupling. For this reason, this route was not pursued.

2.4.6 Characterisation of **T12**

The D_{6h} symmetry of the template meant that the final product should exhibit a simple spectrum resembling the summation of the two starting materials **15** and **27**. By comparison of ^{1}H NMR data from the previously characterised pyrrole precursor **15**,[131] template protons 1–9 and i–xi could easily be assigned, as shown in Figure 2.13. The chemical shifts of these resonances are very similar to those of the corresponding protons of pyrrole **15**.

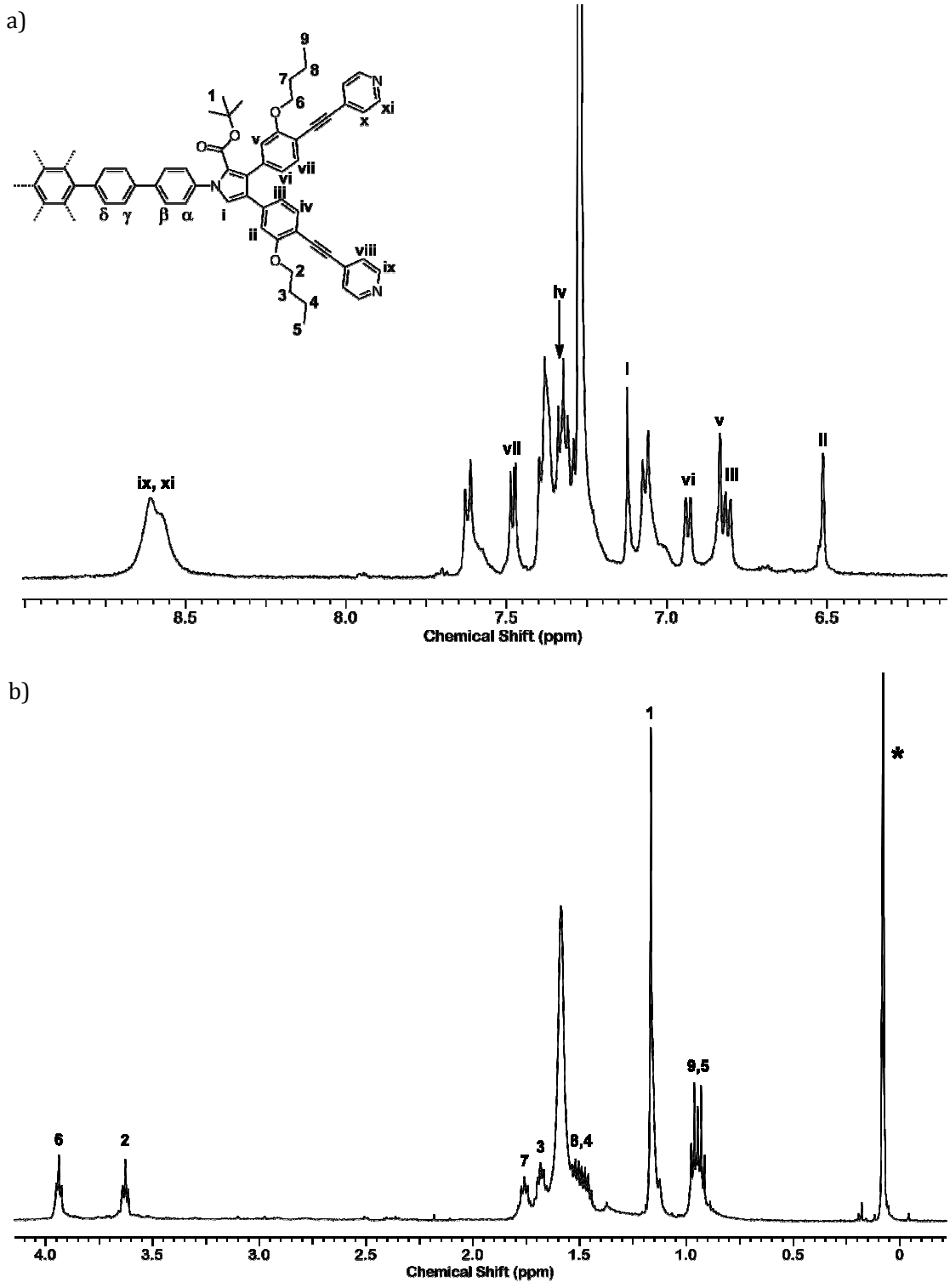

Figure 2.13 ^{1}H NMR (700 MHz, $CDCl_3$, 298 K) of 12-dentate template **T12**: a) Aromatic region showing pyrrole assignments; b) alkyl region of the spectrum; * indicates a silicon grease impurity.

A 1D NOESY spectrum was recorded, irradiating pyrrole proton i. As expected, NOEs with aryl protons ii and iii were observed, but it was also possible for the central hub protons α and β to be characterised (Figure 2.14). The crosspeak with β is not a direct NOE, but more likely a result of spin diffusion;[158] shortening of the mixing time from 800 ms to 500 ms resulted in a dramatic decrease in the intensity of this peak.

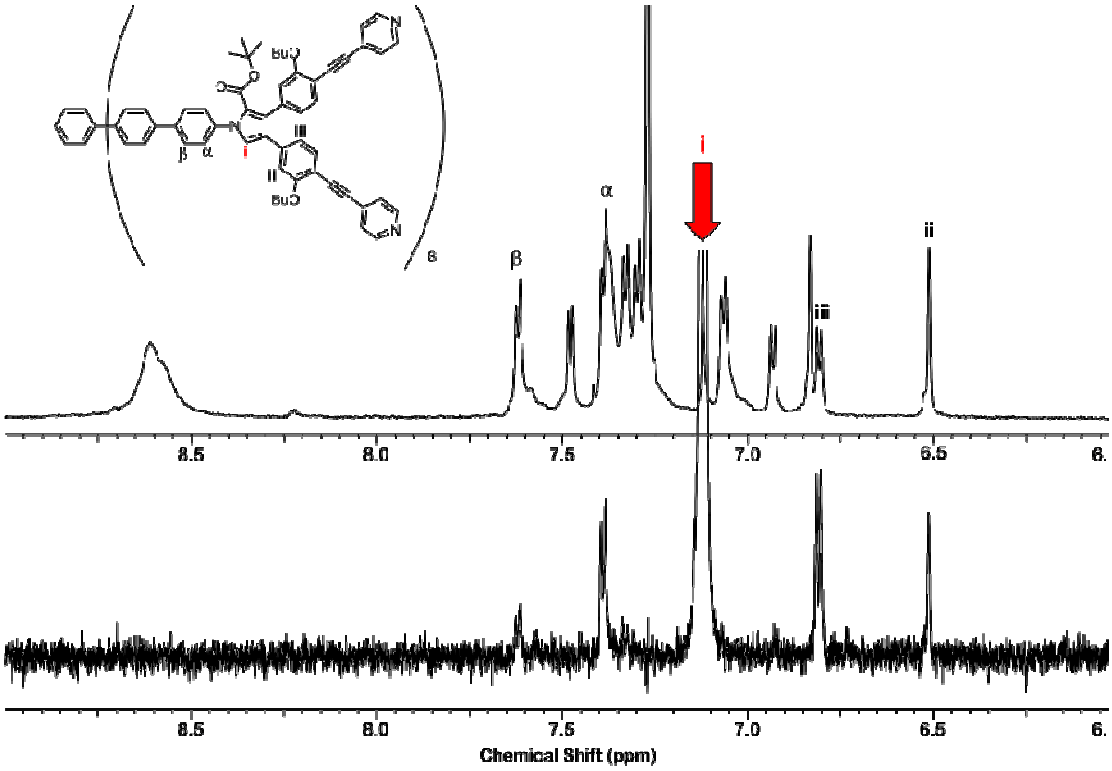

Figure 2.14 1D NOE (500 MHz, $CDCl_3$, 298 K), irradiating the marked singlet at 7.12 ppm, corresponding to the pyrrolic proton i. A mixing time of 500 ms was used.

A 2D ROESY showed a strong NOE between protons γ and δ, but also allowed proton β to be assigned due to its proximity to γ (Figure 2.15). The α–δ assignments were confirmed by COSY correlations (Figure 2.16).

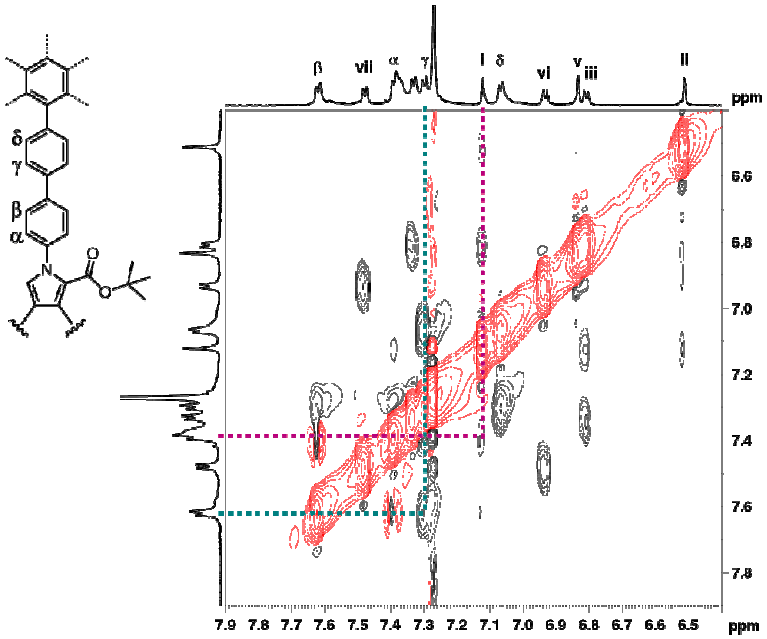

Figure 2.15 ^{1}H 2D ROESY (500 MHz, $CDCl_3$, 298 K) of 12-dentate template **T12**, showing crosspeaks between protons i–α, and β–γ.

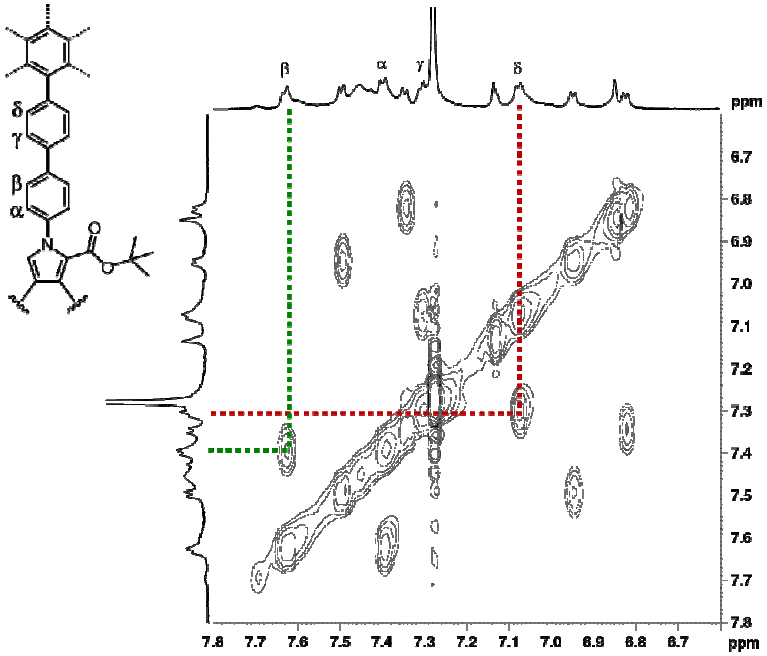

Figure 2.16 ^{1}H COSY (500 MHz, $CDCl_3$, 298 K) of 12-dentate template **T12**, showing crosspeaks between α–β and γ–δ.

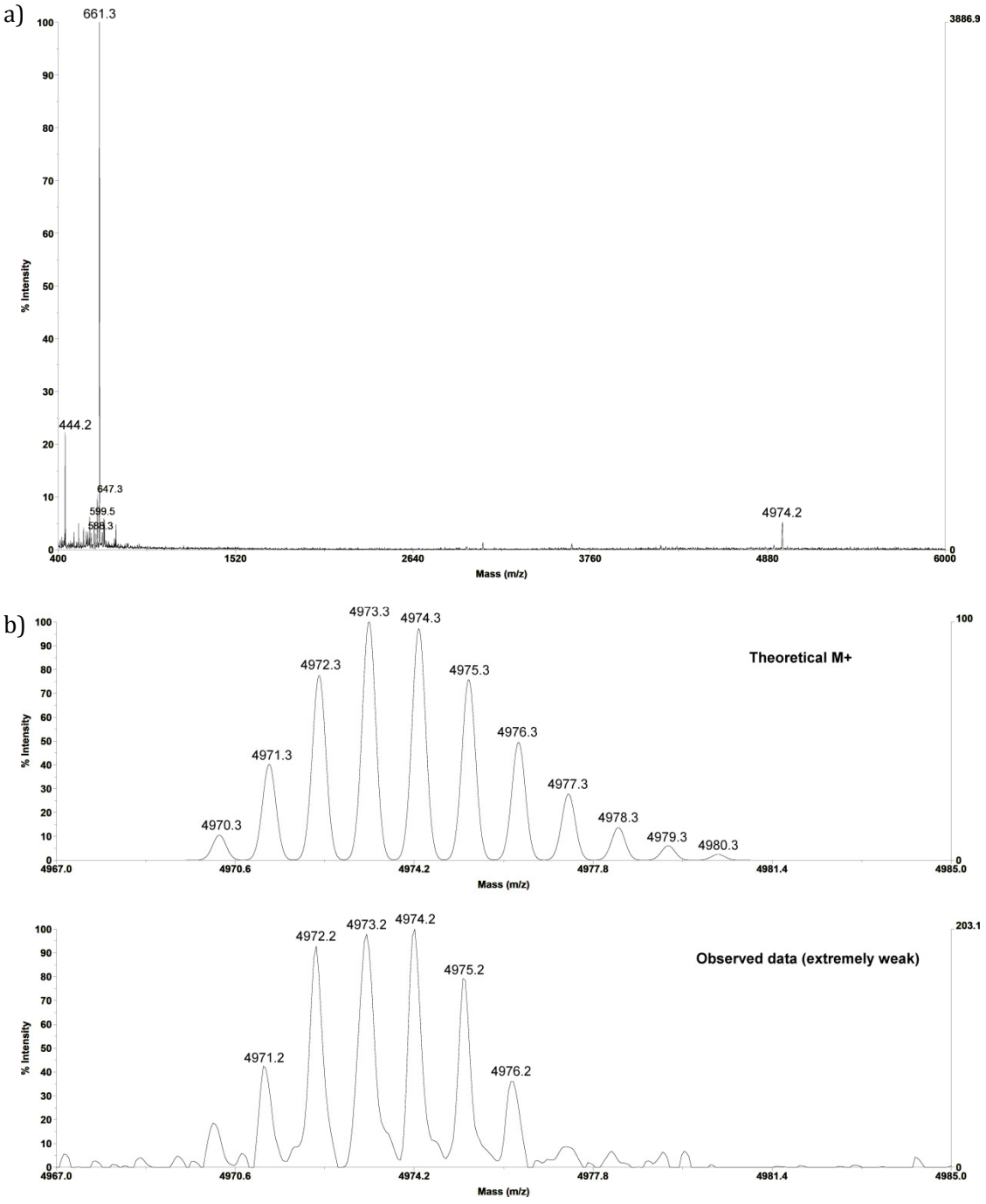

Figure 2.17 a) MALDI-ToF MS analysis of template **T12** (DCTB matrix, reflectron mode). The peak at high molecular weight corresponds to the expected mass for **T12** (*m/z* 4974, expected 4974); b) MALDI-ToF MS isotope patterning of template **T12** (*bottom*) and theoretical pattern calculated for $C_{336}H_{300}N_{18}O_{24}$ (*top*). Courtesy of EPSRC National Mass Spectrometry Service Centre, Swansea.

MALDI-MS showed a single peak at 4974 corresponding to **T12**, with no evidence of partially-substituted side products. The isotope patterning matched well with the theoretical data (Figure 2.17).

2.5 Conclusions

A dodecadentate template to direct the synthesis of a cyclic porphyrin dodecamer ring ***c*-P12** has been designed and synthesised. Molecular modelling using an MM+ forcefield shows template **T12**, with a calculated diameter of 44.7 Å is an excellent fit for the 48.6 Å diameter cavity of ***c*-P12**. Coupling conditions to construct template **T12** from known compounds pyrrole **15** and iodohexacore **27** were explored using a model pyrrole and iodobenzene. The successful conditions were applied to the synthesis of **T12**. Purification of **T12** from partially substituted byproducts was problematic due to the low solubility and high polarity of the target compound. Separation was finally achieved using reverse phase chromatography with a cyano column to give **T12** in 4% yield. Characterisation by ^{1}H NMR and MALDI-MS confirmed the structure of the template.

Chapter Three
Synthesis of a [12]Nanoring

This chapter begins by discussing Vernier assembly as a method of length regulation in both biological and synthetic systems. Fully conjugated cyclic nanorings, and cyclic porphyrin arrays as mimics of light harvesting complexes are reviewed. The utility of ***T12*** *to template the cyclisation of linear porphyrin tetramer* ***l-dP4*** *is demonstrated by the synthesis of target cyclic dodecamer complex* ***c-P12·T12****. This complex is characterised by NMR and small angle X-ray scattering (SAXS). As ambitions turn to larger nanorings, larger templates are required, which are themselves difficult to access, as demonstrated by the synthesis of* ***T12*** *in Chapter 2. Vernier templating, using a mismatch in the number of binding sites between a linear porphyrin tetramer* ***l-dP4*** *and hexadentate template* ***T6****, is explored as a route to cyclic dodecamer* ***c-P12*** *through the synthesis of figure-of-eight complex* ***c-P12·(T6)$_2$****. The structure of this complex is confirmed by NMR, MALDI-MS and SAXS studies. Removal of the templates from both* ***c-P12·T12*** *and* ***c-P12·(T6)$_2$*** *by titration with pyridine gives cyclic dodecamer* ***c-P12****, which is imaged by STM to confirm the formation of 12-membered cyclic structures.*

3.1 Self-assembly

The attraction of self-assembly in synthesis is that it provides an efficient route to complex assemblies from simple monomeric starting materials. It plays a huge role in length regulation of biological systems, from muscle fibres to filamentous viruses. Studies on bacteriophage T4 have shown the tail to be a rod 1000 Å long and 80 Å wide, consisting of 144 chemically identical units in 24 annuli. The tails show a remarkable level of monodispersity, with deviations of less than 7% from this length.[159] Although the exact mechanism for most biological self-assembly processes has not been ascertained, several models have been proposed, including cumulative strain,[160] conformational switching,[161] diffusion controlled growth,[162] and Vernier assembly, the latter of which will be discussed in detail later.

The assembly of the tobacco mosaic virus (TMV) is one of the few well understood biological self-assembly processes.[163] TMV consists of approximately 2130 protein subunits which assemble into a hollow, helical rod structure of 3000 Å in length, encapsulating a single strand of RNA.[164] The virus can be reassembled spontaneously from its constituent parts *in vitro*. Self-assembly of the protein subunits occurs in the absence of the core RNA to give helical rods of the native width, however with a variety of lengths. In this way, the controlled growth of TMV is shown to be *templated* by the central RNA strand, which acts as a biological tape measure.[159][165]

3.1.1 Vernier assembly

Pierre Vernier, in 1631, invented the Vernier scale as a method of accurately measuring lengths. His instrument used a secondary sliding scale with graduations slightly smaller than the main scale. Where the two scales came into register gave the accurate length reading.[166] The Vernier mechanism works on the same principle: two complementary components of unit lengths *m* and *n* undergo linear aggregation. Growth of the linear aggregate continues until the

two strand ends come into register. The final component length, provided *m* and *n* have no common denominator, is the lowest common multiple of *m* and *n*. The simplest Vernier, a 3+2 Vernier, is shown in Figure 3.1.

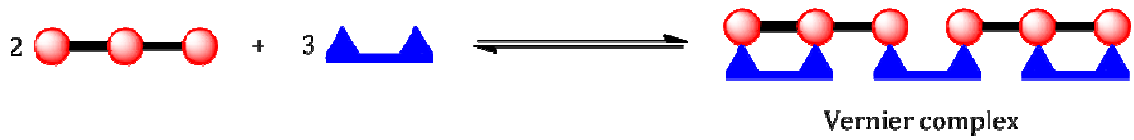

Figure 3.1 Formation of a 3+2 molecular Vernier.

The Vernier concept has been suggested in a number of biological systems as a way of precisely controlling molecular length. Tropocollagen macromolecule, the constituent monomer of soluble collagen, consists of three helical polypeptide chains identical in length.[167] Each macromolecule consists of two chemically distinct polypeptides; two α_1 chains, and one α_2 chain. α_1 consists of a repeating sequence of a subunit σ_1, and α_2 is of a shorter repeating sequence σ_2, with σ_1 and σ_2 having lengths in the ratio 7:5. The total length of the macromolecule is determined by when the repeating sequences of strands α_1 and α_2 come into register, at 35 repeat units. Similarly, the Vernier mechanism has been proposed for length control in assembly of muscle filaments[168] and the tail length of T6-bacteriophages.[169]

Lindsey first proposed the utility of the Vernier mechanism in 1991 as a method of controlling macromolecular length in synthesis,[170] however very few examples of non-biological Vernier complexes exist. In 1998, Kelly *et al.* reported a 3+2 molecular Vernier with a carboxylate-guanidinium binding motif.[171] The binding groups in the respective monomers **56** and **57** were held at a fixed distance by a rigid aromatic backbone. Mixing the two monomers resulted in precipitation of the Vernier complex $\mathbf{(56)_2 \cdot (57)_3}$ in quantitative yield (Scheme 3.1). Any deviation from the required 3:2 monomer stochiometry did not influence the complex formed.

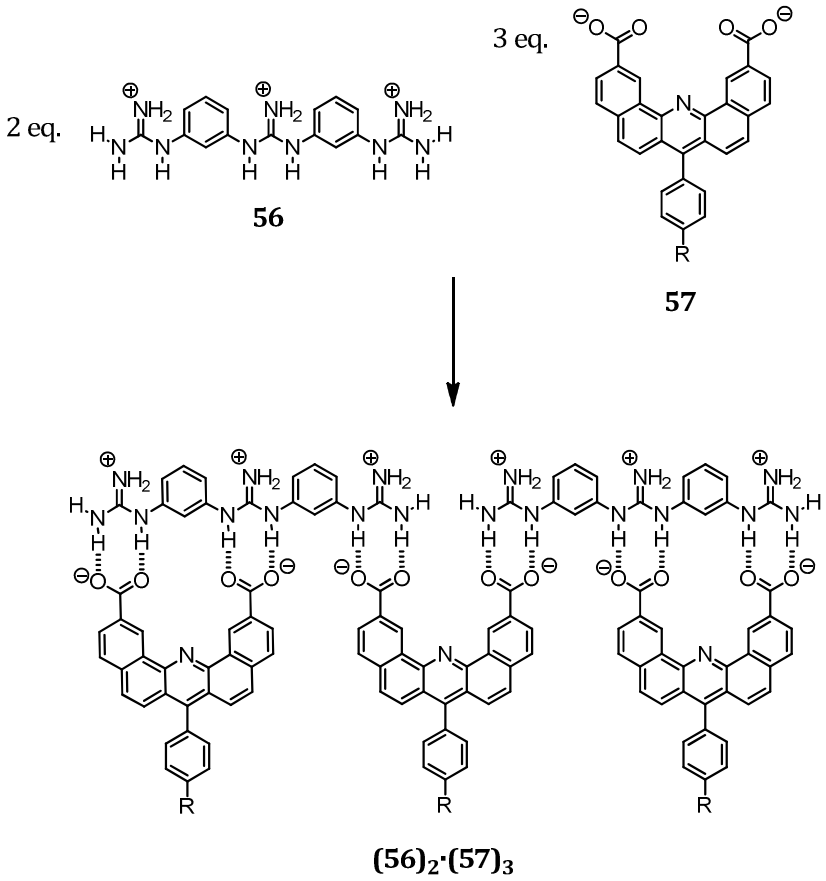

Scheme 3.1 Kelly's synthesis of a guanidinium-carboxylate 3+2 molecular Vernier. R = ^{t}Bu.

The insolubility of $\mathbf{(56)_2 \cdot (57)_3}$ limited characterisation of the complex to elemental analysis and NMR analysis of the supernatant, giving no conclusive evidence that the complex had the proposed structure.

Prior theoretical studies indicated that Vernier assemblies are subject to competition from partially formed assemblies, and need a secondary mechanism, such as a capping agent, to stabilise them.[172] In the case of Kelly's Vernier, the insolubility of the complex may provide a thermodynamic 'sink' for quantitative formation of the complex. Hunter recognised that the stability of a Vernier complex is limited by the weakest interaction.[173] In the case of the

simple 3+2 Vernier complex in Figure 3.1, the weakest interaction is a single-point binding interaction of binding constant *K* (Figure 3.2a).

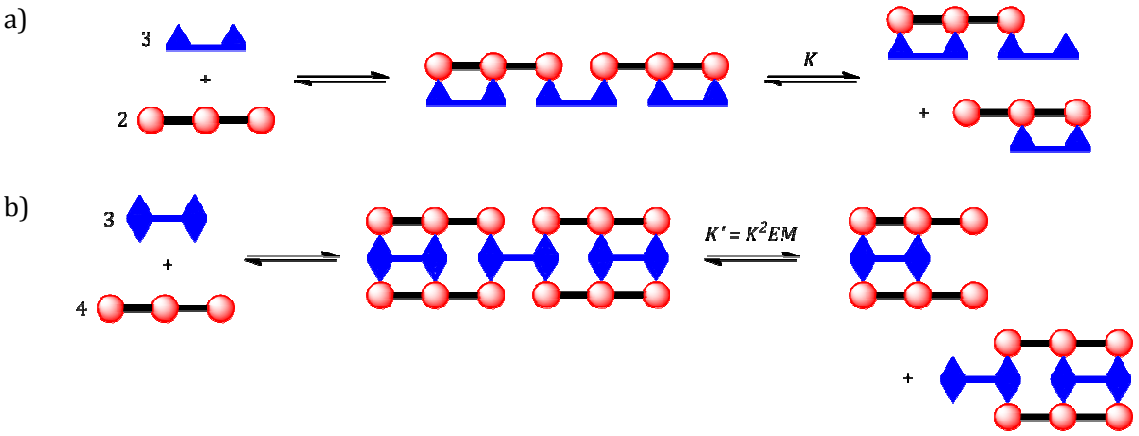

Figure 3.2 a) The stability of a double stranded Vernier complex is limited by a monodentate interaction of binding strength *K*; b) The weakest interaction in a triple stranded Vernier complex is a stronger cooperative bidentate interaction of binding constant $K^2 EM$. Statistical factors are ignored for simplicity.

This was circumvented by using a triple strand approach, as shown in Figure 3.2b. In this system, the weakest interaction is now a cooperative bidentate interaction,[116] which is significantly stronger, making the whole Vernier complex more stable.

Hunter's system utilised identical porphyrin oligomer backbones to ensure equal spacing between monomer binding points. A tin porphyrin dimer was treated with isonicotinic acid; the resulting complex **58** was sufficiently stable to be isolated and characterised. Zinc porphyrin trimer **59** (Figure 3.3) was used for the complementary binding unit, and bound to the free pyridyl functionality of the tetraisonicotinate complex.

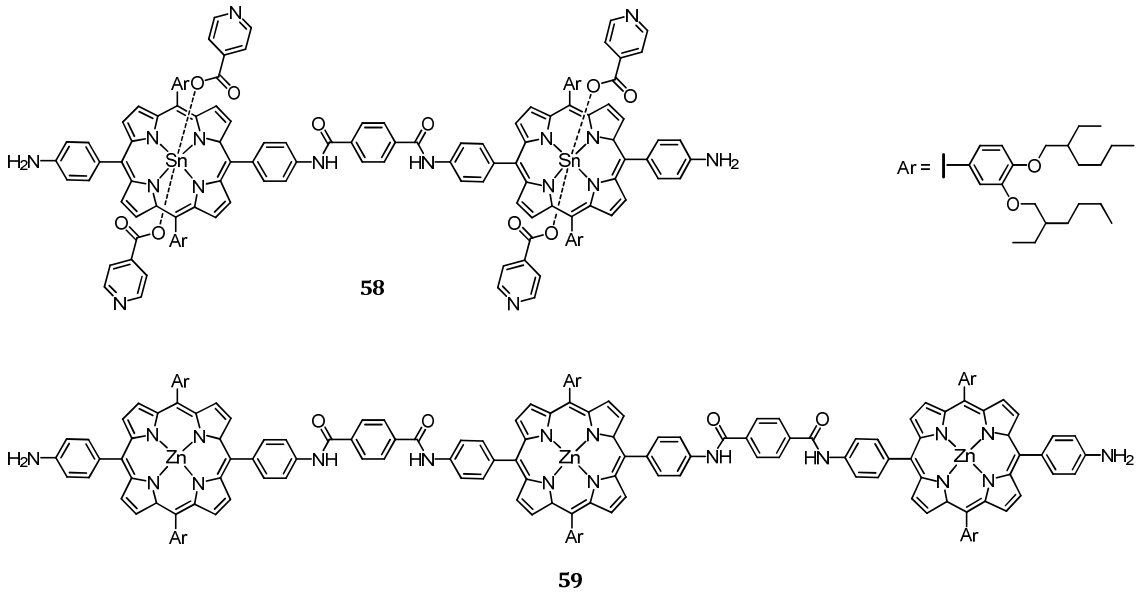

Figure 3.3 Tetraisonicotinate tin porphyrin dimer **58** and zinc porphyrin trimer **59** used in the formation of Hunter's triple stranded 3+2 Vernier assembly.

Studies by UV-vis and size-exclusion chromatography (SEC) studies showed that the 4:3 Vernier complex was formed, but was highly sensitive to changes in concentration and the relative stochiometries of **58** and **59**. At non-optimum conditions, significant proportions of intermediates could be detected.

3.2 Cyclic arrays

Normally, π-conjugated systems have their p orbitals aligned perpendicular to the molecular plane (Figure 3.4a). The resulting aromaticity (or antiaromaticity) is well understood in terms of molecular structure, and the resulting magnetic and electronic properties.[174] Since the discovery of fullerenes[175][176] and nanotubes,[177] there has been a huge interest in π-conjugated systems on a curved surface. In these systems, the p orbitals are arranged radially (Figure 3.4b).

a) b)

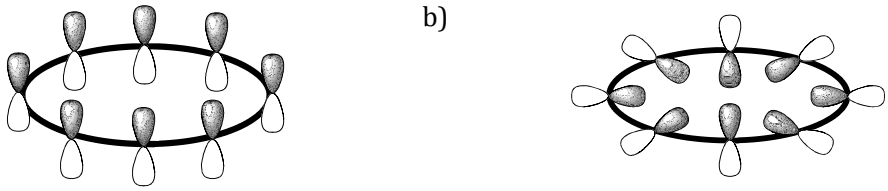

Figure 3.4 a) Aromatic systems such as benzene, have p orbitals aligned perpendicular to the molecular framework; b) molecular loops have p orbitals arranged radially.

Model systems, in the form of molecular belts or loops, have been synthesised to further understand the properties of curved aromatic compounds.[174][178] Bending of the aromatic system imparts more s character to the sp/sp^2 hybridised atoms, giving an uneven distribution of electron density on the convex and concave surfaces. The defined and preorganised ring cavity leads to more favourable van der Waals interactions with hosts, which is important for molecular recognition.

Well-defined oligomers can provide an insight into the electronic and structural properties of the parent polymer. Cyclic systems allow the study of an infinite π-conjugated polymer with the advantages of a well defined oligomer length, but without the effect of end groups.

Cyclic π-conjugated rings have been shown to have very small singlet-triplet energy gaps, giving them interesting magnetic properties.[179] Although C_{60} has been shown both theoretically[180] and experimentally[181][182] to have a very small magnetic susceptibility, anions, such as C_{60}^{6-}, are strongly diamagnetic.[180][183] Mesoscopic metal rings with a diameter less than 1 μm, support persistent currents at low temperatures due to coherence of electron wavefunctions over the ring.[184]–[186] These Aharonov-Bohm oscillations, which oscillate with the magnetic field, have not been observed to date in organic molecules. In part, this is because there are very few examples of π-conjugated molecular rings of sufficient diameter. In order to observe a full oscillation, the radius of the ring *r* must satisfy the following equation:

$$r = \sqrt{\frac{h}{eB\pi}} \qquad \text{Eq. 21}$$

where h is Planck's constant, e is the elementary charge, and B is the magnetic field strength in Tesla.[187] The largest static magnetic field available is approximately 40 Tesla, so Equation 21 requires a molecular ring of approximately 12 nm in diameter. For this reason, it is interesting to create larger π-conjugated rings.

In addition to their intriguing properties, molecular loops and belts are synthetically interesting targets. The challenge of overcoming molecular strain to create bent aromatic systems sees the use of molecular templates, unstrained cyclic precursors, or stepwise syntheses with a high dilution cyclisation step.

Molecular belts are characterised by upper and lower edges that are conjugated but have no atoms in common, for example the [*n*]cyclacenes and [*n*]cyclophenacenes.[188] Molecular loops on the other hand, have portions of the molecule where the conjugation pathway coincides, for example acetylene or vinylene linked chromophores. For the sake of brevity, only molecular loops will be the focus of the following review.

3.2.1 Fully-conjugated cyclic arrays

Cyclo[*n*]carbons are *n*-membered monocyclic all-carbon rings comprised of alternating single and triple bonds (Figure 3.5).

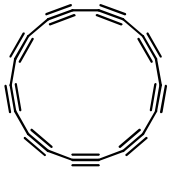

Figure 3.5 Cyclo[18]carbon **C_{18}**.

Theoretical studies predicted rings of C_{10}–C_{29} to be as stable as the singlet state acyclic analogue, due to the distribution of strain over a large number of bonds.[189][190] Particular stability is conferred to rings where $n = 4k + 2$ (where k is an integer) due to aromaticity; similarly, rings of $n = 4k$ will be destabilised.[191]

Diederich first published the synthesis of cyclo[18]carbon **C_{18}** in 1989 *via* a retro [2+2] Diels-Alder reaction of **60-*18*** by laser flash heating.[192] Analysis of the reaction by resonant two photon ionisation time of flight mass spectrometry showed sequential loss of three anthracene molecules from **60-*18*** to yield cyclo[18]carbon **C_{18}**. However, attempts to isolate macroscopic quantities of **C_{18}** by solution spray flash vacuum pyrolysis[193] led to isolation of only anthracene and polymers.[194]

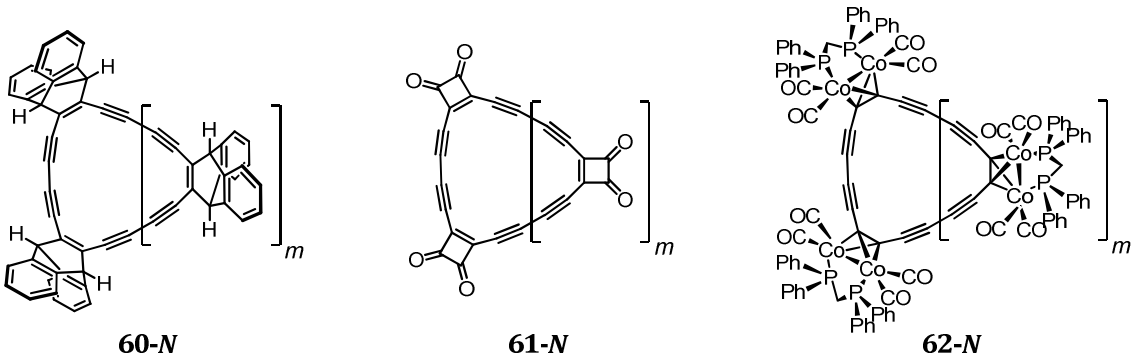

60-*N* **61-*N*** **62-*N***

Figure 3.6 Cyclo[18]carbon precursors: a) Elimination of anthracenes from **60-*18*** via a retro [2+2] Diels Alder reaction yields **C_{18}**; b) Butenedione stabilised **61-*N***; c) $Co_2(CO)_4$(dppm) stabilised **62-*N***. dppm = methylenebis(diphenylphosphine). *N* is the number of carbon atoms in the corresponding cyclocarbon.

Alternative routes to cyclo[*n*]carbons via complex **62-*N*** were tried,[195][196] but the stability of the cobalt-phosphine complex meant attempts to demetallate the complex by oxidation or ligand exchange failed. The use of cyclobutenedione precursor **61-*N*** was more successful, with **C_{18}^-**, **C_{24}^-** and **C_{30}^-** being observed by laser desorption Fourier transform mass spectrometry

(LD-FTMS).[197] Low temperature FT-IR showed loss of carbon monoxide *via* a ketene intermediate. Isolation of the free rings however was not realised.

Tobe and co-workers have managed to observe **C_{12}**, **C_{16}**, **C_{18}**, **C_{20}**, **C_{24}**, **C_{30}** and **C_{36}** by LD-ToF MS by a similar retro [2+2] Diels-Alder synthesis eliminating indane.[198][199] The properties of cyclo[*n*]carbons are of particular interest because they are a novel allotrope of carbon, and are thought to be an intermediate in the formation of fullerenes.[200]

The Oda group first reported the syntheses of cyclic [*n*]paraphenylacetylenes ([*n*]CPPAs, where *n* is the number of phenylacetylene units) in 1996. Precursor **63** was formed from the McMurry coupling of 4,4'-diformyl-(*Z*)-stilbene[201] to give a 4:1 mixture of [2_6]paracyclophanehexaene (*l* = 2) and [2_8]paracyclophaneoctaene (*l* = 4) in 20% yield. Bromination and elimination with potassium *tert*-butoxide gave **[6]CPPA** (*m* = 1) and **[8]CPPA** (*m* = 3) in 85% yield (Scheme 3.2).[202]

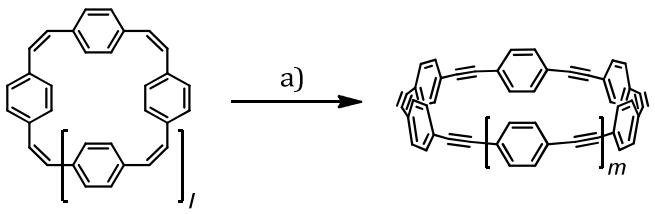

63 **[*n*]CPPA**

Scheme 3.2 Synthesis of [*n*]CPPAs: a) 1. Br_2, $CHCl_3$; 2. ^{t}BuOK, Et_2O, 0 °C.

The strain of the rings was evident by the explosive decomposition of **[6]CPPA** and **[8]CPPA** in air at 80 °C and 120 °C, respectively. **[6]CPPA**, with a calculated diameter of 13.1 Å, has been shown to be an ideal receptor for fullerenes, with UV-vis measured association constants of $K_a(C_{60}) = 1.6 \pm 0.3 \times 10^4$ M^{-1} and $K_a(C_{70}) = 1.8 \pm 0.2 \times 10^4$ M^{-1}.[203][204] The high affinity of the fullerenes for the CPPA cavity cannot be solely attributed to dispersion forces, but must be

partially due to the electrostatic attraction between the concave and convex π surfaces. The same group later reported the syntheses of **[5]CPPA**, **[7]CPPA** and **[9]CPPA**.[205][206]

The synthesis of [4_6]paracyclophanedodecayne **65**, with six alternating *para*-phenylene and butadiyne moieties was reported.[207] A Dewar benzene was utilised as an angular *para*-phenylene precursor; irradiation with light gave **65** in quantitative yields (Scheme 3.3).

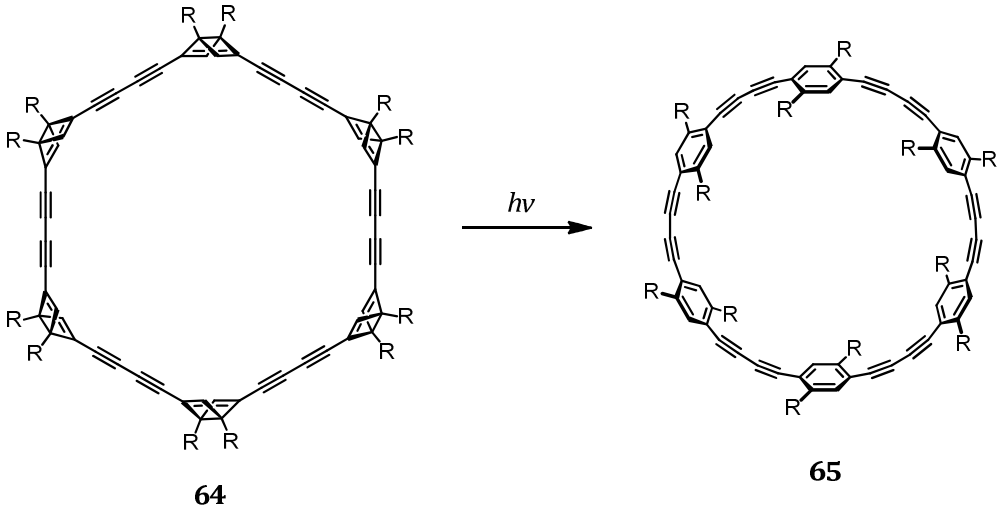

64 **65**

Scheme 3.3 Irradiation of Dewar benzene precursor **64** gives [4_6]paracyclophanedodecayne **65** in quantitative yields. R = $CH_2OSiMe_2(^tBu)$.

[*n*]Cycloparaphenylenes ([*n*]CPPs, where *n* is the number of paraphenylene units) are of great interest as they are the smallest structural unit of armchair nanotubes. Bertozzi first reported the synthesis of **[9]CPP**, **[12]CPP** and **[18]CPP** in 2008.[208] To promote cyclisation, a masked aromatic ring in the form of a 3,6-*syn*-dimethoxycyclohexa-1,4-diene intermediate **66** (Scheme 3.4) was used to provide curvature and relieve strain. The enthalpic cost of cyclising a linear paraphenylene oligomer has been calculated to be 230 kJ mol^{-1}, hence direct coupling yields only linear polymer.[209] Cyclising a cyclohexane substituted paraphenylene oligomer however, reduces this value by an order of magnitude.

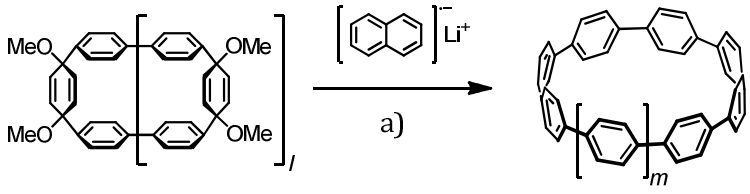

66 **[*n*]CPP**

Scheme 3.4 Bertozzi's synthesis of [*n*]cycloparaphenylenes **[*n*]CPP** *via* dimethoxycyclohexene intermediate **66**: a) THF, –78 °C, 26–52%.

Aromatisation using lithium naphthalenide gave a mixture of **[9]CPP** (*m* = 2), **[12]CPP** (*m* = 5) and **[18]CPP** (*m* = 11) in yields of 43%, 52%, and 26%, respectively. Using a similar method, Itami *et al*. has reported the syntheses of [14]-, [15]- and [16]cycloparaphenylenes.[210]

An alternative method to the cycloparaphenylenes has recently been reported by Yamago and co-workers, using the preferred square planar geometry of platinum complexes to construct a cyclic precursor (Scheme 3.5).[211]

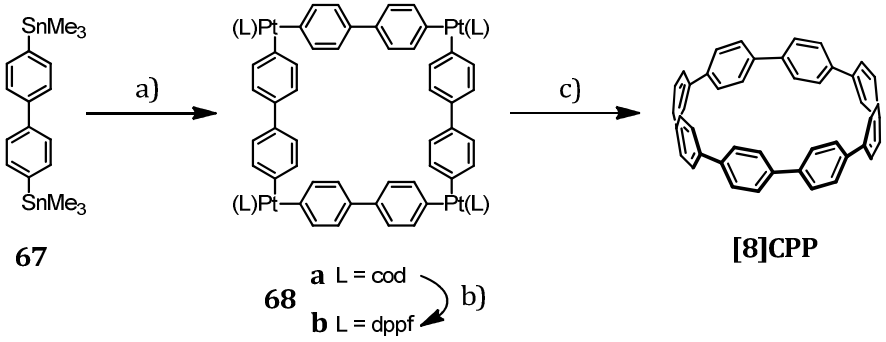

67 **68** **[8]CPP**

Scheme 3.5 Yamago's synthesis of [*n*]cycloparaphenylenes via a tetranuclear platinum(II) complex **68**: a) $PtCl_2$(cod), THF, reflux, 36 h, 84%; b) dppf, CH_2Cl_2, rt, 20 h, 91%; c) Br_2, toluene, 95 °C, 17 h, 49%. cod = 1,5-cyclooctadiene; dppf = 1,1'-bis(diphenylphosphino)ferrocene.

4,4'-Bis(trimethylstannyl)biphenyl **67** was treated with $PtCl_2$(cod) in THF to yield the platinum complex **68a** in 84% yield. Precipitation of **68a** from THF due to poor solubility shifted the

position of equilibrium, suppressing the formation of linear side products under thermodynamic conditions. Ligand exchange to dppf, and reductive elimination of **68b** initiated by addition of bromine, yielded **[8]CPP** in 37% overall yield. The same procedure was used to synthesise rings **[8]CPP**–**[12]CPP**, with **[8]CPP** being the smallest cyclic paraphenylene synthesised to date.[212]

While the HOMO–LUMO gap of linear paraphenylene oligomers decreases with increasing length due to an increase in effective conjugation, the opposite trend is seen for the cyclic species.[211] Theoretical studies have suggested that the larger rings adopt a benzenoid character, whereas smaller rings prefer the quinodimethane form.[174][213] The crystal structure of **[12]CPP** (Figure 3.7) has confirmed this large ring adopts the benzenoid form, with the benzene ring C–C bonds equal (1.39 Å) and the *ipso*-*ipso* C–C bonds exhibiting single bond character.[214]

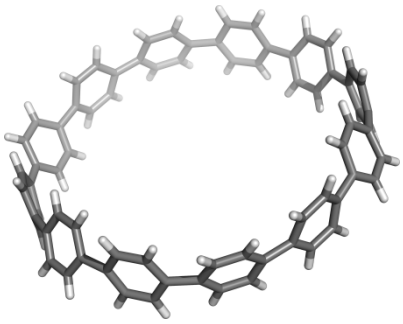

Figure 3.7 Crystal structure of **[12]CPP** obtained from $CHCl_3$/cyclohexane. Solvent molecules are omitted for clarity.

Bäuerle reported the first α-conjugated cyclo[*n*]thiophenes (**C*n*T**, where *n* is the number of thiophene units) in 2000 with the syntheses of **C12T**, **C16T** and **C18T**.[215][216] The original conditions formed cyclic oligomers by coupling thiophenediyne **69** using modified Eglington-Glaser conditions[217] at pseudo-high dilutions. A more efficient coupling method, using the

cyclic bisplatinum σ-acetylide complex **70** (Scheme 3.6) as a cyclic precursor, was reported in 2003 to form the highly strained **C8T**.[218]

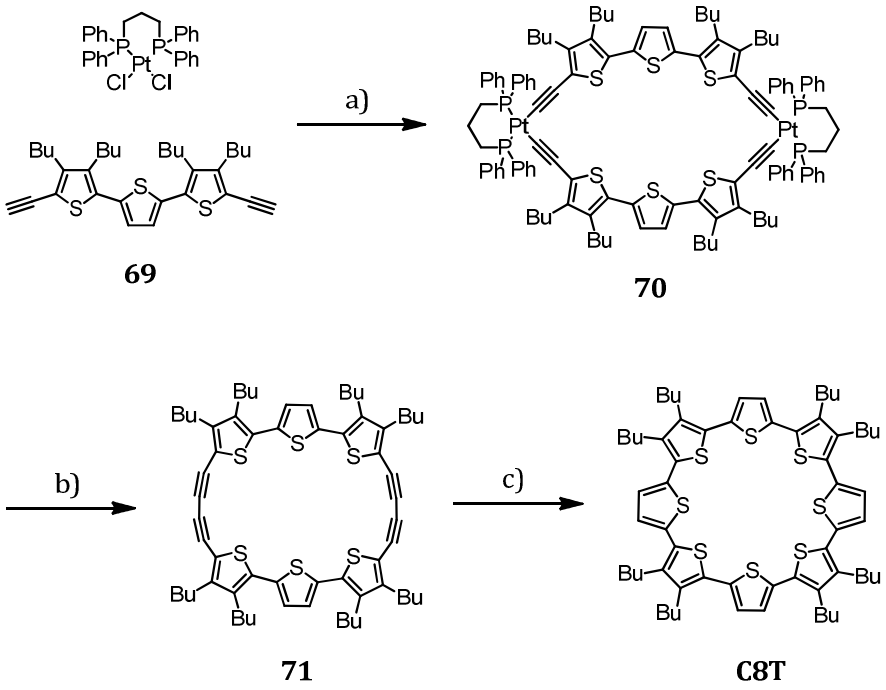

Scheme 3.6 Synthesis of strained **C8T** via a bisplatinum macrocycle **70:** a) CuI, NEt_3, toluene, rt, 72 h, 91%; b) I_2, THF, 60 °C, 24 h, 54%; c) $Na_2S{\cdot}9H_2O$, xylene, 2-methoxyethanol, 140 °C, 24 h, 19%.

Elemental iodine was used to oxidise the platinum 'corners' to facilitate reductive elimination to give butadiyne-linked thiophene macrocycle **71**. The crystal structure of **71** (Figure 3.8) showed dihedral angles between acetylene carbons ranging between 160.3°–167.7°, the most distorted ever reported.

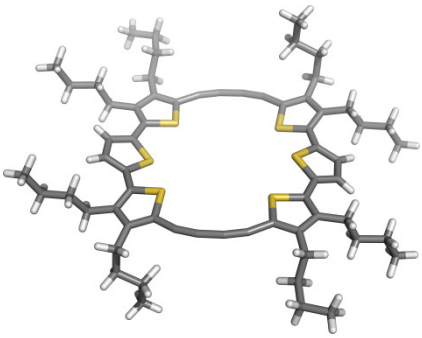

Figure 3.8 Crystal structure of butadiyne-linked cyclic thiophene precursor **71**. Crystals were grown from slow evaporation from $CHCl_3$ solutions.

Reaction of the strained butadiynes with sulfide ions yielded cyclo[8]thiophene **C8T** in 19% yield. It was suggested that the high strain of **71** along with the high temperatures of the reaction attributed to the modest yield of this step.

Recently, the same group has reported the synthesis of **C10T**, **C15T**, **C20T**, **C25T**, **C30T** and **C35T** using the platinum conditions reported by Yamago in the synthesis of the [*n*]cycloparaphenylenes (Scheme 3.5).[219] With increasing ring size, the HOMO–LUMO gap decreased, from 2.63 eV measured for **C10T**, to 2.39 eV for **C35T**. Proton NMR shifts of the larger rings approached that of linear analogues showing increasing conformational flexibility.

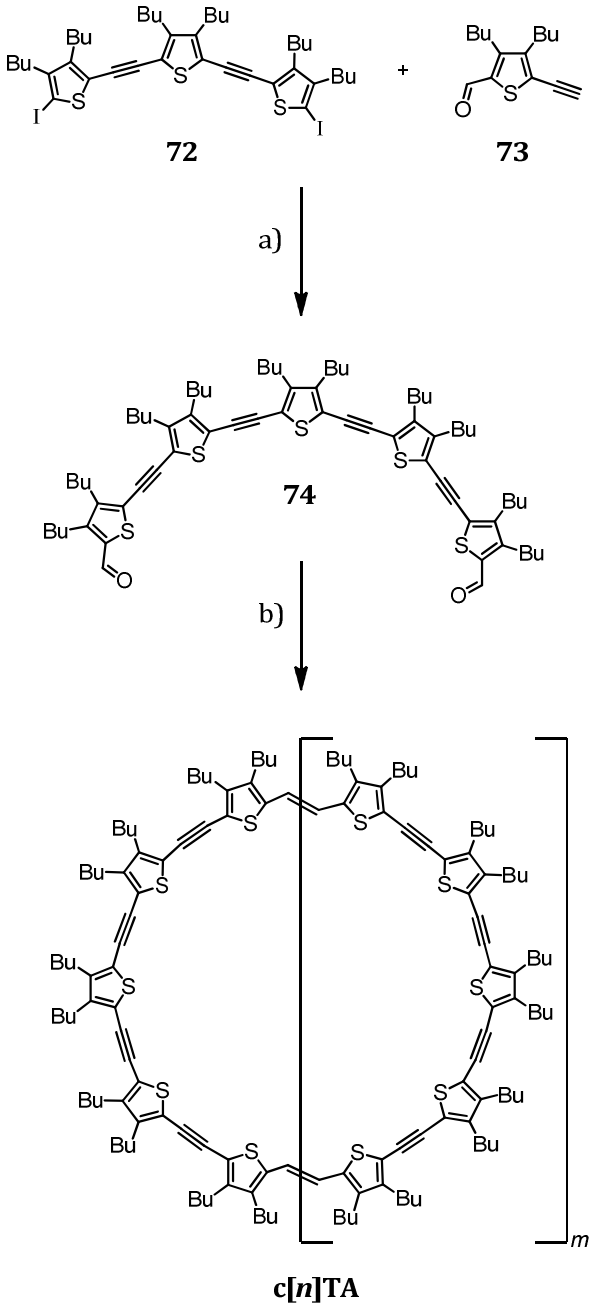

Scheme 3.7 Iyoda's synthesis of π-extended cyclic oligothiophenes **c[*n*]TA** (*m* = 1–5): a) $Pd(PPh_3)_4$, CuI, NEt_3, rt, 85%; b) $TiCl_4$, Zn, pyridine, THF, reflux, yields **c10TA** (*m* = 1) 20%, **c15TA** (*m* = 2) 5.7%, **c20TA** (*m* = 3) 3.8%, **c25TA** (*m* = 4) 2.5%, **c30TA** (*m* = 5) 1.3%.

Iyoda and co-workers reported the synthesis of π-extended cyclic oligothiophenes ranging from 4 to 30 thiophene units.[220][221][222] Sonogashira coupling of thiopheneyne **73** with diodo-oligothiophene derivative **72** gave dialdehyde **74**. McMurry coupling of **74** with a low-valent titanium reagent formed from $TiCl_4$ and Zn yielded a mixture of the oligothiophene macrocycles, which were separated by gel permeation chromatography. The absorption spectra of the π-extended oligothiophenes showed a red shift of the absorption maximum with increasing size, with a saturation at n = 18 (where n is the number of thiophene units). This contrasted with the linear oligo(thienyleneethynylene) derivatives, which showed saturation at around the octamer.[223] Up to 18 thiophene units, full conjugation over the ring is possible; at larger ring sizes conformational flexibility reduced the π-orbital overlap.

The largest fully π-conjugated ring synthesised to date is Mayor's hexadecagon ring **76**, with a calculated diameter of 11.8 nm.[187] 2,5-Diethynylthiophene units **75**, with an angle of 155° between acetylene units,[224] made ideal corner units to construct a hexadecagon, which requires an internal angle of 157.5°.

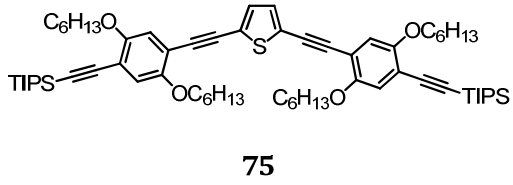

75

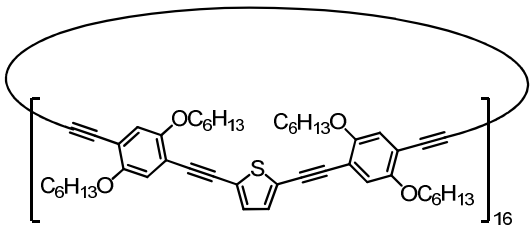

76

Figure 3.9 Thiophene bridged building block **75**, and hexadecagon ring **76** synthesised by Mayor.

Statistical deprotection of building block **75** with TBAF, and oxidative Hay coupling[225] yielded the dimer, which was carried through in the same manner over several steps to the bisdeprotected linear hexadecamer. Cyclisation under high dilutions (8.3×10^{-6} M^{-1}) yielded cyclic **76** in 38% yield. The absorption maximum for **76** of 461 nm was very close to the

theoretical maximum calculated for infinite chain length of 462 nm, showing the near perfect conjugation around the ring.

3.2.2 Non-conjugated cyclic porphyrin arrays

5,15-Substituted bis(*N*-methylimidazole) zinc porphyrin monomers form highly stable dimers in a slipped cofacial orientation in non-coordinating solvents (Figure 3.10). The cooperative binding, further facilitated by π-stacking interactions between the two porphyrins, gives an association constant for this bidentate interaction of $K > 10^{10}$ M^{-1}.[226] With a monodentate interaction binding constant of $\sim 10^4$ M^{-1},[108] this corresponds to an effective molarity (See Chapter 2) in an excess of 100 M.

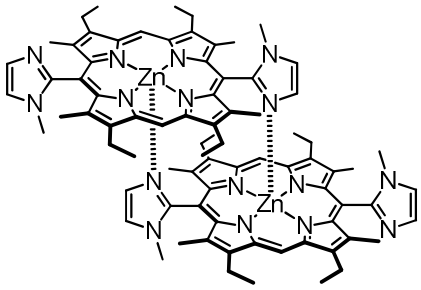

Figure 3.10 A 5,15-substituted bis(*N*-methylimidazole) zinc porphyrin forms a stable dimer in a slipped cofacial orientation.

The stability of this interaction was utilised by Kobuke to synthesise cyclic porphyrin arrays which mimic the structure of naturally occurring photosynthetic systems.[227][228] A 1,3-phenylene spacer was used to connect free-base imidazolylporphyrins in a 120° spatial arrangement, which was predicted to favour the closed cyclic hexamer structure over extended linear arrays.[229] Insertion of zinc and reorganisation under competitive high dilutions gave porphyrin decamer and dodecamer **78**.

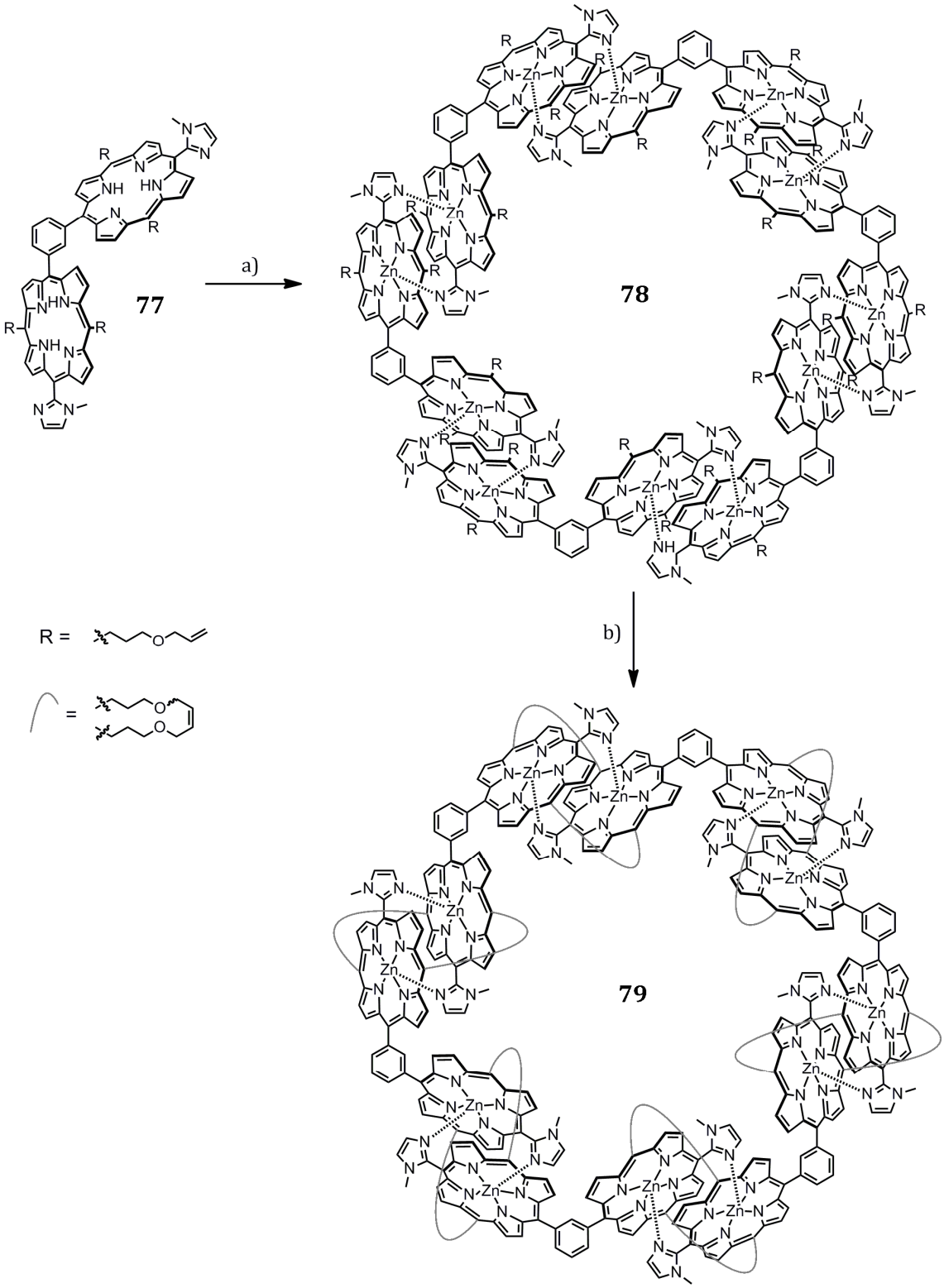

Scheme 3.8 Synthesis of Kobuke's cyclic porphyrin dodecamer array **79**: a) 1. $Zn(OAc)_2$. 2. Self-assembly in $CHCl_3$/MeOH; b) Grubbs first generation catalyst, CH_2Cl_2.

Olefin metathesis[230] of neighbouring *meso*-allyloxypropyl sidechains stabilised the complexes[231] and allowed conclusive characterisation. Covalently linked decamer and dodecamer **79** were isolated in 28% and 17% yield, respectively (Figure 3.10).[232] The absorption spectra of the ring complexes gave a large splitting in the Soret band showing efficient exciton coupling between chromophores. The fluorescence quantum yields relative to the constituent dimer were similar to that found in natural LH complexes.[233]

Osuka also used 1,3-phenylene spacers to direct formation of cyclic arrays. *Meso*-*meso* *m*-phenylene bridged porphyrin dimer **80** was synthesised by Suzuki-Miyaura coupling of 1,3-diodobenzene with a *meso*-boronated porphyrin monomer. Successive oligomerisations using a silver(I) salt gave directly *meso*-*meso* linked porphyrin oligomers **81**. Dimerisation of **81** (k = 2) was carried out at high dilution to favour intramolecular reaction, yielding cyclic dodecamer **82** (l = 1) in 12% yield (Scheme 3.9).[229] In the same manner, rings with 10, 18, 24 and 32 porphyrin units have all been synthesised, with a calculated diameter for the latter of 10.7 nm at full extension.[234][235]

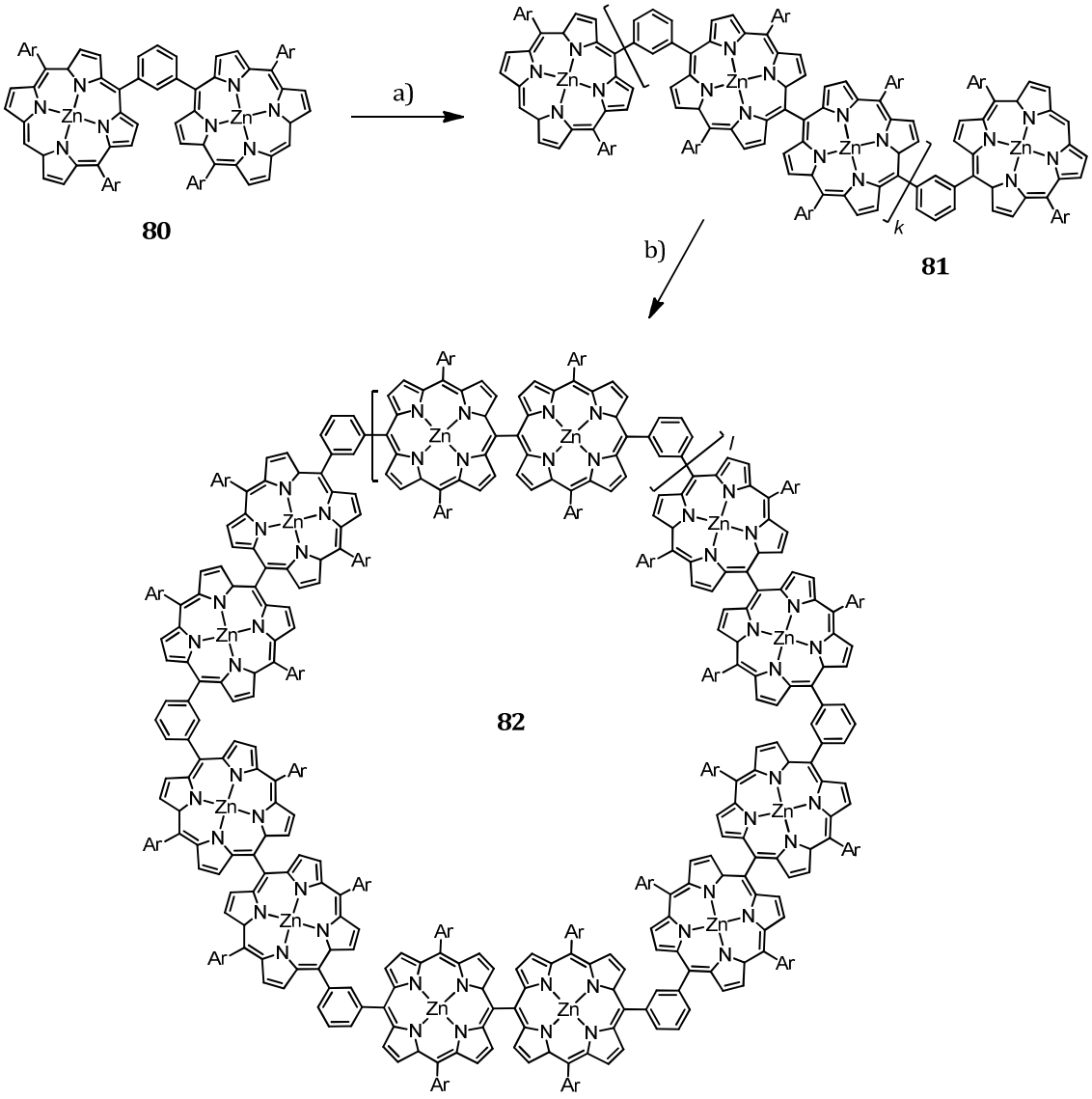

Scheme 3.9 Osuka's record-breaking *m*-phenylene bridged porphyrin macrocycles (*l* = 0, 1, 3, 4, 14 and 22): a) $AgPF_6$, $CHCl_3$, rt, 5 min (*k* = 1–3); b) $AgPF_6$, $CHCl_3$, (conc. ~ 10^{-6} M), CH_3CN, rt, 60 h. Ar = *p*-dodecyloxyphenyl.

The presence of a 1,3-phenylene linker weakens electronic coupling between adjacent chromophores, so Osuka investigated a class of directly linked all-porphyrin rings. Treating zinc porphyrin monomer with a Ag(I) salt had previously been shown to cause regioselective oligomerisation *via* porphyrin *meso*- positions (Chapter 1).[53][55] *Meso-meso* linked porphyrin tetramer was cyclised under high dilution (20 μM) with $AgPF_6$ to yield cyclic octamer **83** in

74% yield (Figure 3.11).[236] Increasing the concentration of the reaction to 3.3 mM preferred the formation of cyclic tetramer in 29% yield.

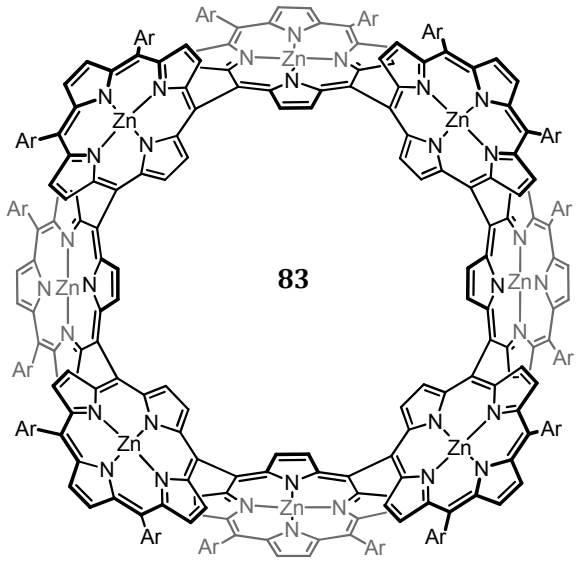

Figure 3.11 Osuka's directly *meso*-*meso* linked cyclic porphyrin octamer **83**.

Directly *meso*-*meso* linked cyclic hexamer could be similarly synthesised from linear porphyrin trimer in 22% yield. The sub-picosecond excitation energy hopping (EEH) times measured for the rings (Chapter 5) reflected the extremely strong exciton coupling between the chromophores.

Gossauer *et al*. reported the template-directed synthesis of cyclic hexamer **87** using tridentate ligand **88** to preorganise the linear oligomers.[237] Initially, **87** was prepared in a divergent-convergent 17-step synthesis, including a final high dilution cyclisation of linear hexamer **84** in highly variable yields between 8–30%.[238] In the presence of the template **88**, linear hexamer was cyclised in a reproducible 59% yield; or could be accessed directly from monomers **85** and **86** (Scheme 3.10) in 7% yield. Template **88** showed a binding affinity for the cavity of **87** of 2.8 $\times 10^9$ M^{-1}, and could be removed by treatment of the complex with THF.

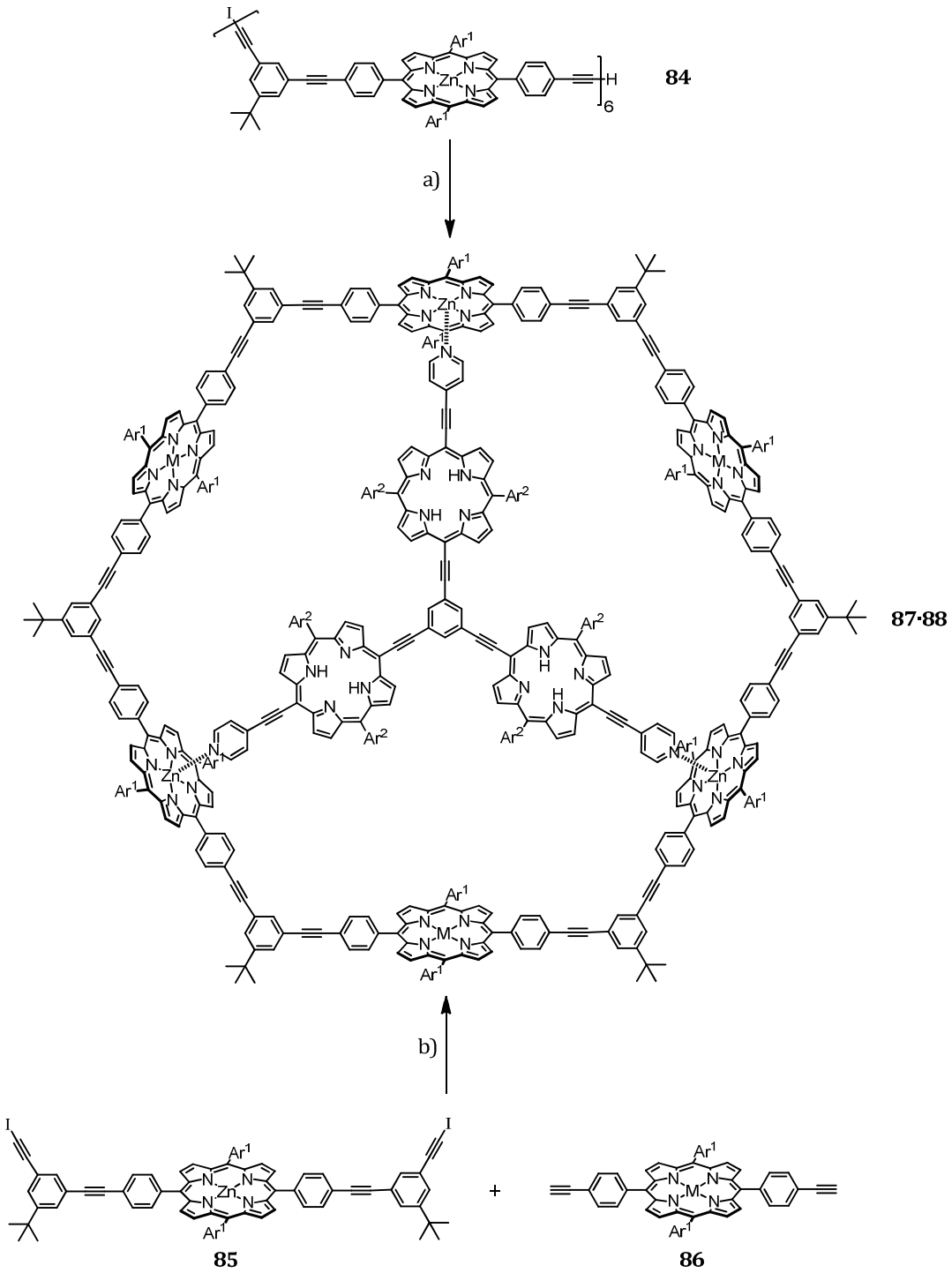

Scheme 3.10 Gossauer's template directed synthesis of cyclic hexamer **87**, from monomers **85** and **86** and hexamer **84**. a) $Pd_2(dba)_3$, P(*o*-tol)$_3$, NEt_3, toluene, 35 °C, 55%. M = Zn; b) $Pd_2(dba)_3$, P(*o*-tol)$_3$, NEt_3, toluene, 35 °C, 7%. M = Ni. Ar^1 = 2,4,6-trimethylbenzene; Ar^2 = 3,5-di(*tert*-butyl)phenyl.

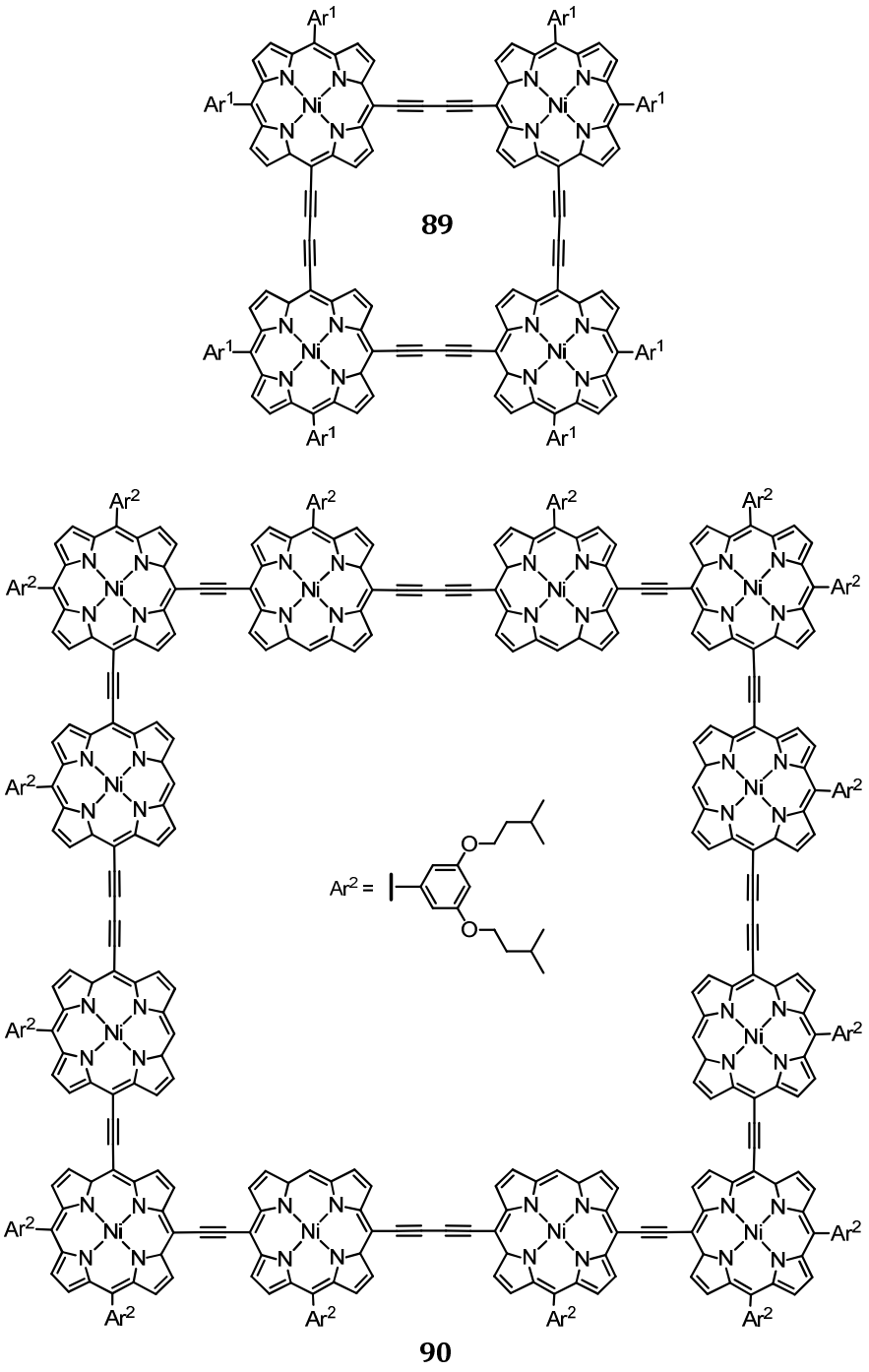

Figure 3.12 Suigara's π-conjugated cyclic porphyrin tetramer **89** and dodecamer **90**.

Two of the few examples of fully π-conjugated cyclic porphyrin arrays are Suigara's cyclic porphyrin tetramer **89** and dodecamer **90**.[239][240] Tetramerisation of 5,10-acetylene

substituted porphyrin cornerpieces under dilute (2.6 mM) Glaser-Hay conditions yielded **89** and **90** in 22% and 9% yields, respectively. The absorption spectrum of **89** showed a 105 nm bathochromic shift of the Soret and Q-like bands relative to the porphyrin monomer showing strong electronic communication between chromophores along the edge of the square.

3.3 Results and Discussion

3.3.1 Synthesis of porphyrin tetramer ***l*-P4**

In this thesis, two different types of porphyrins have been used to synthesise cyclic porphyrin oligomers: porphyrins with di(octyloxy)phenyl sidechains ***l*-P*N*^{C8}**,[131] and di(*tert*-butyl)phenyl sidechains **l-P*N*** (Figure 3.13).[128]

a)

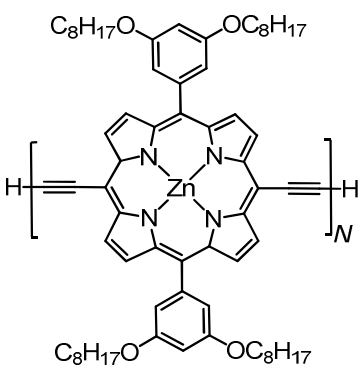

***l*-P*N*^{C8}**

b)

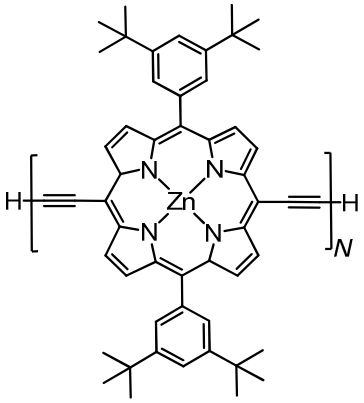

l*-P*N

Figure 3.13 Porphyrin oligomers with differing *meso*-aryl sidechains: a) "Octyloxy" porphyrins with 3,5-di(octyloxy)phenyl side chains ***l*-P*N*^{C8}**; b) "*Tert*-butyl" porphyrins with 3,5-di(*tert*-butyl)phenyl side chains ***l*-P*N***.

Tert-butyl porphyrins ***l*-P*N*** have limited solubility above the linear hexamer ***l*-P6**, so longer oligomers with these *meso*-aryl sidechains have not been reported.[69] Bending these oligomers into a cyclic conformation however increases their solubility, as the porphyrin π-systems can

no longer undergo efficient π-stacking. For this reason, *tert*-butyl cyclic hexamer ***c*-P6** is soluble in most organic solvents.

Di(octyloxy)phenyl *meso*-aryl groups were used to solubilise Osuka's 128-mer after solubility issues with *tert*-butyl porphyrins.[55] Butadiyne-linked porphyrin polymers up to an average degree of polymerisation of $N \approx 96$ are known to be soluble with these side-chains.[241] Octyloxy cyclic hexamer ***c*-P6^{C8}** and octamer ***c*-P8^{C8}** show excellent solubility.

It has been found that the solubility discrepancy of *tert*-butyl porphyrins between linear and cyclic oligomers facilitates purification of the cyclisation reactions. Oligomers that fail to cyclise precipitate due to the low solubility of *tert*-butyl porphyrin polymer. Once the polymer is filtered at the end of the reaction, the only soluble species in solution are cyclic oligomers.

3-5-Di(*tert*-butyl) porphyrin tetramer ***l*-P4** was synthesised as detailed previously (Scheme 3.11).[75] Karl Thorley, a DPhil in the group, prepared 3,5-di(*tert*-butyl)benzaldehyde **91** in two steps from toluene using a published route.[242] Dipyrromethane **5** was synthesised by acid-catalysed condensation of formaldehyde with an excess of pyrrole.[9]

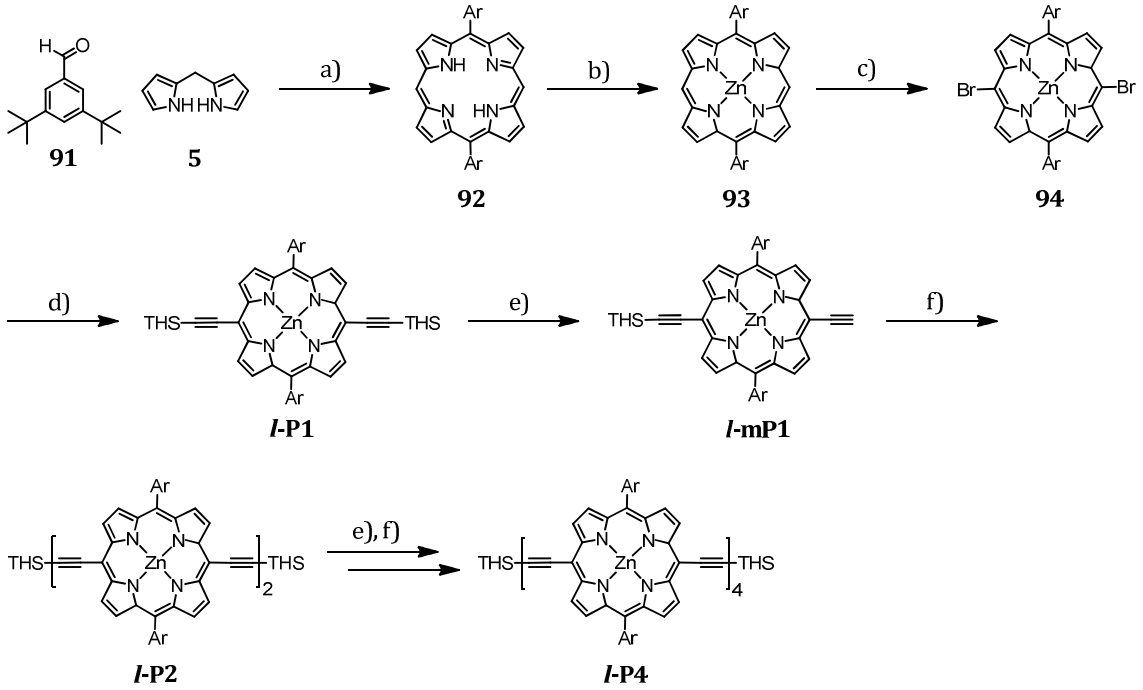

Scheme 3.11 Synthesis of bis-3,5-di(*tert*-butyl)phenyl porphyrin tetramer ***l*-P4**: a) 1. Trifluoroacetic acid, CH_2Cl_2, rt, 3 h. 2. DDQ, rt, 30 min. 3. NEt_3; b) $Zn(OAc)_2.2H_2O$, $CHCl_3$, methanol, rt, 1 h, 35% over two steps; c) *N*-bromosuccinimide, pyridine, $CHCl_3$, rt, 1 h, 80%; d) Ethynyltrihexylsilane, $Pd_2(dba)_3$, CuI, PPh_3, NEt_2H, toluene, pyridine, 80 °C, 2 h, 75%, e) TBAF, CH_2Cl_2, $CHCl_3$; f) CuCl, TMEDA, CH_2Cl_2, air, 30% over two steps. Ar = 3,5-di(*tert*-butyl)phenyl; THS = trihexylsilyl.

Free-base porphyrin **92** was synthesised in 35% yield from the acid-catalysed condensation of dipyrromethane **5** and 3,5-di(*tert*-butyl)benzaldehyde **91**, followed by oxidation with 2,3-dichloro-5,6-dicyanobenzoquinone (DDQ). Free-base porphyrin was converted quantitatively into zinc porphyrin **93** by addition of zinc acetate.[69] Bromination occurred selectively at the porphyrin *meso*-positions with addition of *N*-bromosuccinimide due to increased electron density on the methine bridge carbons.[10] This gave dibromoporphyrin **94** in 80% yield. Sonogashira coupling with ethynyltrihexylsilane gave 10,20-bis-ethynyl porphyrin, "porphyrin monomer" ***l*-P1** in 75% yield. Ethynyltrihexylsilane was prepared by the reaction of chlorotrihexylsilane with ethynyl magnesium bromide, in quantitative yield.[243]

Higher porphyrin oligomers could be prepared by sequential statistical deprotection and Glaser-Hay coupling steps. Statistical deprotection of porphyrin monomer ***l*-P1** with TBAF yielded a mixture of mono-deprotected porphyrin ***l*-mP1** (48%), bisdeprotected porphyrin monomer ***l*-dP1** (29%), and starting material (16%). The steric bulk of the THS groups allowed facile separation of this mixture by size-exclusion chromatography. Mono-deprotected monomer ***l*-mP1** was then homo-coupled using Glaser-Hay conditions,[225] yielding the porphyrin dimer ***l*-P2** in 83% yield. A statistical deprotection of porphyrin dimer ***l*-P2** gave mono-deprotected dimer ***l*-mP2** and deprotected dimer ***l*-dP2** in 50% and 25% yields, respectively. Dimerisation of mono-deprotected dimer ***l*-mP2** finally gave the porphyrin tetramer ***l*-P4** in 67% yield.

Linear porphyrin tetramer ***l*-P4** was deprotected with excess TBAF to give the deprotected linear tetramer ***l*-dP4** in 75% yield (Scheme 3.12).

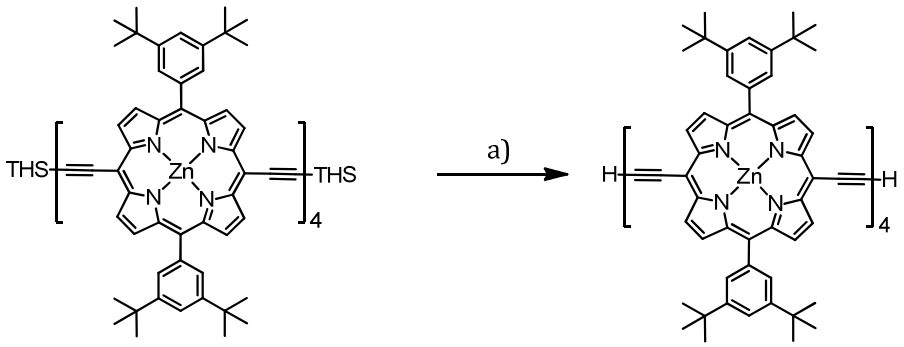

***l*-P4** ***l*-dP4**

Scheme 3.12 Deprotection of linear tetramer ***l*-P4**: a) TBAF, CH_2Cl_2, pyridine, rt, 15 min, 75%. THS = trihexylsilyl.

3.4 Classical templated synthesis of ***c*-P12**

THS-protected linear tetramer ***l*-P4** was titrated with dodecadentate template **T12** (Chapter 2) to test the ability of the latter to bind porphyrin oligomers. Deprotected tetramer ***l*-dP4** could

not be used due to issues with aggregation and poor solubility in non-coordinative solvents. The titration showed simple isosbestic behaviour (Figure 3.14a) and the resulting binding curve could be a fit to a simple 1:1 binding model, saturating at approximately a 1:3 ratio of template to oligomer (Figure 3.14b). Binding of tetramer ***l*-P4** caused a 68 nm red-shift in Q band absorption, indicating planarisation of the porphyrin subunits upon binding.

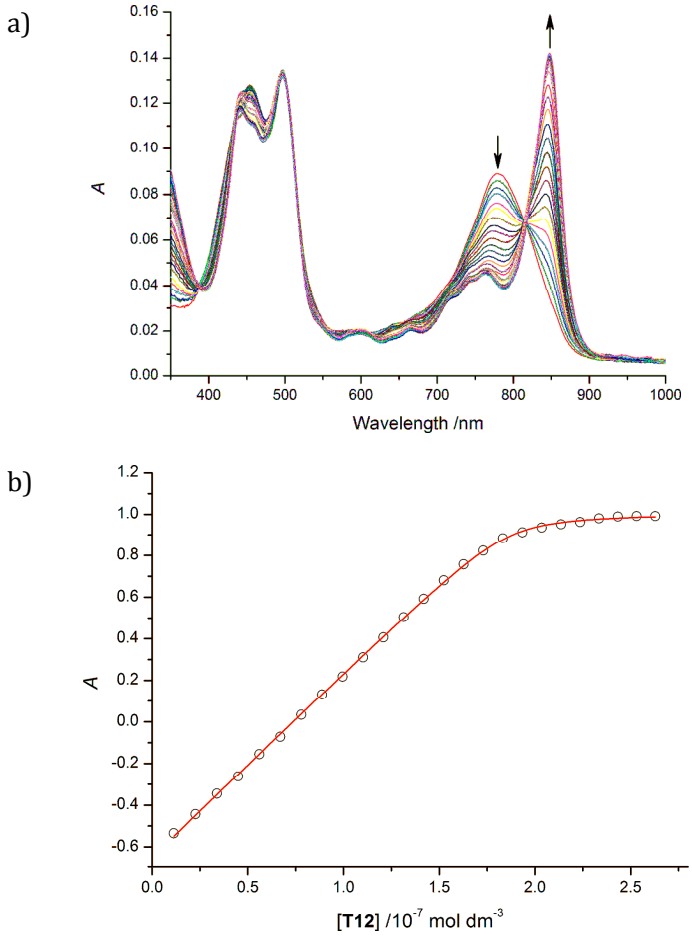

Figure 3.14 a) UV-Vis titration (CH_2Cl_2, 298 K) of linear porphyrin tetramer ***l*-P4** with dodecadentate template **T12**: $[\textbf{\textit{l}-P4}]_0 = 5.3 \times 10^{-7}$ M, arrows indicate areas of increasing or decreasing absorption over the course of the titration; b) Change of absorption, A with the concentration of template **T12**. Experimental data (○) is the absorption at 783 nm subtracted from that at 847 nm; theoretical data (–) is calculated from a 1:1 binding model to give a formation constant $K_f = (1.0 \pm 0.2) \times 10^9$ M^{-3} (see the Appendix for details).

Previously, cyclic hexamer and octamer complexes ***c*-P6·T6** and ***c*-P8·T8** were synthesised by oxidative coupling of linear oligomers coordinated to template **T6** and **T8**, respectively,[131][128] using conditions reported by Burton.[129] The conditions coupled terminal acetylenes in the presence of iodine in diisopropylamine with catalytic copper(I) iodide and $Pd(PPh_3)_2Cl_2$. Formation of the diyne was suggested to occur *via* reductive elimination of the bis(triphenylphosphine)dialkynyl palladium complex. The resulting Pd(0) was then reoxidised to Pd(II) by iodine (Figure 3.15).

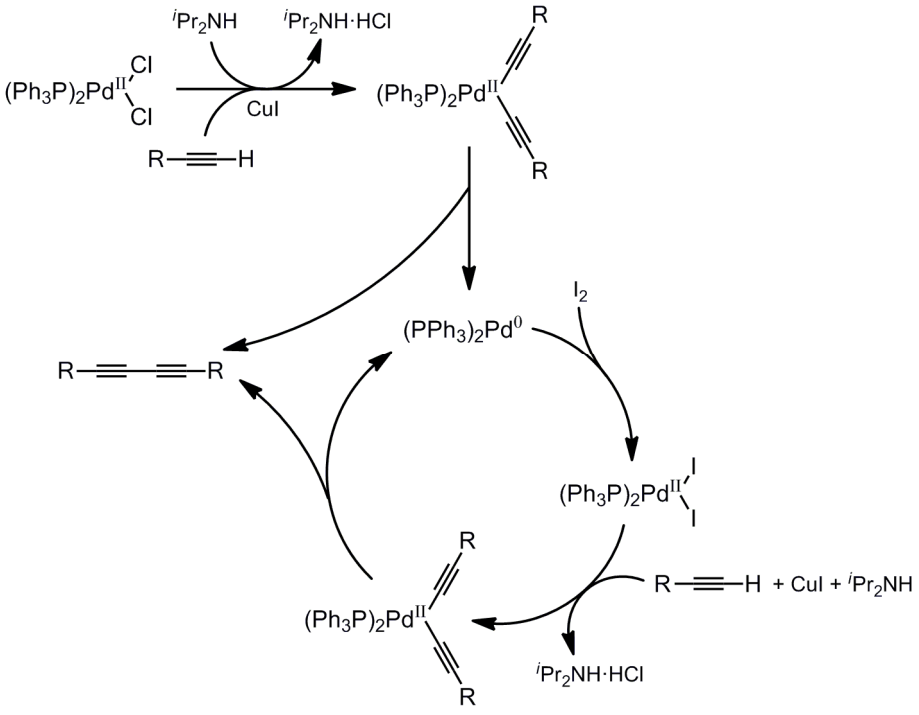

Figure 3.15 The catalytic cycle proposed by Burton *et al.* for the oxidative coupling of alkynes with a $Pd(PPh_3)_2Cl$ and CuI catalytic system, with iodine as the oxidant.**[129]**

Recently, an improved synthetic route to cyclic hexamer complex ***c*-P6·T6** was reported by the group which uses catalytic conditions reported by Swager.[135][244] These conditions use 1,4-benzoquinone in place of iodine as the oxidant to address the reactivity issues of iodine with terminal acetylenes.[245] These conditions have been found to produce higher molecular weight

porphyrin polymers than when using Burton's conditions.[246] Applied to the cyclic hexamer synthesis, the catalytic system allowed access to cyclic hexamer complex ***c*-P6·T6** directly from the monomer in 21% yield, compared to 5% using the conditions reported by Burton. The higher catalytic activity of the benzoquinone system allows the coupling reaction to be carried out at room temperature, whereas the iodine system required temperatures of 60 °C in order to proceed. It has been suggested that the increased efficiency of the benzoquinone system in the synthesis of ***c*-P6·T6** is due to the stronger porphyrin-template interactions as a result of the lower reaction temperatures.[247]

The new conditions were applied to the synthesis of ***c*-P12·T12**. Template **T12** was sonicated in solution for an hour with deprotected linear tetramer ***l*-dP4** to aid solubilisation of the porphyrins and coordination to the template. A catalyst solution of $Pd(PPh_3)_2Cl_2$, copper(I) iodide and 1,4-benzoquinone was prepared. Addition of diisopropylamine solubilised the catalysts and turned the solution from yellow to deep orange. The catalyst solution was added to a solution of the porphyrin-template complex **(*l*-dP4)$_3$·T12** at room temperature. The temperature was raised after an hour to 50 °C to speed up polymerisation of non-cyclic products to simplify the purification process. After purification, the ***c*-P12·T12** complex was isolated in 35% yield (Scheme 3.13).

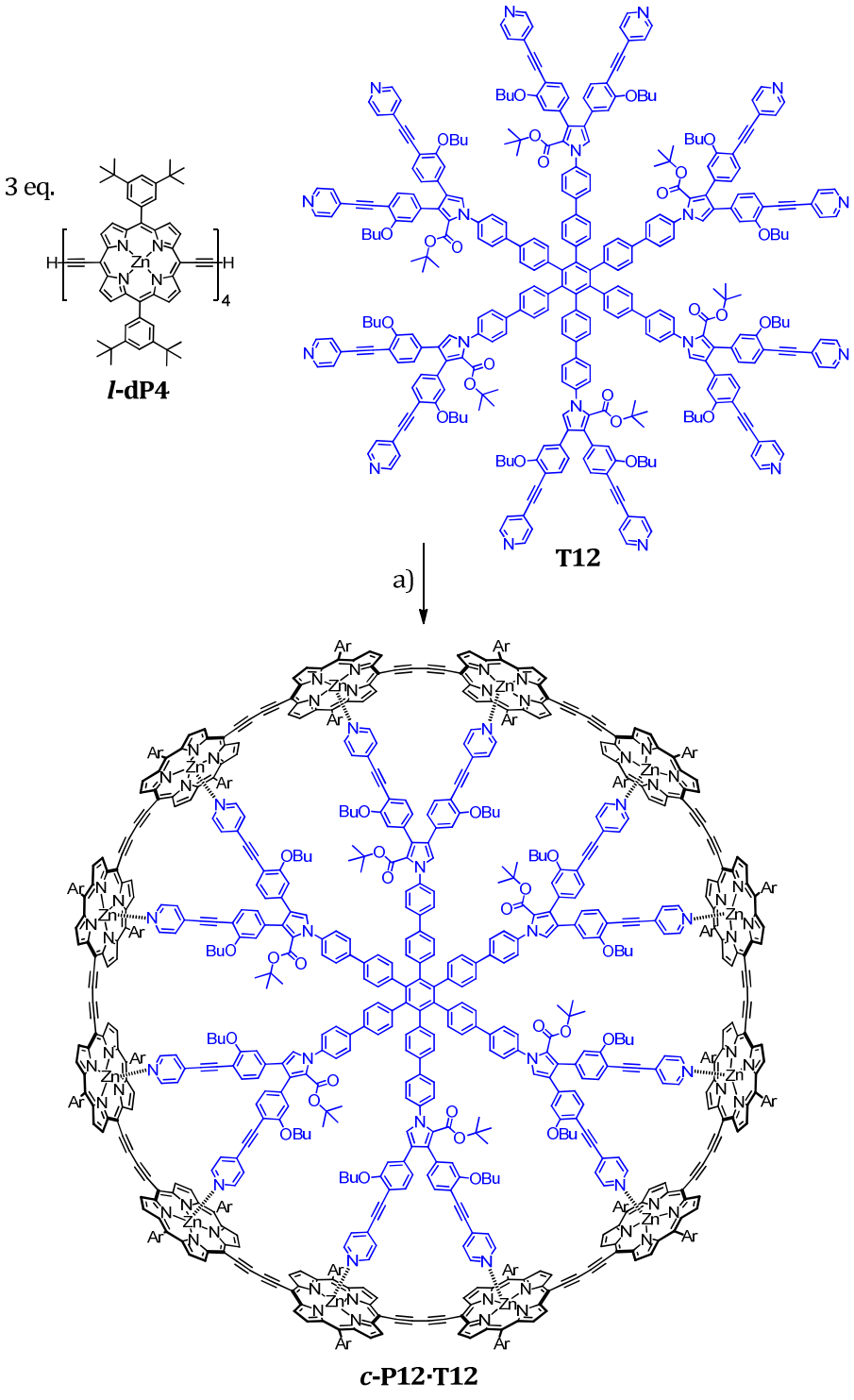

Scheme 3.13 Synthesis of the dodecadentate complex ***c*-P12·T12**: a) $Pd(PPh_3)_2Cl_2$, CuI, 1,4-benzoquinone, $^{i}Pr_2NH$, $CHCl_3$, air, 35%. Ar = 3,5-di(*tert*-butyl)phenyl.

The UV-vis absorption spectra of ***c*-P12·T12** showed an 32 nm red shift of the Q band relative to that of the acyclic precursor **(*l*-dP4)$_3$·T12** and an intensification of the Q band relative to that of the Soret (Figure 3.16). This suggested an increase in the π-conjugation length on cyclisation.

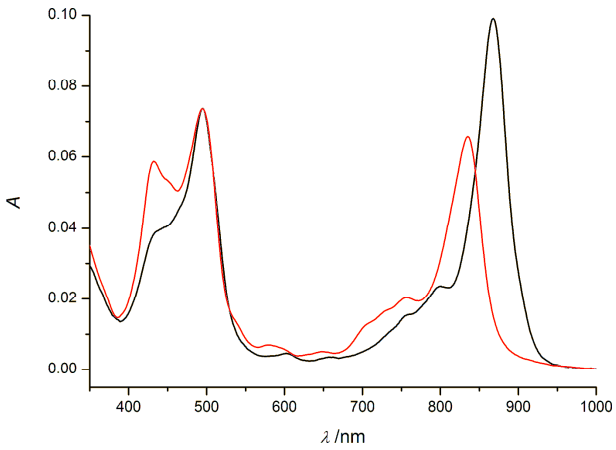

Figure 3.16 Normalised UV-vis absorption spectra ($CHCl_3$, 298 K) of linear tetramer-template complex **(*l*-dP4)$_3$·T12** (*red*) and cyclic dodecamer complex ***c*-P12·T12** (*black*).

The UV-vis absorption spectrum of ***c*-P12·T12** obtained by **T12** templated synthesis was compared to that of the complex obtained by ^{1}H NMR titration of cyclic dodecamer ***c*-P12** with **T12**. Cyclic dodecamer ***c*-P12**, obtained from the knock-out of the Vernier complex ***c*-P12·(T6)$_2$** (see Sections 3.6 and 3.8) was titrated with a solution of **T12** until 1:1 binding was observed. The UV-vis absorption of the two complexes are compared in Figure 3.17 and show an excellent match.

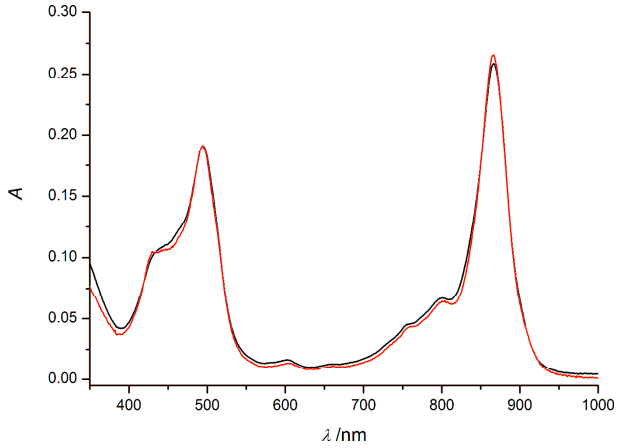

Figure 3.17 Normalised UV-vis absorption (CH_2Cl_2, 298 K) of complex ***c*-P12·T12** obtained by titration of cyclic dodecamer ***c*-P12** with 12-dentate template **T12** (*black*) and that by cyclisation of deprotected tetramer ***l*-dP4** bound to 12-dentate template **(*l*-dP4)$_3$·T12** (*red*).

3.5 Characterisation of ***c*-P12·T12**

3.5.1 ^{1}H NMR studies of model system ***l*-P2·15**

To facilitate the assignment of the ^{1}H NMR of cyclic dodecamer complex ***c*-P12·T12**, model system ***l*-P2·15** (Figure 3.18) was studied by NMR. A solution of dipyridyl pyrrole **15** in deuterated chloroform was titrated with porphyrin dimer ***l*-P2** until a 1:1 complex was formed, measured by NMR peak integration.

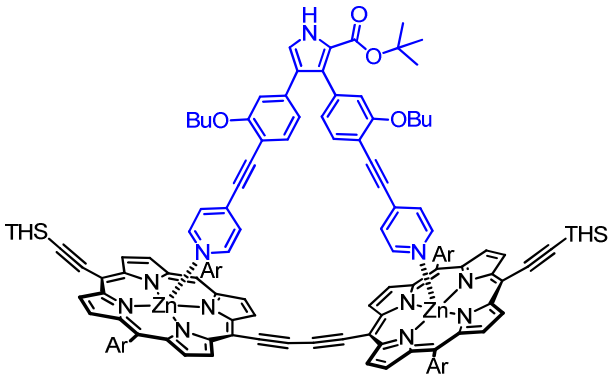

***l*-P2·15**

Figure 3.18 Structure of model system ***l*-P2·15** used to study the ^{1}H NMR shifts of complex ***c*-P12·T12**. Ar = 3,5-di(*tert*-butyl)phenyl; THS = trihexylsilyl.

Due to a relatively weak association constant between dipyridyl pyrrole **15** and porphyrin dimer ***l*-P2** (4×10^{7} M^{-1} for bis-3,5-di(octyloxy)phenyl-porphyrin dimer ***l*-P2^{C8}** with dipyridyl pyrrole **15**)[62], with an excess of either porphyrin or ligand, the excess titrant would be in fast exchange between bound and unbound states on the NMR timescale. As the chemical shifts of the bound pyridyl ligand are of most interest in order to assign the NMR of ***c*-P12·T12**, ***l*-P2·15** was synthesised ensuring a slight excess of ***l*-P2**, in order to retain sharp ligand peaks. The ^{1}H NMR of ***l*-P2·15** is shown in Figure 3.19. The full details of assignment can be found in the Appendices.

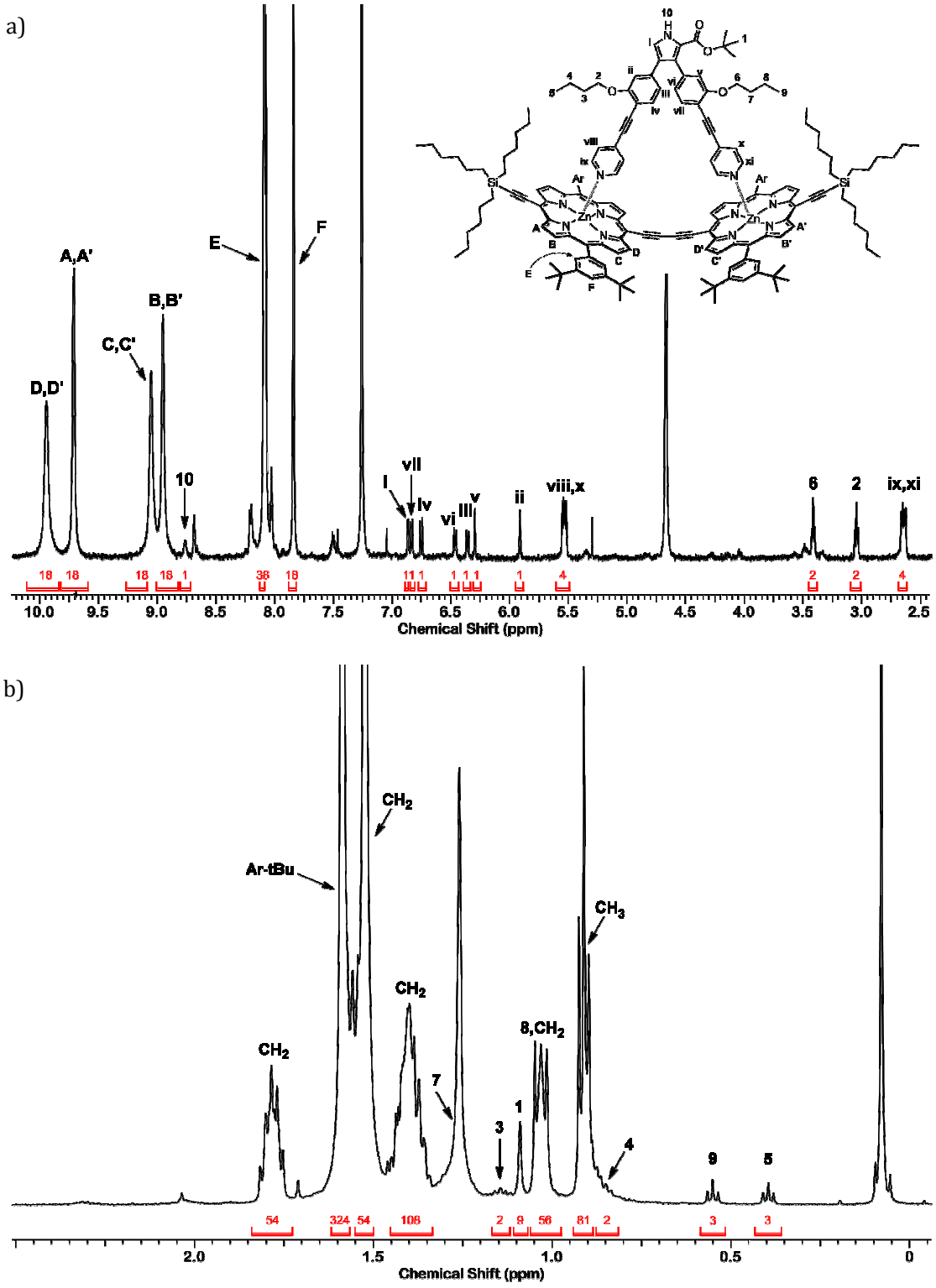

Figure 3.19 Fully assigned ^{1}H NMR spectrum of ***l*-P2·15** (500 MHz, $CDCl_3$, 298 K); a) aromatic region; b) aliphatic region.

The change in the proton shifts of the pyrrole ligand upon binding, $\Delta\delta_H$, is plotted in Figure 3.20. As with previous porphyrin-pyridyl complexes, the greatest chemical shift is seen closest to the porphyrin plane, at the α-pyridyl position, due to shielding from the porphyrin aromatic π-system.

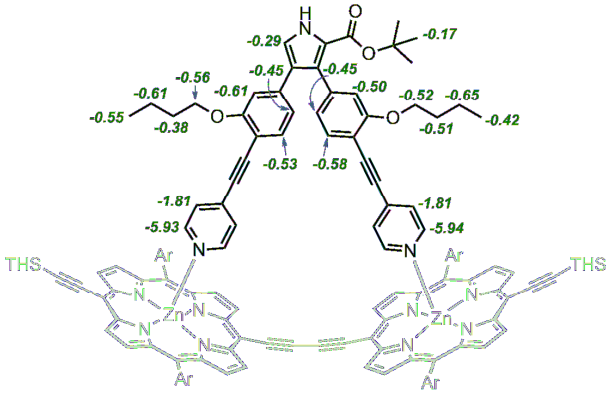

Figure 3.20 Binding induced shifts $\Delta\delta_H$ in ppm for dipyridyl pyrrole ligand **15**, calculated from ^{1}H NMR studies in $CDCl_3$. The $\Delta\delta_H$ for the pyrrole N*H* is not shown due to the high chemical shift dependence on hydrogen bonding.

3.5.2 ^{1}H NMR assignment of ***c*-P12·T12**

Overlaying the proton spectrum of complex ***l*-P2·15** with the dodecamer complex ***c*-P12·T12** allowed many of the peaks to be assigned immediately, and confirmed the binding of template **T12** in the cavity of the ring (Figure 3.21).

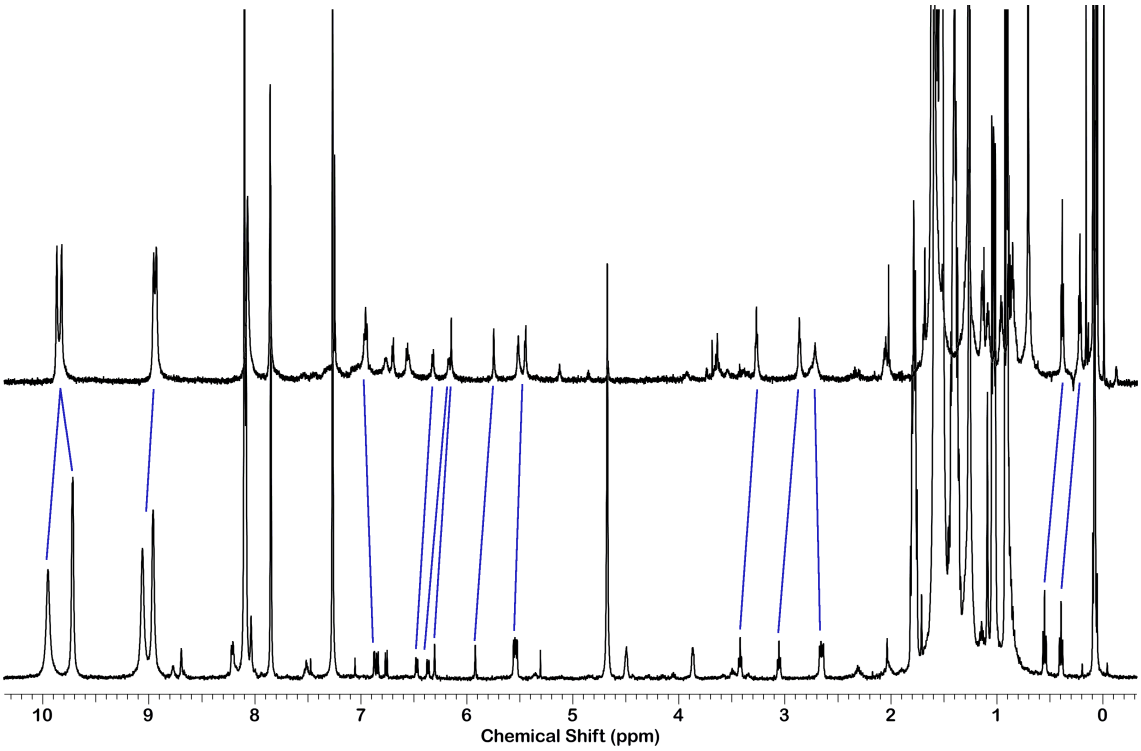

Figure 3.21 Diffusion edited ^{1}H NMR spectra of cyclic dodecamer complex ***c*-P12·T12** (*top*: 700 MHz, $CDCl_3$, 298 K), and dipyridyl pyrrole-dimer complex ***l*-P2·15** (bottom: 500 MHz, $CDCl_3$, 298 K) show many similarities.

As with previous ring-template systems,[128][131] the ^{1}H NMR of the ***c*-P12·T12** complex could be split into distinct regions. Peaks from porphyrin *β*-pyrrole protons occurred between 9.0–10.0 ppm, followed by the aryl porphyrin solubilising groups. Due to the shielding effect of the porphyrin ring π-system, the template protons were shifted upfield to between 2.5–7.0 ppm on binding. In the aliphatic region of the spectrum, the alkyl protons of the template, and *tert*-butyl protons from the porphyrin *meso*-aryl sidechains could be found (Figure 3.22).

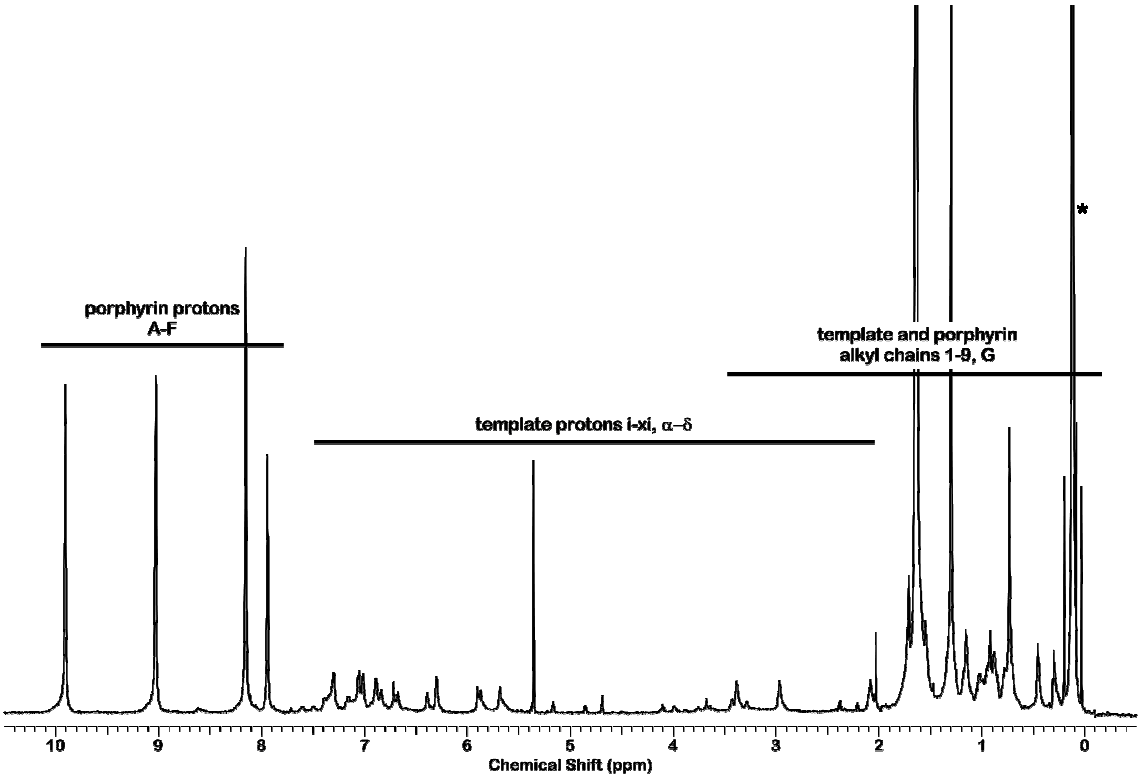

Figure 3.22 Diffusion-edited ^{1}H NMR spectrum of ***c*-P12·T12** (700 MHz, CD_2Cl_2/0.4% d_5-pyridine, 298 K; * indicates a silicon grease impurity).

By comparison with other porphyrin ring-template systems, the singlet at 8.12 ppm, integrating to 48H, could be assigned as *ortho*-aryl protons E (Figure 3.19a). Similarly, the singlet at δ 7.91, integrating to 24H, could be assigned as *para*-aryl protons F. E showed a strong NOE to the doublet at δ 8.99, which could be assigned to adjacent β-pyrrole protons B and C. A and D, at a greater distance from the solubilising aryl groups, showed a weaker NOE (Figure 3.23).

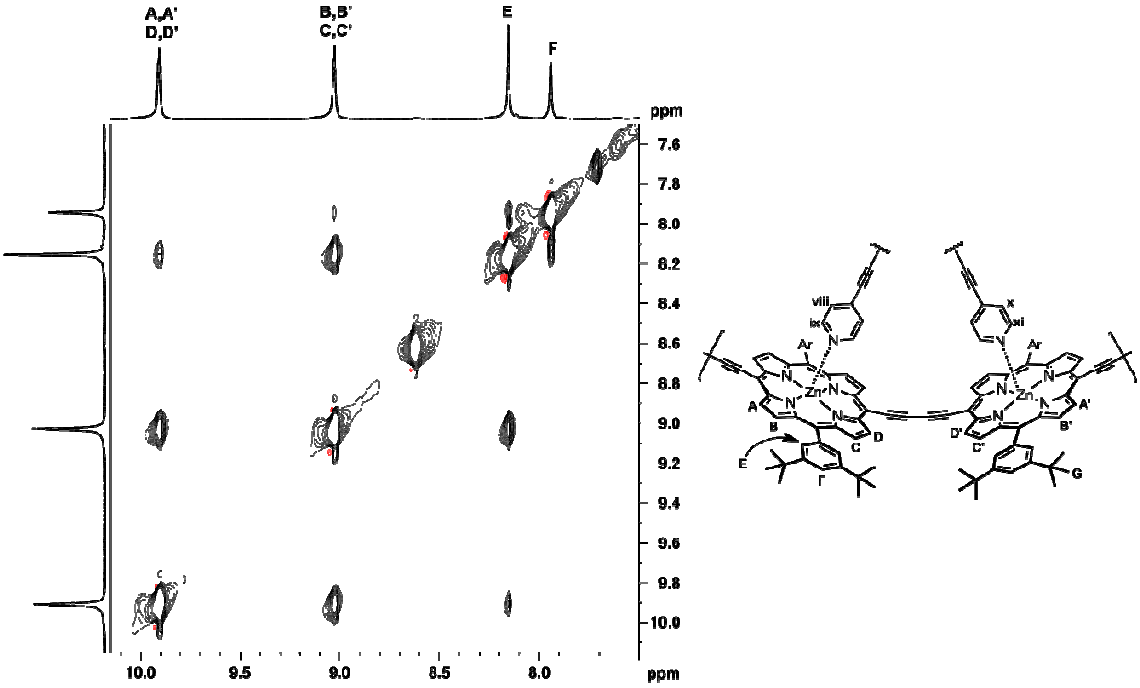

Figure 3.23 ^{1}H 2D NOESY spectrum (700 MHz, CD_2Cl_2/0.4% d_5-pyridine, 298 K) of ***c*-P12·T12** showing the porphyrin region of the spectrum. A mixing time of 250 ms was used (applied as a phase-alternating spin-lock pulse).

Tert-butyl protons G exhibited NOEs to protons A–F, allowing it to be assigned (Figure 3.24).

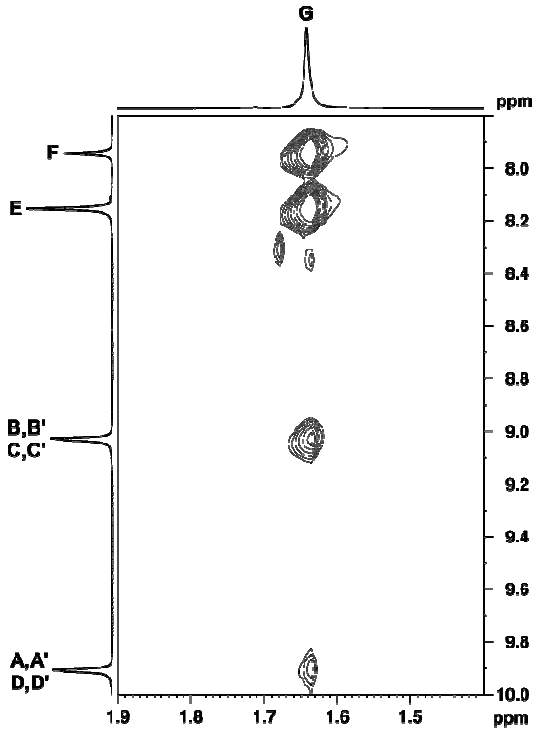

Figure 3.24 ^{1}H 2D NOESY spectrum (700 MHz, CD_2Cl_2/0.4% d_5-pyridine, 298 K) of ***c*-P12·T12** showing NOEs between *tert*-butyl protons G with porphyrin protons A–F. A mixing time of 250 ms was used (applied as a phase-alternating spin-lock pulse).

Due to the shielding effect of the porphyrin ring π-system, all the bound template protons were found at lower chemical shift to that of the unbound template. As with the unbound template, the presence of the *tert*-butyl ester on the 2-position of the pyrrole made protons on the binding arms inequivalent. The template butoxy side chain protons 2–9 could be assigned by following the crosspeaks in the COSY (Figure 3.25).

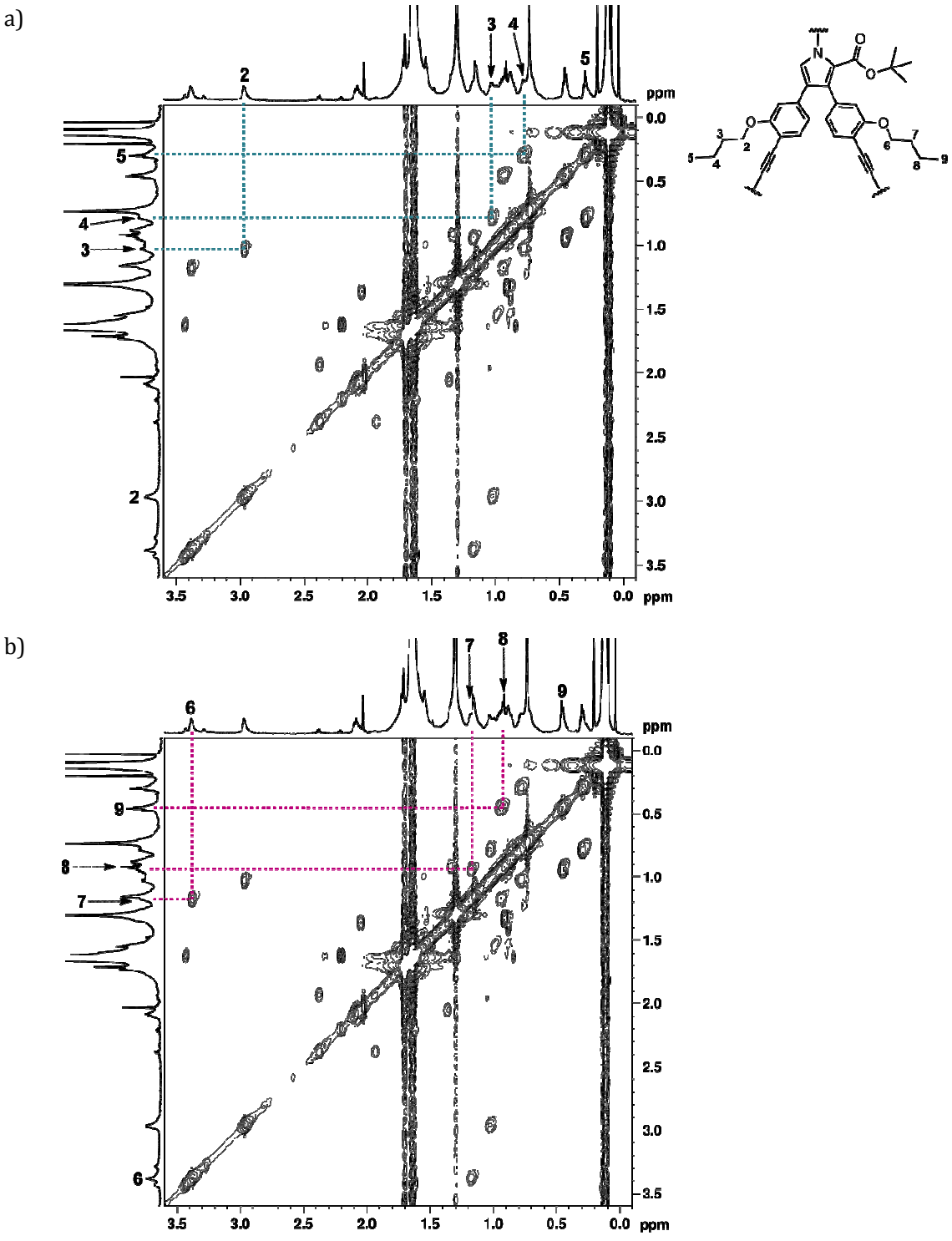

Figure 3.25 ^{1}H COSY (700 MHz, CD_2Cl_2/0.4% d_5-pyridine, 298 K) of the alkyl region of the spectrum showing characterisation of a) alkyl protons 2–5, and b) alkyl protons 6–9.

NOEs between alkoxy protons 2 and 6 allowed neighbouring aryl protons ii and v, respectively, to be assigned (Figure 3.26).

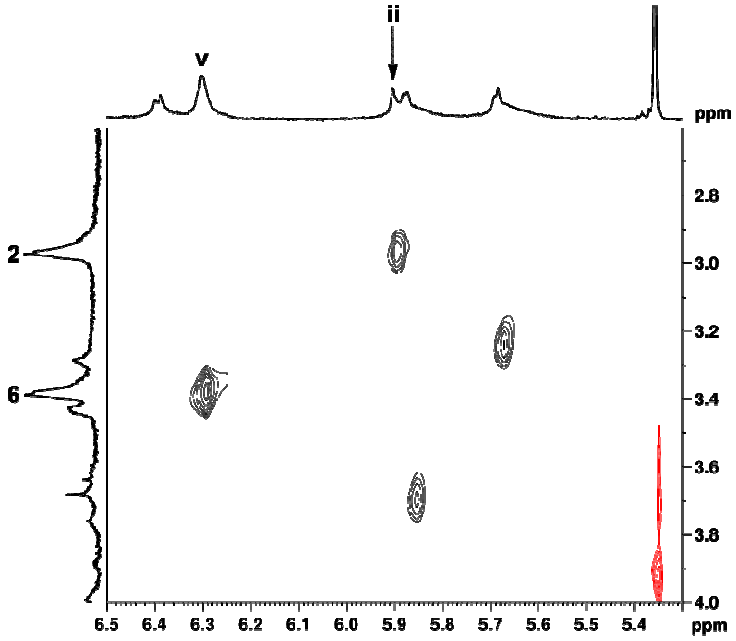

Figure 3.26 ^{1}H 2D NOESY (700 MHz, CD_2Cl_2/0.4% d_5-pyridine, 298 K) of complex ***c*-P12·T12**, showing NOEs between protons 2–ii and 6–v. A mixing time of 250 ms was used (applied as a phase-alternating spin-lock pulse).

Template *tert*-butyl protons 1 are expected to show NOEs with aromatic protons v–vii and α–β. A singlet at δ 0.70 showed multiple NOEs to signals in the template aromatic region. 1 showed a strong NOE with the broad singlet at δ 6.27, and no NOE with the singlet at δ 5.87, confirming their assignments as v and ii, respectively (Figure 3.27).

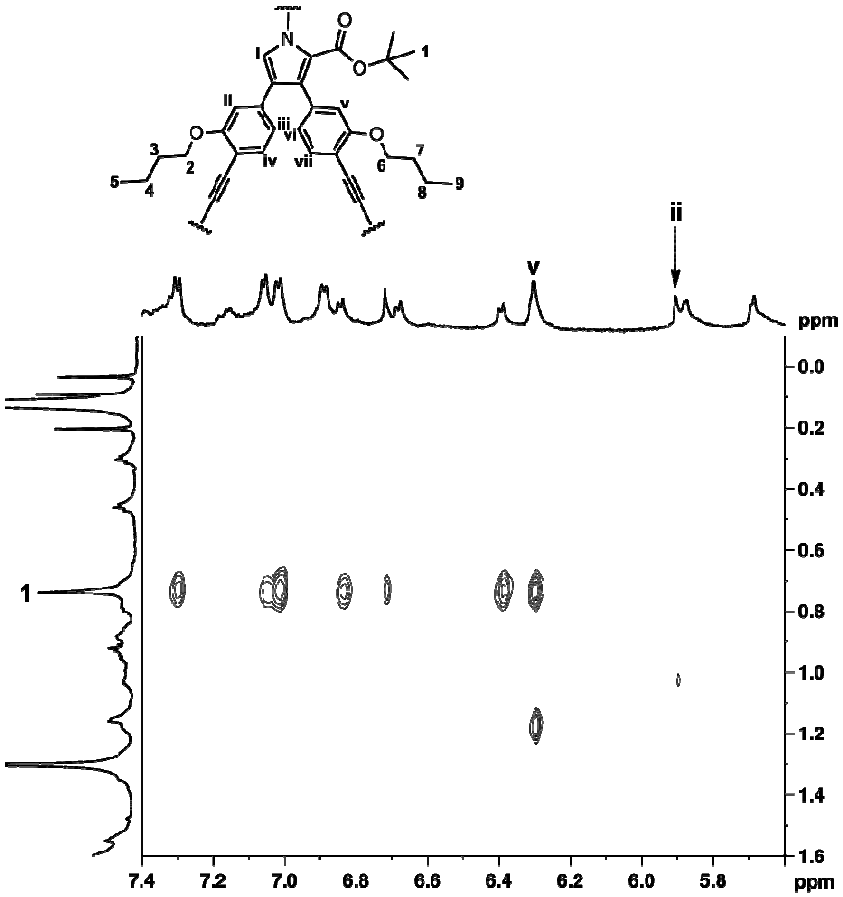

Figure 3.27 ^{1}H 2D NOESY (700 MHz, CD_2Cl_2/0.4% d_5-pyridine, 298 K) of complex ***c*-P12·T12**, showing NOEs between template *tert*-butyl protons 1 and template aromatic protons. A mixing time of 250 ms was used (applied as a phase-alternating spin-lock pulse).

The remaining singlet, integrating to 6H at δ 6.68 could thus be assigned to pyrrole proton i. Proton i showed a weak NOE with a doublet integrating to 12H at δ 6.98, which could be assigned to hub protons α (Figure 3.28).

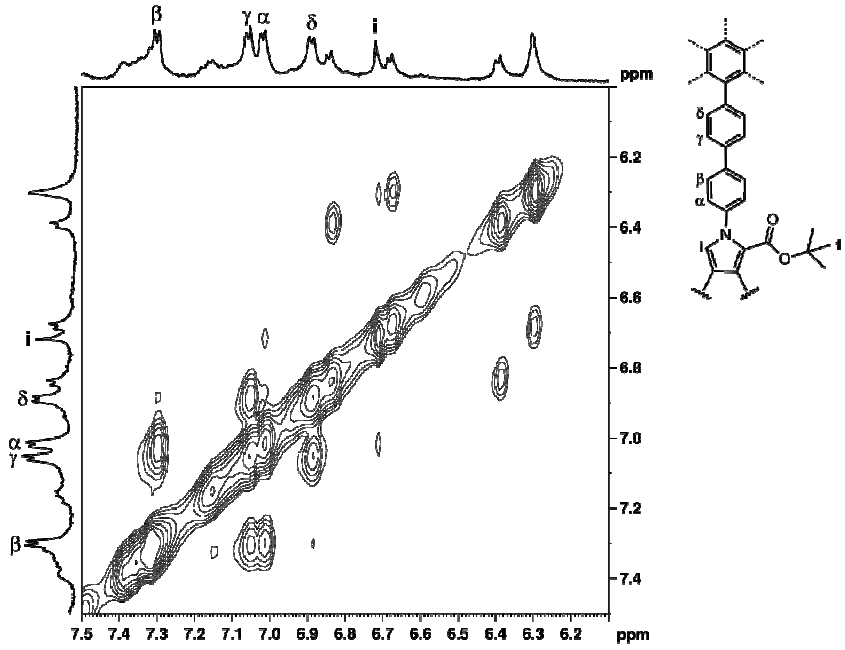

Figure 3.28 ^{1}H 2D NOESY (700 MHz, CD_2Cl_2/0.4% d_5-pyridine, 298 K) of complex ***c*-P12·T12**, showing NOEs between pyrrole proton i and hub proton α. A mixing time of 250 ms was used (applied as a phase-alternating spin-lock pulse).

Hub protons α and β are expected to couple with one another; similarly are γ and δ. This could be seen in the COSY (Figure 3.29). Furthermore, crosspeaks between aryl protons iii–iv, and vi–vii were seen. One crosspeak lies under the broad singlet at *δ* 6.27 which is assigned to aryl proton v. This singlet integrated to 12H, showing that protons iii and v overlap in the spectrum. This was confirmed in both the ^{1}H NMR run in $CDCl_3$ and the HSQC where these two peaks are resolved. In the uncoordinated template, protons adjacent to the *tert*-butyl ester were deshielded and came at higher chemical shifts to the protons opposite the ester. This pattern transfers to the bound template so the two doublet pairs iii–iv and vi–vii could be assigned with certainty.

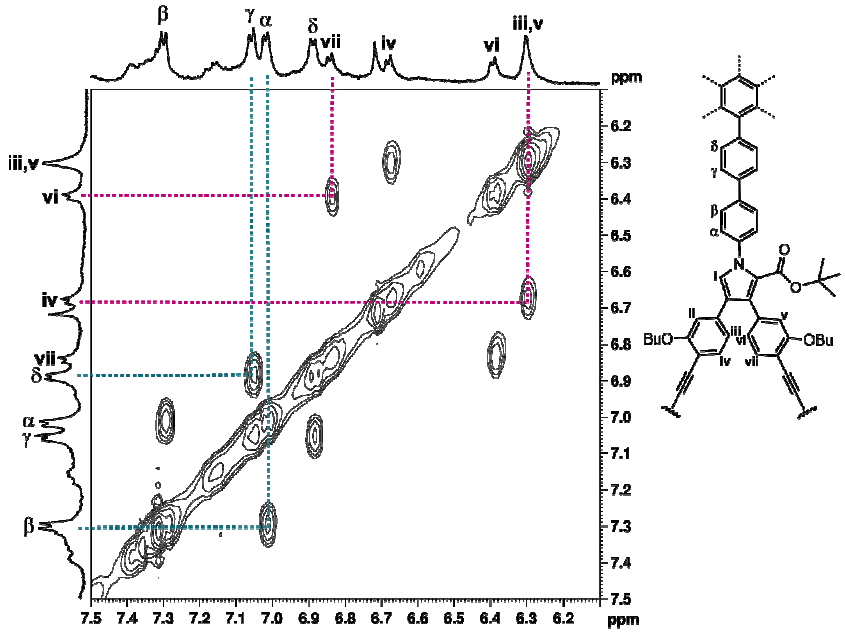

Figure 3.29 ^{1}H COSY (700 MHz, CD_2Cl_2/0.4% d_5-pyridine, 298 K) of the template aryl region of the spectrum showing characterization of hub protons α–δ and aryl protons iii, iv, vi, and vii.

It was necessary to add a small amount of deuterated pyridine (0.4% *v/v*) to the NMR sample as the complex ***c*-P12·T12** aggregated in dichloromethane, leading to broadening of the signals. This made assignment of pyridyl protons viii–xi in the CD_2Cl_2/d_5-pyridine solvent more challenging, as the presence of competitive pyridine caused the pyridyl arms to go into fast exchange between bound and unbound states. Originally, the ^{1}H NMR of ***c*-P12·T12** was acquired in $CDCl_3$, which is a superior solvent for the complex thus no additional pyridine is required. However, in chloroform, slow rotation of the inner phenylene ring due to steric constraints caused significant broadening of protons δ. In addition, signals α and γ overlapped, and the doublet due to β was obscured by residual chloroform, making the hub protons difficult to assign. However, in the absence of pyridine, no fast exchange of the template arms occurs, so viii–xi is well resolved in the chloroform spectrum. *α*-Pyridyl protons ix and xi showed strong NOEs to porphyrin *β*-pyrrole protons A–D (Figure 3.30). Weaker NOEs, as a

result of spin diffusion, were also seen for the *β*-pyridyl protons viii and x. The chemical shifts for viii–ix are in agreement with previous porphyrin ring-template systems.[128][131]

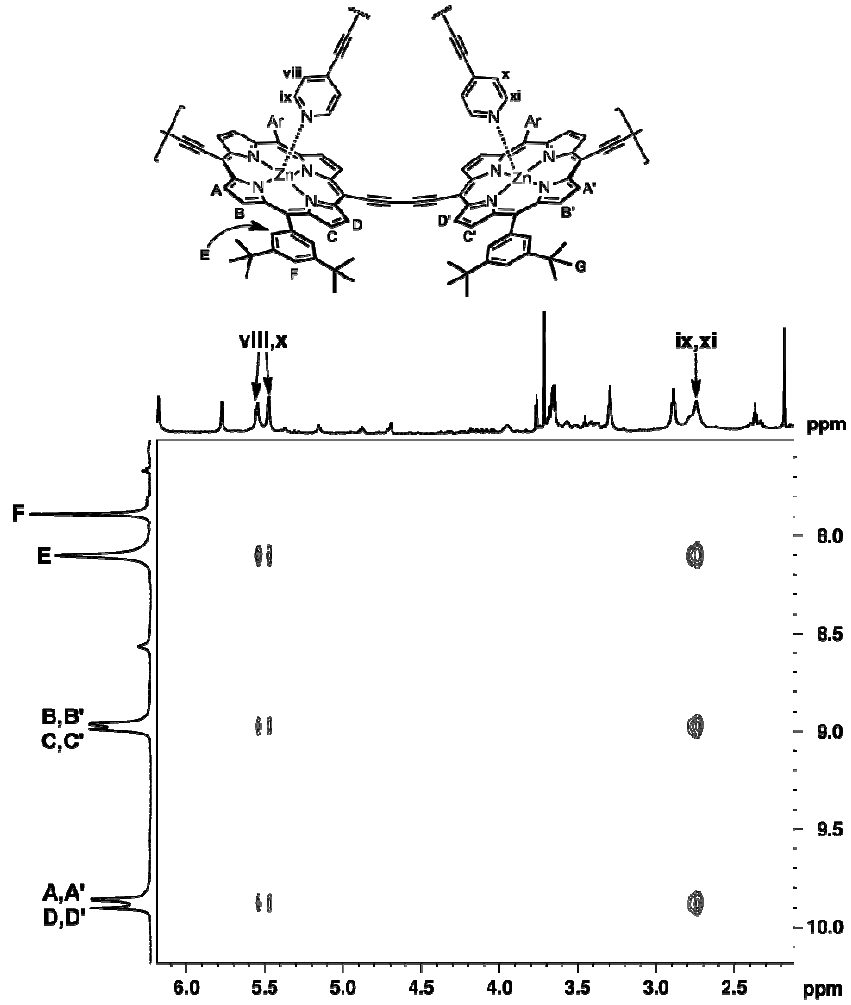

Figure 3.30 ^{1}H 2D NOESY (700 MHz, $CDCl_3$, 323 K) of complex ***c*-P12·T12**, showing NOEs between porphyrin *β*-pyrrole protons A–D with *α*-pyridyl protons ix and xi and *β*-pyridyl protons viii and x. A mixing time of 250 ms was used (applied as a phase-alternating spin-lock pulse).

In Figure 3.30 it is also noteworthy that peaks due to porphyrin protons A–D resolve into four distinct doublets, in contrast to the two doublets in the dichloromethane/pyridine spectrum. This suggests that in the presence of a small amount of pyridine, the template is 'hopping' in and out of the porphyrin ring, causing the A/D and B/C pairs to become equivalent.

Overlapping the ^{1}H spectra run in both solvents immediately makes apparent that the two doublets at δ 5.66 and δ 5.84 in the dichloromethane/pyridine spectrum are due to β-pyridyl protons viii and x. These two peaks couple to two very broad peaks at δ 3.25 and δ 3.75 in the COSY (Figure 3.31). This is a relatively high chemical shift for bound α-pyridyl protons, but this, coupled with the broadness of the peaks is consistent with a template in fast exchange between bound and unbound states.

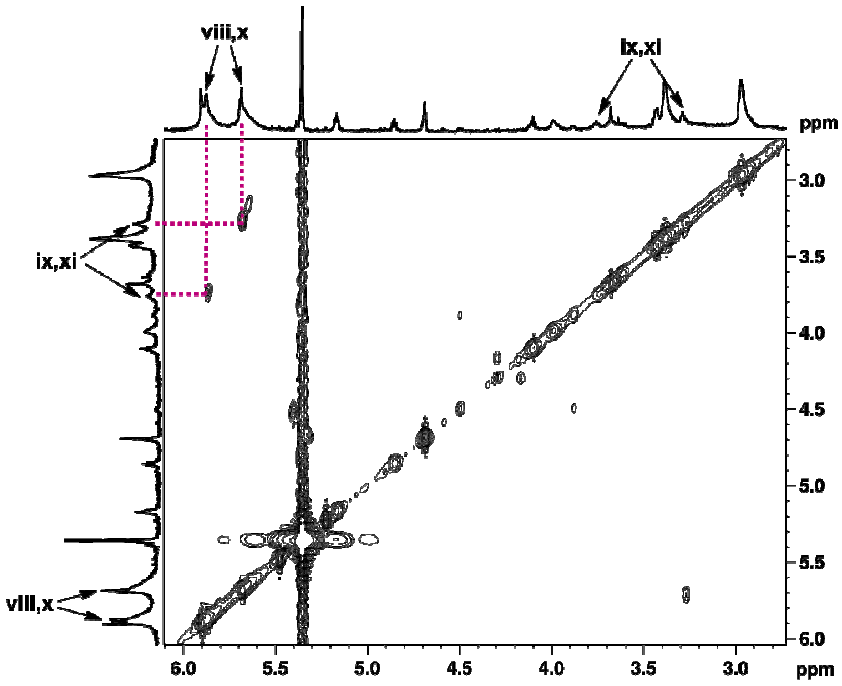

Figure 3.31 ^{1}H COSY (700 MHz, CD_2Cl_2/0.4% d_5-pyridine, 323 K) of ***c*-P12·T12** showing coupling between α-pyridyl protons ix and xi with β-pyridyl protons viii and x.

The fully assigned ^{1}H spectrum can be seen in Figure 3.32. The small amount of baseline impurity, particularly at δ 7.13 and δ 7.30–7.35 can be assigned as fully unbound template from the HSQC.

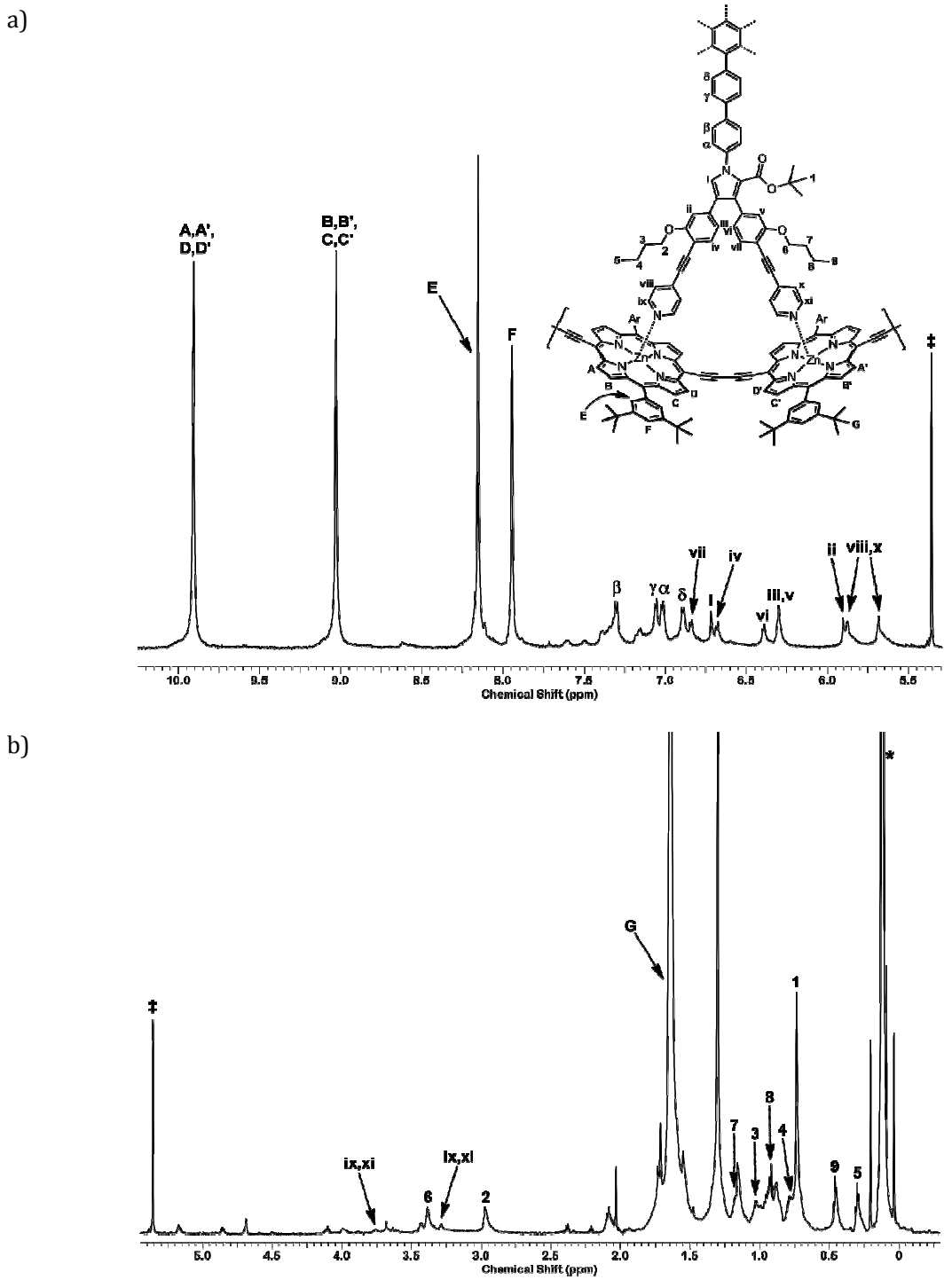

Figure 3.32 Fully assigned diffusion edited ^{1}H spectrum of ***c*-P12·T12** (700 MHz, CD_2Cl_2/0.4% d_5-pyridine, 298 K); a) aromatic region; b) aliphatic region; ‡ indicates residual solvent, * indicates a silicon grease impurity.

The changes in chemical shift of the template protons upon binding to the nanoring, $\Delta\delta_H$, were calculated and found to be comparable to that of previous porphyrin ring-template systems, showing that **T12** is binding in the cavity of the porphyrin nanoring (Figure 3.33). The values were calculated from the $CDCl_3$ ^1H NMR spectra of bound and unbound template **T12**.

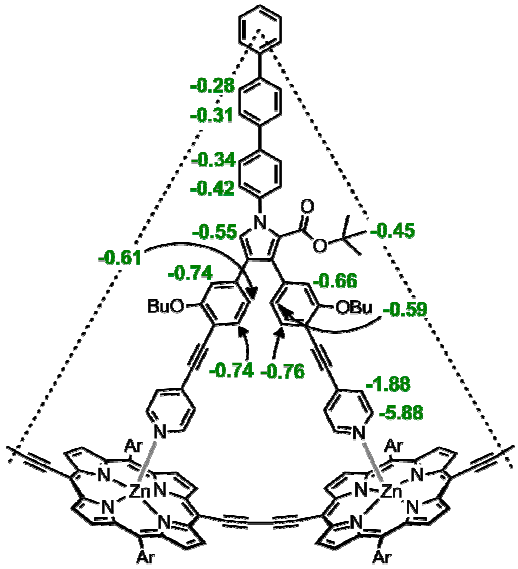

Figure 3.33 Binding induced shifts $\Delta\delta_H$ in ppm for template **T12**, calculated from ^1H NMR studies in $CDCl_3$.

3.5.3 SAXS characterisation of *c*-P12·T12

Solution-phase small-angle X-ray scattering (SAXS) has recently emerged as a powerful tool for characterising synthetic supramolecular architectures.[248] The method gives low-resolution structural information on the overall size and shape of molecules in the absence of single crystals.[249] At very small scattering angles $q < 1.3/R_g$, the particle scattering intensity $I(q)$, can be described by the Guinier relationship[250]

$$I(q) = I(0)\exp\left(\frac{-q^2{R_g}^2}{3}\right) \qquad \text{Eq. 22}$$

where R_g is the radius of gyration and characterises particle size, and $I(0)$ is the scattering intensity at zero angle.

SAXS experiments on cyclic dodecamer complex ***c*-P12·T12** were carried out by Dmitry Kondratuk using synchrotron radiation at Diamond Light Source (UK) in collaboration with Marc Malfois. The experimental scattering data were compared to a simulated scattering profile, created by the program "Crysol"[251] using an MM+ geometry optimised molecular model created in Hyperchem™ of ***c*-P12·T12** (Figure 3.34c). The simulated data are in very good agreement with the experimental data (Figure 3.34a). The pair-distribution function (PDF), calculated from the raw scattering data using the program "Gnom",[252] features an intense characteristic peak at 50 Å, close to the predicted dimensional size for ***c*-P12·T12** of 49 Å (Figure 3.34b). The scattering distances are dominated by the zinc-zinc distances in the molecule, due to the high electron density of these atoms.

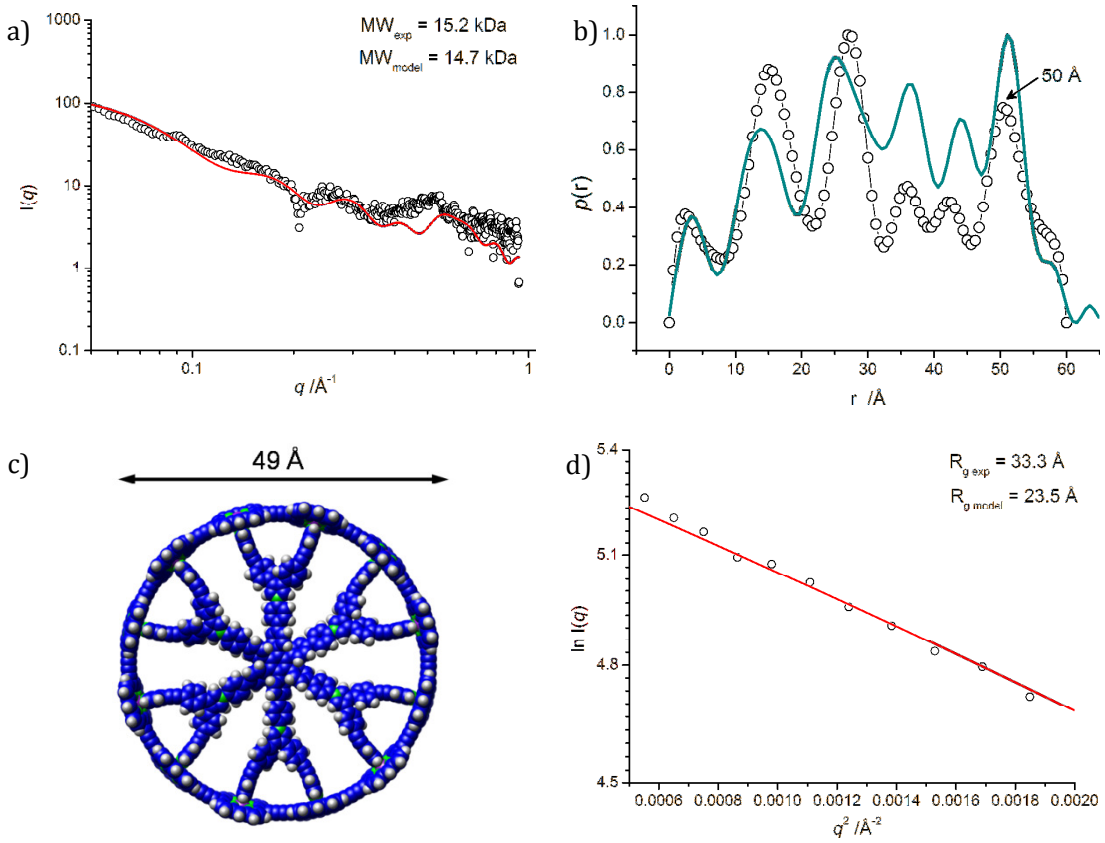

Figure 3.34 SAXS analysis (toluene, 298 K) of cyclic dodecamer complex ***c*-P12·T12**: a) Experimental scattering curve (○) plotted on a double log scale with fitted data from the molecular model (–). The experimental molecular weight was determined from the extrapolated scattering intensity at zero angle (q = 0) with ***c*-P6·T6** as standard;[244] b) Experimental (⊖) and model based (–) pair distribution function, obtained using the software "Gnom". The measured dimensions correspond well to the calculated diameter of the molecule within the 3 Å resolution of the experiment; c) Molecular model used for fitting of and comparison with experimental data. The geometry was optimised using the MM+ forcefield in HyperChem™; d) Guinier plot of the experimental scattering data of ***c*-P12·T12** (○) at very small angles. The fit (–) to the Guinier equation was obtained using the software "Primus".

The scattering intensity at zero angle $I(0)$ is directly proportional to the number of electrons in the sample, which is itself dependant on the mass concentration c of the sample, and the molecular weight MW.[253] Using a solution of cyclic hexamer complex ***c*-P6·T6** as a standard s,[244] the molecular weight of the analyte x can be calculated[254]

$$MW_x = \frac{I(0)_x}{c_x} \times \frac{c_s}{I(0)_s} MW_s \qquad \text{Eq. 23}$$

The calculated molecular weight for ***c*-P12·T12** of 15.2 kDa is in good agreement with the expected mass of 14.5 kDa (Figure 3.34a).

The scattering data in the Guinier region are very linear, confirming the monodispersity of the sample (Figure 3.34d). The experimental radius of gyration, obtained from the gradient of the plot (R_g = 33.3 Å) is significantly larger than that for the simulated scattering profile from the modelled structure ($R_{g\ model}$ = 23.5 Å). The latter, however, is very close to the value obtained from the experimental data using the program "Gnom" ($R_{g\ exp,\ \mathrm{GNOM}}$ = 23.8 Å).

The radius of gyration, calculated molecular weight, PDF and scattering data obtained for ***c*-P12·T12** match well with calculated values, and thus confirm the structure of the cyclic complex.

3.6 Vernier templated synthesis of ***c*-P12**

The difficulty in the synthesis and purification of the dodecadentate template **T12** illustrated that the classical templating route, where the number of binding sites on the template equals the number of porphyrins in the final structure, was limited in its scope for the synthesis of larger rings. The Vernier approach, as introduced in Section 3.1.1, provides an attractive alternate route to cyclic dodecamer ***c*-P12** *via* a hexadentate template **T6** and deprotected linear porphyrin tetramer ***l*-dP4**. The two species bind together to form the Vernier complex **(*l*-dP4)$_3$·(T6)$_2$**, which probably consists of two isomers (Scheme 3.14). Covalent coupling of the tetramer units would yield a 'figure-of-eight' complex ***c*-P12·(T6)$_2$**, which, when the templates are removed, would give the cyclic dodecamer ring ***c*-P12**.

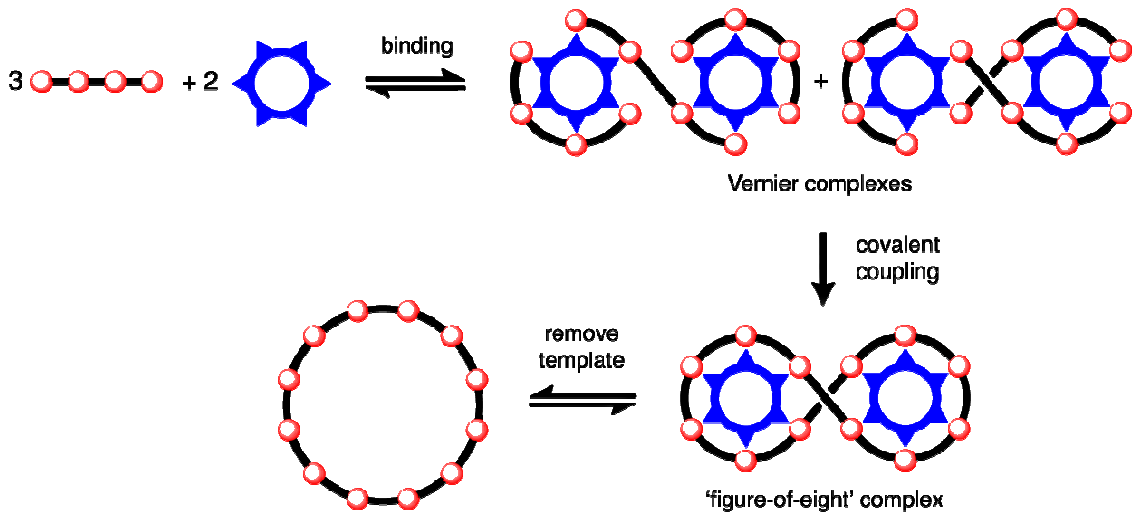

Scheme 3.14 Vernier templated synthesis of cyclic dodecamer ***c*-P12** *via* a hexadentate template (*blue*) and linear tetramer (*red circles*).

3.6.1 Synthesis of hexadentate template **T6**

Hexadentate template **T6** was synthesised as described previously.[128] Hexaphenylbenzene **95** was selectively brominated at the *para*-positions by stirring in neat bromine to give **96** quantitatively.[255] The regioselectivity of this reaction stems from steric hindrance of the bulky bromine atoms. Suzuki coupling with 4-pyridine boronic acid gave template **T6** in 35% yield (Scheme 3.15).[128]

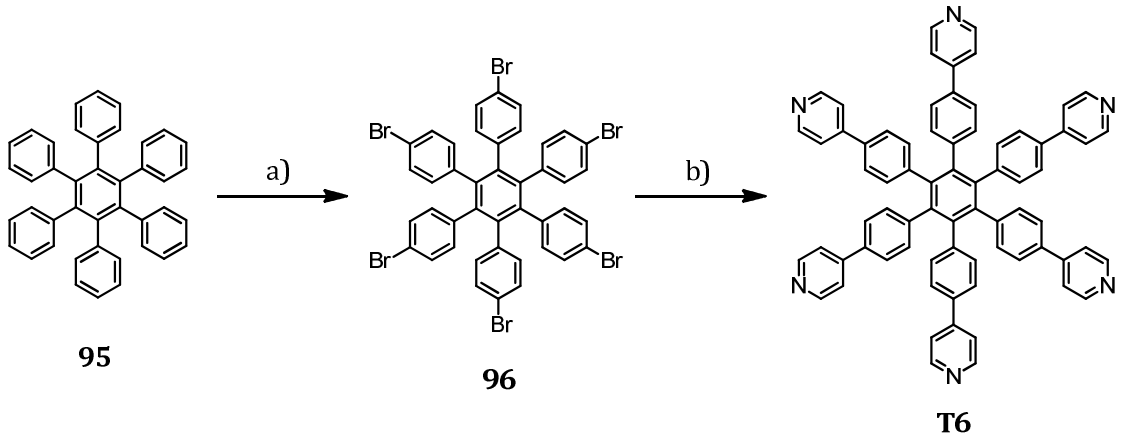

Scheme 3.15 Synthesis of hexadentate template **T6**: a) Br_2, rt, 1 h, 99%; b) 4-pyridine boronic acid, $Pd(PPh_3)_2Cl_2$, $NaHCO_3$, THF, DME, water, 70 °C, 5 d, 35%.

3.6.2 Synthesis of figure-of-eight complex ***c*-P12·(T6)$_2$**

The binding of deprotected linear tetramer ***l*-dP4** with hexadentate template **T6** was studied by UV-vis titration. In this case, THS-protected tetramer ***l*-P4** was not used as it was thought that the bulky trihexylsilyl groups would prevent formation of the Vernier complex **(*l*-P4)$_3$·(T6)$_2$** due to unfavourable steric interactions. The resulting spectra did not show isosbestic behaviour, due to aggregation issues of the sparingly soluble oligomer ***l*-dP4** in the absence of template (Figure 3.35).

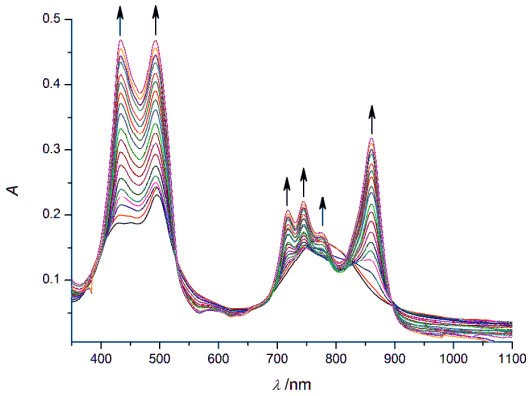

Figure 3.35 a) UV-Vis titration (CH_2Cl_2, 298 K) of deprotected porphyrin tetramer ***l*-dP4** with hexadentate template **T6** to form Vernier complex **(*l*-dP4)$_3$·(T6)$_2$**. Arrows indicate areas of increasing absorption during the titration.

Binding of ***l*-dP4** to the template caused the Q band in the absorption spectrum to split and become more defined, with an intensification of the low-energy Q_y component at 860 nm indicating planarisation of the porphyrin system.

Using the same method as in the synthesis of ***c*-P12·T12**, linear tetramer ***l*-dP4** was coordinated to template **T6**, and the terminal acetylenes oxidatively coupled with $Pd(PPh_3)_2Cl_2$, copper(I) iodide and benzoquinone, to give the ***c*-P12·(T6)$_2$** complex in 39% yield (Scheme 3.16).

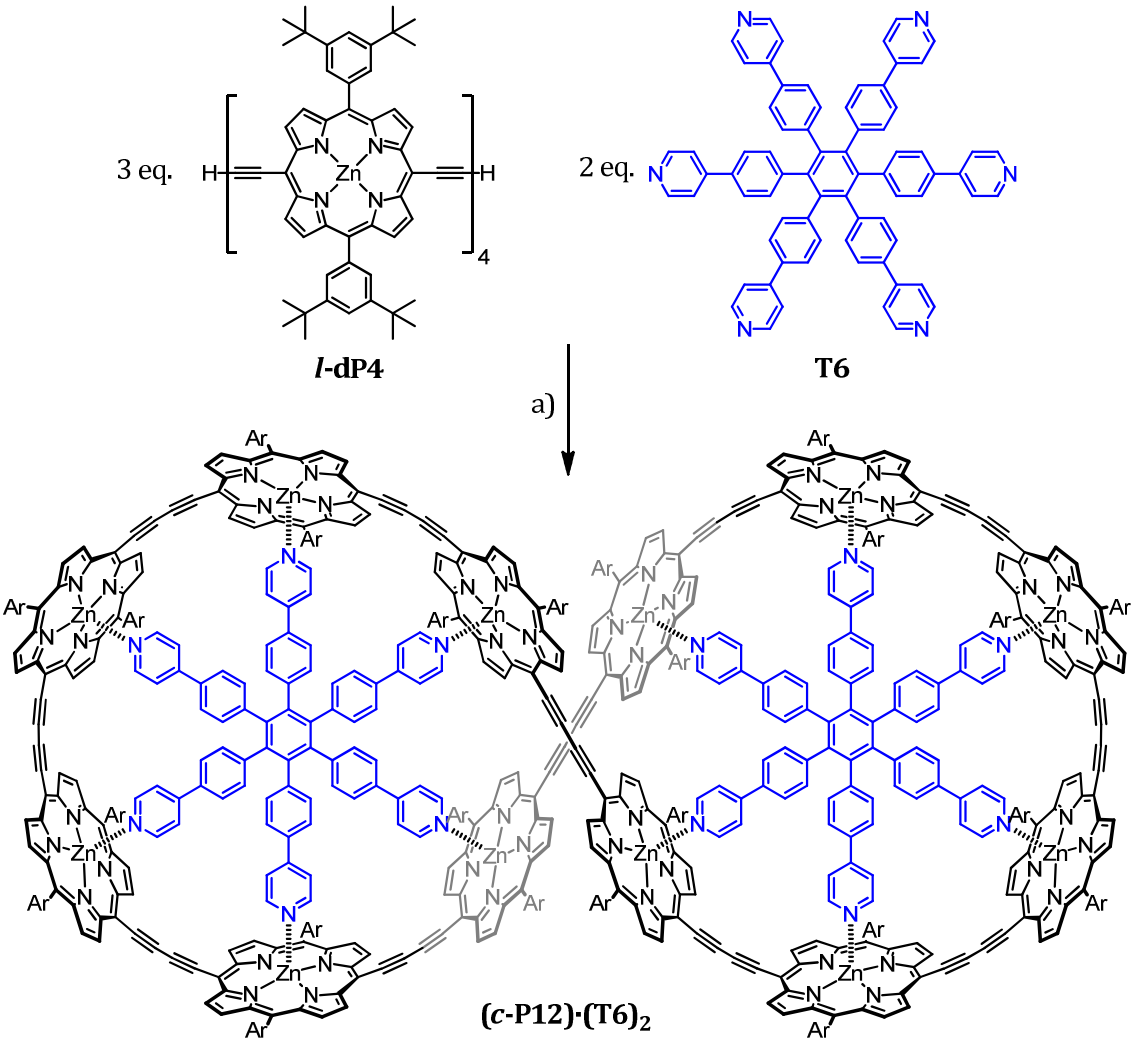

Scheme 3.16 Synthesis of figure-of-eight complex ***c*-P12·(T6)$_2$** from linear tetramer ***l*-dP4** and hexadentate template **T6**: a) $Pd(PPh_3)_2Cl_2$, CuI, 1,4-benzoquinone, $^iPr_2NH$, $CHCl_3$, rt → 50 °C, 39%.

The reaction mixture was passed through an alumina column to remove the catalysts and any acyclic polymeric material, and the resulting crude compound was analysed by GPC. A single peak showed selective formation of a single cyclic product (Figure 3.36).

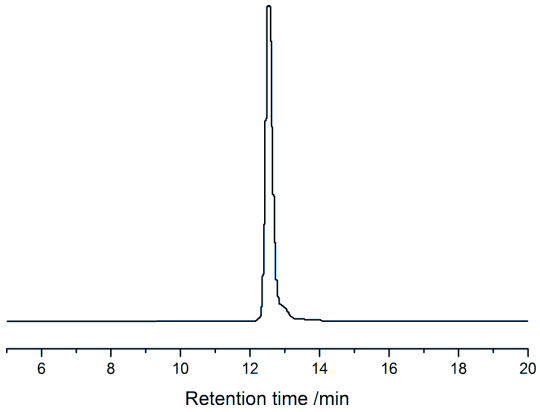

Figure 3.36 Analytical GPC analysis (toluene, 1 mL min^{-1}, 495 nm) of the crude product from the cyclisation reaction to form figure-of-eight complex ***c*-P12·(T6)$_2$**.

The UV-vis absorption spectra of ***c*-P12·(T6)$_2$** showed a 21 nm red shift of the Q band relative to that of the acyclic precursor **(*l*-dP4)$_3$·(T6)$_2$**, and an intensification of the Q band relative to that of the Soret (Figure 3.37). This suggested an increase in the π-conjugation length on cyclisation.

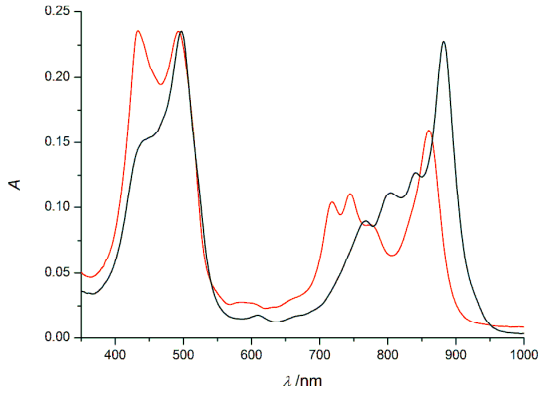

Figure 3.37 Normalised UV-vis absorption spectra ($CHCl_3$, 298 K) of linear tetramer-template complex **(*l*-dP4)$_3$·(T6)$_2$** (*red*) and figure-of-eight complex ***c*-P12·(T6)$_2$** (*black*).

3.7 Characterisation of figure-of-eight complex ***c*-P12·(T6)$_2$**

3.7.1 ^{1}H NMR characterisation of ***c*-P12·(T6)$_2$**

^{1}H NMR characterisation of the complex ***c*-P12·(T6)$_2$** was carried out by Johannes Sprafke and can be seen in Figure 3.38.[d]

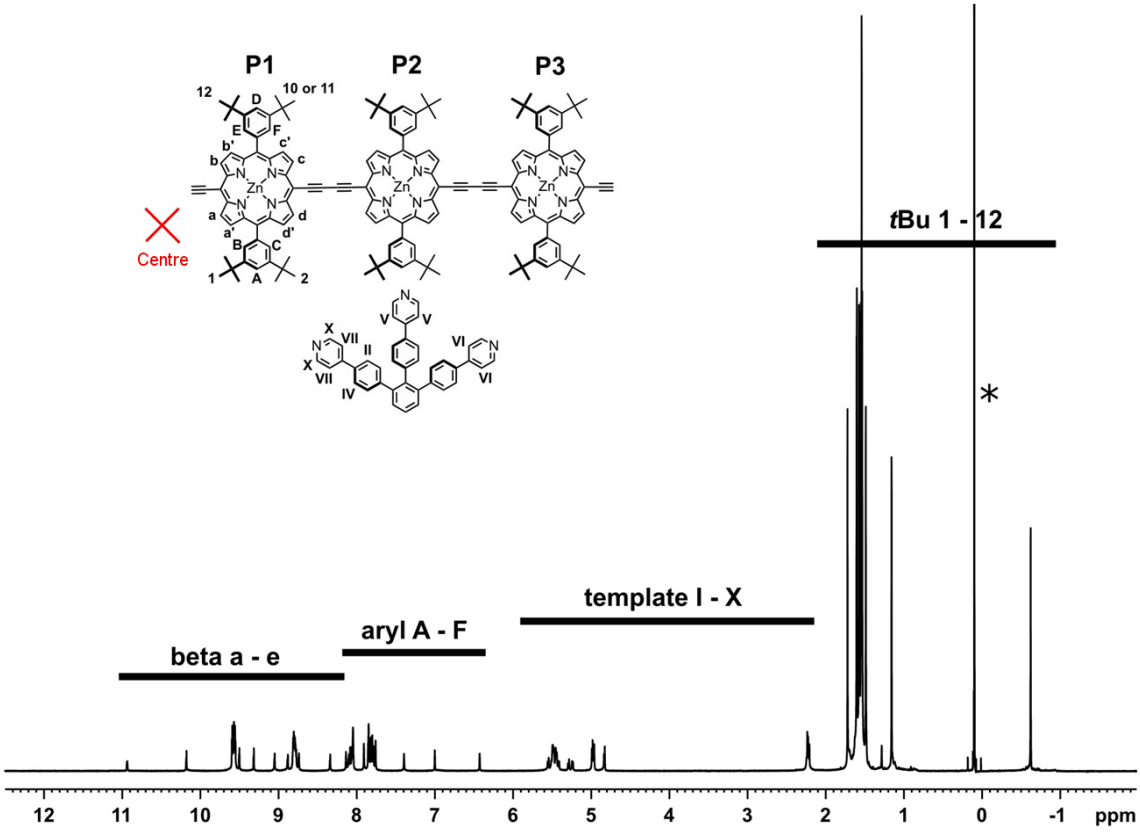

Figure 3.38 Diffusion edited ^{1}H NMR (700 MHz, $CDCl_3$, 298 K) of figure-of-eight complex ***c*-P12·(T6)$_2$**. * indicates a silicon grease impurity.

The complex has three perpendicular C_2 axes running through the centre, giving ***c*-P12·(T6)$_2$** D_2 symmetry. The complex therefore could be regarded as a three porphyrin unit P1–P3, with P1 being closest to the central crossover point (Figure 3.39). As seen in the ^{1}H NMR spectra of

[d] The full details of the peak assignment can be found elsewhere.[244][256]

***c*-P6·T6** and ***c*-P8^{C8}·T8**, rotation of the *meso*-aryl groups is restricted when complexed, so the top and bottom faces of the oligomer are inequivalent. The top side of the molecule, with bonds facing away from the template, are drawn in bold.

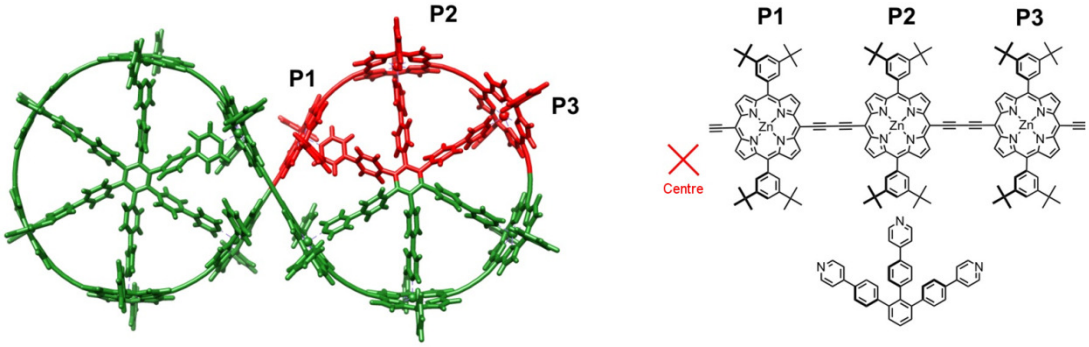

Figure 3.39 Molecular model of complex ***c*-P12·(T6)$_2$** showing D_2 symmetry.

With these symmetry requirements, twelve signals were expected for *tert*-butyl protons, which is what was observed (Figure 3.40).

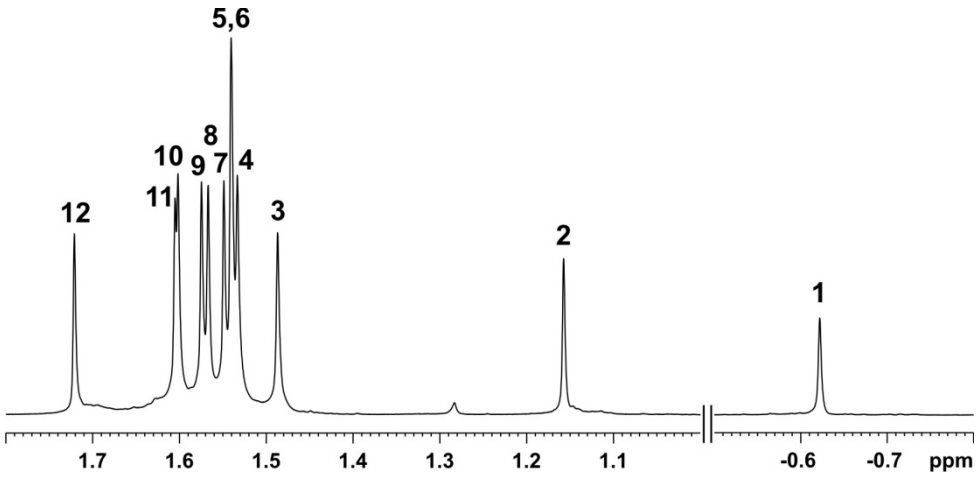

Figure 3.40 Alkyl region of ^{1}H NMR (700 MHz, $CDCl_3$, 298 K), showing the 12 *tert*-butyl resonances of ***c*-P12·(T6)$_2$**.

The template protons I–X are shielded by the ring current of the porphyrins and were found at high field. The *α*-pyridyl protons are closest to the porphyrin and thus, as in ***c*-P6·T6**, resonated at 2.2 ppm, showing that the templates reside within the cavity of the ring.

Porphyrin P1 is closest to the centre of the complex, and so these protons were expected to show unusual chemical shifts as a result. This could be seen in particular for *β*-pyrrole proton a, which was highly deshielded at 10.92 ppm; and *tert*-butyl protons 12, which were highly shielded at –0.64 ppm. NOESY data gave good structural evidence for formation of a figure-of-eight conformation using correlations between different porphyrin units in the centre of the molecule. Strong NOEs were observed between ^{t}Bu protons 1 and 2 with *β*-pyrrole protons b and b', found on the opposite side of the porphyrin macrocycle. The distance between these protons across one macrocycle is 8–9 Å, which would result in no detectable NOE. Therefore, the interaction must occur between two symmetrically equivalent proximal porphyrins, as shown in Figure 3.41. Molecular modelling of ***c*-P12·(T6)$_2$** showed a through-space distance between *tert*-butyl protons 1 and *β*-pyrrole protons of 2.5 Å, hence a strong NOE was observed.

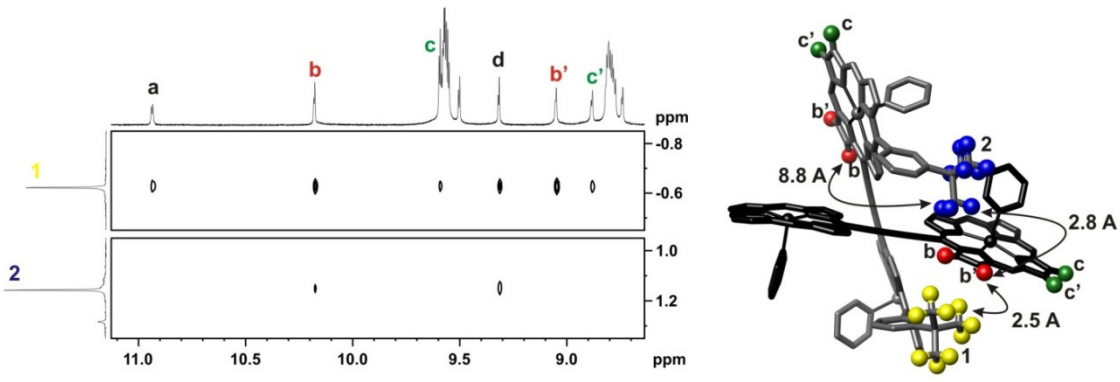

Figure 3.41 Interporphyrin NOEs between *β*-pyrrole and ^{t}Bu protons and model of the central cross-over point of ***c*-P12·(T6)$_2$**.

3.7.2 MALDI-MS of ***c*-P12·(T6)$_2$**

The hexadentate templates **T6** in the figure-of-eight complex ***c*-P12·(T6)$_2$** are labile under the ionisation conditions of MALDI. MALDI-MS analysis using a DCTB matrix showed peaks corresponding to the intact complex ***c*-P12·(T6)$_2$**, the free cyclic dodecamer ***c*-P12**, and the dodecamer ring complexed to one template, ***c*-P12·T6** (Figure 3.42).

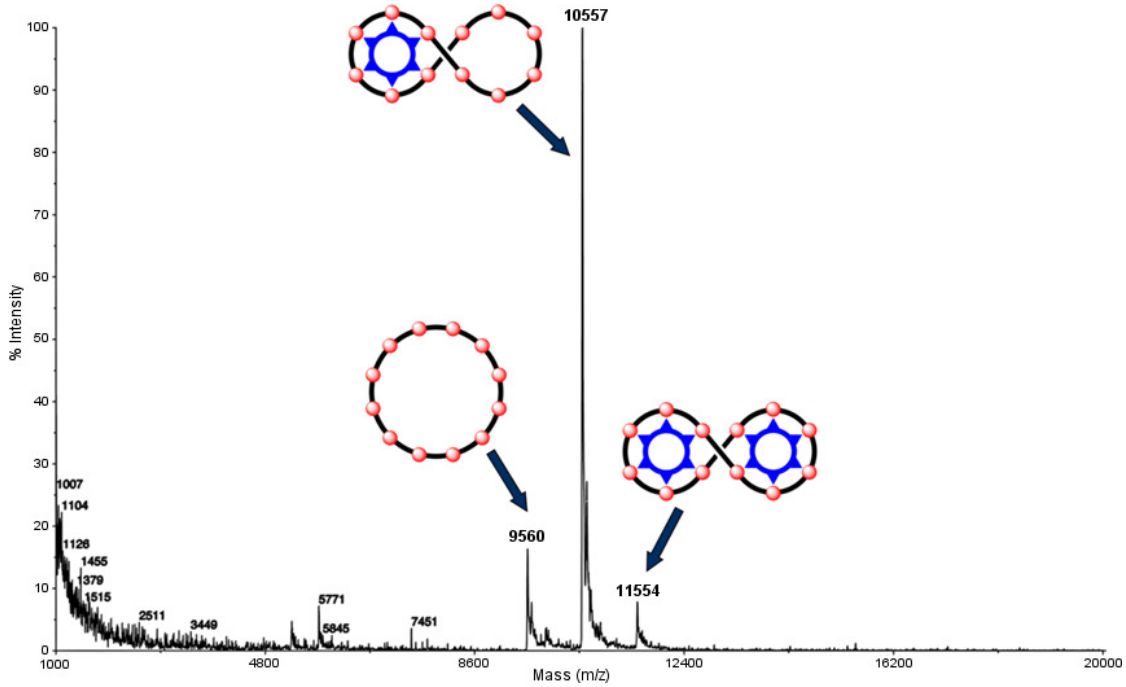

Figure 3.42 MALDI-ToF MS analysis of figure-of-eight complex ***c*-P12·(T6)$_2$** (DCTB matrix, reflectron mode). The three peaks correspond to ***c*-P12·(T6)$_2$** (m/z 11554, expected 11551), ***c*-P12·T6** (m/z 10557, expected 10554) and ***c*-P12** (m/z 9560, expected 9557). Courtesy of EPSRC National Mass Spectrometry Service Centre, Swansea.

In order to obtain a MALDI-MS of satisfactory resolution for all the cyclic species, it was crucial to prepare both the sample and matrix in toluene before spotting onto the plate, otherwise broad, inconclusive spectra resulted.

3.7.3 SAXS characterisation of figure-of-eight complex ***c*-P12·(T6)$_2$**

SAXS data for figure-of-eight complex ***c*-P12·(T6)$_2$** were acquired at Diamond Light Source and processed by Johannes Sprafke, in the same manner as for ***c*-P12·T12**. The simulated data, calculated from an energy minimised structure of ***c*-P12·(T6)$_2$** (Figure 3.43c), matched well to the experimental data (Figure 3.43a). The PDF showed distinct peaks at 51 Å and 23 Å corresponding well to the calculated length (53 Å) and width (24 Å) of the molecule (Figure 3.43b).

The linearity of the scattering data in the Guinier region confirmed the monodispersity of the sample (Figure 3.43d). The experimental radius of gyration of 20.1 Å was slightly larger than the calculated value, but the molecular weight (11.0 kDa) matched the expected value of 11.6 kDa well (Figure 3.43a).

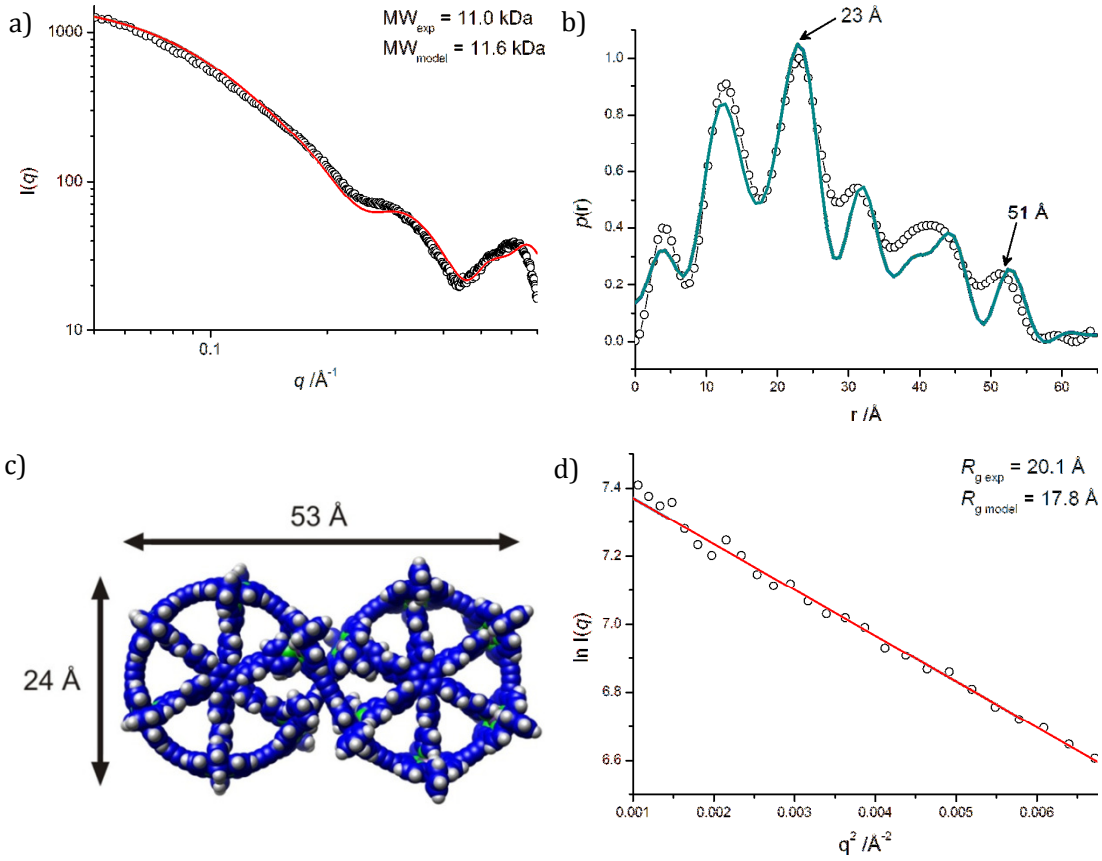

Figure 3.43 SAXS analysis (toluene, 298 K) of figure-of-eight complex ***c*-P12·(T6)$_2$**: a) Experimental scattering curve (○) for ***c*-P12·(T6)$_2$** plotted on a double log scale with fitted data from the molecular model (–). The experimental molecular weight was determined from the extrapolated scattering intensity at zero angle (q = 0) with ***c*-P6·T6** as standard;[244] b) Experimental (⊖) and model based (–) pair distribution function, obtained using the software "Gnom". The measured dimensions correspond well to the calculated length and width of the molecule within the 3 Å resolution of the experiment; c) Molecular model used for fitting of and comparison with experimental data. The geometry was optimised using the MM+ forcefield in HyperChem™; d) Guinier plot of the experimental scattering data of ***c*-P12·(T6)$_2$** (○) at very small angles. The fit (–) to the Guinier equation was obtained using the software "Primus".

3.8 Isolating cyclic dodecamer *c*-P12

The ultimate proof of the utility of the Vernier concept was to illustrate that the knockout of ***c*-P12·(T6)$_2$** with a competitive monodentate ligand would give the same product as from the

knockout of ***c*-P12·T12**. The complicated ^{1}H NMR spectra of both ***c*-P12·(T6)$_2$** and ***c*-P12·T12** made the purity and identity of the two complexes difficult to authenticate, however the D_{12h} symmetry of the cyclic dodecamer ***c*-P12** should give only 5 signals in the ^{1}H NMR.

For the knockout, ***c*-P12·T12** or ***c*-P12·(T6)$_2$** were passed down a size-exclusion column, eluting with 10% pyridine in toluene to give the free cyclic dodecamer ring ***c*-P12** quantitatively (Scheme 3.17).

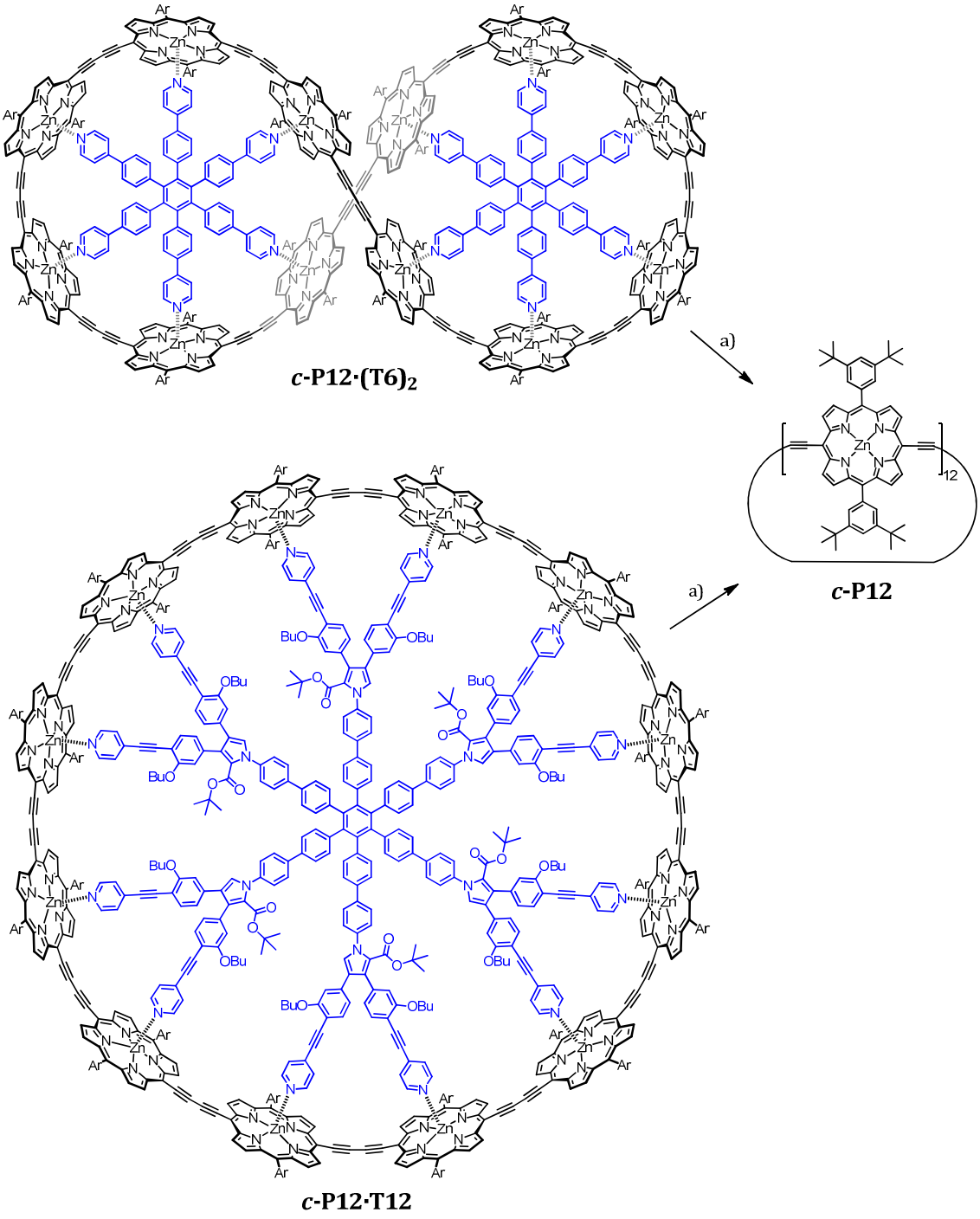

Scheme 3.17 Knockout of figure-of-eight complex ***c*-P12·(T6)$_2$** and cyclic dodecamer complex ***c*-P12·T12** to give cyclic dodecamer ***c*-P12**: a) 10% pyridine in toluene, 99%.

The dodecamer ring ***c*-P12** obtained by knockout of cyclic dodecamer complex ***c*-P12·T12** and complex ***c*-P12·(T6)$_2$** were analysed by GPC. Each source gave a single peak at identical retention times. Co-injection of the samples gave a single peak (Figure 3.44).

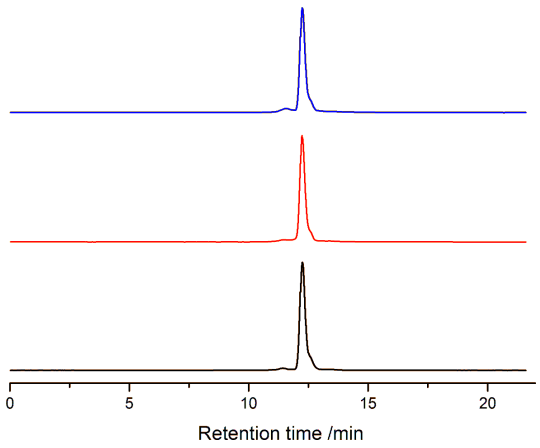

Figure 3.44 Analytical GPC traces (15% pyridine in toluene, 1 mL min^{-1}, 476 nm) of 12-porphyrin nanoring ***c*-P12** obtained by knockout of figure-of-eight ***c*-P12·(T6)$_2$** (*black*), and ***c*-P12·T12** (*red*). Coinjection of both compounds (*blue*) gives a perfect overlap of GPC peaks.

The UV-vis spectra of ***c*-P12** from both sources also showed a good match (Figure 3.45).

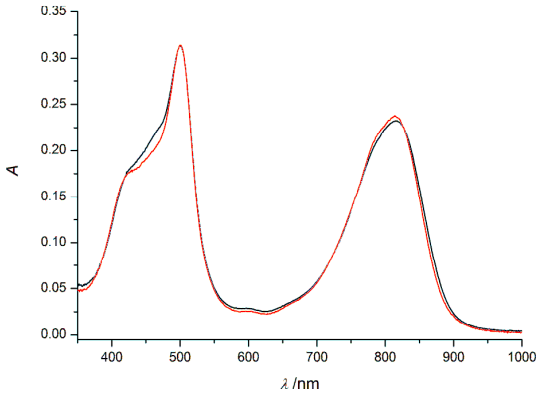

Figure 3.45 Normalised UV-vis absorption spectra ($CHCl_3$, 298 K) of dodecamer ring ***c*-P12** obtained by knockout of cyclic dodecamer complex ***c*-P12·T12** (*black*), and that obtained by Vernier templating with hexadentate template **T6** (*red*).

3.8.1 ^{1}H NMR characterisation of cyclic dodecamer ***c*-P12**

As predicted the ^{1}H NMR of cyclic dodecamer ***c*-P12** consisted of only five signals, and resembled that of ***c*-P6** and ***c*-P8** (Figure 3.46).

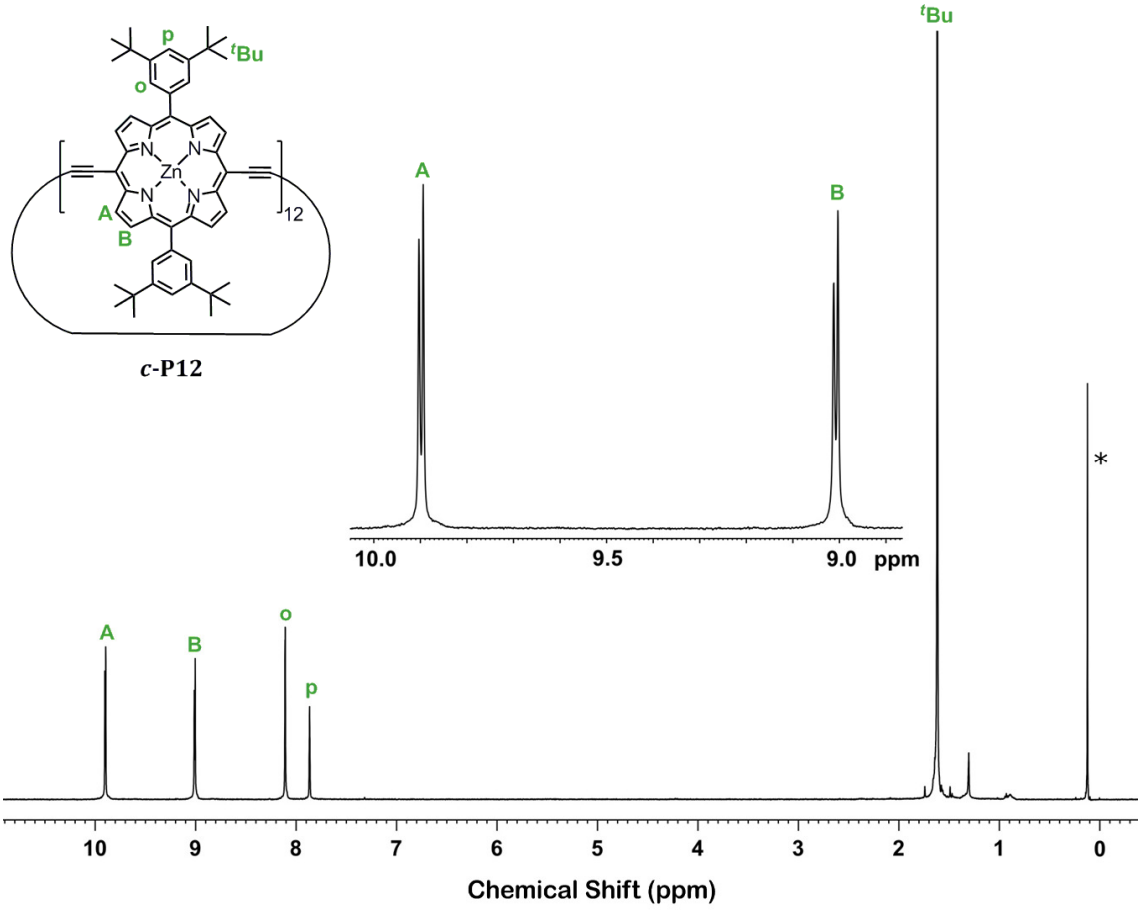

Figure 3.46 Diffusion edited ^{1}H NMR (700 MHz, $CDCl_3$/1% d_5-pyridine, 298 K) of cyclic dodecamer ***c*-P12** from the knockout of figure-of-eight complex ***c*-P12·(T6)$_2$**. Inset: zoom region showing the β-pyrrole region of the spectrum. * indicates a grease impurity. Spectrum acquired by Johannes Sprafke.

The extreme simplicity of the spectrum indicated the formation of a highly symmetrical, monodisperse species.

Doping cyclic dodecamer ***c*-P12** obtained by **T12** mediated cyclisation with that from the figure-of-eight knockout gave perfect overlap of the doublets arising from the porphyrin *β*-pyrrole protons (Figure 3.47).

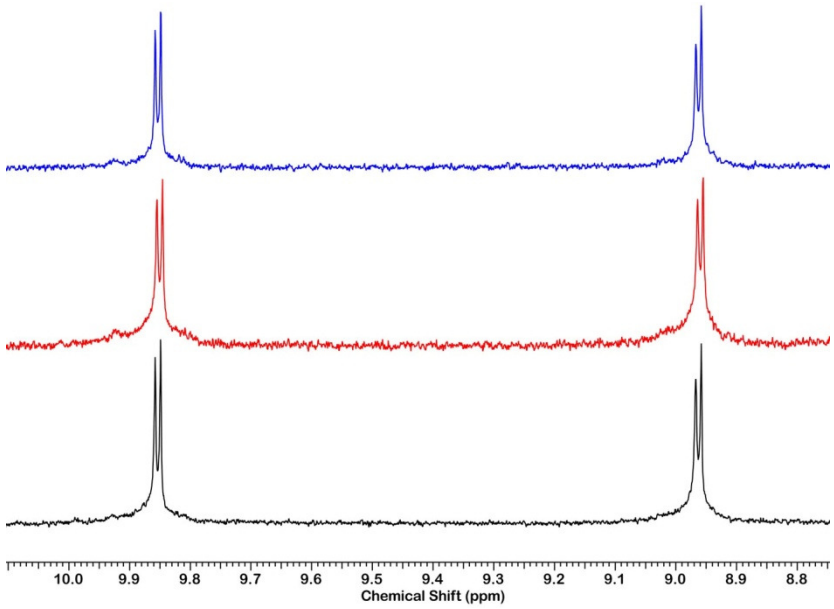

Figure 3.47 ^{1}H NMR spectra (500 MHz, $CDCl_3$/1% d_5-pyridine, 298 K) showing the porphyrin *β*-pyrrole region of cyclic dodecamer ***c*-P12** obtained by knockout of figure-of-eight complex ***c*-P12·(T6)$_2$** (*black*) and of dodecamer complex ***c*-P12·T12** (*red*). Mixing both samples (*blue*) shows a perfect overlap of porphyrin peaks.

The ^{1}H NMR of ***c*-P12** obtained from the knockout of ***c*-P12·T12** complex was not as clean as that obtained from the Vernier complex knockout, due to difficulty in purification from the template **T12**. This further demonstrates the utility of the Vernier mechanism for synthesising the dodecamer ring.

3.8.2 SAXS characterisation of cyclic dodecamer ***c*-P12**

SAXS data for ***c*-P12** were acquired at Diamond Light Source and processed by Johannes Sprafke, in the same manner as for ***c*-P12·T12** and ***c*-P12·(T6)$_2$**.

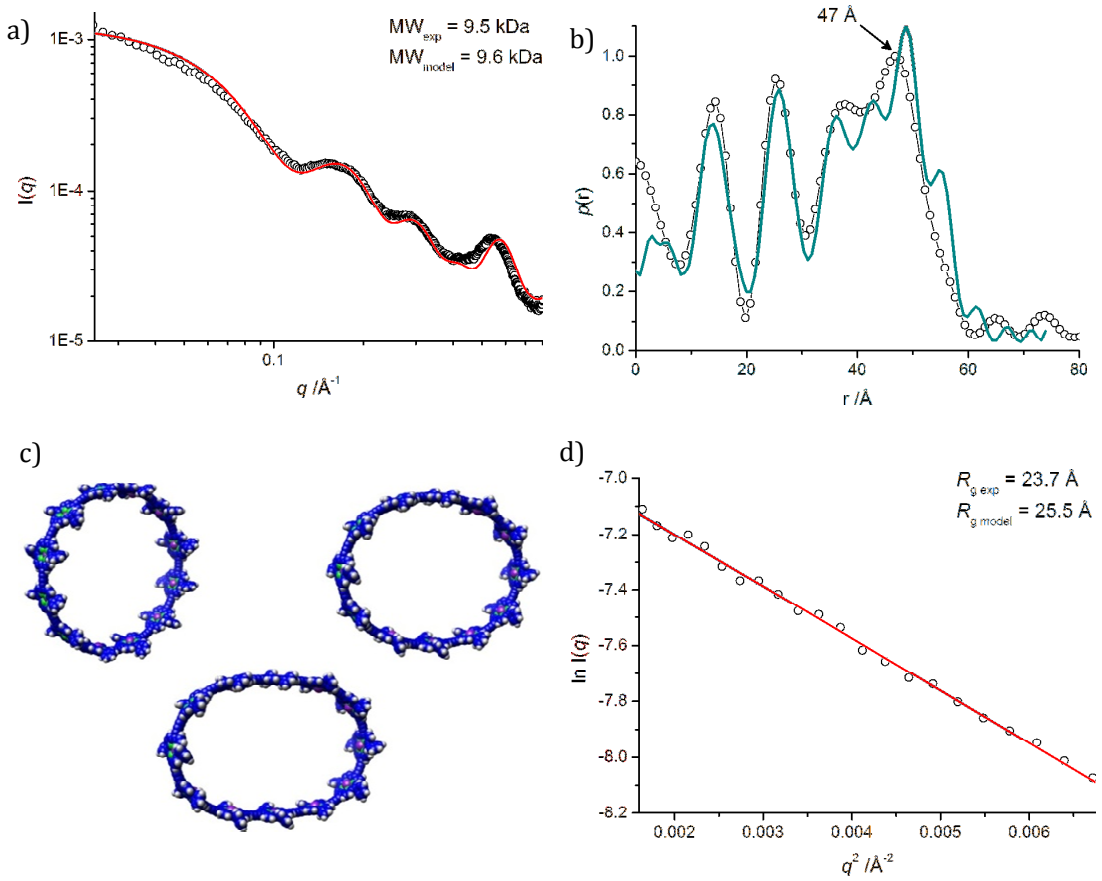

Figure 3.48 SAXS analysis (1% pyridine in toluene, 298 K) of cyclic dodecamer ***c*-P12**: a) Experimental scattering curve (○) for ***c*-P12** plotted on a double log scale with fitted data from the molecular model (–). The experimental molecular weight was determined from the extrapolated scattering intensity at zero angle (q = 0) with ***c*-P6·T6** as standard;[244] b) Experimental (⊖) and model based (–) pair distribution function, obtained using the software "Gnom". The measured dimensions correspond well to the calculated diameter of the molecule within the 3 Å resolution of the experiment; c) Three of the six conformations of ***c*-P12** modelled using the MM+ forcefield in Hyperchem™ to simulate molecular dynamics in solution; d) Guinier plot of the experimental scattering data of ***c*-P12** (○) at very small angles. The fit (–) to the Guinier equation was obtained using the software "Primus".

The simulated data, calculated from a molecular model of ***c*-P12** minimised in Hyperchem™, did not adequately fit to the experimental data. While the two template complexes are relatively rigid in solution, ***c*-P12** is expected to exhibit a degree of conformational flexibility.

Molecular dynamics simulations can significantly improve simulation of scattering data for conformationally flexible molecules.[257] Six different conformations of ***c*-P12** were modelled using MM+ in Hyperchem™, fixing the distance between opposite porphyrins to values between 37–47 Å (Figure 3.48c). Scattering curves were simulated for each of these structures, and the average value used to fit the experimental data. This simulated data gave an excellent fit to the experimental data (Figure 3.48a).

The PDF matches the conformationally averaged simulated data well, and features a peak at 47 Å, which is in exact agreement with the calculated ring diameter (Figure 3.48b). At longer distances, the experimental data become broader, reflecting structural dynamics in solution.

The data at small angles formed a straight line in the Guinier plot, confirming monodispersity of the sample (Figure 3.48d). The molecular weight obtained from $I(0)$ using ***c*-P6·T6** as standard[244] (9.5 kDa) matches almost perfectly the expected value of 9.6 kDa.

3.8.3 STM characterisation of ***c*-P12**

Recently, octyloxy oligomers ***l*-P4^{C8}**, ***l*-P6^{C8}** and ***l*-P*N*^{C8}** (where N = 30–50) were imaged by scanning tunnel microscopy (STM), using ultrahigh vacuum electrospray deposition (UHV-ESD) to transfer the oligomers or polymer onto a Au(111) surface.[258] The octyloxy *meso*-aryl groups promote solubility in organic solvents, thereby facilitating deposition onto the substrate. Johannes Sprafke, a DPhil in the group, synthesised octyloxy cyclic porphyrin dodecamer ***c*-P12^{C8}** by Vernier templation. The ring was deposited onto a Au(111) surface by UHV-ESD by Peter Beton's group in Nottingham. The high resolution images showed discrete cyclic structures of approximately 5 nm diameter. The porphyrin plane was seen to lie parallel to the substrate surface,[258] and the high resolution of the image allowed each porphyrin subunit to be resolved, with a total of 12 porphyrins in each ring (Figure 3.49).

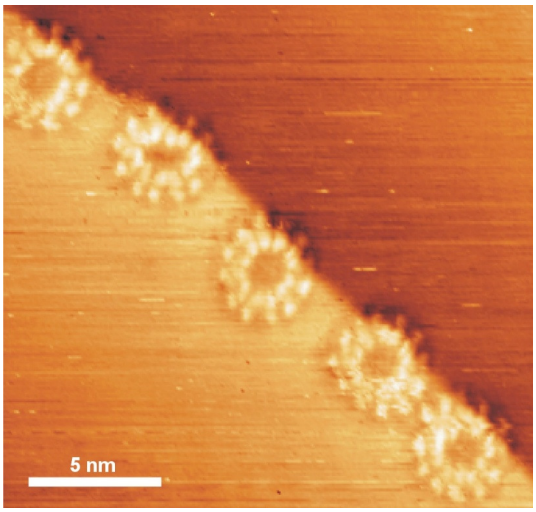

Figure 3.49 High resolution STM image of five ***c*-P12^{C8}** molecules on a Au(111) surface, aligned along a step-edge. Images were acquired by Alex Saywell and Matthew Blunt under ultrahigh vacuum with a base pressure of 5×10^{-11} Torr, a sample voltage of –1.80 V and a tunnelling current of 0.03 nA.

3.9 Conclusions

Cyclic dodecamer ***c*-P12** can be accessed *via* two routes. A classical templating route, where the number of binding sites on the template equals the number of porphyrins in the cyclic oligomer, yields ***c*-P12** in 35% from the linear porphyrin tetramer ***l*-dP4**. The template itself however is synthetically challenging and difficult to purify, due to solubility and stability issues. This route to porphyrin rings becomes limited in the quest for larger targets, as the templates themselves are difficult to access.

A Vernier templating route, which uses a mismatch in the number of binding sites between a porphyrin tetramer ***l*-dP4** and hexadentate template **T6**, gives the cyclic dodecamer ***c*-P12** in 39% yield. Although this yield is comparable to that of the classical templating route, **T6** is accessible in two steps from commercially available starting materials, and is easy to purify. The group's access to templates **T6**, **T8** and **T12** and a range of porphyrin oligomers means a

wide variety of large rings can potentially be accessed using this new methodology. One of these rings, 24-ring ***c*-P24**, is discussed in Chapter 4.

Chapter Four
Towards Synthesis of a [24]Nanoring

*Progress towards the synthesis of a cyclic tetracosamer **c-P24** is described, via complex **c-P24·(T8)$_3$**. First, compatibility of the new cyclisation conditions with template **T8** are explored by synthesis of the novel 3,5-di(tert-butyl)phenyl meso-aryl substituted cyclic porphyrin octamer complex **c-P8·T8** from a range of oligomers. Higher yields than that previously reported are obtained for the complex from linear dimer **l-dP2**, greatly improving the accessibility of **c-P8·T8**. A more efficient synthetic route to linear hexamer **l-P6** is discussed. The product obtained from the cyclisation of linear hexamer **l-dP6** in the presence of octadentate template **T8** is investigated by UV-vis, NMR and MALDI-MS. Results indicate the formation of **c-P24·(T8)$_3$** in an inseparable mixture of other species. Template exchange from octadentate template **T8** to hexadentate template **T6** as a route to aiding separation by GPC is described.*

4.1 Results and Discussion

4.1.1 Routes to cyclic tetracosamer ***c*-P24**

There are two potential routes to cyclic tetracosamer ***c*-P24** *via* Vernier templating. The first is through the cyclisation of linear porphyrin octamer ***l*-dP8** in the presence of hexadentate template **T6** to give complex ***c*-P24·(T6)$_4$** (Figure 4.1a). In exploring the synthesis of cyclic hexamer complex ***c*-P6·T6** directly from porphyrin monomer, a small amount of ***c*-P24·(T6)$_4$** was isolated as a side product and characterised by Dmitry Kondratuk, a DPhil in the group.[259] One of the disadvantages of approaching the cyclic tetracosamer from ***c*-P24·(T6)$_4$** is that deprotected *tert*-butyl octamer ***l*-dP8** is completely insoluble,[69] therefore, octyloxy derivatised porphyrins would be required. This would make purification of the complex from soluble linear polymeric byproducts potentially more challenging.

a)

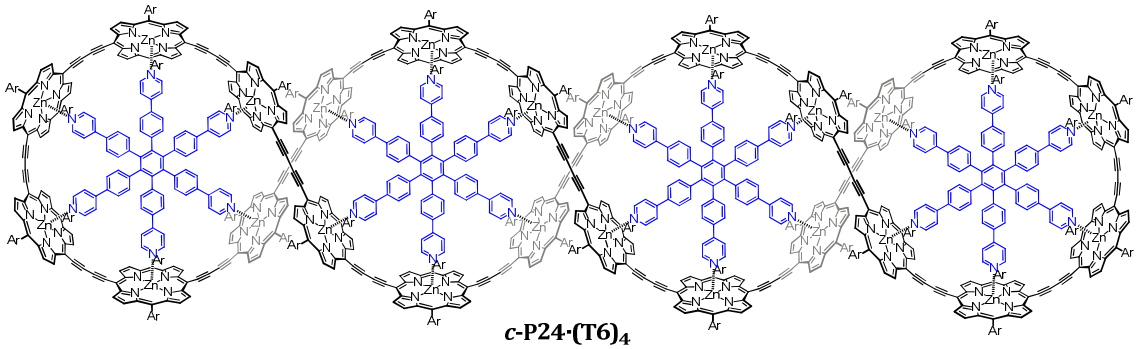

***c*-P24·(T6)$_4$**

b)

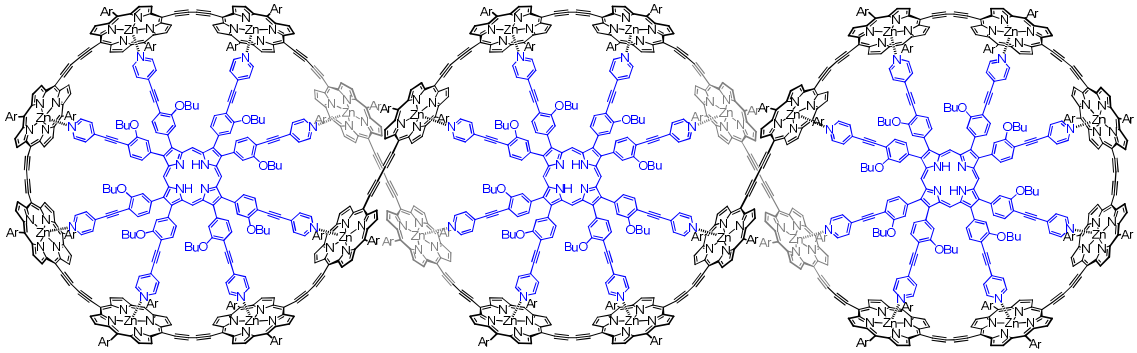

***c*-P24·(T8)$_3$**

Figure 4.1 Two potential routes to cyclic tetracosamer ***c*-P24**: a) linear porphyrin octamer ***l*-dP8** and hexadentate template **T6** to yield complex ***c*-P24·(T6)$_4$**; b) linear porphyrin hexamer ***l*-dP6** and octadentate template **T8** to yield complex ***c*-P24·(T8)$_3$**.

Another route to ***c*-P24** could be through cyclisation of linear porphyrin hexamer ***l*-dP6** in the presence of octadentate template **T8** to give complex ***c*-P24·(T8)$_3$** (Figure 4.1b). Unlike porphyrin octamer ***l*-dP8**, deprotected *tert*-butyl hexamer ***l*-dP6** has sufficient solubility for synthesis and characterisation. It was thought that the thermodynamic stability of the Vernier complexes could be potentially limited by the number of cross-over points in the molecule, due to unfavourable steric interactions between porphyrin *meso*-aryl groups. Octadentate complex ***c*-P24·(T8)$_3$** has two cross-over points relative to three for ***c*-P24·(T6)$_4$**, suggesting a higher thermodynamic stability for the former. In addition, **T8** templated complexes are less strained than their **T6** analogues as the larger template requires less bending of the porphyrin aromatic π-system. The disadvantage of this route is octadentate template **T8** mediated cyclisations are relatively little understood, in contrast to **T6** cyclisations where both ***c*-P6** and ***c*-P12** can be accessed from a range of oligomer lengths.[128][135][256][259]

It was decided due to the insolubility of ***l*-dP8**, and the predicted higher stability of octadentate templated complex ***c*-P24·(T8)$_3$**, that the route *via* ***c*-P24·(T8)$_3$** should be pursued. First, the

synthesis of cyclic octamer complex ***c*-P8·T8** was reinvestigated to better understand octadentate template **T8** mediated reactions. This reaction would also be interesting as the *tert*-butyl derivative of this cyclic oligomer was yet unknown.

4.1.2 Synthesis of octadentate template **T8**

The synthesis of **T8** was carried out as described previously.[75] Dipyridyl pyrrole **15** was reduced with lithium aluminium hydride at 0 °C. The resulting alcohol **97** was isolated and immediately condensed by addition of catalytic *p*-toluene sulfonic acid. Oxidation of the porphyrinogen with DDQ yielded the octadentate template **T8** in 11% yield (Scheme 4.1).

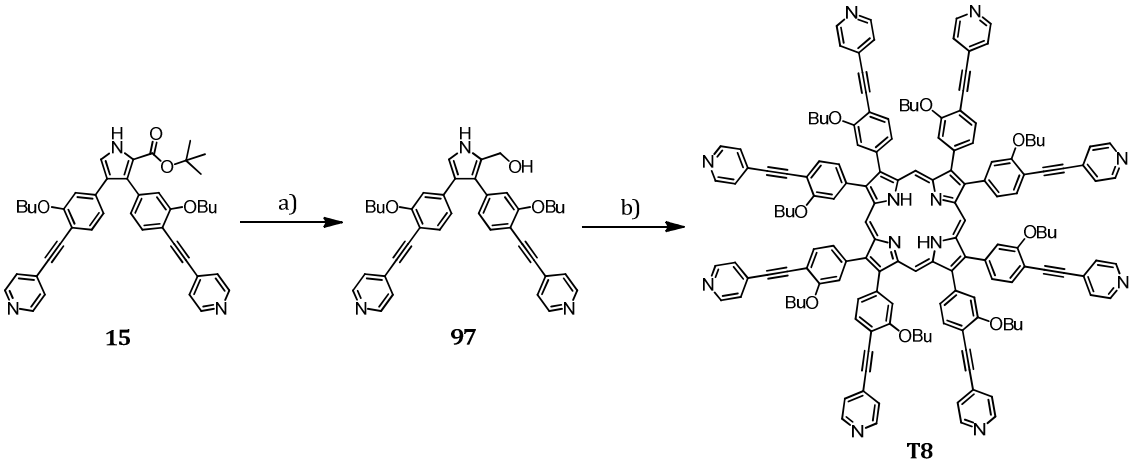

Scheme 4.1 Synthesis of octadentate template **T8**: a) $LiAlH_4$, THF, 0 °C, 30 min; b) 1. TsOH, CH_2Cl_2, dimethoxymethane, rt, 12 h. 2. DDQ, 30 min. 3. NEt_3, 11% over two steps.

4.1.3 Synthesis of cyclic octamer complex ***c*-P8·T8** using short oligomers

Previously, octyloxy cyclic octamer complex ***c*-P8^{C8}·T8** was synthesised[75] by oxidative coupling of linear octamer ***l*-dP8^{C8}** coordinated to template **T8** using the conditions reported by Burton[129] (see Chapter 3).

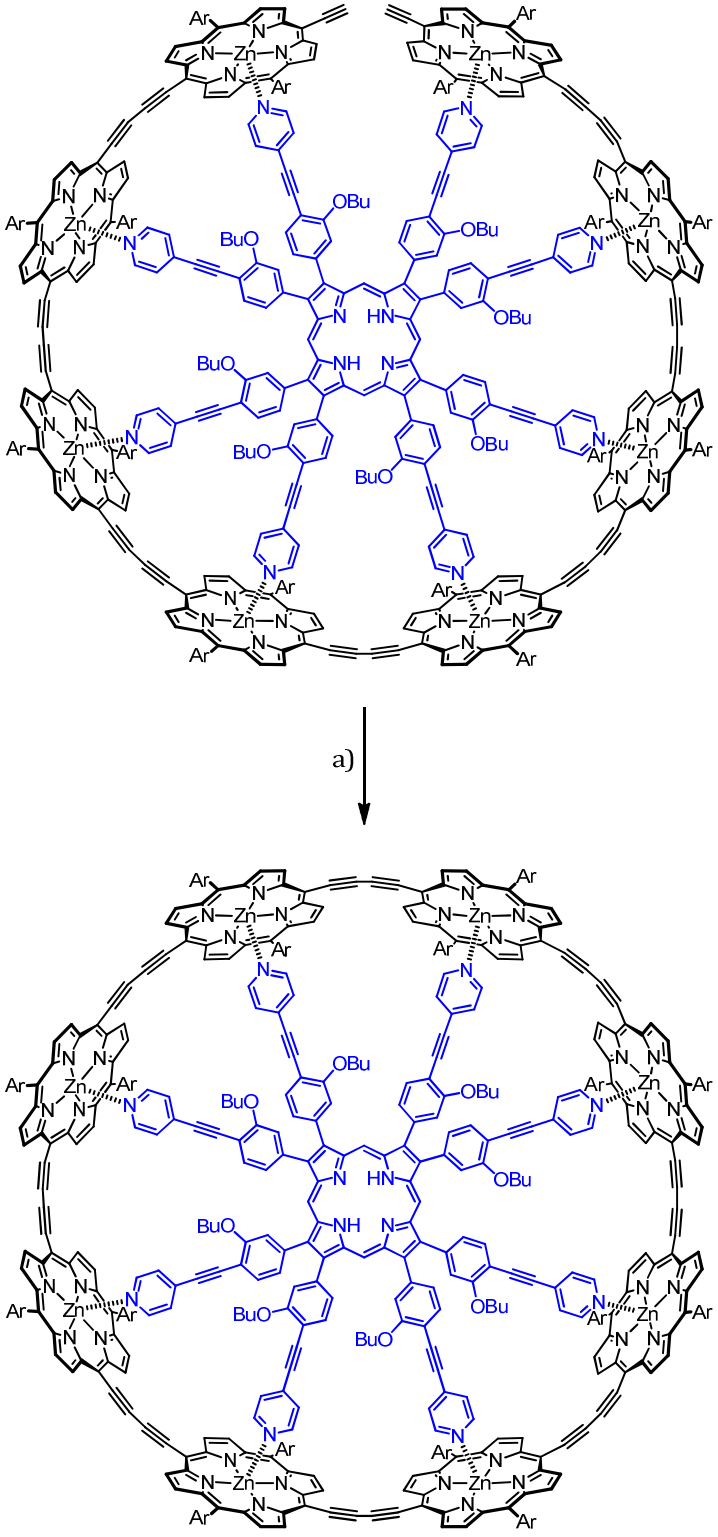

***l*-P8^{C8}·T8**

***c*-P8^{C8}·T8**

Scheme 4.2 Wilson's synthesis of cyclic octamer complex ***c*-P8^{C8}·T8** via linear octamer-template complex ***l*-dP8^{C8}·T8**: a) $Pd(PPh_3)_2Cl_2$, CuI, I_2, $^iPr_2NH$, air, 60 °C, 14%. Ar = 3,5-di(octyloxy)phenyl.

Craig Wilson, a previous DPhil student in the group, found that applying Swager's conditions[245] to the cyclic octamer system resulted in slow decomposition of the linear porphyrin octamer.[145] However, the subsequent success using these conditions in both the synthesis of the cyclic hexamer complex ***c*-P6·T6**[135][244] and cyclic dodecamer complexes ***c*-P12·T12** and ***c*-P12·(T6)$_2$** (Chapter 3) it was decided that the reaction should be reinvestigated. It was important to determine whether these conditions could be applied to **T8**-templated reactions, for use in the synthesis of ***c*-P24**.

Although the synthesis of ***c*-P8^{C8}·T8** from linear tetramer ***l*-dP4^{C8}** had been previously attempted by Wilson,[145] difficulty in purifying the final complex led to Hoffmann approaching the complex using the linear octamer ***l*-dP8^{C8}**.[75] The difficulty in accessing ***l*-dP8^{C8}** made ***c*-P8^{C8}·T8** only available in very small quantities. The ability to access cyclic octamer complex from shorter oligomers would improve the availability of this complex enormously.

Tert-butyl *meso*-aryl porphyrins were to be used for the synthesis of the 24-ring complex ***c*-P24·(T8)$_3$** due to the ease of purification from polymeric side products (Chapter 3). As only the 3,5-di(octyloxy)phenyl cyclic porphyrin octamer complex **c-P8^{C8}·T8** had previously been synthesised, it was important to first investigate the *tert*-butyl derivative of the cyclic octamer complex to ensure adequate solubility, and to aid in the ^{1}H NMR assignment of the Vernier complex.

Using the same method as in the synthesis of figure-of-eight complex ***c*-P12·(T6)$_2$**, linear oligomer ***l*-dP*N*** (*N* = 1, 2, 4) was coordinated to template **T8** and the terminal acetylenes oxidatively coupled with $Pd(PPh_3)_2Cl_2$, copper(I) iodide and benzoquinone. The results of the cyclisations with different oligomer lengths is summarised in Table 4.1.

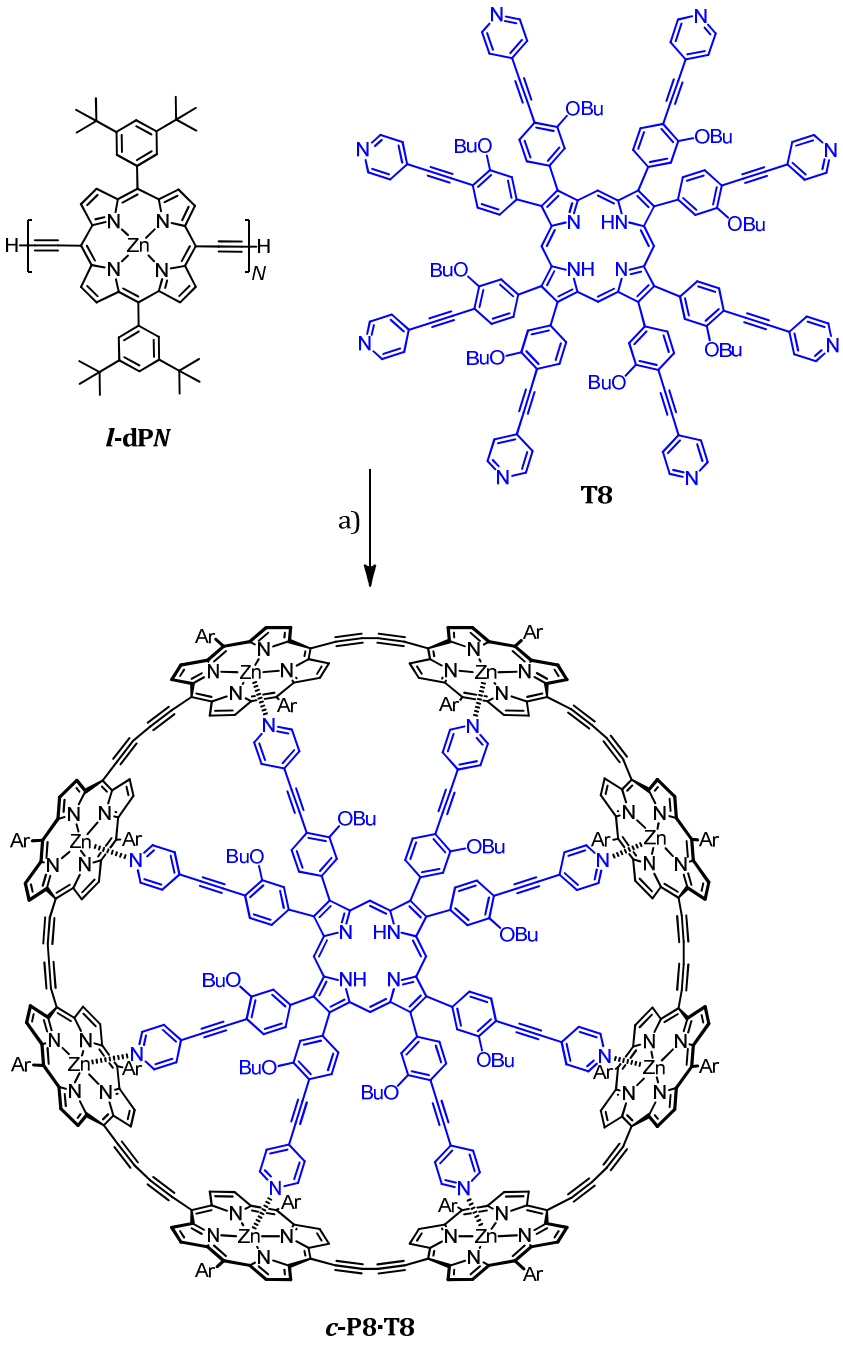

Scheme 4.3 Optimised synthesis of cyclic octamer complex ***c*-P8·T8** from oligomers ***l*-dP1** (*N* = 1), ***l*-dP2** (*N* = 2) and ***l*-dP4** (*N* = 4): a) $Pd(PPh_3)_2Cl_2$, CuI, 1,4-benzoquinone, $^iPr_2NH$, $CHCl_3$, rt → 50 °C. Ar = 3,5-di(*tert*-butyl)phenyl.

Entry	Number of porphyrins, *N*	Isolated yield ***c*-P8·T8 /%**
1	1	–
2	2	25
3	4	22

Table 4.1 Yields from the cyclisation reactions of linear oligomer ***l*-dP*N*** (*N* = 1, 2, 4) in the presence of octadentate template **T8**.

GPC analysis of the crude reaction mixture for the cyclisation of linear tetramer ***l*-dP4** in the presence of octadentate template **T8** (Entry 3, Table 4.1) showed selective formation of a single product (Figure 4.2).

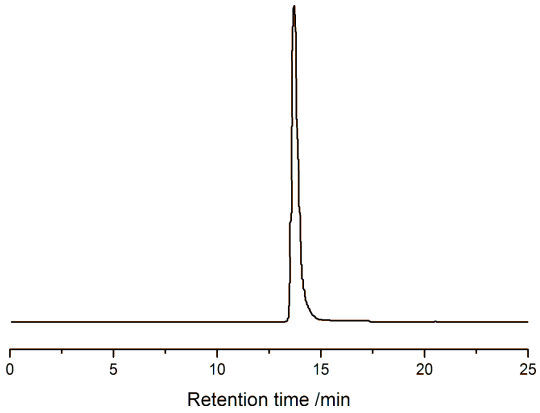

Figure 4.2 GPC analysis (toluene, 1 mL min^{-1}, λ = 517 nm) of the crude reaction mixture from the coupling of porphyrin tetramer ***l*-dP4** in the presence of octadentate template **T8**, showing selective formation of a single product.

The UV-vis absorption spectrum of the isolated product matched that of Hoffmann's original 3,5-octyloxy derivatised cyclic octamer complex ***c*-P8^{c8}·T8** well (Figure 4.3). The blue-shifting of the octyloxy complex Q band relative to that of the *tert*-butyl complex is also seen for the cyclic hexamer ***c*-P6** and cyclic hexamer complex ***c*-P6·T6**.[128]

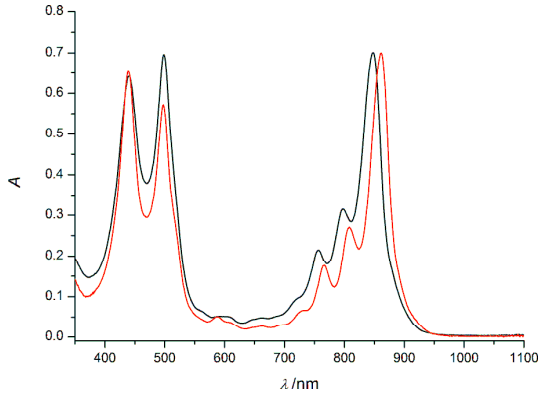

Figure 4.3 Normalised UV-vis absorption spectra ($CHCl_3$, 298 K) of di(octyloxy) derivatised ***c*-P8^{C8}·T8** as synthesised by Markus Hoffmann (*black*), and *tert*-butyl cyclic octamer complex ***c*-P8·T8** formed by cyclisation of **(*l*-dP4)$_2$·T8** (*red*).

As with the octyloxy complex **c-P8^{C8}·T8**, the peaks in the ^{1}H NMR spectrum were broad, reflecting the pseudo-symmetry imposed by template **T8** (Figure 4.4).[e]

The template protons a–h were shifted to high field, with the *α*- and *β*-pyridyl protons most shifted at *δ* 2.58 and *δ* 5.41 respectively, showing shielding of these protons by the porphyrin aromatic π-system. Rotation around the porphyrin–*meso*-aryl bond is restricted, and the bound template makes each side of the porphyrin face inequivalent. This led to splitting of the *tert*-butyl and *ortho*-phenyl proton signals, as seen in the ^{1}H NMR of the cyclic hexamer complex ***c*-P6·T6**.

[e] NOESY and COSY spectra for cyclic octamer complex ***c*-P8·T8** can be found in the Appendix.

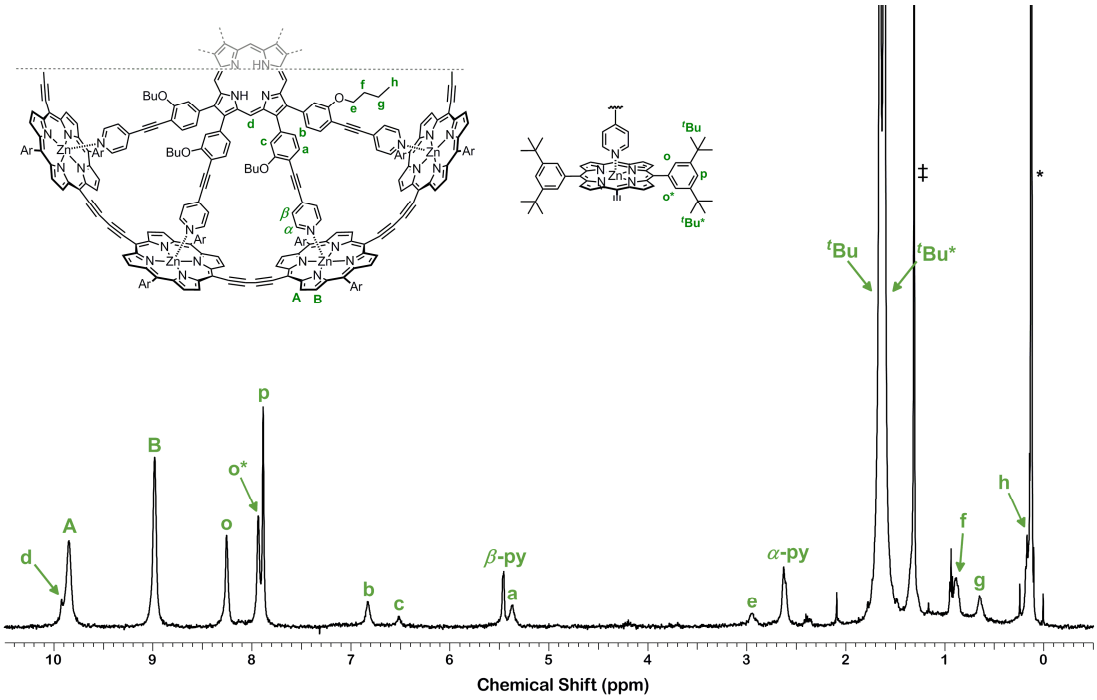

Figure 4.4 Diffusion edited ^{1}H NMR spectrum (500 MHz, $CDCl_3$, 298 K) of *tert*-butyl cyclic octamer complex ***c*-P8·T8** synthesised by oxidative coupling of **(*l*-dP4)$_2$·T8**; * indicates grease; ‡ indicates water. The dashed line indicates a plane of symmetry.

MALDI-MS also confirmed the structure of ***c*-P8·T8**, with a major peak at 6366 Da corresponding to the free cyclic octamer ***c*-P8**, and a weak molecular ion peak at 8670 Da (Figure 4.5). As in the figure-of-eight complex ***c*-P12·(T6)$_2$**, the bound templates show lability under the ionisation conditions.

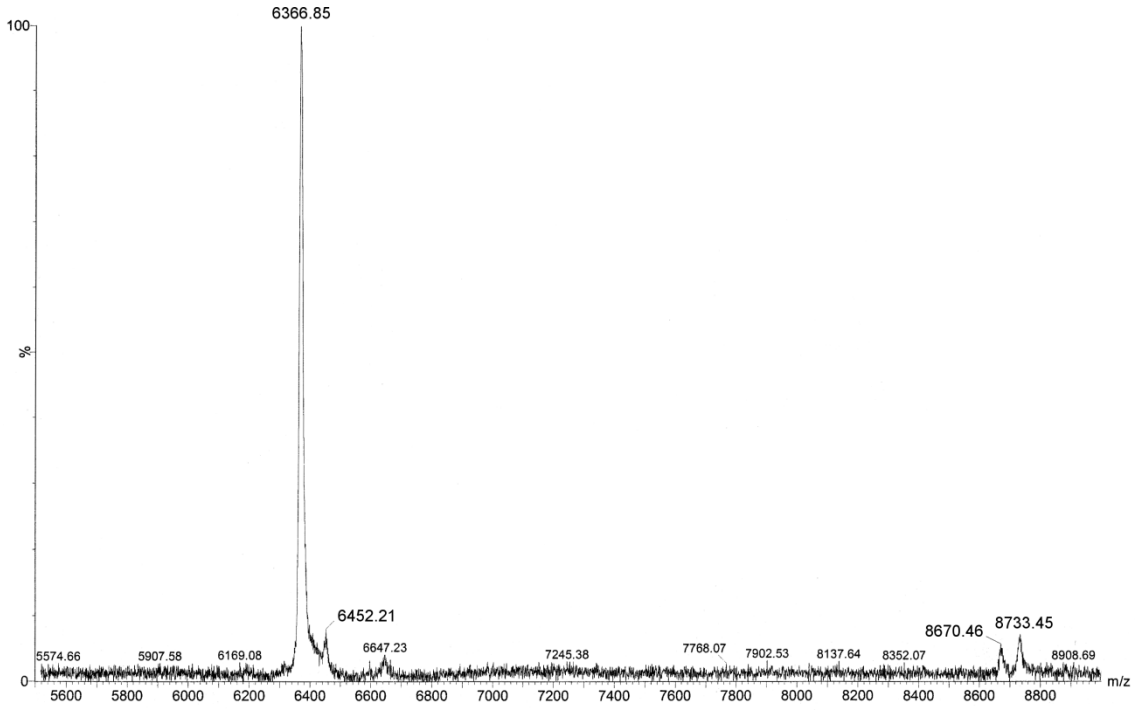

Figure 4.5 MALDI-ToF MS analysis of cyclic octamer complex ***c*-P8·T8** (dithranol matrix, reflectron mode). Peaks corresponding to ***c*-P8·T8** (*m*/*z* 8670, expected 8676) and ***c*-P8** (*m*/*z* 6367, expected 6371) can be seen.

The 22% yield for cyclisation of **(*l*-dP4)$_2$·T8** exceeds that previously reported for ***c*-P8^{C8}·T8**, which was obtained in 14% yield.[131]

The broadness of the peaks in the ***c*-P8·T8** ^{1}H NMR spectrum made it difficult to confirm the purity of the cyclic oligomer from these reactions. Like cyclic dodecamer ***c*-P12**, the free cyclic octamer ***c*-P8** is expected to give a simple spectrum due to its D_{8h} symmetry. To remove the template, cyclic octamer complex ***c*-P8·T8** formed from the cyclisation of **(*l*-dP4)$_2$·T8** was passed down a size-exclusion column with 10% pyridine in toluene to give the free cyclic octamer ring ***c*-P8** quantitatively (Scheme 4.4).

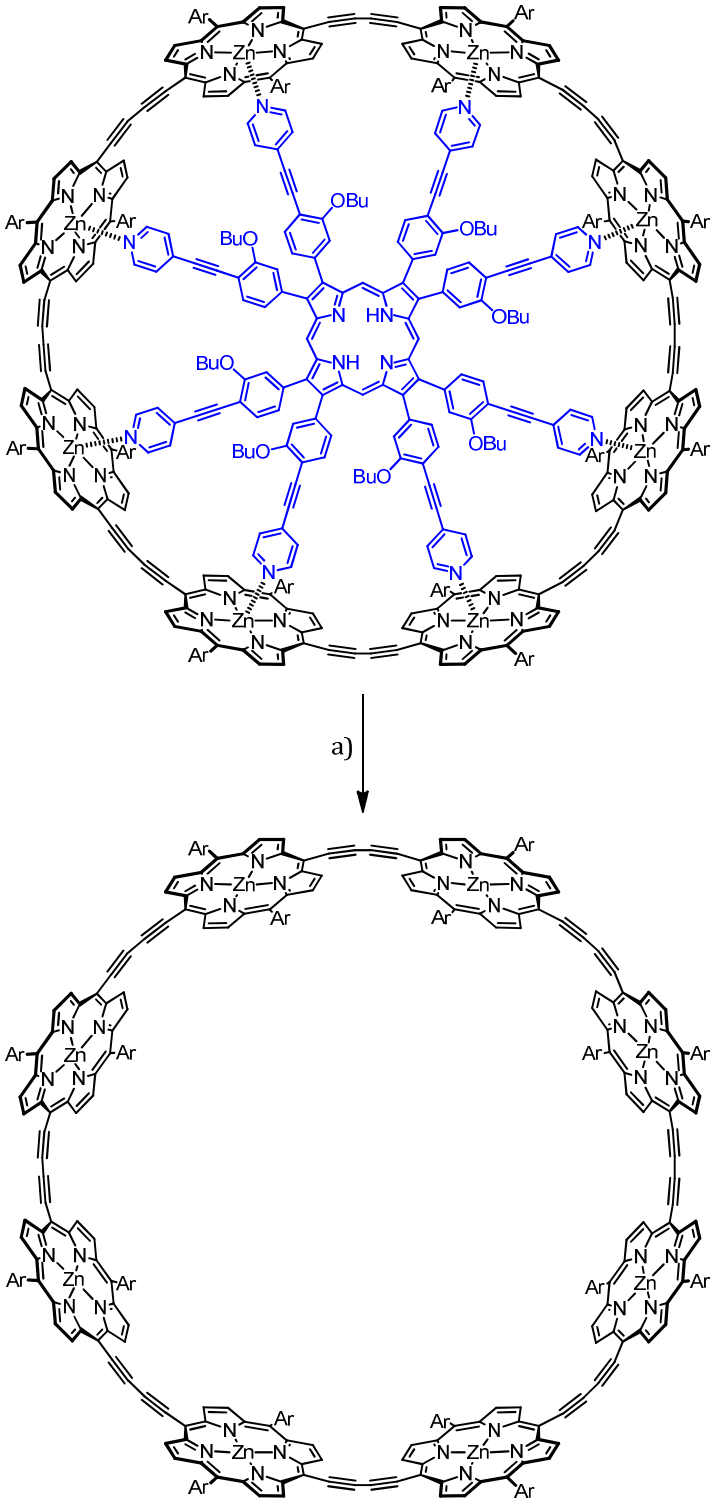

***c*-P8·T8**

***c*-P8**

Scheme 4.4 Knockout of cyclic octamer complex ***c*-P8·T8** to give free cyclic octamer ***c*-P8**: a) 10% pyridine in toluene, 99%.

As expected, the ^{1}H NMR of the free cyclic octamer ***c*-P8** consisted of only five signals indicating formation of a highly symmetric species (Figure 4.6). The two doublets corresponding to *β*-pyrrole protons A and B were well defined showing selective formation of a single species.

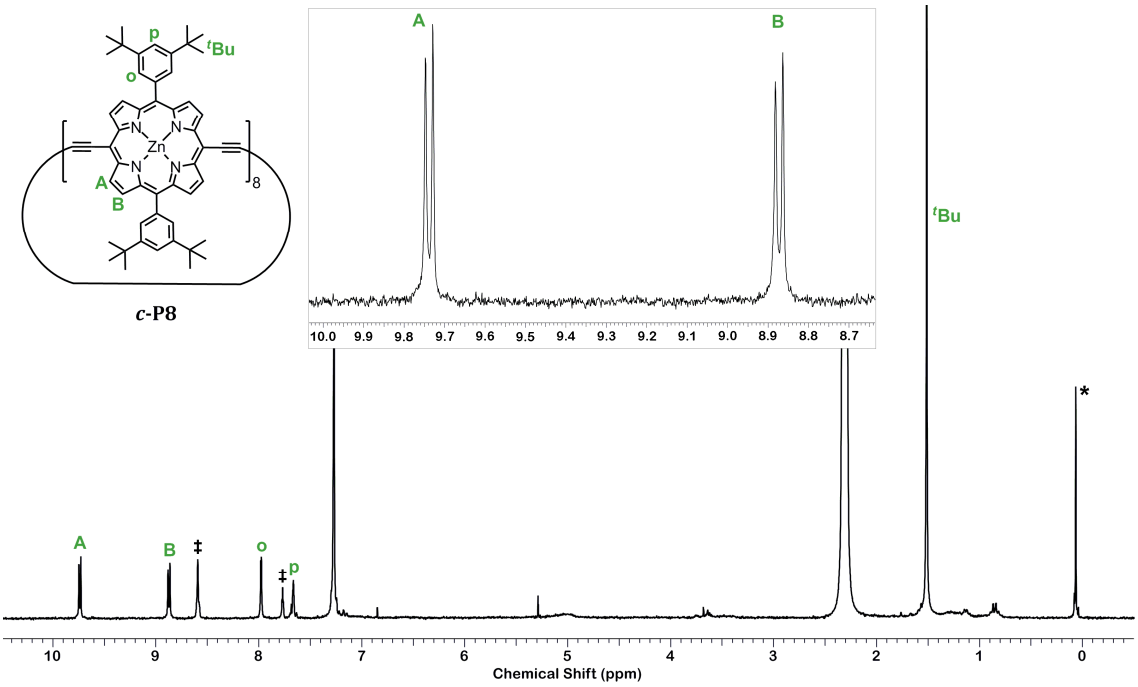

Figure 4.6 ^{1}H NMR (250 MHz, $CDCl_3$/1% d_5-pyridine, 298 K) of free cyclic octamer ***c*-P8**. Inset: zoom region showing the *β*-pyrrole region of the spectrum. * indicates grease; ‡ indicates peaks due to pyridine.

Synthesis of cyclic octamer from porphyrin dimer ***l*-dP2** gave even higher yields of 25% (Entry 2, Table 4.1). The analytical GPC trace of the crude reaction mixture from cyclising **(*l*-dP2)$_4$·T8** showed ***c*-P8·T8** to be the major product, with a minor impurity at shorter retention times (Figure 4.7).

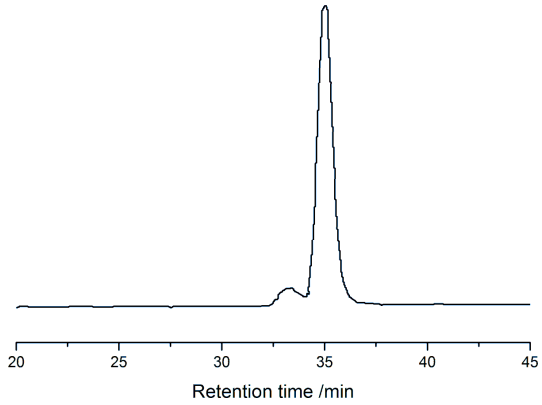

Figure 4.7 Preparative GPC analysis (toluene, 8.5 mL min^{-1}, λ = 440 nm) from the coupling reaction of porphyrin tetramer ***l*-dP2** in the presence of octadentate template **T8**.

The UV-vis absorption of the isolated ***c*-P8·T8** matched well with that isolated from the cyclisation of **(*l*-dP4)$_2$·T8** (Figure 4.8).

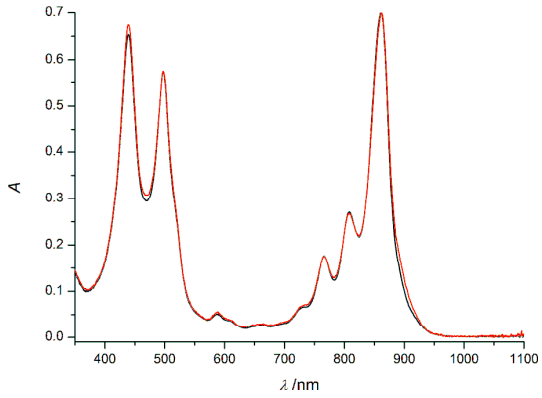

Figure 4.8 Normalised UV-vis absorption spectra ($CHCl_3$, 298 K) of ***c*-P8·T8** formed by cyclisation of **(*l*-dP2)$_4$·T8** (*red*), and **(*l*-dP4)$_2$·T8** (*black*).

Both the complex ***c*-P8·T8** and free ring ***c*-P8** obtained from dimer ***l*-dP2** gave identical ^{1}H NMR spectra to that obtained from tetramer ***l*-dP4**.

Results from the cyclisation of monomer ***l*-dP1** with template **T8** (Entry 1, Table 4.1) were ambiguous. GPC of the crude reaction mixture indicated selective formation of a single product

(Figure 4.9). Comparison of the UV-vis absorption spectra of the isolated product and pure ***c*-P8·T8** however, showed that the former had a broader Q band at long wavelengths, and the Soret band had a slightly different splitting pattern (Figure 4.10).

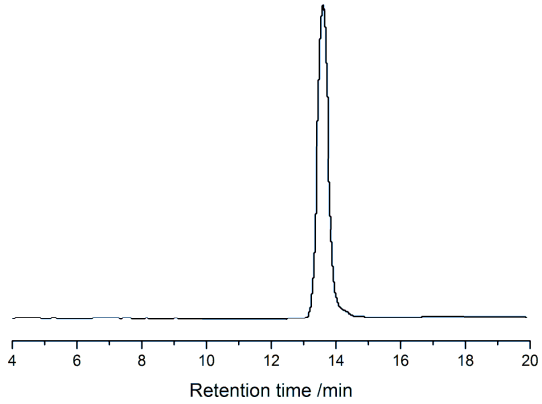

Figure 4.9 GPC analysis (toluene, 1 mL min^{-1}, λ = 498 nm) of the crude reaction mixture from the cyclisation of porphyrin monomer ***l*-dP1** in the presence of octadentate template **T8** (*black*).

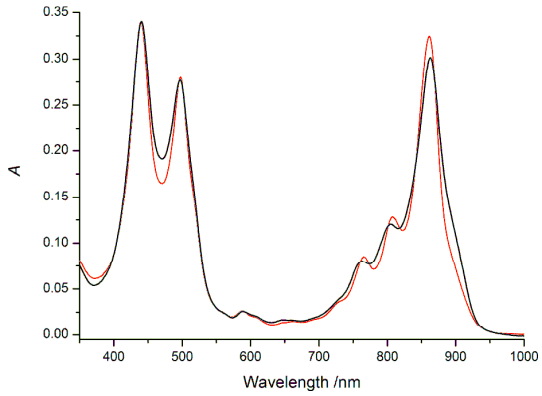

Figure 4.10 Normalised UV-vis spectrum ($CHCl_3$, 298 K) of the cyclic product formed by cyclisation of porphyrin monomer ***l*-dP1** with octadentate template **T8** (*black*) overlaid with the spectrum of pure ***c*-P8·T8** (*red*).

Analysis of the crude reaction mixture by MALDI-MS showed formation of both ***c*-P8·T8** and ***c*-P16·(T8)$_2$** (Figure 4.11).

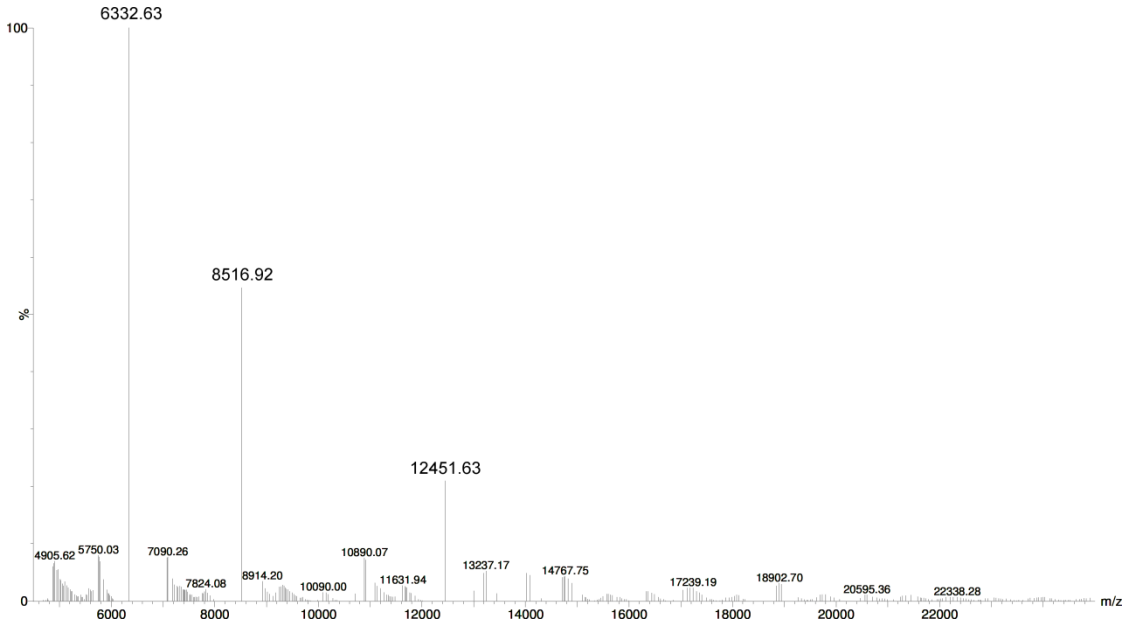

Figure 4.11 MALDI-ToF MS analysis (DCTB matrix, linear mode) of the crude reaction mixture from cyclisation of monomer ***l*-dP1** in the presence octadentate template **T8**. The three major peaks correspond to ***c*-P8** (m/z 6332, expected 6371), ***c*-P8·T8** (m/z 8517, expected 8676) and ***c*-P16** (m/z 12451, expected 12742). Peaks due to ***c*-P16·(T8)$_2$** and ***c*-P16·T8** cannot be seen due to the lability of template **T8** under the ionisation conditions of MALDI. The resolution of linear mode is 1000 Da.

Cyclisation of monomer ***l*-dP1** in the presence of template **T8** produced a mixture of cyclic octamer complex ***c*-P8·T8** and cyclic hexadecamer ***c*-P16** which was inseparable by GPC. Attempts to purify ***c*-P8·T8** from this mixture by recrystallisation failed.

There are two mechanisms that can account for the formation of ***c*-P16·(T8)$_2$** from cyclisation with porphyrin monomer ***l*-dP1**. The first involves chain growth in free solution before capture of the growing oligomer around the two templates, followed by cyclisation. The second mechanism sees chain growth while coordinated to template **T8**, with ***c*-P16·(T8)$_2$** forming by coupling of two template-oligomer complexes. Using the binding constant for the interaction of pyridine with porphyrin monomer,[131] under cyclisation concentrations, 97% of ***l*-dP1** is bound to template **T8**, suggesting that the latter mechanism is predominant. The multidentate

interaction of the longer oligomers ***l*-dP2** and ***l*-dP4** means that when coordinated, the terminal acetylenes are held more rigidly into a conformation which favours cyclisation to form the 'monomeric' ***c*-P8·T8**. On the other hand, porphyrin monomer ***l*-dP1** retains a degree of torsional freedom about the Zn–N coordination bond meaning reaction with a neighbouring oligomer-template complex is more likely.

Tert-butyl cyclic porphyrin octamer ***c*-P8** has been successfully synthesised from linear dimer ***l*-dP2** and tetramer ***l*-dP4** in higher yields than that previously reported for octyloxy cyclic porphyrin octamer ***c*-P8^{C8}**.[131] The synthetic accessibility of ***l*-dP2** greatly increases the availability of the cyclic octamer. Furthermore, it has been demonstrated that the conditions reported by Swager are compatible with **T8**-mediated cyclisations, thus can be applied to the Vernier synthesis of tetracosamer complex ***c*-P24·(T8)$_3$**.

4.1.4 Synthesis of porphyrin hexamer ***l*-P6**

Previously, linear porphyrin hexamer ***l*-P6** was obtained by dimerisation of mono-deprotected porphyrin trimer ***l*-mP3**.[128] There are two possible routes to trimer ***l*-P3**: 1. Coupling of mono-deprotected monomer ***l*-mP1** with mono-deprotected dimer ***l*-mP2** in a 2:1 ratio (Route A, Scheme 4.5);[75] 2. Statistical coupling of mono-deprotected and deprotected monomer ***l*-mP1** and ***l*-dP1** in a 4:1 ratio (Route B).[69]

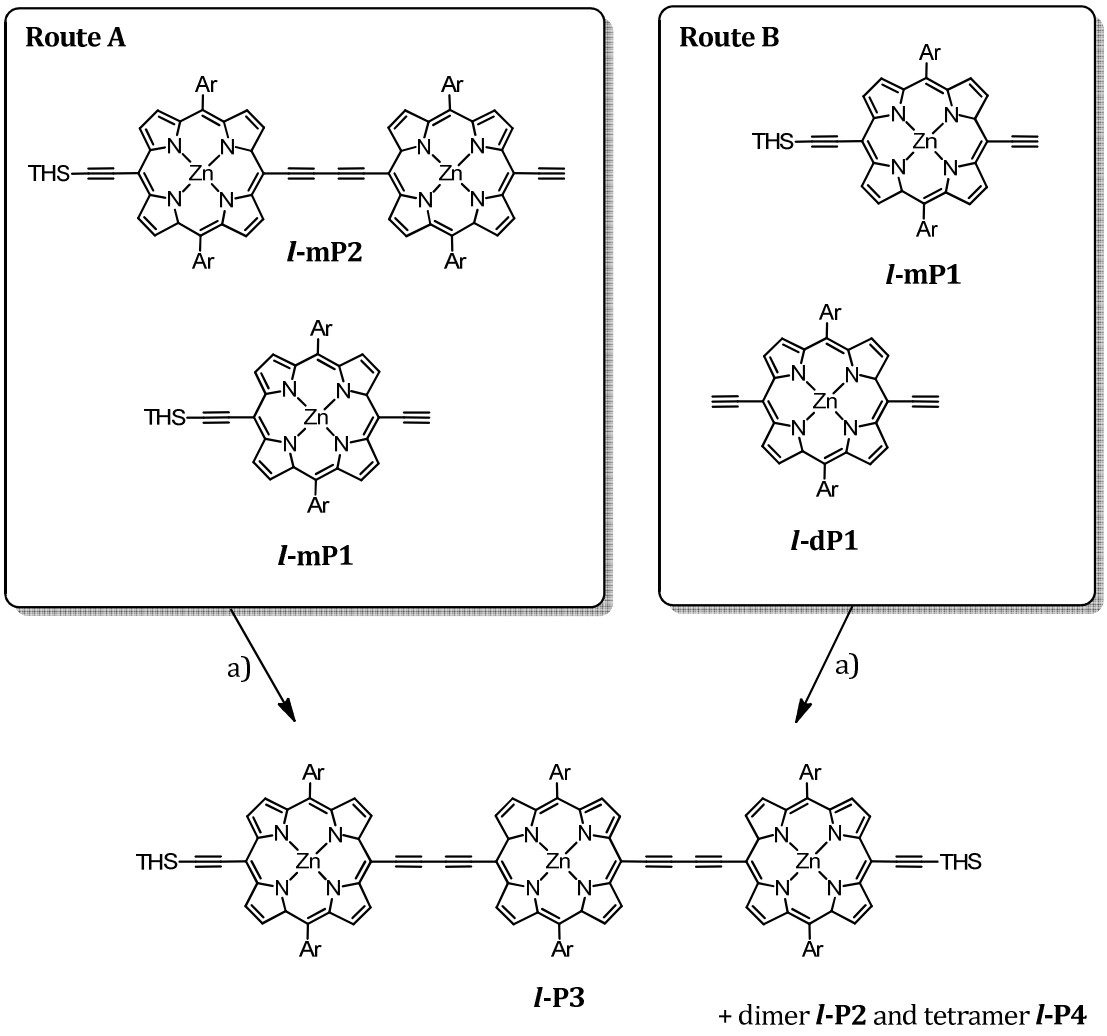

Scheme 4.5 Statistical coupling methods previously reported as a route to linear porphyrin trimer ***l*-P3**: a) CuCl, TMEDA, CH_2Cl_2, air.

Route A reported yields of 46% for the trimer ***l*-P3**; Route B gave ***l*-P3** in 34%, with the major product being porphyrin dimer ***l*-P2**. The high number of low-yielding statistical deprotection and coupling steps required to make porphyrin hexamer ***l*-P6** therefore makes this precious material.

Dmitry Kondratuk, a DPhil in the group, demonstrated a more direct route to linear hexamer by statistical coupling of monodeprotected and bisdeprotected porphyrin dimer (Scheme

4.6).[260] By coupling ***l*-mP2** and ***l*-dP2** in a 9:1 ratio, hexamer ***l*-P6** could be obtained in 49% yield, based on ***l*-dP2**. The major product of the reaction, porphyrin tetramer ***l*-P4**, was useful for the synthesis of ***c*-P12** (Chapter 3).

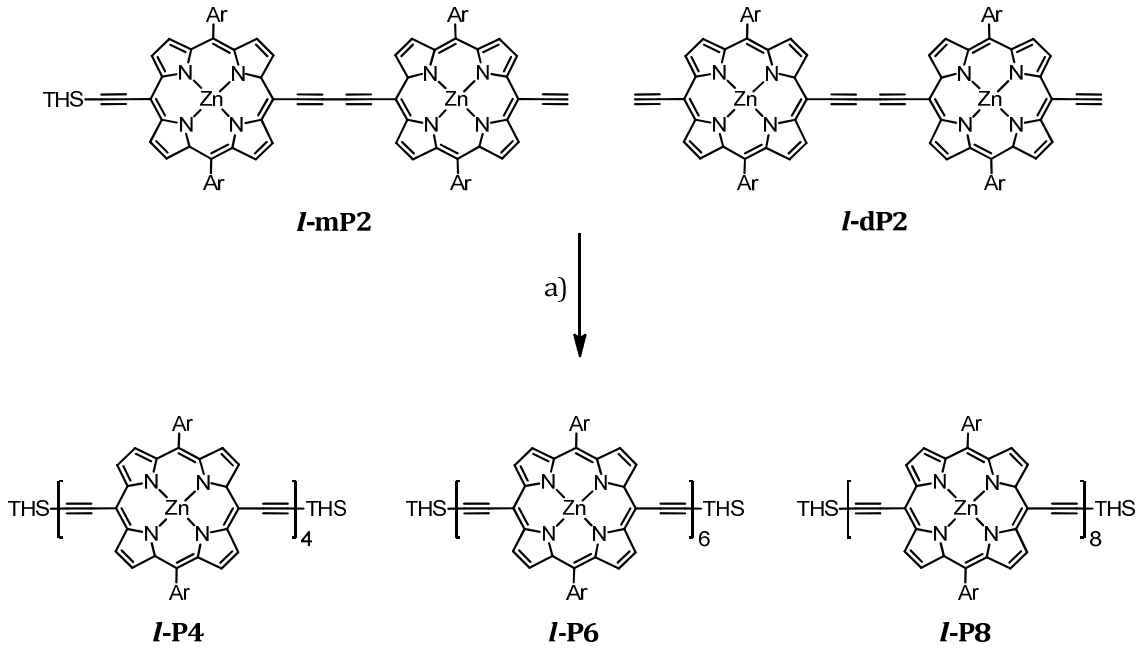

Scheme 4.6 Statistical coupling of monodeprotected ***l*-mP2** and deprotected dimer ***l*-dP2** as a route to linear porphyrin hexamer ***l*-P6**: a) CuCl, TMEDA, CH_2Cl_2, air.

The low hexamer to tetramer product ratio prompted re-examination of the coupling probabilities. It was calculated that an 8:2 ratio of ***l*-mP2** to ***l*-dP2** would improve the hexamer to tetramer ratio, without a significant increase in polymer yield. Eight equivalents of monodeprotected dimer ***l*-mP2** were reacted with two equivalents of bisdeprotected dimer ***l*-dP2** under Glaser-Hay coupling conditions (Scheme 4.6). As discussed in Chapter 3, the trihexylsilyl groups amplify steric bulk to facilitate the separation of porphyrin oligomers by size-exclusion chromatography (SEC). This effect decreases with increasing oligomer size, making separation of hexamer ***l*-P6** from the tetramer side product ***l*-P4** difficult. Furthermore,

porphyrin hexamer with 3,5-di(*tert*-butyl)phenyl *meso*-aryl sidechains has limited solubility, so yields are significantly decreased due to streaking on the column. The high pressure used in gel permeation chromatography (GPC) provides superior resolution to SEC which runs under gravity. The reaction mixture was separated by GPC (Figure 4.12) to give pure hexamer ***l*-P6** in an improved yield of 58% after one injection cycle.

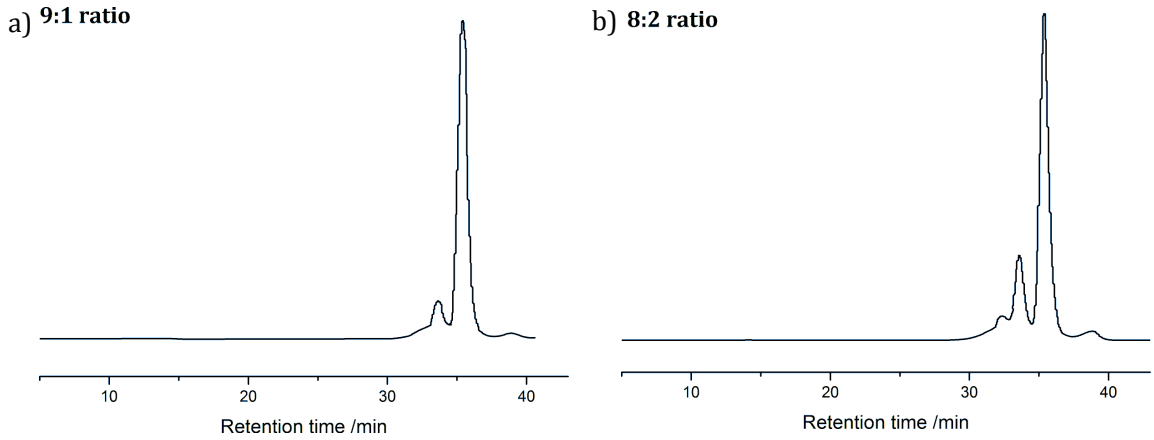

Figure 4.12 GPC traces (10% pyridine in toluene, 8.5 mL min^{-1}, λ = 592 nm) of crude reaction mixtures from a) 9:1 ratio of ***l*-mP2** to ***l*-dP2**; b) 8:2 ratio of ***l*-mP2** to ***l*-dP2**. The major peak in both spectra at R_T = 35.4 min corresponds to porphyrin tetramer ***l*-P4**; the secondary peak running at R_T = 33.6 min is porphyrin hexamer ***l*-P6**.

The shoulder at 32.3 min was also isolated (Figure 4.12). Interestingly, MALDI-MS identified this peak as linear porphyrin octamer ***l*-P8**, which was previously thought to be too insoluble for the di(*tert*-butyl)phenyl family of porphyrins.[58] However, the compound was found to be sufficiently soluble in 10% pyridine in toluene to acquire a ^{1}H NMR spectrum which showed excellent purity. Linear octamer ***l*-P8** was obtained in 19% yield (based on ***l*-dP2**).

4.1.5 Synthesis of cyclic tetracosamer complex ***c*-P24·(T8)$_3$**

The binding of THS-protected linear hexamer ***l*-P6** with octadentate template **T8** was studied by a UV-vis titration (Figure 4.13). Deprotected hexamer ***l*-dP6** could not be used due to its

near insolubility in non-coordinative solvents. The binding of hexamer ***l*-P6** caused a 61 nm bathochromic shift in Q band absorption, and the resulting spectrum strongly resembled that of linear hexamer coordinated to hexadentate template ***l*-P6^{C8}·T6**.[135] This indicated bending of the porphyrin hexamer around the octadentate template, causing planarisation of the porphyrin subunits.

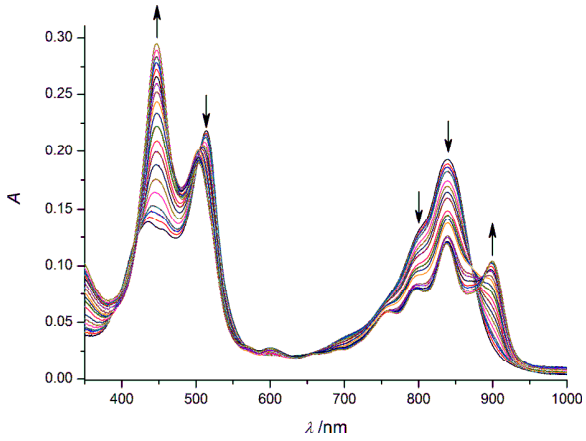

Figure 4.13 UV-Vis titration ($CHCl_3$, 298 K) of linear porphyrin hexamer ***l*-P6** with octadentate template **T8**: [***l*-P6**]$_0$ = 5.4×10^{-7} M, arrows indicate areas of increasing or decreasing absorption over the course of the titration. Absorption due to template **T8** is subtracted from the data.

Using the same method as in the synthesis of ***c*-P12·(T6)$_2$**, linear hexamer ***l*-dP6** was coordinated to template **T8**, and the terminal acetylenes oxidatively coupled with $Pd(PPh_3)_2Cl_2$, copper(I) iodide and benzoquinone (Scheme 4.7).

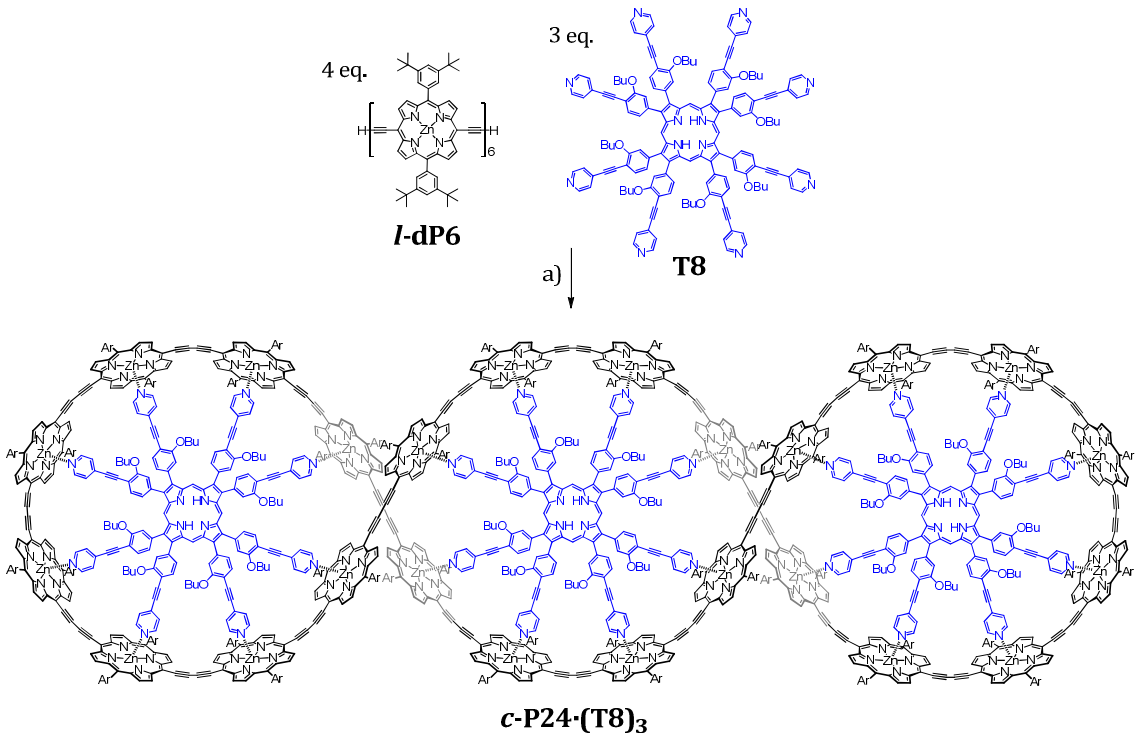

Scheme 4.7 Synthesis of cyclic tetracosamer complex ***c*-P24·(T8)$_3$** from linear hexamer ***l*-dP6** and octadentate template **T8**: a) $Pd(PPh_3)_2Cl_2$, PPh_3, CuI, 1,4-benzoquinone, rt → 50 °C; recovered mass yield 50%.

The UV-vis absorption spectrum of the isolated product showed a change in the shape of the Q band, but with no red-shift on cyclisation (Figure 4.14). Linear porphyrin hexamer is close to the effective conjugative length for linear porphyrin oligomers, as is the cyclic porphyrin tetracosamer ***c*-P24** for the cyclic series (see Chapter 5). As both the linear and cyclic series reach the same asymptotic limit for the optical energy gap, no red-shifting is seen upon cyclisation.[213]

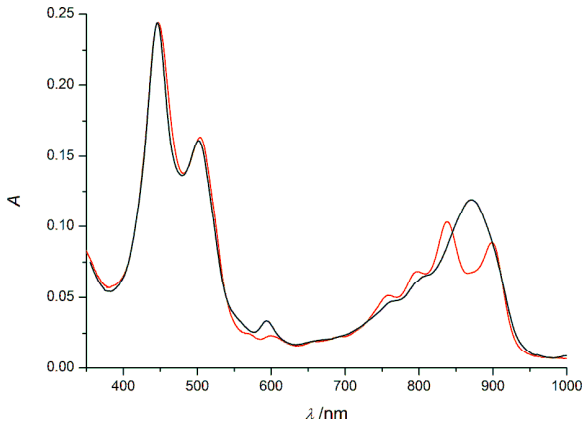

Figure 4.14 Normalised UV-vis absorption spectra ($CHCl_3$, 298 K) of linear hexamer-template complex **(*l*-dP6)$_4$·(T8)$_3$** (*red*) and the isolated product from the cyclisation reaction (*black*).

The selectivity of the reaction for formation of ***c*-P24·(T8)$_3$** was examined by analytical GPC. Despite the complex being sufficiently soluble in chloroform or toluene to allow acquisition of a ^{1}H NMR spectrum, using either of these solvents as eluent on the GPC caused the reaction product to stick to the column, resulting in blank or irreproducible spectra. THF could not be used as the mobile phase as concentrations above 2% *v/v* in chloroform resulted in knockout of template **T8** from the complex, and precipitation of the insoluble free ring. Mixed solvent systems produced similar results. Instead, the crude reaction mixture from the cyclisation of **(*l*-dP6)$_4$·(T8)$_3$** was analysed by ^{1}H NMR and MALDI-MS to see whether ***c*-P24·(T8)$_3$** had been formed.

4.1.6 ^{1}H NMR characterisation of ***c*-P24·(T8)$_3$** crude mixture

The ^{1}H NMR spectrum of the ***c*-P24·(T8)$_3$** crude reaction mixture was extremely broad. However, overlaying the spectrum with that of the cyclic octamer complex ***c*-P8·T8** showed similarities and suggested formation of a template-bound complex (Figure 4.15).

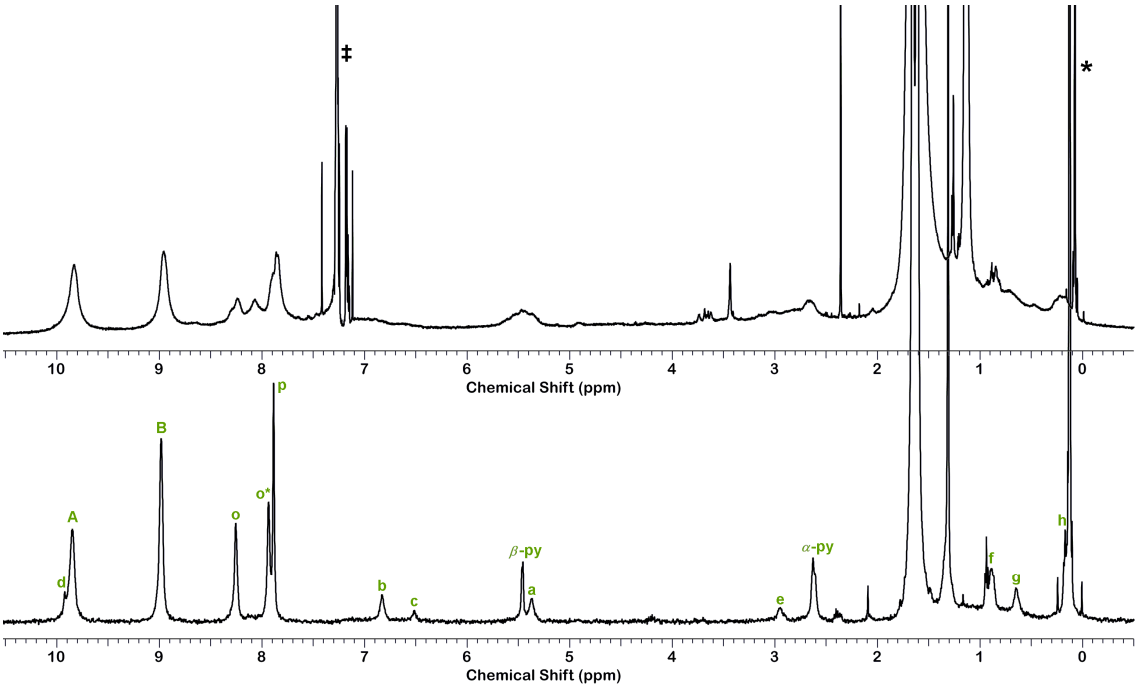

Figure 4.15 ^{1}H NMR spectra of ***c*-P24·(T8)$_3$** (*top*: 700 MHz, $CHCl_3$, 298 K) and ***c*-P8·T8** (*bottom*: 500 MHz, $CDCl_3$, 298 K). ‡ indicates residual protonated solvent; * indicates a silicon grease impurity.

Broad peaks at δ 2.66 and δ 5.46 ppm in the spectrum of the ***c*-P24·(T8)$_3$** crude reaction mixture could be assigned to the α- and β-pyridyl protons of template **T8** bound inside the cavity of a cyclic porphyrin assembly. A further broad peak at approximately 7.00 ppm, which partially lies under the $CHCl_3$ peak corresponded well to protons b and c of the bound template in the ***c*-P8·T8** spectrum. This peak was better resolved in the diffusion edited spectrum run in toluene (not shown). Similarly, broad peaks at 3.02, 0.72, 0.48 and 0.16 ppm matched well with the alkoxy template protons e–h seen in the ***c*-P8·T8** NMR. The coincidence of chemical shifts could not be due to formation of the cyclic octamer complex ***c*-P8·T8**, as this is impossible from linear porphyrin hexamer starting material, so suggests formation of a 'higher' ring.

The broadness of the ^{1}H NMR spectrum could be attributed to several factors. Firstly, the product may not be pure and the spectrum may be a sum of several cyclic oligomers of varying size. Secondly, the NMR spectrum of the corresponding 'monomeric' cyclic octamer complex ***c*-P8·T8** was also broad, owing to the desymmetrisation effect of template **T8**. The higher complexity of the ***c*-P24·(T8)$_3$** complex means that sufficient peak resolution for structural assignment may be impossible to achieve. Thirdly, the single crossover point in figure-of-eight complex ***c*-P12·(T6)$_2$** makes the molecule chiral. Tetracosamer complex ***c*-P24·(T8)$_3$** has two crossover points, thus is diastereomeric. The ^{1}H NMR spectrum might therefore consist of peaks due to different diastereomers. This is further complicated by the variety of different ways that ***l*-dP6** and **T8** can assemble, leading to numerous stereoisomers of both the Vernier complex **(*l*-dP6)$_4$·(T8)$_3$** and the resulting cyclic complex ***c*-P24·(T8)$_3$** (Figure 4.16).

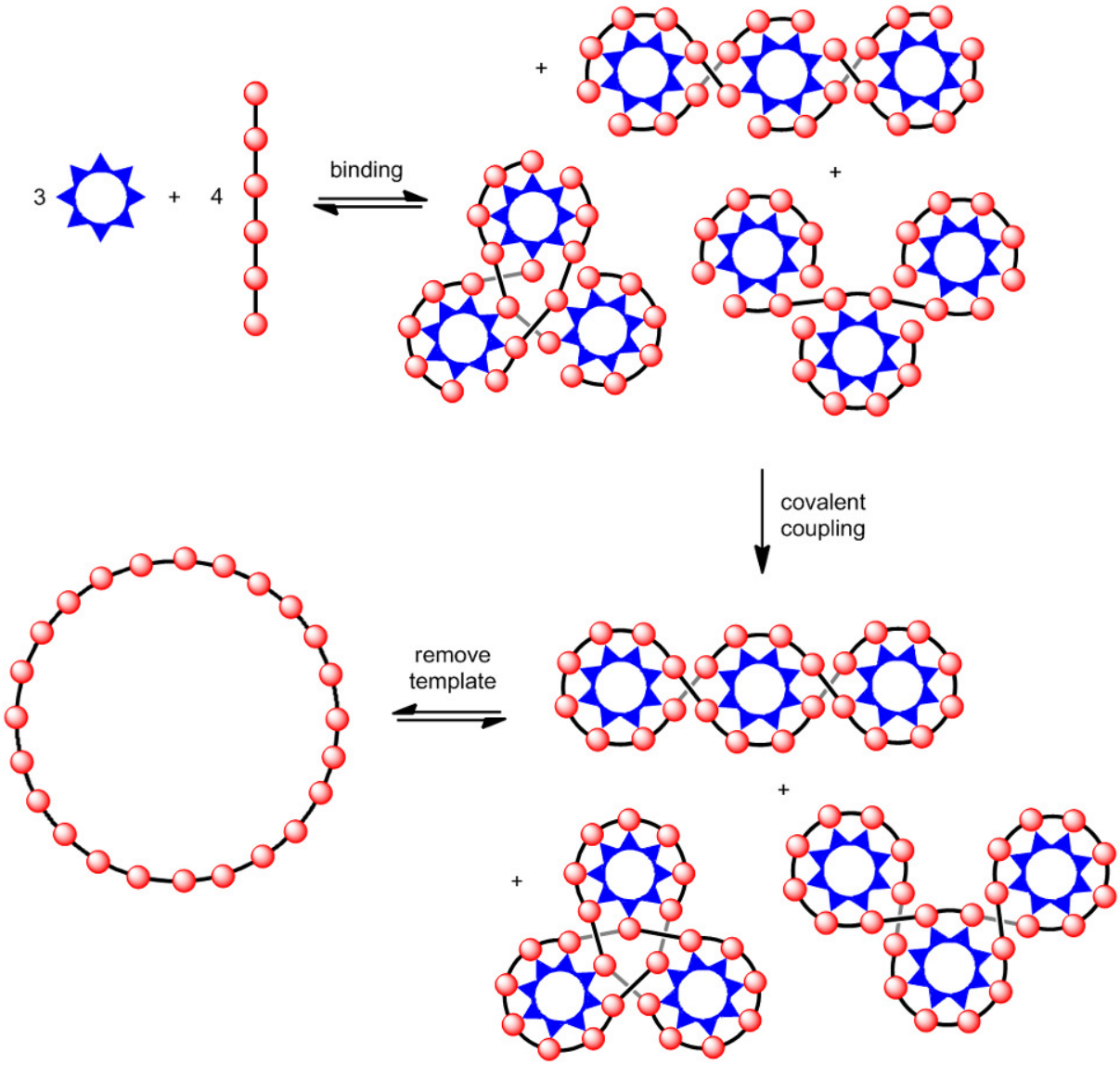

Figure 4.16 Linear porphyrin hexamer ***l*-dP6** can assemble with octadentate template **T8** in a number of different ways, leading to stereoisomers of Vernier complex **(*l*-dP6)$_4$·(T8)$_3$** and the resulting cyclic tetracosamer complex ***c*-P24·(T8)$_3$**. Knockout of the templates from these isomers however will give rise to the same cyclic porphyrin oligomer ***c*-P24**.

Knockout of the templates from these isomers with pyridine would give the same cyclic tetracosamer product ***c*-P24**. Due to the high symmetry of the cyclic tetracosamer ***c*-P24**, a

simple NMR spectrum as seen for ***c*-P8** and ***c*-P12** (Chapter 3) would provide conclusive evidence for formation of a single species. The ***c*-P24·(T8)$_3$** crude mixture was titrated with pyridine, but immediate precipitation showed that the free cyclic oligomers were too insoluble. Recently, it has been shown that the increased flexibility of larger rings allows the porphyrin subunits in ***c*-P12** to lie flat in the plane of the ring.[261] This increases the propensity of larger rings to π-stack and therefore aggregate, which would account for the low solubility of free ***c*-P24**.

4.1.7 ^{1}H NMR diffusion experiments on ***c*-P24·(T8)$_3$** crude mixture

DOSY NMR has been used to determine the molecular weight of compounds where traditional mass spectrometry techniques fail, for example in polymers[262] and biomaterials.[263] Initial difficulties in obtaining a MALDI-MS spectrum of the ***c*-P24·(T8)$_3$** crude mixture led to DOSY being used to investigate the molecular weight of the product.

The formula weight of a molecular species is inherently related to its volume and size, and therefore the rate of diffusion in solution. The Einstein-Smoluchowski equation[264] describes the rate of diffusion, D as

$$D = \frac{k_b T}{f} \qquad \text{Eq. 24}$$

where k_b is the Boltzmann constant, T is the absolute temperature and f is the hydrodynamic frictional coefficient, which for a spherical colloid in a continuous medium of viscosity η can be defined as

$$f = 6\pi\eta r_s \qquad \text{Eq. 25}$$

r_s is termed the hydrodynamic, or Stokes radius.

Equation 24 and 25 can be combined to give the Stokes-Einstein equation:[265]

$$D = \frac{k_b T}{6\pi\eta r_s} \qquad \text{Eq. 26}$$

Different theories are needed to describe molecular species that deviate from the ideal spherical conformation.[266] Experimentally, diffusion coefficients of conformationally similar compounds with known formula weight are first determined to obtain a calibration curve. Unknown compounds can then be interpolated or extrapolated to obtain the formula weight. The relationship between diffusion coefficient *D* and formula weight *FW* can be described as

$$\log D = a \log FW + b \qquad \text{Eq. 27}$$

where a and b are constants relating to the density and viscosity of the solution under study.[267] Halogenated solvents, such as $CDCl_3$ or CD_2Cl_2 show wide variations in solution density and viscosity with concentration, so often give poor formula weight predictions.[266] Toluene has been found to show the least variation of the two parameters with concentration, making it an ideal solvent for diffusion experiments.[267]

The diffusion constants of figure-of-eight complex ***c*-P12·(T6)$_2$**, cyclic hexamer complex ***c*-P6·T6** and cyclic octamer complex ***c*-P8·T8** were determined from deutero-toluene solutions at approximately 10^{-4} M concentrations. The diffusion of residual protonated toluene was used as an internal standard. The experimentally determined diffusion constants were plotted as a function of expected formula weight to obtain values for a and b of –0.58 and –7.39, respectively (Figure 4.17). These values matched well with reported average values for diffusion in toluene of –0.56 and –7.59.[267]

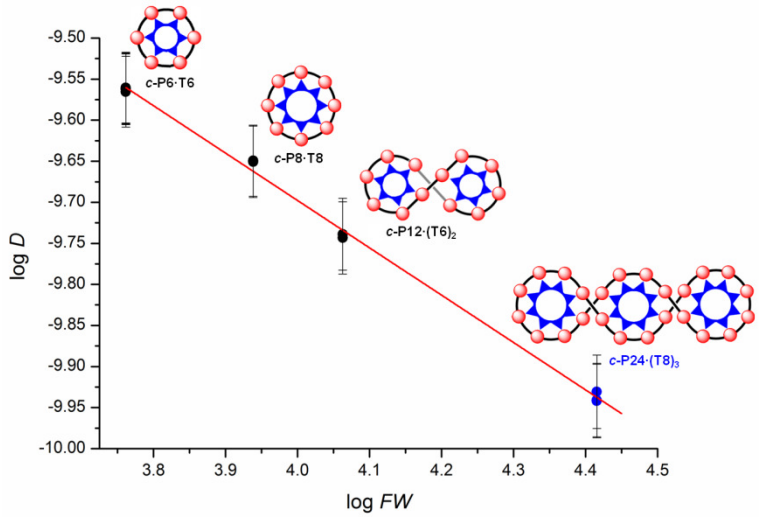

Figure 4.17 The log *D* of a series of porphyrin nanorings ***c*-P6·T6**, ***c*-P8·T8** and ***c*-P12·(T6)$_2$** were plotted against log *FW* (*black circles*) to obtain a calibration curve (*red line*). The corresponding data for the cyclic tetracosamer complex ***c*-P24·(T8)$_3$** is plotted (*blue circles*) showing an excellent fit to the extrapolated data.

A diffusion time of 1.15 × 10^{-10} m^2 s^{-1} was determined for ***c*-P24·(T8)$_3$**, which using our determined values of *a* and *b* corresponded to a molecular weight of 26070 Da, in excellent agreement with the expected value of 26027 Da for ***c*-P24·(T8)$_3$**. Plotting the diffusion times on the calibration curve also showed an excellent fit to the data.

4.1.8 MALDI-MS characterisation of ***c*-P24·(T8)$_3$** crude mixture

MALDI reflectron mode has a molecular weight limit of approximately 10000 Da, so linear mode was required to obtain the mass spectrum of tetracosamer complex ***c*-P24·(T8)$_3$**. A linear calibration file was made using samples of cyclic hexamer complex ***c*-P6·T6**, cyclic octamer complex ***c*-P8·T8** and the figure-of-eight complex ***c*-P12·(T6)$_2$**. The tetracosamer sample was analysed by MALDI-MS by spotting from a toluene solution with a dithranol matrix. Similar to all the other cyclic oligomer-template complexes, template **T8** was labile under the ionisation conditions of MALDI, so the spectrum showed peaks due to the intact

complex ***c*-P24·(T8)$_3$**, the free ring ***c*-P24**, and partially templated complexes ***c*-P24·T8** and ***c*-P24·(T8)$_2$** (Figure 4.18).

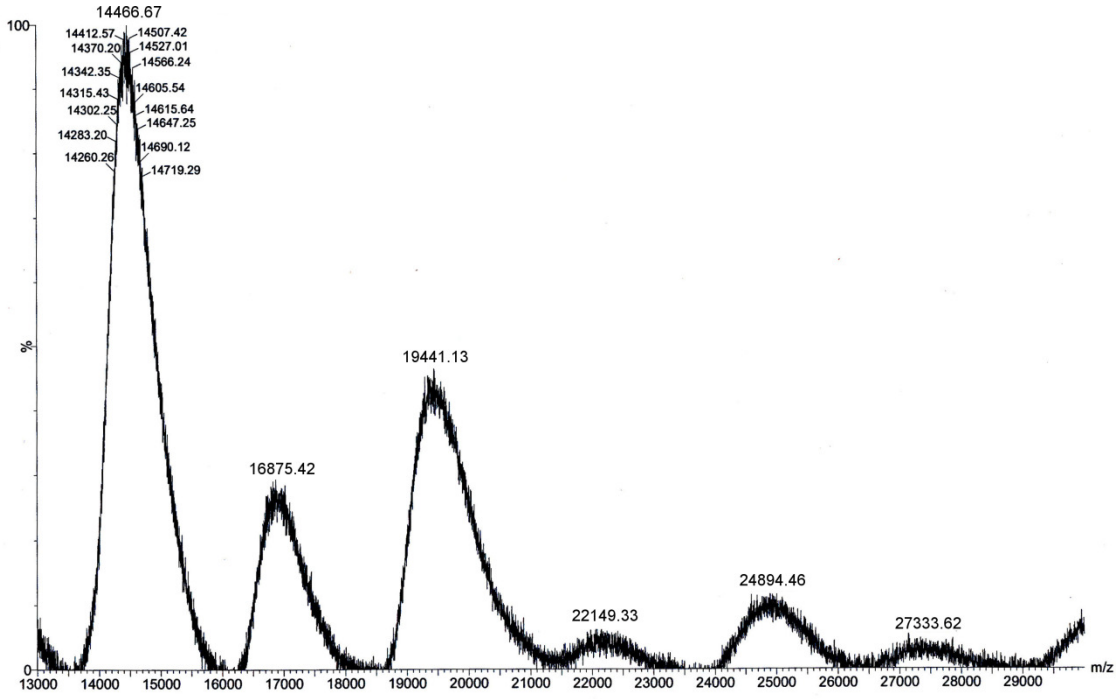

Figure 4.18 MALDI-ToF MS analysis of octadentate tetracosamer complex ***c*-P24·(T8)$_3$** crude reaction mixture (dithranol matrix, linear mode). The four peaks at higher molecular weight correspond to ***c*-P24·(T8)$_3$** (*m*/*z* 27334, expected 26027), ***c*-P24·(T8)$_2$** (*m*/*z* 24894, expected 23722), ***c*-P24·T8** (*m*/*z* 22149, expected 21417), and ***c*-P24** (*m*/*z* 19441, expected 19113). The two remaining peaks correspond to ***c*-P18** (*m*/*z* 14467, expected 14334) and ***c*-P18·T8** (*m*/*z* 16875, expected 16639).

Two additional peaks appeared at lower molecular weight at the mass expected for cyclic octadecamer ***c*-P18** and template-complexed cyclic octadecamer ***c*-P18·T8**. Within the 1000 Da resolution of the MALDI linear mode, assignment of the peak at 19441 Da was ambiguous. The peak falls within the mass region of cyclic tetracosamer ***c*-P24** with an expected mass of 19113 Da, but also of the cyclic octadecamer complex ***c*-P18·(T8)$_2$** with an expected mass of 18944 Da. It is likely that the observed peak is a summation of the two species. At the edge of

the spectral region, a peak at higher molecular weight (> 30000 Da) also showed the formation of larger rings, or possibly polymer.

MALDI-MS conclusively showed that the cyclisation of linear hexamer ***l*-dP6** in the presence of octadentate template **T8** gave ***c*-P24·(T8)$_3$** as a mixture with ***c*-P18** and other rings. This result initially appeared to conflict with the findings obtained by diffusion NMR. However, the large errors associated with extrapolating diffusion coefficients on the calibration curve in Figure 4.17 means that the experimental diffusion coefficient for a octadecamer complex ***c*-P18·(T8)$_2$** could fall in the expected mass range for ***c*-P24·(T8)$_3$**. By MALDI-MS alone it was not clear what the proportion of ***c*-P24·(T8)$_3$** to other rings was, as smaller rings have been observed to fly better by this technique. It was therefore crucial to develop a GPC method which allowed analysis and purification of the ***c*-P24·(T8)$_3$** reaction.

4.1.9 Template exchange

As mentioned in Section 4.1.1, a small amount of hexadentate templated tetracosamer complex ***c*-P24·(T6)$_4$** had been isolated from the synthesis of cyclic hexamer complex ***c*-P6·T6** directly from *tert*-butyl porphyrin monomer ***l*-dP1**. The complex had been purified by preparative GPC in toluene, suggesting that the hexadentate-templated complex had better solubility under GPC conditions. A template exchange of ***c*-P24·(T8)$_3$** with **T6** was carried out to improve the solubility of the ring.

To avoid mixed-template complexes, complex ***c*-P24·(T8)$_3$** was sonicated with an excess of template **T6** to push the exchange equilibrium towards ***c*-P24·(T6)$_4$** (Scheme 4.8).

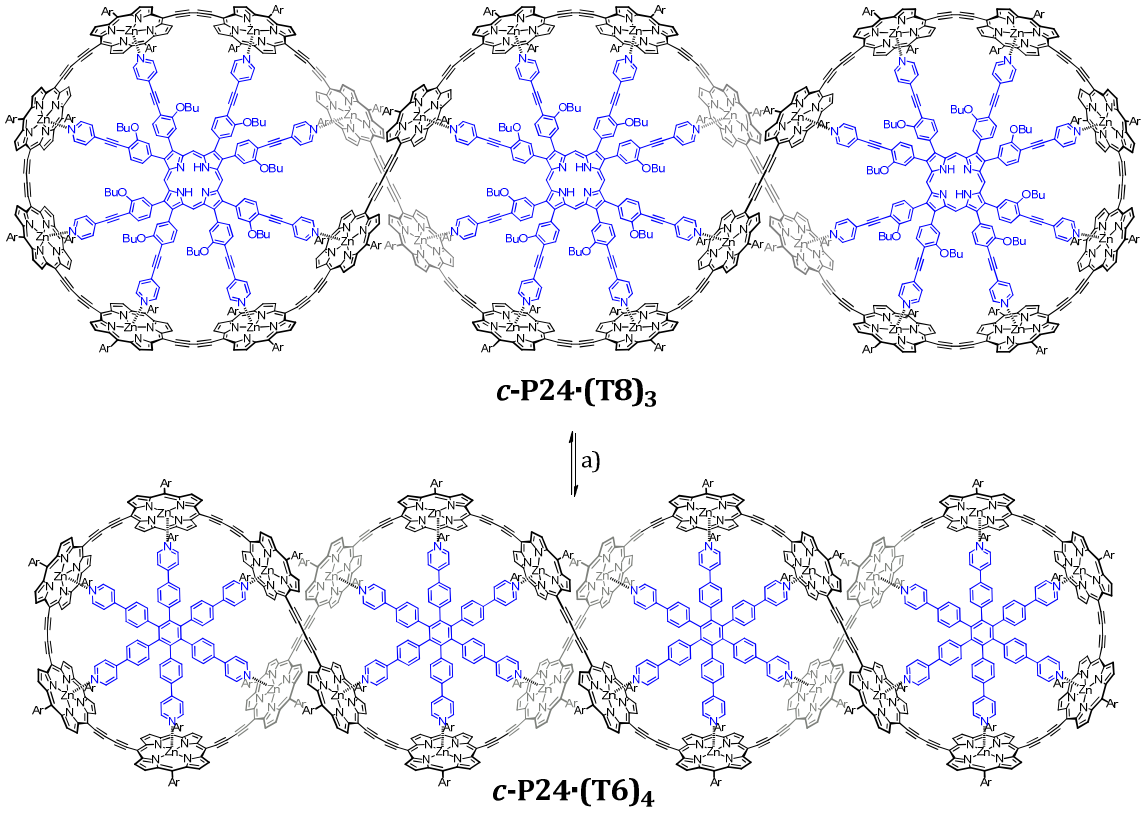

Scheme 4.8 Synthesis of complex ***c*-P24·(T6)$_4$** *via* template exchange of octadentate templated tetracosamer ring ***c*-P24·(T8)$_3$**: a) **T6**, $CHCl_3$, pyridine.

Competitive conditions by addition of catalytic pyridine were required for template exchange to occur. A series of recrystallisations in toluene first yielded the octadentate template **T8** quantitatively, and removed the excess hexadentate template **T6**.

The absorption spectrum of the isolated complex had a structured Q band, showing that the cyclic oligomer was binding to template **T6** (Figure 4.19).

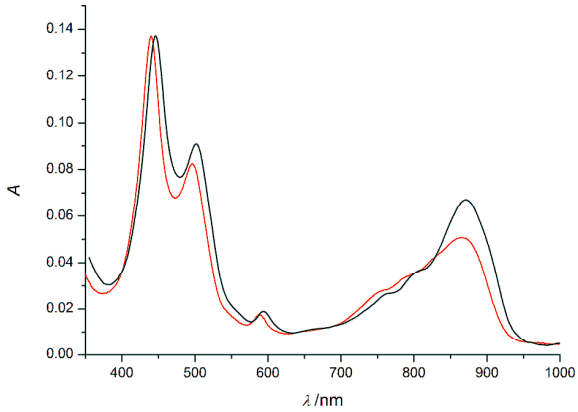

Figure 4.19 Normalised UV-vis spectra ($CHCl_3$, 298 K) of hexadentate templated tetracosamer complex ***c*-P24·(T6)$_4$** (*black*) and octadentate template tetracosamer complex ***c*-P24·(T8)$_3$** (*red*).

The hexadentate templated complex ***c*-P24·(T6)$_4$** was injected onto GPC, however, suffered the same insolubility issues as octadentate templated ***c*-P24·(T8)$_3$**, with blank or irreproducible spectra resulting. Changing the eluent from toluene to THF had no effect.

The complete insolubility of ***c*-P24**, and the inability to analyse complexes ***c*-P24·(T8)$_3$** and ***c*-P24·(T6)$_4$** by GPC demonstrated that a more soluble porphyrin such as octyloxy derivatised oligomer ***l*-dP*N*^{C8}** was required to obtain structural characterisation. This however, was outside the time-frame of this thesis. MALDI-MS indicated that Vernier templated synthesis of ***l*-dP6** with octadentate template did give the cyclic tetracosamer complex ***c*-P24·(T8)$_3$**, however showed that this complex was not formed selectively. An efficient method for template exchange from octadentate template **T8** to hexadentate template **T6** has been developed.

4.1.10 Addendum

Since the conclusion of the above experiments, Dmitry Kondratuk has been successful in isolating the octyloxy-derivatised cyclic tetracosamer ***c*-P24^{C8}**. Linear porphyrin hexamer ***l*-dP6^{C8}** was cyclised in the presence of octadentate template **T8** as shown in Scheme 4.7

(Section 4.1.5). As with the *tert*-butyl derivative, the resulting ***c*-P24^{C8}·(T8)$_3$** could not be analysed by GPC due to poor solubility. Template exchange using the methodology discussed above yielded ***c*-P24^{C8}·(T6)$_4$**, which was sufficiently soluble for analysis. Analytical GPC confirmed the result obtained by MALDI-MS (Figure 4.18) that tetracosamer ring ***c*-P24^{C8}** was produced as a mixture along with the octadecamer ***c*-P18^{C8}** and dodecamer ***c*-P12^{C8}**. Separation by preparative GPC yielded the ***c*-P24^{C8}·(T6)$_4$** complex in 24% yield. The free tetracosamer ring ***c*-P24^{C8}**, obtained by knockout of ***c*-P24^{C8}·(T6)$_4$** with pyridine has now been characterised by ^{1}H NMR, MALDI-ToF MS and STM.

Chapter Five

Steady State and Time-Resolved Fluorescence Anisotropy of Cyclic Porphyrin Oligomers

This chapter begins by outlining the theory of time-resolved photoluminescence (PL) anisotropy as a method of studying excitation transfer dynamics. The rates of excitation energy transfer in naturally occurring light harvesting complexes is reviewed. Previous investigations into the photophysical properties of linear porphyrin oligomers is introduced. The study continues by examining the degree of π-conjugation in the cyclic porphyrin series ***c-PN*** *and* ***c-PN·TN*** *using UV-vis spectroscopy. The effect of structural flexibility on quantum yield is discussed. Finally, femtosecond PL anisotropy on* ***c-P6***, ***c-P6·T6***, ***c-P8***, ***c-P8·T8*** *and* ***c-P12*** *show complete depolarisation of fluorescence within an 800 fs timescale, indicative of a completely delocalised excited state over the oligomer backbone. Parallels between the cyclic porphyrin oligomers and light harvesting complexes are thus drawn.*

5.1 Background

5.1.1 Photoluminescence anisotropy

As outlined in Chapter 1, when an organic molecule is photoexcited it is promoted to an excited state S_n before falling back to the ground state S_0. This relaxation can occur via internal conversion, intersystem crossing, charge separation, energy transfer to neighbouring chromophores, or radiative decay. Understanding the mechanisms of relaxation is important when designing systems for electroluminescent devices, where exciton hopping can be detrimental to device performance if quenching sites are present. Time-resolved photoluminescence (PL) anisotropy can give information on the mechanism of relaxation, in addition to the lifetimes for each process.

Time-resolved anisotropy $\gamma_{(t)}$ is defined as the difference in fluorescence intensities detected with the polarisation parallel ($I_{\parallel}$) and perpendicular ($I_{\perp}$) to the excitation polarisation, over the total fluorescence intensity ($I_{\parallel} + 2I_{\perp}$).[268][269]

$$\gamma_{(t)} = \frac{I_{\parallel} - I_{\perp}}{I_{\parallel} + 2I_{\perp}} \qquad \text{Eq. 28}$$

For a transition dipole randomly oriented in three dimensions, the initial anisotropy γ_0 for a one photon process is given by

$$\gamma_0 = \frac{2}{5}\left(\frac{3\cos^2\theta - 1}{2}\right) \qquad \text{Eq. 29}$$

where θ is the angle between the absorption and emission transition moments. Therefore, for a single photon process, rod shaped molecules with a θ value of 0° have a maximum initial anisotropy of 0.4, while disk shaped molecules (θ = 45°) expect a value of 0.1.[270]

5.1.2 Excitation energy transfer in light harvesting complexes

Excitation energy transfer in the LH1 complex of *Rhodobacter sphaeroides* (Chapter 1) was studied by fluorescence upconversion studies on the LH1-only mutant M2192.[271] The fluorescence anisotropy was found to decay from an initial anisotropy value γ_0 of 0.4 to a final value of 0.07 with a biphasic decay characterised by time constants of approximately 110 fs (dominant) and 400 fs. Assuming a symmetric arrangement of 16 chromophores based on a ring structure derived from electron diffraction studies,[272] an average nearest-neighbour hopping time τ_{hop} of 80 fs was calculated where

$$\tau_{\text{depol}} = \frac{\tau_{\text{hop}}}{4(1-\cos^2\alpha)} \qquad \text{Eq. 30}$$

where $\alpha = 360°/N$, τ_{depol} is the fluorescence depolarisation time, and N is the number of chromophores.

The non-exponential decay could be accounted for by the inhomogeneous distribution of donor and acceptor sites within the absorption band. This broadening arises from coupling between chromophore electronic states and interactions with the protein scaffold and solvent surroundings.[273] The isotropic decay also showed oscillations of frequency 105 cm^{-1} with a damping time of between 300–500 fs. These oscillations are absent for BChl monomers in dilute solution,[274] but have been seen for the 'special pair' dimer found in the reaction centre (Chapter 1),[275][276] therefore were assigned to ground state intramolecular vibrations of a dimeric system coupling strongly to the electronic transition.

The same group also carried out fluorescence upconversion studies of isolated complexes of LH2 from *Rb*. *sphaeroides* (Chapter 1).[277] A similar biexponential anisotropy decay to 0.08 was observed for B850 with time constants of 50–90 fs (dominant) and 400–500 fs. Excitation of B800 gave only emission from B850, which exhibited a monoexponential rise time of 655 fs,

corresponding to the energy transfer time between chromophore rings. The initial emission from B850 after excitation of B800 had a high anisotropy value of 0.35, indicating that the transition dipoles of the two chromophore types are in a parallel arrangement.

Intra-ring energy transfer rates between B800 chromophores have been more difficult to resolve. Hole burning experiments[278] carried out at 1.2 K showed an excitation wavelength dependence on hole width. A linear increase in hole width at excitation wavelengths between 799 nm and 789 nm showed a downhill B800→B800 energy transfer of time constant 850 fs occurred before inter-ring transfer to B850.[279] Similarly, transient absorption[280] and polarised pump-probe measurements[281] at 77 K determined B800→B800 energy transfer to occur in 700 fs and 400 fs, respectively. On the other hand, Fleming *et al.* argued that the 330 fs component observed in transient absorption measurements could be assigned to vibrational relaxation within the B800 absorption band,[273] as observed in similar measurements for BChl monomers in solution.[274] The large separation between B800 BChls suggested that ultrafast energy transfer between these chromophores was unlikely;[79] this was further supported by three-pulse stimulated photon echo (3PE)[282] experiments.

Energy transfer from LH2 (B850) to LH1 (B875) has been found to be consistent with a direct Förster-type energy transfer[283] where an LH1 complex is surrounded by a sea of LH2 complexes (Figure 5.1).

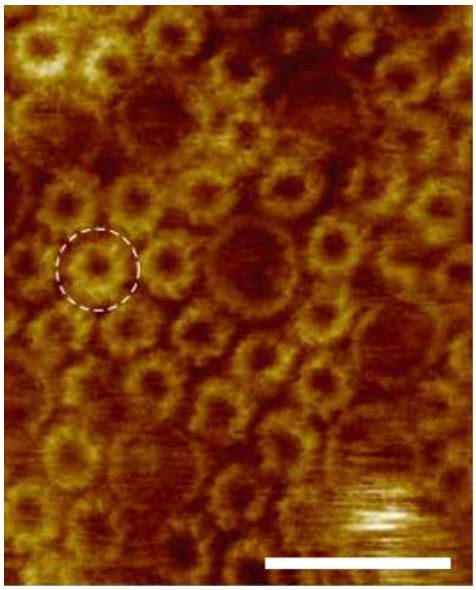

Figure 5.1 High resolution AFM image of high light-adapted photosynthetic apparatus of *Rsp. photometricum*, showing LH1 complexes (large elliptical rings) surrounded by a sea of LH2 complexes (small rings, *circled*).[77] Scale bar 20 nm.

Studies of a mutant strain of *Rb. sphaeroides* lacking a RC showed energy transfer from B850 to B875 to occur on a time scale of 4.6 ps.[284] Studies of the wild type bacteria gave a corresponding value of 3 ps at room temperature.[285] A second decay component of 26.3 ps was assigned to a random walk of excitations within the LH2 pool before transfer to LH1.

A series of LH2-absent *Rb. sphaeroides* with mutations to alter the rate of primary charge separation in the RC[286][287] were studied by low intensity picosecond pump-probe spectroscopy.[288] A time constant of 35 ps for the energy transfer from LH1 to the RC showed that this step, rather than charge separation, was the rate-limiting step for the overall light-harvesting process.

A summary of the timescales involved in the light harvesting process can be seen in Figure 5.2.[289]

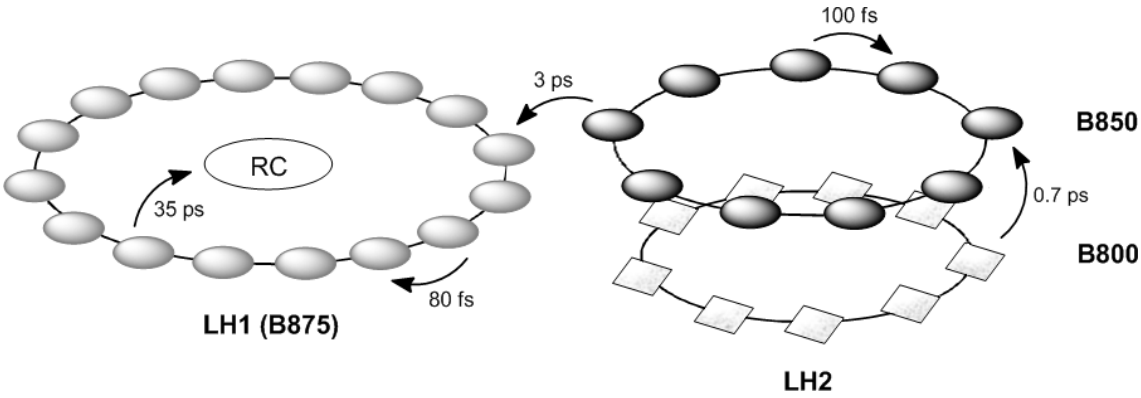

Figure 5.2 Schematic summary of the time scales for energy transfer processes occurring in purple bacteria. B875 and B850 are shown as dimers (*ovals*); B800 pigments are shown as monomers (*diamonds*).

5.1.3 Excitation energy transfer in supramolecular systems

The efficiency of excitation energy transfer (EET) in LH complexes has prompted research into supramolecular mimics of these antenna systems. Crossley and co-workers studied a series of porphyrin-appended dendrimers **D*N*** (*N* = 1, 4, 16, 64; where *N* is the number of porphyrin subunits) by time-resolved fluorescence anisotropy (Figure 5.3).[290]

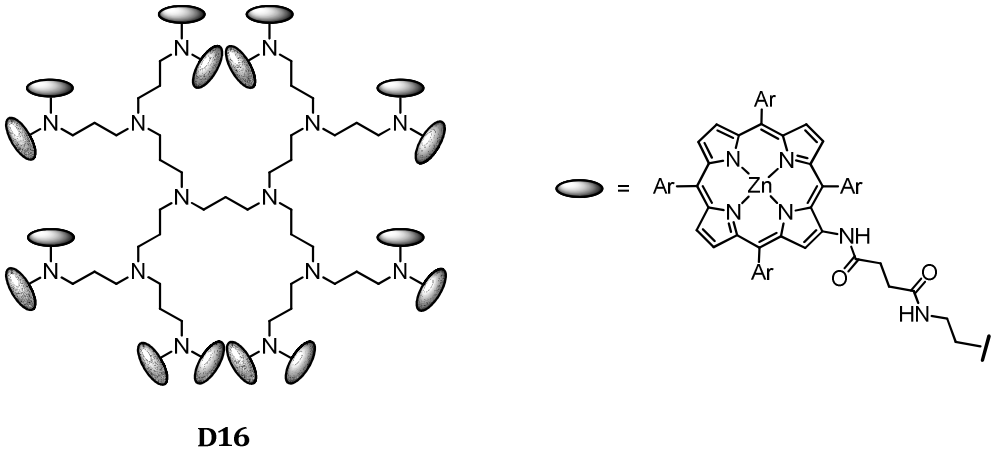

D16

Figure 5.3 Crossley's third generation porphyrin dendrimer **D16**; Ar = 3,5-di(*tert*-butyl)phenyl.

Fluorescence anisotropy at 200 K for **D4**, **D16** and **D64** could be modelled using a double-exponential decay function with time constants of 100 ps and 1.7 ns. The long time component was also observed for the porphyrin monomer **D1**, so was assigned to rotational motion of porphyrin units within the dendrimer. The absence of the 100 ps time component in the monomer decay meant this could be assigned to energy transfer processes between porphyrin subunits. This decay constant showed no dependence on dendrimer size, so it was concluded that energy delocalisation was limited to a maximum of four porphyrin units within a dendron.

Osuka studied the excitation dynamics of a series of *m*-phenylene bridged (Figure 5.4) and directly *meso*-*meso* linked cyclic porphyrin arrays (Figure 5.5), which were introduced in Chapter 3.[291]

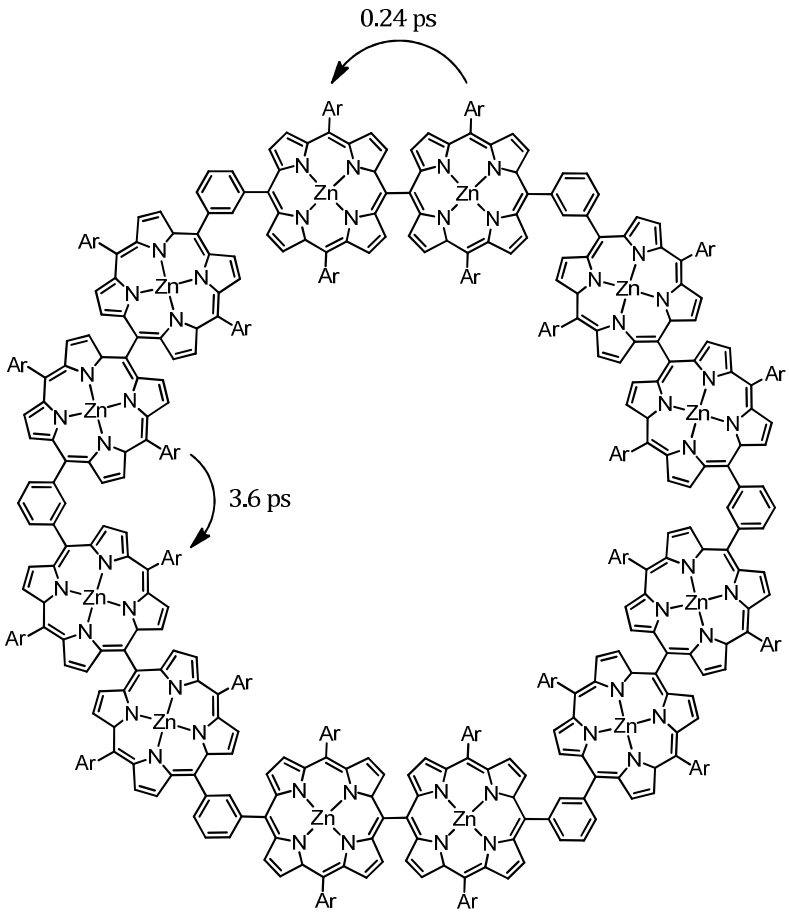

82

Figure 5.4 Osuka's *m*-phenylene bridged cyclic porphyrin dodecamer **82**; Ar = *p*-dodecyloxyphenyl.

m-Phenylene bridged cyclic dodecamer **82** and cyclic 24-mer were studied by femtosecond time-resolved transient absorption anisotropy (TAA) measurements. A time component of 240 fs showed energy was initially delocalised over the *meso*-linked diporphyrin subunit of dodecamer **82**.[292][293] Subsequent energy migration between diporphyrin subunits bridged by the *m*-phenylene spacer occurred at rates of $(3.6\ ps)^{-1}$ for the dodecamer and $(35\ ps)^{-1}$ for the 24-membered ring.[234] The large discrepancy in EET rates between the two macrocycles could be accounted for by the difference in the centre-to-centre distance between *meso*-linked porphyrin subunits.

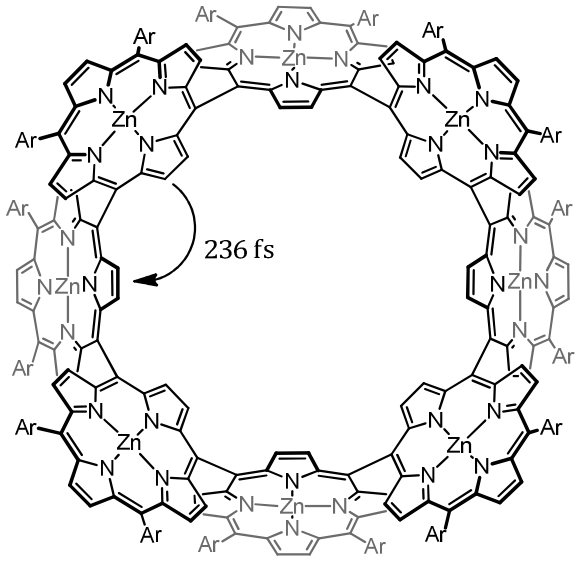

83

Figure 5.5 Osuka's directly *meso-meso* linked cyclic porphyrin octamer **83**.

Directly *meso-meso* linked cyclic porphyrin arrays (Figure 5.5) were expected to show rapid EET due to large electronic coupling between the porphyrin subunits. Transient absorption (TA) and TAA experiments measured excitation energy hopping times of 119 fs, 342 fs and 236 fs for the cyclic tetramer, hexamer, and octamer **83** respectively.[236] These EET rates rival those seen in naturally occurring light harvesting systems.

5.1.4 Excitation and energy transfer pathways

Exciton migration and conformational relaxation cause a Stokes shift between the absorption and emission spectra.[294] If chromophores are chemically identical but in physically different environments, this can result in an inhomogeneous broadening of the absorption band representative of the statistical variation in each chromophore's environment (density of states).[295] Polymers can be considered as an array of ordered segments separated by defects such as twists in the polymer backbone.[296] This causes an interruption of π-conjugation, so the observed absorption represents the variation in the effective conjugation length. In this

case, an exciton can 'hop' via Förster energy transfer from higher energy segments to lower energy segments, causing a red-shift of emission with time.[297] This has been shown to occur in poly(*p*-phenylenevinylene)s and their derivatives.[298][299]

On photoexcitation, a conjugated polymer will first undergo vibrational 'cooling'. This is expected to occur at a rate of the C–C stretching vibration on a sub-picosecond time scale, with the emission spectrum showing vibronic modes spaced at approximately 180 meV. Vibrational relaxation leads to a rapid contraction of the excited state wavefunction causing ultrafast fluorescence depolarisation,[300] the effect of which is more pronounced for longer oligomers. This phenomenon is referred to as "exciton self-trapping"[301] and is absent in rigid rod-like structures where all the polymer segments are aligned.

As previously discussed in Chapter 1, the ground state of π-conjugated polymers exhibit aromatic resonance character, while the excited state is more quinoidal, resulting in a preferred planar S_1 conformation. Vibrational relaxation is therefore followed by torsional relaxation of the polymer substituents on a slower time scale. This conformational change is significant in polymers which adopt non-zero torsional angles in the ground state due to steric constraints, such as poly(thiophenes),[302][303] poly(fluorenes)[294] and porphyrin oligomers.[304] Planarisation increases the effective conjugation length of the emissive state, so this phenomenon is often characterised by a red-shifting and intensification of emission on a picosecond timescale.

The interplay of vibrational and torsional relaxation on fluorescence decay has been explored by Chang *et al.* using single stranded porphyrin oligomers ***l*-P*N*^{C8}·Py$_N$** (N = 4, 6, 8), ladder complex (***l*-P8^{C8})$_2$·Bipy$_8$** and bent porphyrin octamer-template complex ***l*-P8^{C8}·T8** (Figure 5.6).[304]

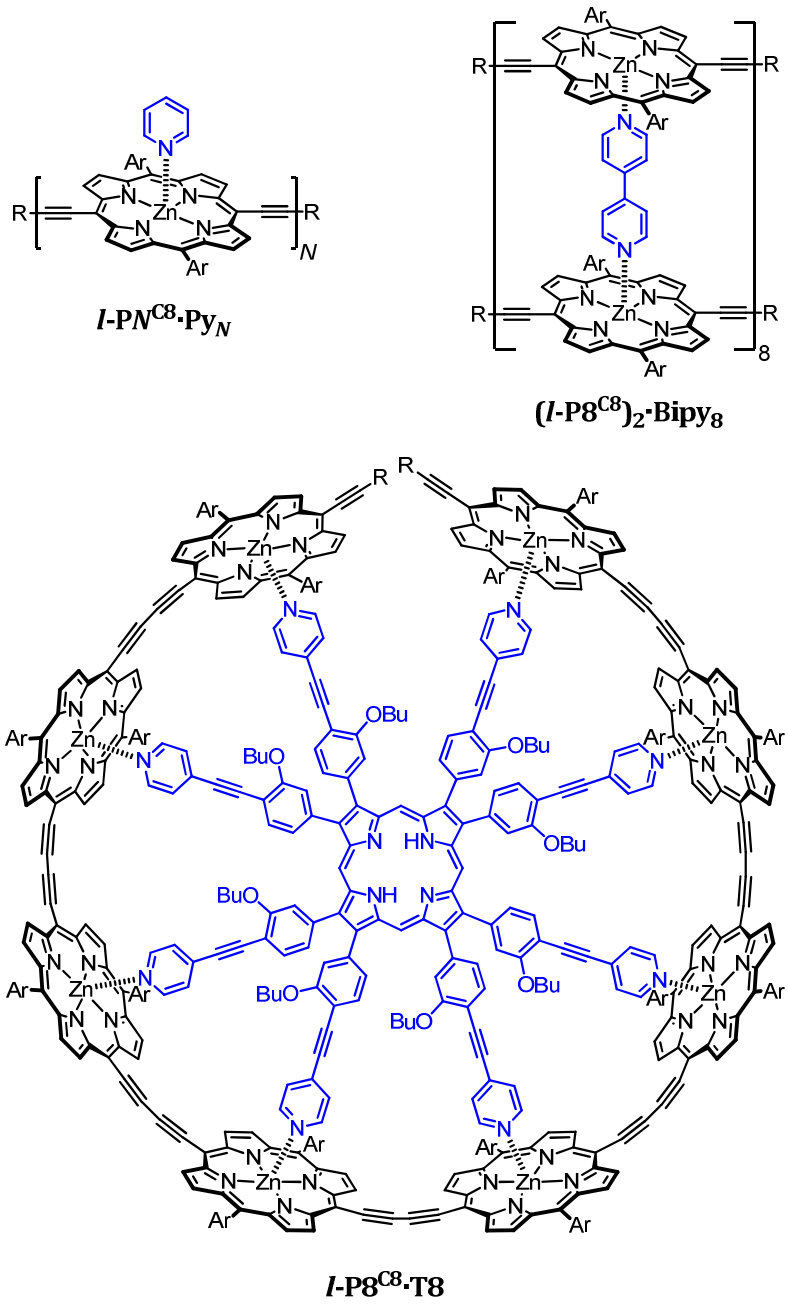

Figure 5.6 Single stranded porphyrin oligomers ***l*-P*N*^{C8}·Py*$_N$*** (*N* = 4, 6, 8), porphyrin ladder **(*l*-P8^{C8})$_2$·Bipy$_8$**, and bent porphyrin octamer-octadentate template complex ***l*-P8^{C8}.T8**. R = trihexylsilyl; Ar = 3,5-di(octyloxy)phenyl.

The initial anisotropy measured for single-stranded porphyrin tetramer ***l*-P4^{C8}.Py$_4$** ($\gamma_0 \sim 0.37$) corresponded well to that previously measured for similar oligomers,[66][305] and predicted

theoretically. However, lower initial anisotropies were obtained for the hexamer and octamer oligomers of 0.31 and 0.24, respectively. Formation of a ladder complex (***l*-P8^{C8})$_2$.Bipy$_8$** increased the initial anisotropy of the octamer to 0.34. Neutron scattering studies have shown porphyrin ladders adopt a rigid rod-like structure in solution with a length approximately 1.5 times that of the corresponding single strand.[306][307] Although covalently the same, the shorter measured length of the single strand reflects its conformational flexibility. The increase in initial anisotropy % of the octamer on forming the ladder therefore confirmed ultrafast depolarisation occurred on the single strand oligomer due to exciton self-trapping on a worm-like backbone.[300] Bending the porphyrin octamer around an octadentate template caused the initial anisotropy to fall to 0.1, indicating that the excited state was delocalised over the length of the molecular backbone at a rate faster than the instrument resolution (800 fs).

Torsional motion was frozen out by the use of the octadentate template and the resulting fluorescence anisotropy compared to that of the free porphyrin octamer ***l*-P8^{C8}.Py$_8$**. Linear porphyrin octamer bent around the octadentate template ***l*-P8^{C8}.T8** showed a monoexponential decay of 420 ps, irrespective of detection wavelength. In contrast, emission of single stranded octamer ***l*-P8^{C8}·Py$_8$** gradually red-shifted and increased in intensity, peaking at 100 ps before decaying. This increase is characteristic of increasing π-conjugation, showing that on excitation, torsional relaxation of the single strand led to a planar system. This agreed experimentally with that seen previously in similar ethynyl-linked porphyrins,[66] and with theoretical studies on π-conjugated PPV oligomers.[301]

5.2 Results and Discussion.

5.2.1 Synthesis of cyclic hexamer rings ***c*-P6** and ***c*-P6·T6**.

The synthesis of the cyclic hexamer complex was carried out as detailed recently.[135] Linear porphyrin dimer ***l*-dP2** was coordinated to hexadentate template **T6**, and the terminal

acetylenes oxidatively coupled using a $Pd(PPh_3)_2Cl_2$, copper(I) iodide and 1,4-benzoquinone catalyst system. The cyclic hexamer complex ***c*-P6·T6** was isolated in 21% yield (Scheme 5.1).

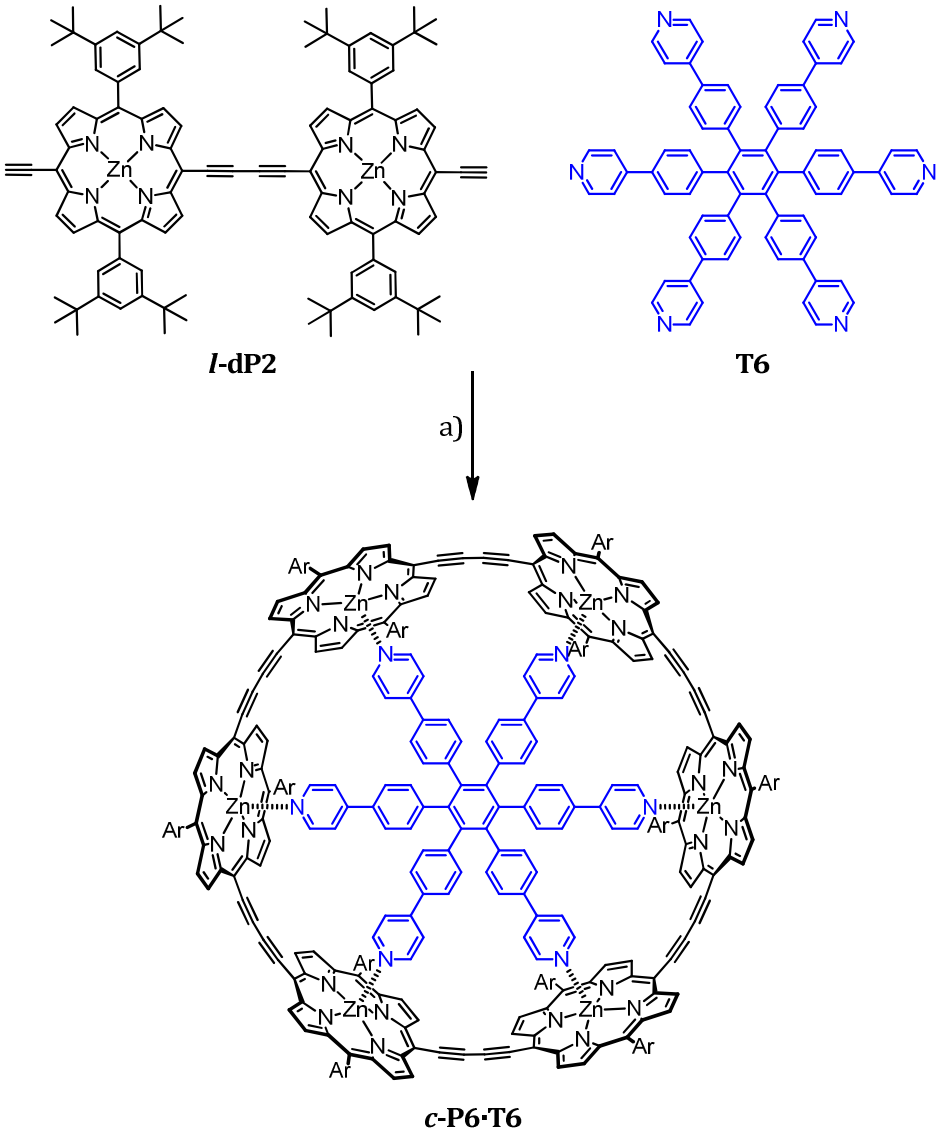

Scheme 5.1 Synthesis of cyclic hexamer complex ***c*-P6·T6** from linear porphyrin dimer ***l*-dP2**: a) $Pd(PPh_3)_2Cl_2$, CuI, 1,4-benzoquinone, $^iPr_2NH$, toluene, rt→50 °C, 21%.

Previously, knock-out of the cyclic hexamer complex ***c*-P6·T6** with a competitive monodentate amine ligand such as DABCO or quinuclidene was used to access free cyclic hexamer ring ***c*-P6**.[128] A large excess (> 250,000 equivalents) was required to achieve knockout. Due to the

high association constant of the template for the ring cavity, it was difficult to isolate ***c*-P6** in sufficient purity for PL anisotropy measurements *via* this route.

Recently, Will Peveler, a Part II in the group, investigated demetallation of the cyclic hexamer complex as a route to varied metal nanorings.[308] Demetallation of butadiyne-linked porphyrin oligomers with acid is known,[309][310] but it was originally thought that the increased strain of the bent alkyne units in the nanorings would increase their reactivity. Peveler found however, that treating cyclic hexamer complex ***c*-P6·T6** with TFA gave the free base ring **2H.*c*-P6** in good yield. This was seen as a potentially efficient route to de-templation: free base ring could be subsequently remetallated with zinc(II) acetate to give the free cyclic hexamer ***c*-P6**. Cyclic hexamer complex ***c*-P6·T6** was treated with TFA, and the reaction quenched with addition of pyridine. The mixture was passed down a short silica plug to remove the template and metal salts, yielding free base cyclic hexamer **2H.*c*-P6** quantitatively. **2H.*c*-P6** was stirred with zinc acetate to give the free cyclic hexamer ***c*-P6** in 58% yield (Scheme 5.2).

The absorption spectra of the free base ring **2H.*c*-P6**, free cyclic hexamer ***c*-P6** and cyclic hexamer complex ***c*-P6·T6** are shown in Figure 5.7.

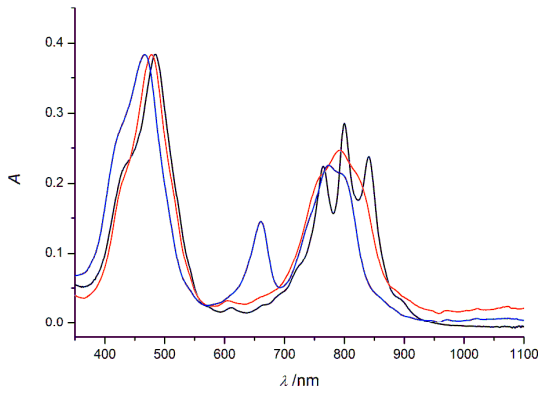

Figure 5.7 Normalised absorption spectra ($CHCl_3$, 298 K) of cyclic hexamer complex ***c*-P6·T6** (*black*), free base cyclic hexamer **2H.*c*-P6** (*blue*) and template-free cyclic hexamer ***c*-P6** (*red*).

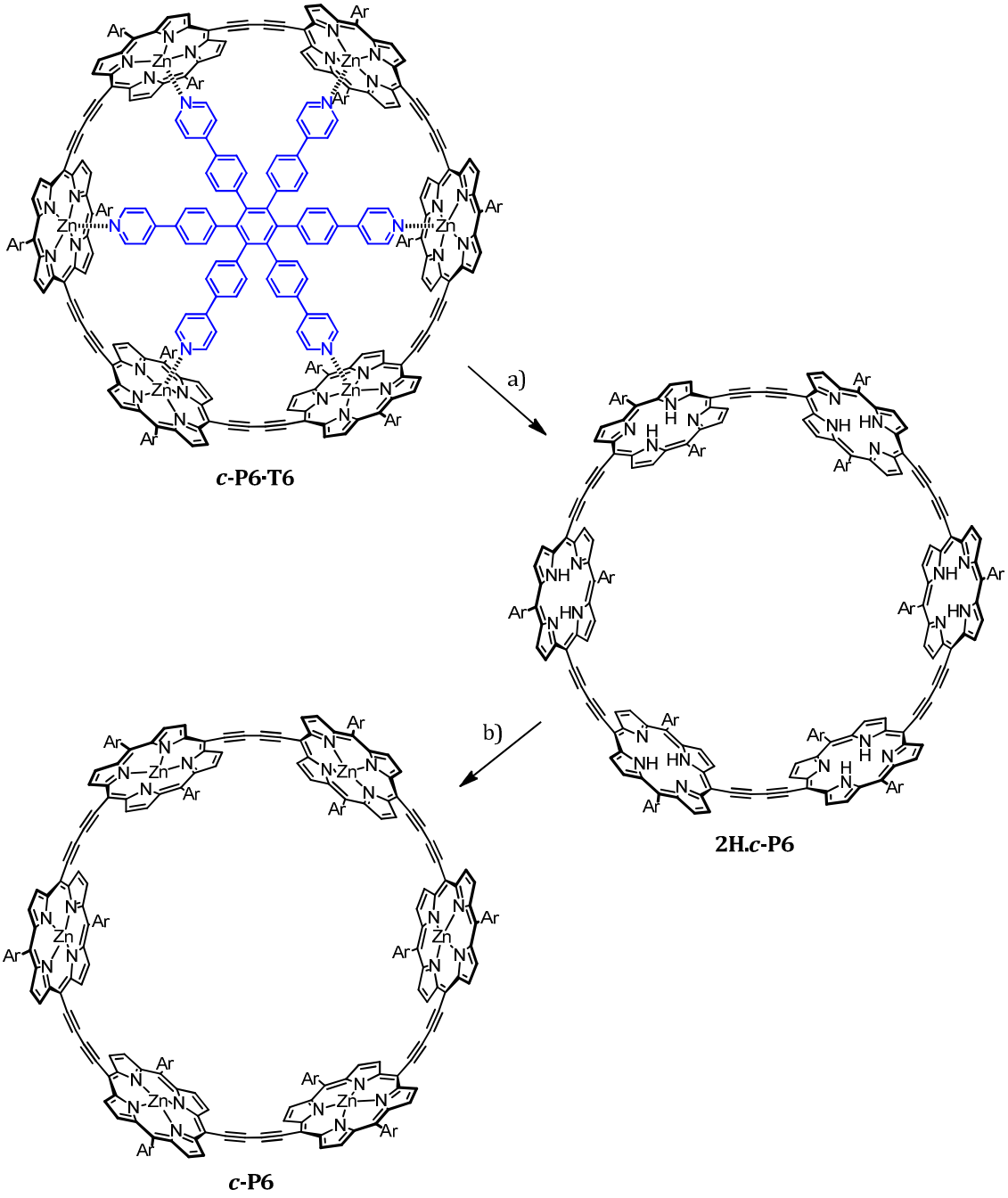

Scheme 5.2 Synthesis of free cyclic hexamer ***c*-P6** by demetallation of cyclic hexamer complex ***c*-P6·T6**: a) 1. 10% *v/v* TFA in $CHCl_3$, 15 min. 2. Pyridine, 15 min, 99%; b) $Zn(OAc)_2$, CH_2Cl_2, MeOH, 35 °C, 2 h, 58%.

The Q bands of ***c*-P6** and **2H.*c*-P6** are broader reflecting the greater conformational flexibility of the rings in the absence of the template. Free base ring **2H.*c*-P6** displays an additional peak

at 661 nm. This is common for free base porphyrins, as desymmetrisation of the porphyrin macrocycle from D_{4h} to D_{2h} results on replacing the central metal ion with two diagonally placed protons.[311][312]

5.2.2 Steady state absorption and emission properties of cyclic oligomers

The absorption and time-integrated emission spectra of templated nanorings ***c*-P6·T6**, ***c*-P8·T8** and ***c*-P12·T12** are shown in Figure 5.8.

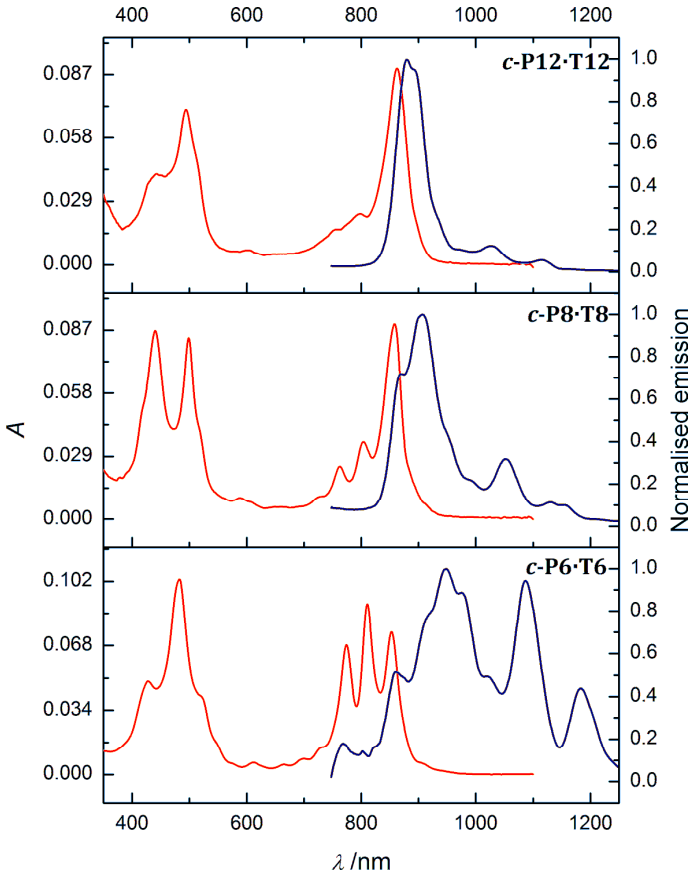

Figure 5.8 Absorption (*red*) and time-integrated emission spectra (*dark blue*) for the cyclic dodecamer complex ***c*-P12·T12** (*top*), cyclic octamer complex ***c*-P8·T8** (*middle*) and cyclic hexamer complex ***c*-P6·T6** (*bottom*) in toluene at 298 K. The emission was recorded after excitation at 489 nm, by Johannes Sprafke.

The Q band of the absorption red-shifted with increasing cyclic oligomer size, and intensified with respect to the Soret band. The emission spectrum blue-shifted with increasing ring size, showing enhanced π-conjugation with decreasing ring size. This initially counterintuitive finding was also observed in theoretical studies of the cyclic paraphenylenes by Wong.[213] It was suggested that the strong deformation of the smaller paraphenylenes distorted the electronic structure, resulting in an increased quinoidal character. The antibonding interactions in the phenyl rings diminish π-overlap, raising the HOMO. Meanwhile, the increased double bond character along the molecular backbone means electronic states are more delocalised, stabilising the LUMO. This overall gives enhanced conjugation for the smaller rings.

Recently, the emission spectrum of ***c*-P6·T6** has been investigated theoretically.[135][244] The geometric constraints of ***c*-P6·T6** meant standard Franck-Condon vibronic progression could not adequately account for the near-IR emission bands observed. It was found that Herzberg-Teller (HT) intensity borrowing[313] by coupling of the symmetry forbidden $S_0 \rightarrow S_1$ transition to an asymmetric vibrational mode, increased the oscillator strength of $S_0 \rightarrow S_1$ transition, while simultaneously decreasing that of the $S_0 \rightarrow S_2$ transition. The calculated HT spectrum matched the low-temperature emission spectrum well. So far, the computational expense of calculating the absorption spectrum of ***c*-P6·T6** means this has not been explored, although it is thought to be a summation of $S_0 \rightarrow S_1$ and $S_0 \rightarrow S_2$ transitions.[244] It is evident from Figure 5.8 that the HT intensity borrowing effect decreases with increasing ring size, as the emission spectra narrow and begin to resemble that of a linear oligomer. Similarly, the complex Q band splitting seen in the absorption spectrum of ***c*-P6·T6** simplifies with ring size, such that the spectrum of ***c*-P12·T12** resembles that of a planarised linear porphyrin oligomer.[62]

The absorption and emission spectra of the free cyclic oligomers ***c*-P6**, ***c*-P8** and ***c*-P12** are shown in Figure 5.9.

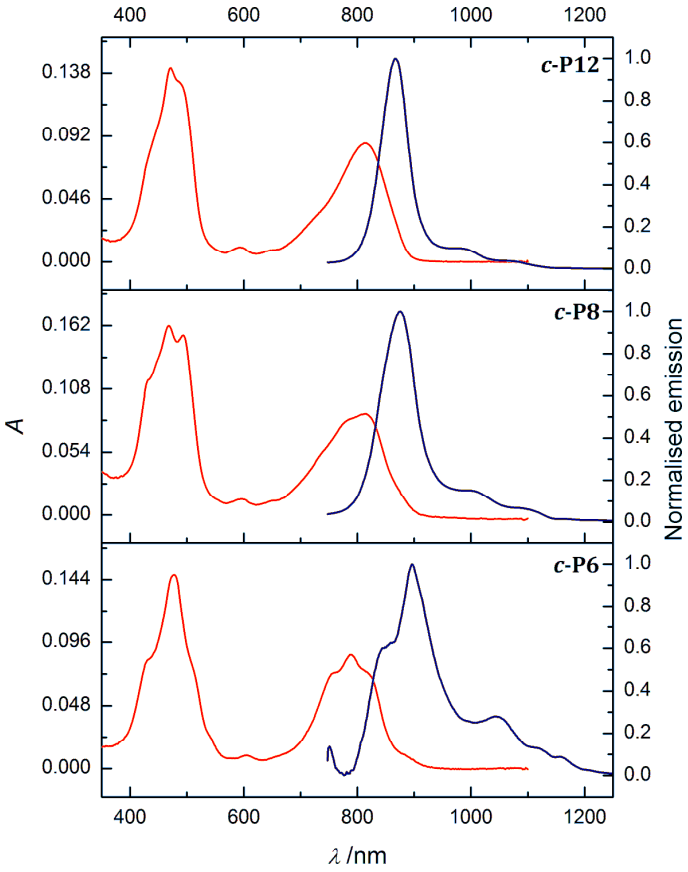

Figure 5.9 Absorption (*red*) and time-integrated emission spectra (*dark blue*) for the cyclic dodecamer ***c*-P12** (*top*), cyclic octamer ***c*-P8** (*middle*) and cyclic hexamer ***c*-P6** (*bottom*) in toluene/1% pyridine at 298 K. The emission was recorded after excitation at 489 nm by Johannes Sprafke.

Similar to the templated cyclic oligomer series ***c*-P*N*·T*N***, emission blue-shifted with increasing ring size, reflecting the enhanced π-conjugation of the smaller rings. Both the Q band absorption and emission were blue-shifted relative to the templated analogue. In the absence of the template, a wide range of torsional angles can be adopted by the porphyrin subunits, partially breaking π-conjugation in the ring. This accounts for the blue shift in the absorption, and also explains the broader, more Gaussian shape of the Q band. The emissive state however, as discussed in Section 5.1.4 and in Chapter 1, has a planarised conformation with small

torsional angles between porphyrin subunits, so a wide range of torsional angles does not account for the observed blue-shifting.

Figure 5.10 compares the absorption and emission spectra for the dodecamer ring in a number of different conformations.

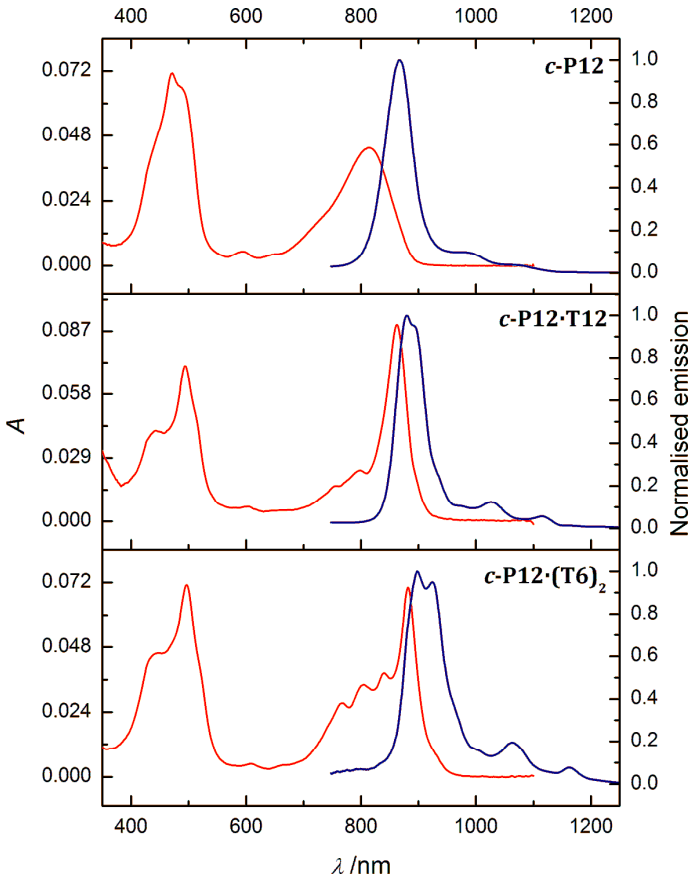

Figure 5.10 Absorption (*red*) and time-integrated emission spectra (*dark blue*) for the cyclic dodecamer family: free ring ***c*-P12** (*top*), classical templated ring ***c*-P12·T12** (*middle*) and figure-of-eight complex ***c*-P12·(T6)$_2$** (*bottom*). The emission was recorded after excitation at 489 nm by Johannes Sprafke. Spectra of ***c*-P12·T12** and ***c*-P12·(T6)$_2$** were recorded in toluene; ***c*-P12** was recorded in toluene/1% pyridine.

The emission spectrum of cyclic dodecamer complex ***c*-P12·T12** is red-shifted by 12 nm (20 meV) relative to the free cyclic dodecamer ***c*-P12**. The spectrum of the figure-of-eight complex

***c*-P12·(T6)$_2$** sees an even greater red shift of 31 nm (49 meV), showing that an increase in strain through the series ***c*-P12** → ***c*-P12·T12** → ***c*-P12·(T6)$_2$** gives an enhancement of π-conjugation due to the greater quinoidal character of the strained cyclic oligomer. This also accounts for the red-shift of emission observed for cyclic hexamer complex ***c*-P6·T6** relative to the free ring ***c*-P6**. The decrease in Stokes shift from 53 nm (93 meV) for ***c*-P12** to 17 nm (28 meV) for ***c*-P12·T12** and 16 nm (25 meV) for ***c*-P12·(T6)$_2$** shows that on coordination of a template, inter-porphyrin torsional motion is suppressed.

The fluorescence quantum yield η rises linearly as a function of the number of porphyrins in the cyclic oligomer, both for the templated and free nanorings (Figure 5.11).

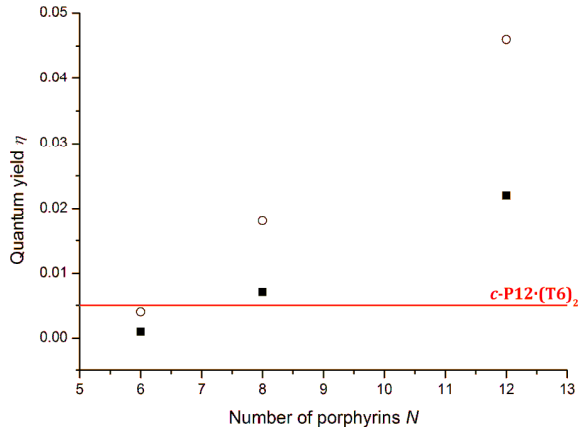

Figure 5.11 Change in the quantum yield η with the number of porphyrins N in a cyclic porphyrin oligomer without template (○) and with template (■). Quantum yields were measured by Johannes Sprafke.

This finding can be rationalised using a simple exciton model, where a transition dipole moment is assigned to each porphyrin subunit (Figure 5.12). As outlined in Chapter 1, these transition dipoles are aligned in a head-to-tail arrangement for the first singlet excitation $S_0 \rightarrow S_1$ for both the linear and cyclic systems. For a linear system, the sum transition dipole moment increases with increasing oligomer size. In cyclic systems, the net transition dipole moment is zero, and the $S_0 \rightarrow S_1$ transition is consequently symmetry-forbidden. Structural

flexibility in larger rings leads to desymmetrisation, so the $S_0 \rightarrow S_1$ transition becomes weakly allowed and the quantum yield increases. The increased flexibility of the free cyclic oligomers relative to the templated rings accounts for the higher observed quantum yields for these.

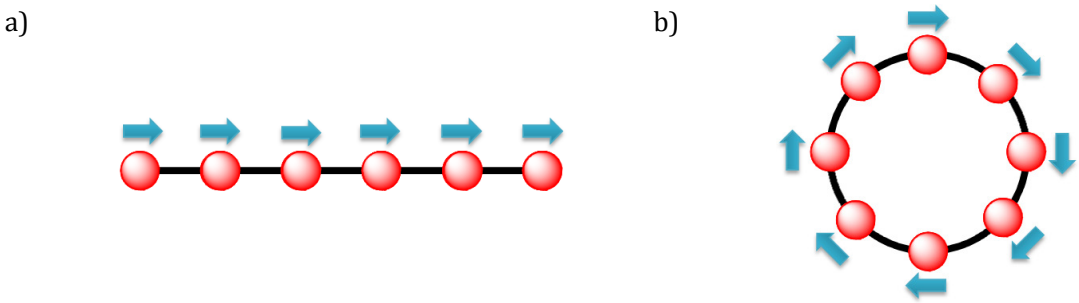

Figure 5.12 A simple exciton model can be used to explain observed quantum yields η in a) linear systems; b) cyclic systems.[128] The arrows indicate the direction of individual transition dipole moments of the chromophores.

Figure-of-eight complex ***c*-P12·(T6)$_2$** exhibits a quantum yield closer to that of the cyclic hexamer ***c*-P6** than cyclic dodecamer ***c*-P12**, reflecting the low flexibility of the complex in solution (Figure 5.11). This agrees with the findings from SAXS studies (Chapter 3), where a simulated PDF from a single molecular model adequately reproduced the experimental data.

A photoluminescence excitation (PLE) map of the cyclic hexamer complex ***c*-P6·T6** recently identified the presence of a highly fluorescent impurity that was not detectable by UV-vis absorption or by ^{1}H NMR.[135][244] These emission peaks were not predicted by simulations of the HT spectrum for ***c*-P6·T6**. The absorption and emission spectra of this impurity strongly resembled that of the linear porphyrin hexamer bent around the hexadentate template ***l*-P6·T6**. The intensity of emission due to this impurity increased with the age of the sample, thus it was concluded that decomposition of the product by reaction of the strained butadiyne links was occurring, breaking the π-conjugation of the ring.

PLE maps of cyclic octamer ***c*-P8**, cyclic octamer complex ***c*-P8·T8**, and cyclic dodecamer complex ***c*-P12·T12** were acquired by Johannes Sprafke to examine for any fluorescent decomposition products (Figure 5.13a–c).

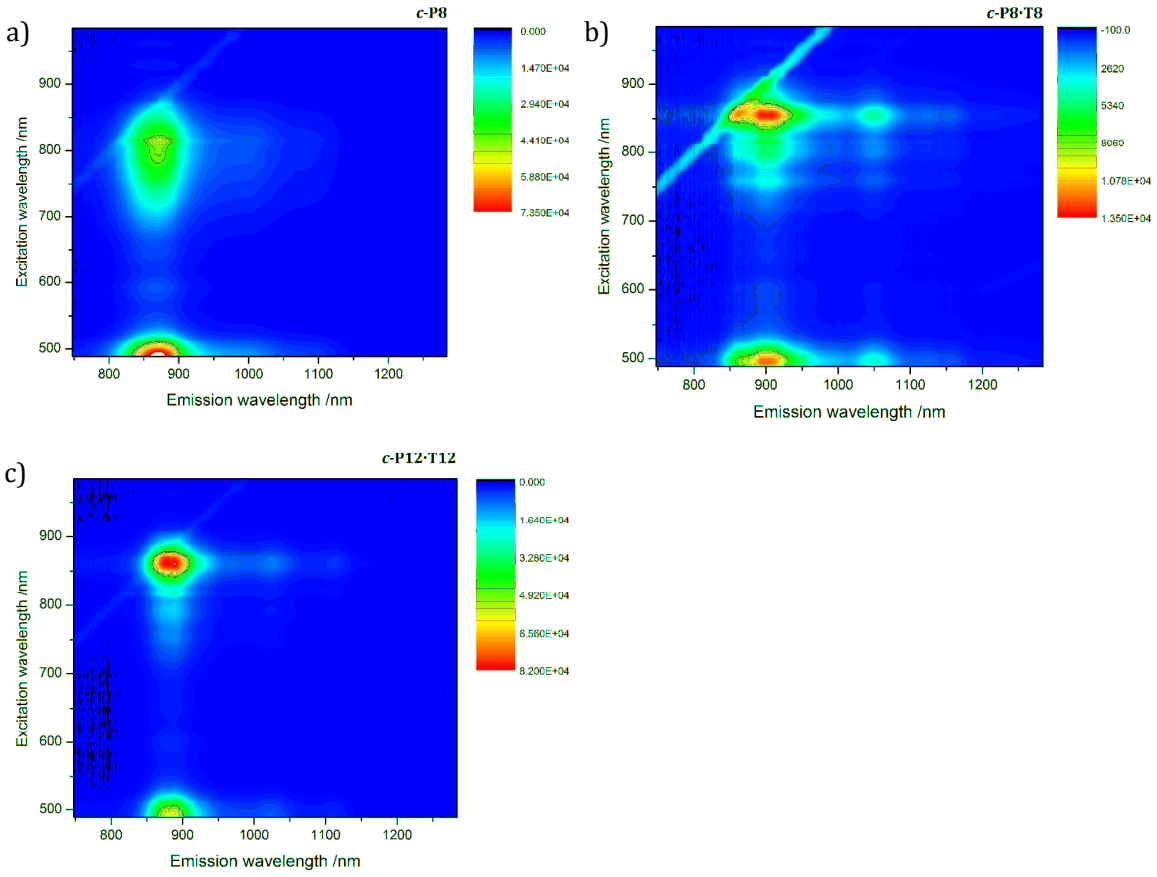

Figure 5.13 Photoluminescence excitation (PLE) map of a) ***c*-P8** in toluene/1% pyridine; b) ***c*-P8·T8** in toluene; c) ***c*-P12·T12** in toluene. Spectra were acquired by Johannes Sprafke.

For each of the samples, excitation over all wavelengths gave identical emission spectra, showing that ***c*-P8**, ***c*-P8·T8** and ***c*-P12·T12** did not contain any emissive impurities.

5.2.3 Femtosecond Photoluminescence Upconversion Spectroscopy

The photoexcitation dynamics of ***c*-P6**, ***c*-P6·T6**, ***c*-P8**, ***c*-P8·T8**, and ***c*-P12** were examined using the photoluminescence upconversion (PL-UC) technique[314] by Wilson Chen, Chaw

Keong Yong and Dr. Laura Herz (Department of Physics, University of Oxford). In this technique, PL emitted by the sample is mixed with an arbitrarily delayed part of the excitation laser (or gate beam) in a non-linear crystal. The resulting photon, of frequency ν_{tot}, has the sum frequency of the gate beam ν_0 and PL frequency ν_F:

$$\upsilon_{\mathrm{tot}} = \upsilon_0 + \upsilon_F \qquad \text{Eq. 31}$$

The intensity of the mixed wave reflects temporal overlap, therefore the time resolution is determined by the width of the excitation pulse rather than the response time of the detector. This technique has advantages over other techniques such as streak camera or time correlated single photon counting (TCSPC), as it offers femtosecond time resolution, allows zero delay to be determined precisely, and has a wide spectral range.

A typical PL-UC setup is shown in Figure 5.14.

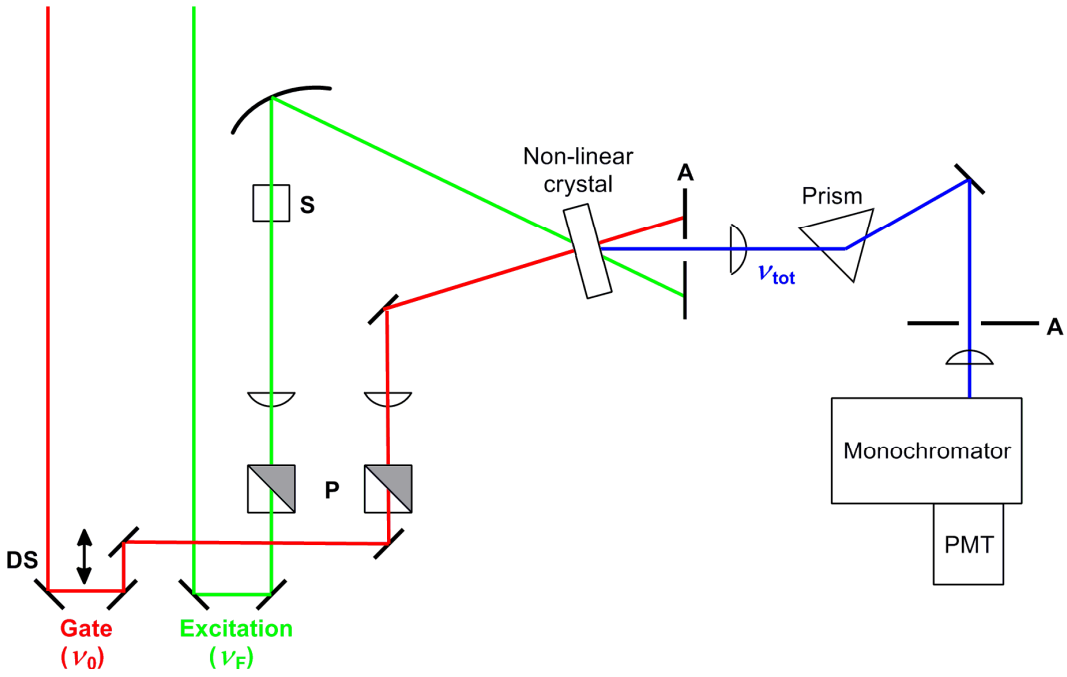

Figure 5.14 A typical femtosecond PL-UC setup. **DS** is the delay stage; **P** is the polarisation control; **S** is the sample; **A** is the aperture; **PMT** is the photomultiplier tube.

The samples, prepared as 1.76×10^{-4} M solutions in toluene (or toluene/1% pyridine for ***c*-P*N***), were excited in a 1.00 cm quartz cuvette with the output beam of a mode-locked Ti:Sapphire laser pumped by a continuous wave Nd-YAG laser (532 nm, 5.5 W). Pulses of 100 fs at a repetition rate of 80 MHz were used. A photon energy of 1.61 eV (770 nm) was chosen to excite in the Q band region of the cyclic oligomers, which was the lowest possible photon energy of the laser system. The gate beam entered the cell close to the front surface in order to avoid artifacts arising from self-absorption. The PL of the sample was upconverted by the vertically polarised gate beam on a β-barium borate (BBO) crystal.[315] The gate beam phase was modified by a delay stage to scan the whole time interval. The collected photon was dispersed in a monochromator and detected by a liquid nitrogen-cooled charged coupled device (CCD). Only the vertical polarisation component $I_{\perp}$ of the PL was upconverted using this setup. In order to detect the parallel component $I_{\parallel}$, the polarisation of the gate beam was changed using a half-wave plate and a Glan-Thompson polariser.

The dynamics of cyclic oligomers ***c*-P6·T6**, ***c*-P8**, ***c*-P8·T8** and ***c*-P12** were studied using polarised upconversion by measuring intensity of emission polarised parallel ($I_{\parallel}$) and perpendicular ($I_{\perp}$) to the excitation polarisation. Short time polarised emission data for the four samples are shown in Figure 5.15a–d.

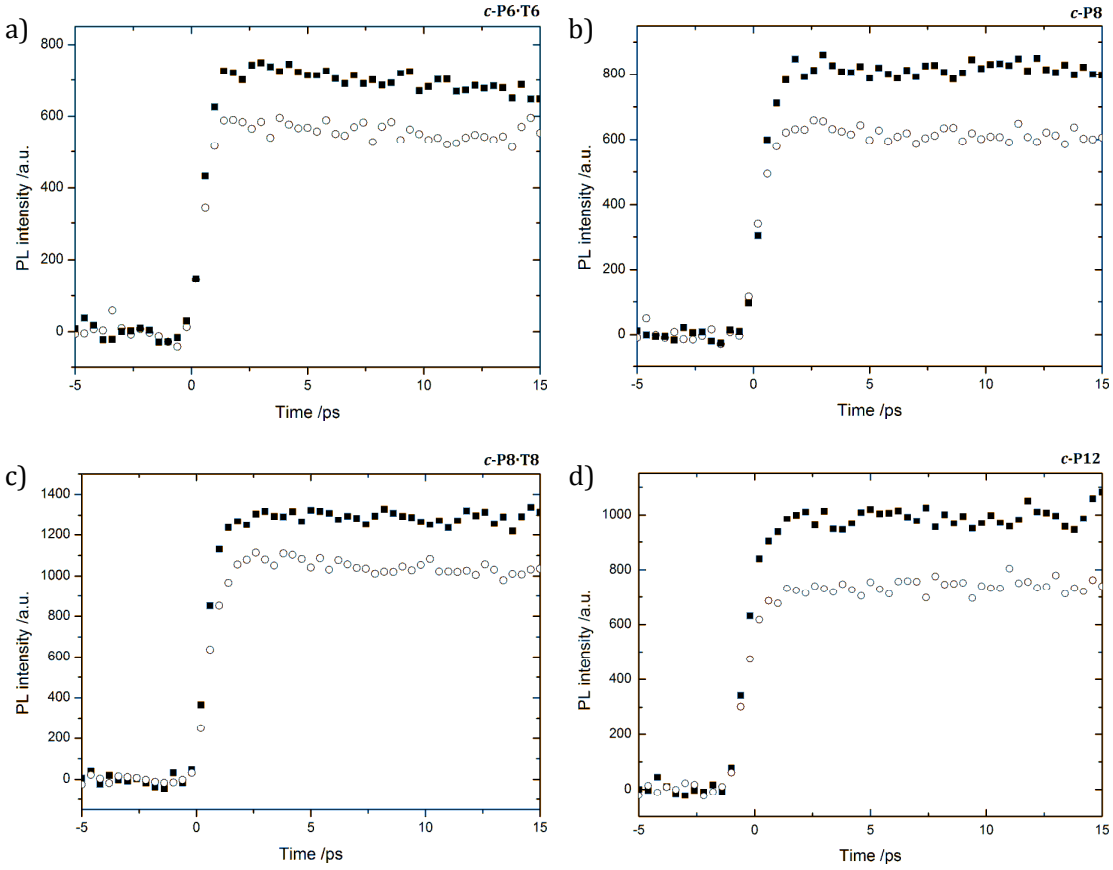

Figure 5.15 Short time PL intensity with vertically polarised illumination (■) and horizontally polarised illumination (○) at 770 nm for a) cyclic hexamer complex ***c*-P6·T6** (laser power 9 mW in 5 s, detection at 945 nm); b) cyclic octamer ***c*-P8** (laser power 7 mW in 5 s, detection at 886 nm); c) cyclic octamer complex ***c*-P8·T8** (laser power 9 mW in 5s, detection at 925 nm); d) cyclic dodecamer ***c*-P12** (laser power 7 mW in 5s, detection at 894 nm).

The total excitation lifetime τ was calculated by fitting of the long time PL emission decay. The radiative lifetime τ_R could be calculated from the total excitation lifetime τ and the quantum yield η:

$$\tau_R = \frac{\tau}{\eta} \qquad \text{Eq. 32}$$

The non-radiative lifetime τ_{NR} could be calculated from the following equation:

$$\tau_{NR} = \tau(1-\eta)^{-1} \qquad \text{Eq. 33}$$

Excitation lifetime τ and decay rate κ are related:

$$\kappa = \frac{1}{\tau} \qquad \text{Eq. 34}$$

The total excitation lifetime, radiative and non-radiative lifetimes of the cyclic oligomers are plotted in Figure 5.16.

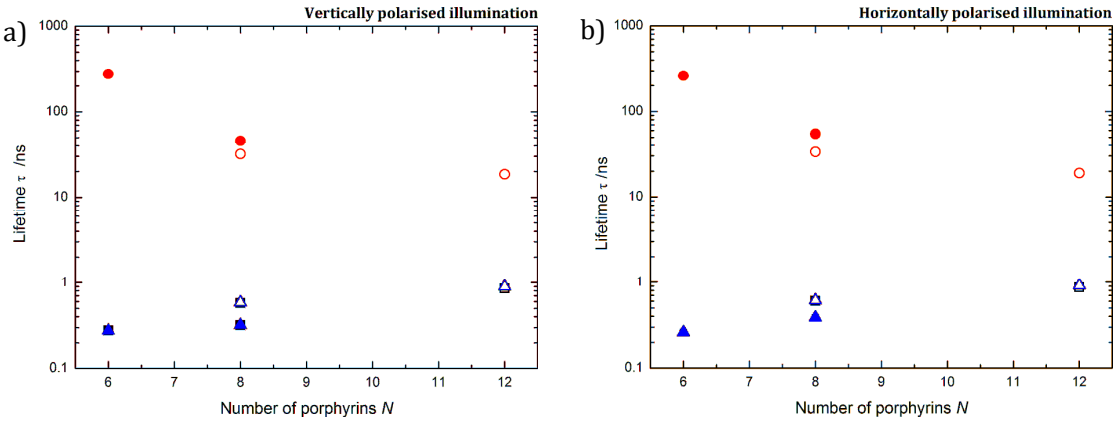

Figure 5.16. Total excitation lifetime τ (*black squares*), radiative lifetime τ_R (*red circles*) and non-radiative lifetime τ_{NR} (*blue triangles*) as a function of porphyrin number *N* measured for a) vertically polarised illumination; b) horizontally polarised illumination. Free cyclic oligomers ***c*-P*N***** are marked as hollow points; templated cyclic oligomers ***c*-P*N*·T*N*** are marked as solid points.

As can be seen in Figure 5.16, the excited state lifetime is dominated by the non-radiative decay pathway, which is expected for a chromophore with low quantum yield. As discussed in Section 5.2.2, structural flexibility in larger rings makes the optically forbidden $S_0 \rightarrow S_1$ transition partially allowed, so larger rings have higher quantum yields. From Equation 32 it can therefore be seen that larger rings have shorter radiative lifetimes. The excited state lifetime is shortest for the smaller rings, with ***c*-P6·T6** having a lifetime of 0.28 ns, increasing

to 0.85 ns for ***c*-P12**. The smaller ring size and enhanced π-conjugation of ***c*-P6·T6** relative to ***c*-P12** may increase the probability of electron-hole recombination. Comparison of free cyclic octamer ***c*-P8** with the corresponding template complex ***c*-P8·T8** shows the template has very little effect on the measured excitation lifetime.

Time resolved PL anisotropy over the first 15 ps after excitation for cyclic oligomers ***c*-P6**, ***c*-P6·T6**, ***c*-P8**, ***c*-P8·T8** and ***c*-P12** is shown in Figure 5.17.

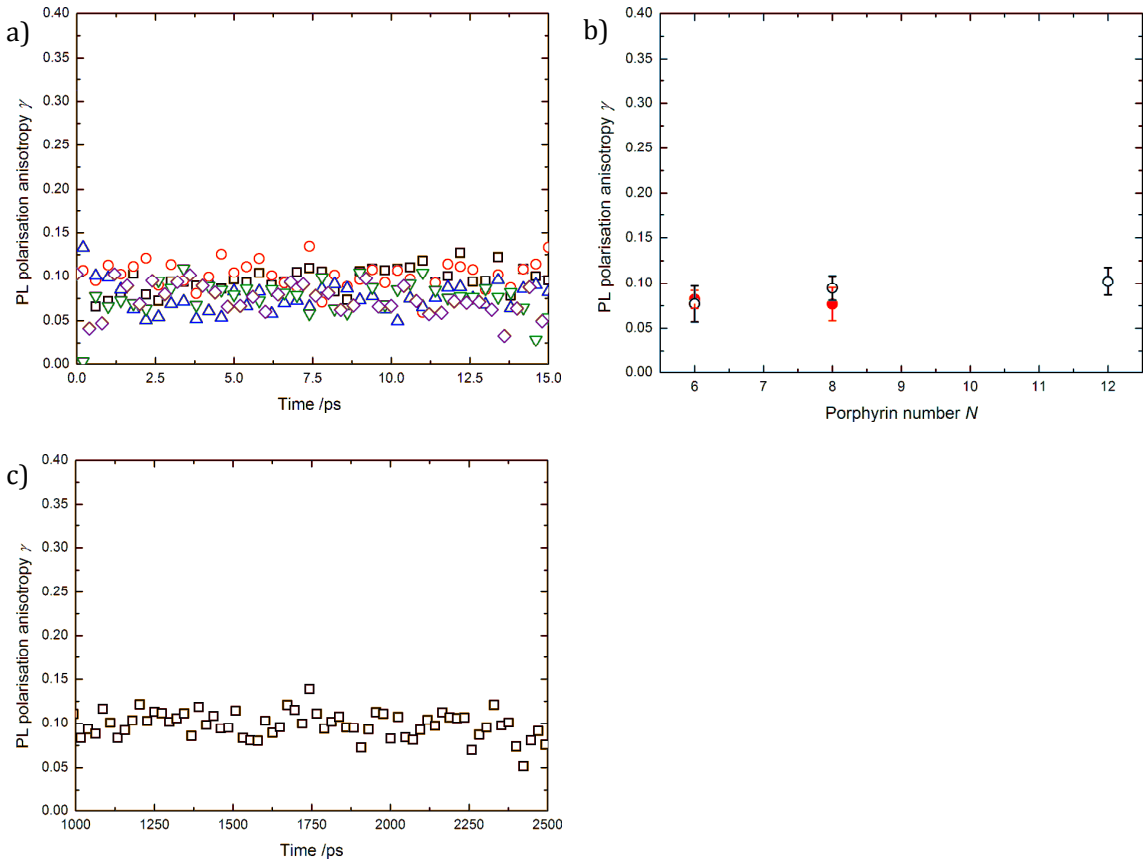

Figure 5.17 a) PL anisotropy as a function of time after excitation at 770 nm for cyclic hexamer ***c*-P6** (◇, detection at 890 nm), cyclic hexamer complex ***c*-P6·T6** (▽, detection at 945 nm), cyclic octamer ***c*-P8** (□, detection at 886 nm), cyclic octamer complex ***c*-P8·T8** (△, detection at 925 nm) and cyclic dodecamer ***c*-P12** (○, detection at 894 nm); b) Initial PL anisotropy γ_0 as a function of ring size for templated (●) and non-templated (○) porphyrin rings; c) Long time PL anisotropy $\gamma_{(t)}$ of cyclic dodecamer ***c*-P12**.

Within experimental error, an initial anisotropy γ_0 of 0.1 was obtained for all the cyclic oligomers, which was identical to that of the steady state anisotropy γ_∞ (shown for ***c*-P12** in Figure 5.17c). This indicated that ultrafast PL depolarisation due to complete electronic delocalisation over the entire oligomer backbone occurred well within the 800 fs resolution of the instrument. This is identical to what was found for ***l*-P8^{C8}·T8**, and is reminiscent of the excitation transfer dynamics seen in naturally occurring light harvesting systems. The excitation may subsequently self-localise through geometric relaxation, which has been shown to occur in B850 within a few hundred femtoseconds.[316]

5.2.4 Conclusions and outlook

The absorption and emission spectra for the free and templated cyclic oligomer series ***c*-P*N*** and ***c*-P*N*·T*N*** (*N* = 6, 8, 12) have been compared and show increasing π-conjugation for smaller values of *N*. The greater conformational flexibility of cyclic porphyrin oligomers in the absence of a template leads to partially allowed $S_0 \rightarrow S_1$ transitions, thus increased quantum yields for these systems. The same effect is seen for increasing ring size in ***c*-P*N***. Figure-of-eight complex ***c*-P12·(T6)$_2$** is shown to have a similar quantum yield to that of ***c*-P6** and ***c*-P6·T6**, reflecting the increased strain energy of the cyclic oligomer from bending around a hexadentate template. Low quantum yields result from a long radiative lifetime; cyclic hexamer complex ***c*-P6·T6** with a quantum yield η of 1×10^{-3}, has a relatively long radiative lifetime τ_R of 277 ns. Femtosecond PL anisotropy experiments were carried out on ***c*-P6**, ***c*-P6·T6**, ***c*-P8**, ***c*-P8·T8** and ***c*-P12**. All of the cyclic oligomer systems examined had an initial anisotropy of γ_0 of 0.1, showing that complete delocalisation of the excitation over the circumference of the porphyrin ring occurred within the 800 fs resolution of the system. Analogies were drawn between the cyclic porphyrin systems and naturally occurring light harvesting systems, where complete depolarisation of fluorescence occurs on a ~110 fs timescale.

Due to earlier problems with the laser system, experiments still continue to examine the PL anisotropy of figure-of-eight complex ***c*-P12·(T6)$_2$**. It will be interesting to see whether the properties of ***c*-P12·(T6)$_2$** resemble that of the cyclic dodecamer ***c*-P12**, or whether the strain of the complex makes the behaviour more like the cyclic hexamer series.

Two dimensional real-space analysis of density matrices for the $S_0 \rightarrow S_1$ transition in cyclic and linear paraphenylenes has been calculated by Wong.[213] It was shown in linear systems that the electron-hole pair became localised in the centre of the molecule away from the end groups. In cyclic systems however, electron hole states were found to delocalise over the entire circumference of the ring up to ring sizes of N = 18. It would therefore be interesting with the recent synthesis of cyclic tetracosamer ***c*-P24** (Chapter 4) and rings ***c*-P16** and ***c*-P18** by Dmitry Kondratuk, to investigate whether in these larger systems, ultrafast delocalisation of the excitation over the entire circumference of the ring continues to occur. It may be that a size limit is reached, and in these higher rings, the exciton becomes localised on part of the ring.

The overall time resolution of 800 fs for the system was predominately limited by the size of the imaged excitation spot in the solution. Reducing the optical path length from 1.00 cm to 0.2 cm could improve the temporal resolution of the system to 200 fs, which may allow fluorescence anisotropy decay of the cyclic oligomers to be observed. This is currently being investigated.

Chapter Six
Experimental

6.1 General procedures

THF, diethyl ether and 1,4-dioxane were distilled from Na / benzophenone under N_2. Dry NEt_3, diisopropylamine and piperidine were distilled from CaH_2. Dry CH_2Cl_2 and toluene were obtained by passing through alumina under N_2 pressure. Pyrrole was distilled under reduced pressure. For cyclisation reactions, $CHCl_3$ stored over potassium carbonate was used. Copper(I) chloride and palladium tetrakis(triphenylphosphine) were freshly prepared using the procedures below. All other reagents were used as commercially supplied.

Flash column chromatography was carried out on silica gel 60 under positive pressure. Analytical thin layer chromatography (TLC) was carried out on Merck© aluminium backed silica gel 60 F254 plates. Visualisation, when required, was achieved using UV light. Where mixtures of solvents were used ratios are reported by volume. Size-exclusion chromatography was carried out under gravity using cross-linked polystyrene Bio-Beads® SX-1 (200 – 400 mesh).

HPLC analysis and preparation was carried out on a Hitachi/VWR LaChrom ELITE HPLC system equipped with L-2130 quaternary pump, L-2455 diode array detector, L-2200 autosampler, L-2350 column oven and Foxy Jr. fraction collector. Analytical HPLC was carried out using either a 5 μm eclipse XDB-C8 4.6 × 150 mm (Agilent) analytical column, ACE 5 μm CN 4.6 × 150 mm, or ACE 5 μm SIL 4.6 × 150 mm column at 1 mL min^{-1} flow.

Analytical GPC was carried out using PLgel 3 μm Mixed-E columns (2 × 300 mm lengths, 7.5 mm diameter) from Polymer Laboratories using 1 mL min^{-1} flow on the HPLC system. Preparative GPC was carried out on a PLGel 10 μm 500 Å 600 × 25 mm column, a PLgel 10 μm 500 Å 300 × 25 mm column, and a PLgel 10 μm 10^3 Å 300 × 25 mm column connected in series. When used, THF and pyridine were pre-distilled.

NMR spectra were recorded on either a Bruker DPX250 (250/62.5 MHz), Bruker DPX400 (400 MHz), Bruker AVANCE AV400 (400/100 MHz), Bruker AVC500 (500/125 MHz) cryoprobe or a Bruker AVIII 700 (700 MHz) cryoprobe. All chemical shifts are given in parts per million relative to residual protonated solvent.

UV-Vis-NIR spectra were recorded on a Perkin-Elmer Lambda 20 spectrometer or a Perkin-Elmer Lambda 25 spectrometer. The experimental data were fit to a theoretically calculated curve using Origin™ software. Fully-corrected emission spectra were measured using a custom-build system consisting of a 75 W xenon lamp focussed into a monochromator, which then illuminated the sample in a quartz fluorescence cell. A silicon photodiode was used to normalise the incident excitation intensities. Luminescence from the sample was collected at 90° to the excitation beam and focussed into a spectrograph fitted with a liquid nitrogen cooled InGaAs photodiode array. The spectral response of the detector was corrected by using a standard tungsten lamp. The linear hexamer ***l*-P6** (η = 8.0% in toluene with 1% pyridine)[304] was used as a standard for determination of fluorescence quantum yields.

Elemental analysis was carried out by Dr. Stephen Boyer at London Metropolitan University.

The majority of MALDI-ToF spectra were recorded on a Micromass ToF Spec 2E at Oxford. MALDI-ToF MS conducted at Swansea used the Applied Systems Voyager-DE-STR. Only molecular ions and major peaks are reported.

The synchrotron radiation small angle X-ray scattering (SAXS) data were collected using standard procedures on the I22 beamline at Diamond Light Source equipped with a photon counting detector. The beam was focussed onto the detector placed at a distance of 1.25 m from the sample cell. The covered range of momentum transfer was $0.03 < q < 1.0$ Å^{-1} ($q = 4\pi \sin(\theta)/\lambda$ where 2θ is the scattering angle and λ = 1.00 Å is the X-ray wavelength). The data were normalised to the intensity of the incident beam; the scattering of the solvent was

subtracted using an in-house program. To check for radiation damage and aggregation during the SAXS experiment, the data were collected in 10 successive 60 s frames. All SAXS measurements were performed in either toluene or 1% pyridine in toluene at known concentrations ($\sim 10^{-4}$ M) in a solution cell with mica windows.

6.1.1 Synthesis of catalysts

$Pd(PPh_3)_4$[317]

Palladium(II) chloride (0.20 g, 1.13 mmol) and triphenylphosphine (1.48 g, 5.64 mmol) were suspended in DMSO (12.0 mL) and the flask was flushed with argon. The suspension was heated to 160 °C to dissolve and hydrazine (0.22 mL, 4.51 mmol) was added rapidly. The solution was cooled and the resulting precipitate was filtered, washed with ethanol (2 × 2.0 mL) and diethyl ether (2 × 2.0 mL) and dried under vacuum to give a mustard yellow crystalline solid (1.12 g, 86%). The catalyst was stored in the freezer under a protective argon atmosphere.

CuCl[318]

An aqueous solution of copper(II) chloride (10.0 g, 74.4 mmol in 15.0 mL) was added to an aqueous solution of sodium sulfite (7.60 g, 60.3 mmol in 50.0 mL) and the resulting suspension immediately poured into a solution of sodium sulfite (1.00 g, 7.44 mmol) and $HCl_{(aq)}$ (37% solution in water, 2.0 mL) in water (1.0 L). The precipitate was filtered, and washed sequentially with a solution of sodium sulfite (0.50 g, 3.72 mmol), $HCl_{(aq)}$ (37% solution in water, 1.0 mL) in water (500 mL), acetic acid (125 mL), ethanol (125 mL) and diethyl ether (125 mL) before the solid was allowed to dry. The resulting white powder (5.06 g, 76%) was stored under N_2 in the freezer.

6.2 Synthesis of previously known compounds

1,2-bis(4-bromophenyl)ethyne 34

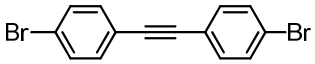

This compound was prepared by adaptation of a published procedure.[144]

Sodium metal (4.30 g, 0.19 mol) was washed with 40/60 petroleum ether to remove any protective oil, then sonicated in ethanol (70.0 mL) under an inert atmosphere until homogeneous. 1,2-dibromo-1,2-bis(4-bromophenyl)ethane **33** (4.60 g, 9.32 mmol) was added and the mixture heated to reflux for 1 h. The crude product was precipitated on cooling by addition of water (160 mL). Recrystallisation in hot toluene gave white crystals (2.26 g, 73%); δ_H (400 MHz, $CDCl_3$, 298 K) 7.50 (d, 4H, J = 8.4 Hz, Ar-H^{ortho}), 7.38 (d, 4H, J = 8.4 Hz, Ar-H^{meta}); Lit.[319] δ_H (400 MHz, $CDCl_3$) 7.48 (d, 4H, J = 8.5 Hz), 7.37 (d, 4H, J = 8.5 Hz).

1,2-bis(4'-(trimethylsilyl)biphenyl-4-yl)ethyne 28

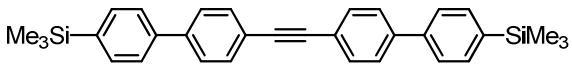

This compound was prepared according to published procedure.[138]

1,2-Bis(4-bromophenyl)ethyne **34** (0.50 g, 1.50 mmol), 4-(trimethylsilyl)phenylboronic acid **99** (0.73 g, 3.74 mmol) and $Pd(PPh_3)_4$ (0.17 g, 150 μmol) were placed under an argon atmosphere. Argon saturated toluene (30.0 mL), ethanol (4.0 mL) and aqueous potassium carbonate solution (2.0 M, 10.0 mL) were added, and the mixture freeze-thaw degassed. After stirring at 50 °C for 1 d, the product was crystallised out by addition of ethyl acetate (50.0 mL) to give a white solid (0.59 mg, 83%); δ_H (400 MHz, $CDCl_3$, 298 K) 7.62 (s, 16H, Ar-*H*), 0.32 (s, 18H, Si(CH_3)$_3$); Lit.[138] δ_H (400 MHz, $CDCl_3$) 7.62 (s, 16H), 0.31 (s, 18H).

1,2,3,4,5,6-hexakis[4-(4-trimethylsilylphenyl)phenyl]benzene 35

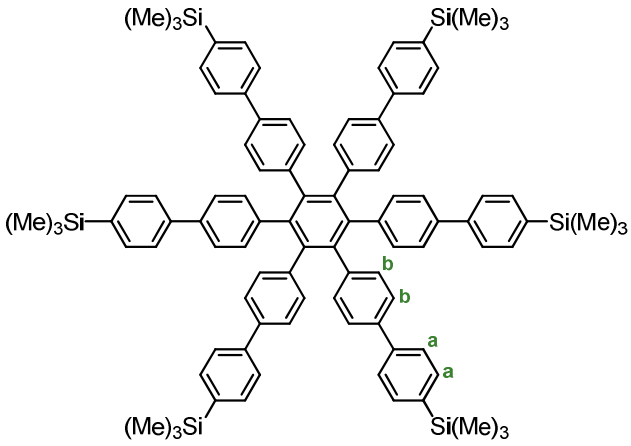

This compound was prepared according to published procedure.[138]

1,2-Bis(4'-(trimethylsilyl)biphenyl-4-yl)ethyne **28** (0.34 g, 0.72 mmol) and dicobalt octacarbonyl (0.12 g, 0.36 mmol) was refluxed at 125 °C in 1,4-dioxane (40.0 mL) for 2 d. The reaction mixture was cooled, filtered through Celite to remove the catalyst, and solvents removed under reduced pressure. The product was precipitated from CH_2Cl_2/MeOH to give a white solid (0.18 g, 54%); δ_H (400 MHz, $CDCl_3$, 298 K) 7.47 and 7.41 (AA'BB' system, 24H, a), 7.16 and 6.95 (AA'BB' system, 24H, b), 0.24 (s, 54H, Si(CH_3)$_3$); *m/z* (ESI MS+) 1441.62 ([M+NH_4]$^{\bullet+}$, $C_{96}H_{106}NSi_6$, requires 1441.70); Lit.[138] δ_H (400 MHz, $CDCl_3$) 7.46 and 7.41 (AA'BB' system, 24H), 7.16 and 6.95 (AA'BB' system, 24H), 0.24 (s, 54H).

1,2,3,4,5,6-hexakis[4-(4-iodophenyl)phenyl]benzene 27

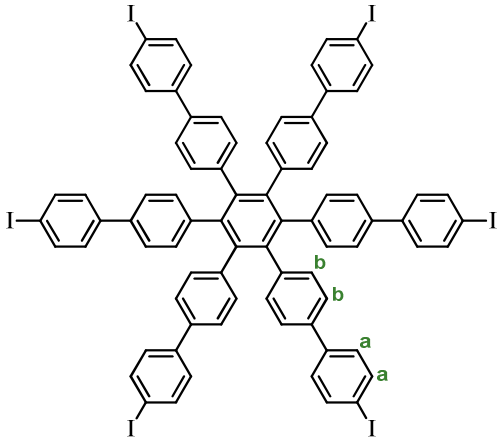

This compound was prepared according to published procedure.[138]

Iodine monochloride (1.0 M solution in CH_2Cl_2, 903 µL, 0.90 mmol) was added dropwise to a solution of 1,2,3,4,5,6-hexakis[4-(4-trimethylsilylphenyl)phenyl]benzene **35** (184 mg, 0.13 mmol) in CH_2Cl_2 (11.0 mL). After stirring at room temperature overnight, methanol was added, and the resulting precipitate was filtered to give a white powder (193 mg, 85%); δ_H (400 MHz, $CDCl_3$, 298 K) 7.65 and 7.15 (AA'BB' system, 24H, a), 7.11 and 6.93 (AA'BB' system, 24H, b); Lit.[138] δ_H (400 MHz, $CDCl_3$) 7.63 and 7.14 (AA'BB' system, 24H), 7.10 and 6.93 (AA'BB' system, 24H).

3-hydroxy-4-iodobenzoic acid 37

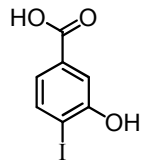

This compound was prepared according to published procedures.[131]

WARNING: NITROGEN TRIIODIDE MAY BE FORMED- TOUCH SENSITIVE AND EXPLOSIVE IN THE DRY STATE. SLOW ADDITION OF IODINE IS NECESSARY.

An aqueous solution (150 mL) of potassium iodide (26.4 g, 159 mmol) and iodine (33.8 g, 133 mmol) was added dropwise over a period of 2 h to a solution of 3-hydroxybenzoic acid (20.0 g, 145 mmol) in concentrated aqueous ammonia (300 mL) heated to 50 °C. The reaction mixture was stirred for an additional 25 min before acidification with concentrated aqueous hydrochloric acid. The resulting precipitate was filtered, and recrystallised at 100 °C with water/ethanol (5:1, 290 mL) to give a white powder (27.5 g, 71%); δ_H (400 MHz, MeOD, 298 K) 7.80 (d, 1H, J = 8.0 Hz, Ar-H^5), 7.46 (d, 1H, J = 1.7 Hz, Ar-H^2), 7.23 (dd, 1H, J_1 = 8.2 Hz, J_2 = 1.9 Hz, Ar-H^6); Lit.[131] δ_H (250 MHz, DMSO-d_6) 7.81 (d, 1H, J = 8.1 Hz), 7.44 (d, 1H, J = 8.1 Hz), 7.14 (m, 1H).

Butyl 3-butoxy-4-iodobenzoate 38

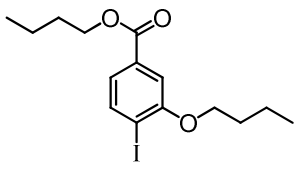

This compound was prepared according to published procedures.[131]

A solution of 3-hydroxy-4-iodobenzoic acid **37** (11.6 g, 44.0 mmol), *n*-butyl bromide (16.9 g, 123 mmol), 18-crown-6 (1.22 g, 8.78 mmol) and potassium carbonate (32.5 g, 123 mmol) in acetone (290 mL) was refluxed for 2 d. After cooling, the reaction mixture was filtered, and solvent removed by evaporation. The crude solid was dissolved in diethyl ether, washed with water, and solvent removed to give a yellow oil (16.3 g, 99%); δ_H (400 MHz, $CDCl_3$, 298 K) 7.83 (d, 1H, J = 8.0 Hz, Ar-H^5), 7.42 (d, 1H, J = 1.7 Hz, Ar-H^2), 7.34 (dd, 1H, J_1 = 8.2 Hz, J_2 = 1.9 Hz, Ar-H^6), 4.31 (t, 2H, J = 6.7 Hz, Ar-OCH_2), 4.07 (t, 2H, J = 6.3 Hz, CO_2CH_2), 1.89–1.81 (m, 2H, CH_2), 1.79–1.72 (m, 2H, CH_2), 1.62–1.53 (m, 2H, CH_2), 1.52–1.42 (m, 2H, CH_2), 1.03–0.97 (m, 6H, CH_3); Lit.[131] δ_H (400 MHz, $CDCl_3$) 7.84 (m, 1H), 7.43 (d, 1H, J = 1.8 Hz), 7.35 (m, 1H), 4.32 (t, 2H, J = 6.7 Hz), 4.09 (t, 1H, J = 6.3 Hz), 1.86–1.72 (m, 4H), 1.62–1.43 (m, 4H), 1.03–0.94 (m, 6H).

(3-butoxy-4-iodophenyl)methanol 39

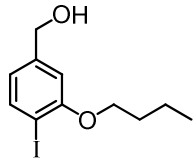

This compound was prepared according to published procedures.[131]

DIBAL (25 *wt*% solution in toluene, 22.5 mL, 132 mmol) was added dropwise to a solution of butyl 3-butoxy-4-iodobenzoate **38** (16.5 g, 44.0 mmol) in toluene (215 mL) at –78 °C under an argon atmosphere. The reaction mixture was stirred for a further hour at –78 °C, before being warmed to 0 °C and quenched with aqueous hydrochloric acid (10 % *v/v*). The mixture was washed with water, and solvent removed to yield a viscous yellow oil (9.90 g, 74%); δ_H (400 MHz, $CDCl_3$, 298 K) 7.71 (d, 1H, J = 7.8 Hz, Ar-H^5), 6.84 (d, 1H, J = 1.5 Hz, Ar-H^2), 6.67 (dd, 1H, J_1 = 8.0 Hz, J_2 = 1.7 Hz, Ar-H^6), 4.64 (d, 2H, J = 5.5 Hz, Ar-CH_2), 4.01 (t, 2H, J = 6.5 Hz, Ar-OCH_2), 1.87–1.79 (m, 2H, CH_2), 1.61–1.52 (m, 2H, CH_2), 0.98 (t, 3H, J = 7.3 Hz, CH_3); Lit.[131] δ_H (400

MHz, $CDCl_3$) 7.73 (d, 1H, *J* = 8.0 Hz), 6.85 (s, 1H), 6.68 (m, 1H), 4.65 (s, 2H), 4.03 (t, 1H, *J* = 6.4 Hz), 1.86–1.80 (m, 2H), 1.62–1.52 (m, 2H), 1.00 (t, 3H, *J* = 7.4 Hz).

3-butoxy-4-iodobenzaldehyde 40

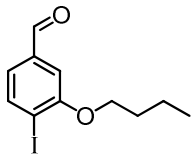

This compound was prepared according to published procedures.[131]

(3-Butoxy-4-iodophenyl)methanol **39** (4.35 g, 14.2 mmol) was added to a solution of pyridinium chlorochromate (6.12 g, 28.4 mmol) in CH_2Cl_2 (25.0 mL). The reaction mixture was stirred at room temperature for 2 h, and the solvent was removed to give a black tarry oil. This was transferred to a short silica plug with the aid of pre-adsorption onto dry silica and eluted with CH_2Cl_2 to give a yellow oil (4.35 g, 99%); δ_H (400 MHz, $CDCl_3$, 298 K) 9.94 (s, 1H, C*H*O), 7.98 (d, 1H, *J* = 7.8 Hz, Ar-*H*^{5}), 7.26 (d, 1H, *J* = 1.7 Hz, Ar-*H*^{2}), 7.16 (dd, 1H, J_1 = 7.8 Hz, J_2 = 1.7 Hz, Ar-*H*^{6}), 4.09 (t, 2H, *J* = 6.3 Hz, Ar-OCH_2), 1.89–1.82 (m, 2H, CH_2), 1.60–1.55 (m, 2H, CH_2), 0.99 (t, 3H, *J* = 7.3 Hz, CH_3); Lit.[4] δ_H (200 MHz, $CDCl_3$) 9.95 (s, 1H), 7.99 (d, 1H, *J* = 7.9 Hz), 7.19–7.15 (m, 2H), 4.10 (t, 2H, *J* = 6.3 Hz), 1.94–1.80 (m, 2H), 1.67–1.49 (m, 2H), 1.02 (t, 3H, *J* = 7.3 Hz).

2-butoxy-4-(chloromethyl)-1-iodobenzene 41

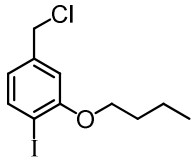

This compound was prepared according to published procedures.[131]

Thionyl chloride (2.9 mL, 40.4 mmol) was added dropwise to a solution of (3-butoxy-4-iodophenyl)methanol **39** (4.81 g, 16.2 mmol) in CH_2Cl_2 (100 mL) at room temperature. The reaction mixture was stirred for 1 h; a silica column (1:3 $CHCl_3$: 40/60 petroleum ether, R_f 0.45) of the crude material yielded a pale yellow oil (4.06 g, 77%); δ_H (400 MHz, $CDCl_3$, 298 K) 7.73 (d, 1H, J = 8.0 Hz, Ar-H^5), 6.82 (d, 1H, J = 1.9 Hz, Ar-H^2), 6.71 (dd, 1H, J_1 = 7.8 Hz, J_2 = 1.7 Hz, Ar-H^6), 4.53 (s, 2H, Ar-CH_2Cl), 4.03 (t, 2H, J = 6.3 Hz, Ar-OCH_2), 1.87–1.80 (m, 2H, CH_2), 1.62–1.53 (m, 2H, CH_2), 0.99 (t, 3H, J = 7.3 Hz, CH_3); Lit.[131] δ_H (200 MHz, $CDCl_3$) 7.74 (d, 1H, J = 7.9 Hz), 6.83 (d, 1H, J = 1.9 Hz), 6.72 (m, 1H), 4.53 (s, 2H), 4.04 (t, 2H, J = 6.3 Hz), 1.91–1.78 (m, 2H), 1.67–1.48 (m, 2H), 1.01 (t, 3H, J = 7.3 Hz).

2-(3-butoxy-4-iodophenyl)acetonitrile 42

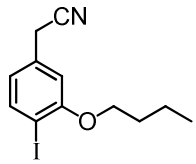

This compound was prepared according to published procedures.[131]

WARNING: NaCN IS HIGHLY TOXIC. NaCN IN DMSO IS VERY TOXIC AND CAN PASS THROUGH NITRILE GLOVES AND SKIN.

DISPOSAL: ALL CONTAMINATED MATERIALS AND RESIDUES SHOULD BE TREATED WITH SODIUM HYPOCHLORITE FOR 24 HOURS BEFORE DILUTING AND DISPOSING DOWN THE SINK.

Sodium cyanide (0.92 g, 18.7 mmol) was added to a solution of 2-butoxy-4-(chloromethyl)-1-iodobenzene **41** (4.06 g, 12.5 mmol) in dimethylsulfoxide (4.0 mL). After stirring at room temperature for 1 d, water (25.0 mL) was added, and the solution extracted into diethyl ether and washed with brine. Removal of solvents gave a bright yellow oil (3.49 g, 89%); δ_H (400

MHz, $CDCl_3$, 298 K) 7.74 (d, 1H, J = 7.8 Hz, Ar-H^5), 6.75 (d, 1H, J = 1.9 Hz, Ar-H^2), 6.65 (dd, 1H, J_1 = 8.0 Hz, J_2 = 2.0 Hz, Ar-H^6), 4.02 (t, 2H, J = 6.5 Hz, Ar-OCH_2), 3.72 (s, 2H, Ar-CH_2CN), 1.88–1.81 (m, 2H, CH_2), 1.62–1.53 (m, 2H, CH_2), 0.99 (t, 3H, J = 7.3 Hz, CH_3); Lit.[131] δ_H (200 MHz, $CDCl_3$) 7.75 (d, 1H, J = 8.0 Hz), 6.76 (d, 1H, J = 1.8 Hz), 6.66 (m, 1H), 4.03 (t, 2H, J = 6.3 Hz), 3.72 (s, 2H), 1.92–1.78 (m, 2H), 1.66–1.48 (m, 2H), 1.01 (t, 3H, J = 7.3 Hz).

2,3-bis(3-butoxy-4-iodophenyl)acrylonitrile 43

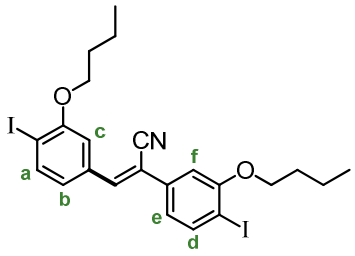

This compound was prepared according to published procedures.[131]

Sodium metal (2.39 g, 24.9 mmol) was washed with 40/60 petroleum ether to remove any protective oil, then sonicated in ethanol (70.0 mL) under an inert atmosphere until homogeneous. The resulting solution was added dropwise to a solution of 2-(3-butoxy-4-iodophenyl)acetonitrile **42** (3.49 g, 11.1 mmol) and 3-butoxy-4-iodobenzaldehyde **40** (3.37 g, 11.1 mmol) in ethanol (8.0 mL). After stirring at room temperature for 1 min, the product precipitated. The resulting solid was filtered, and the remaining mother liquor was partitioned with CH_2Cl_2 and water; the organic layer was evaporated under reduced pressure. The two solids were combined and recrystallised with a minimum volume of refluxing ethanol to give a yellow solid (5.33 g, 80%); δ_H (400 MHz, $CDCl_3$, 298 K) 7.85 (d, 1H, J = 8.0 Hz, d), 7.81 (d, 1H, J = 8.0 Hz, a), 7.48 (d, 1H, J = 1.7 Hz, f), 7.46 (s, 1H, C(CN)=CH), 7.06 (dd, 1H, J_1 = 8.0 Hz, J_2 = 1.9 Hz, e), 7.04 (d, 1H, J = 2.0 Hz, c), 6.99 (dd, 1H, J_1 = 8.2 Hz, J_2 = 2.0 Hz, b), 4.14–4.09 (m, 4H, Ar-OCH_2), 1.91–1.84 (m, 4H, CH_2), 1.64–1.54 (m, 4H, CH_2), 1.00 (t, 3H, J = 7.3 Hz, CH_3), 1.00 (t, 3H, J = 7.3 Hz, CH_3); Lit.[131] δ_H (200 MHz, $CDCl_3$) 7.75 (d, 1H, J = 8.2 Hz), 7.71 (d, 1H, J = 8.4 Hz), 7.41–

7.38 (m, 2H), 7.03–6.87 (m, 2H), 4.03 (m, 4H), 1.89–1.76 (m, 4H), 1.66–1.47 (m, 4H), 1.05–0.90 (m, 6H).

***Tert*-butyl 3,4-bis(3-butoxy-4-iodophenyl)-1H-pyrrole-2-carboxylate 44**

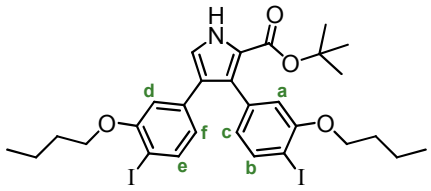

This compound was prepared according to published procedures.[131]

WARNING: KCN IS PRODUCED AS A SIDEPRODUCT AND IS HIGHLY TOXIC.

DISPOSAL: ALL CONTAMINATED MATERIALS AND RESIDUES SHOULD BE TREATED WITH SODIUM HYPOCHLORITE FOR 24 HOURS BEFORE DILUTING AND DISPOSING DOWN THE DRAIN.

A solution of 2,3-bis(3-butoxy-4-iodophenyl)acrylonitrile **43** (4.77 g, 7.92 mmol) and *tert*-butyl isocyanoacetate (1.68 g, 11.8 mmol) in dry THF (31.0 mL) was added to a suspension of potassium *tert*-butoxide (3.20 g, 28.5 mmol) in dry THF (31.0 mL) at 0 °C under argon. The reaction mixture was stirred at 50 °C for 2 h, then passed through a short silica plug with CH_2Cl_2 to give a viscous orange oil (5.41 g, 95%); δ_H (400 MHz, $CDCl_3$, 298 K) 9.20 (br s, 1H, N*H*), 7.70 (d, 1H, *J* = 8.5 Hz, b), 7.60 (d, 1H, *J* = 8.0 Hz, e), 7.11 (d, 1H, *J* = 3.1 Hz, C-*H*), 6.68–6.66 (m, 2H, a, c), 6.58 (dd, 1H, J_1 = 8.0 Hz, J_2 = 1.9 Hz, f), 6.39 (d, 1H, *J* = 1.9 Hz, d), 3.86 (t, 2H, *J* = 6.5 Hz, Ar-OCH_2 adj. $CO_2{}^t$Bu), 3.57 (t, 2H, *J* = 6.3 Hz, Ar-OCH_2 opp. $CO_2{}^t$Bu), 1.72–1.63 (m, 4H, CH_2), 1.52–1.44 (m, 4H, CH_2), 1.36 (s, 9H, ^{t}Bu), 0.94 (t, 3H, *J* = 7.5 Hz, CH_3), 0.93 (t, 3H, *J* = 7.3 Hz, CH_3); Lit.[131] δ_H (400 MHz, $CDCl_3$) 9.17 (br s, 1H), 7.71 (d, 1H, *J* = 8.4 Hz), 7.61 (d, 1H, *J* = 8.4 Hz), 7.11 (d, 1H, *J* = 3.3 Hz), 6.68–6.59 (m, 3H), 6.40 (d, 1H, *J* = 1.8 Hz), 3.86 (t, 2H, *J* = 6.4 Hz), 3.57 (t, 2H, *J* = 6.4 Hz), 1.71–1.66 (m, 4H), 1.52–1.46 (m, 4H), 1.37 (s, 9H), 0.98–0.94 (m, 6H).

***Tert*-butyl 3,4-bis(3-butoxy-4-((trimethylsilyl)ethynyl)phenyl)-1H-pyrrole-2-carboxylate 45**

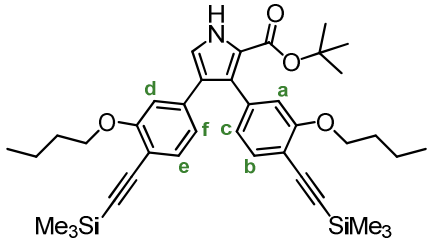

This compound was prepared according to published procedures.[131]

Tert-butyl 3,4-bis(3-butoxy-4-iodophenyl)-1H-pyrrole-2-carboxylate **44** (5.53 g, 7.73 mmol), $Pd_2(dba)_3$ (142 mg, 0.16 mmol), copper(I) iodide (58.9 mg, 0.31 mmol) and triphenylphosphine (162 mg, 0.62 mmol) were dried under vacuum for 2 h. Dry, argon saturated triethylamine (40.0 mL) was added, and the solution freeze-thaw degassed. Trimethylsilylacetylene (4.4 mL, 30.9 mmol) was added, and the reaction mixture was stirred at room temperature for 5 h. Solvents were removed and the residue was purified on a silica column (1:1 → 13:7 CH_2Cl_2 : 40/60 petroleum ether) to give a light brown solid (5.07 g, 99%); δ_H (400 MHz, $CDCl_3$, 298 K) 9.18 (br s, 1H, N*H*), 7.34 (d, 1H, *J* = 7.8 Hz, b), 7.24 (d, 1H, *J* = 7.8 Hz, e), 7.11 (d, 1H, *J* = 3.1 Hz, C-*H*), 6.80 (dd, 1H, J_1 = 7.68 Hz, J_2 = 1.2 Hz, c), 6.69 (dd, 1H, J_1 = 9.4 Hz, J_2 = 1.5 Hz, f), 6.68 (d, 1H, *J* = 1.0 Hz, a), 6.41 (d, 1H, *J* = 1.0 Hz, d), 3.83 (t, 2H, *J* = 6.3 Hz, Ar-OCH_2 adj. $CO_2{}^t$Bu), 3.58 (t, 2H, *J* = 6.5 Hz, Ar-OCH_2 opp. $CO_2{}^t$Bu), 1.75–1.64 (m, 4H, CH_2), 1.55–1.45 (m, 4H, CH_2), 1.35 (s, 9H, ^{t}Bu), 0.97–0.94 (m, 6H, CH_3), 0.26 (s, 9H, Si(CH_3)$_3$ adj. $CO_2{}^t$Bu), 0.23 (s, 9H, Si(CH_3)$_3$ opp. $CO_2{}^t$Bu); Lit.[131] δ_H (400 MHz, $CDCl_3$) 9.54 (br s, 1H), 7.36 (d, 1H, *J* = 7.8 Hz), 7.26 (d, 1H, *J* = 7.7 Hz), 7.12 (t, 1H, *J* = 3.1 Hz), 6.82 (m, 1H), 6.72 (m, 1H), 6.68 (d, 1H, *J* = 1.1 Hz), 6.41 (d, 1H, *J* = 1.2 Hz), 3.83 (t, 2H, *J* = 6.3 Hz), 3.57 (t, 2H, *J* = 6.4 Hz), 1.75–1.64 (m, 4H), 1.56–1.44 (m, 4H), 1.36 (s, 9H), 0.98–0.94 (m, 6H), 0.27 (s, 9H), 0.23 (s, 9H).

4-iodopyridine 48

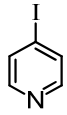

This compound was prepared by adaptation of a published procedure.[152]

Sodium nitrite (1.61 g, 23.4 mmol) was added portionwise to a solution of 4-aminopyridine (2.00 g, 21.3 mmol) in tetrafluoroboric acid (48% aqueous solution, 13.0 mL) at –10 °C, ensuring no gas evolution was detected. The resultant slurry was stirred at –10 °C for 30 min, then was filtered to afford a white solid.

CAUTION! DIAZONIUM SALT. POTENTIALLY EXPLOSIVE, KEEP DAMP!

The solid was quickly transferred portionwise to a stirring saturated solution of potassium iodide (5.64 g, 34.0 mmol) in acetone/water (2:3, 30.0 mL). The resulting brown slurry was decolourised with saturated sodium thiosulfate solution (10.0 mL), neutralised with sodium carbonate and extracted into diethyl ether. The organic layer was washed with water, dried with magnesium sulfate and solvent removed under reduced pressure to give a yellow powder. Sublimation under high vacuum (2.5×10^{-1} mbar, 70 °C) gave white needles (1.60 g, 36%); δ_H (500 MHz, $CDCl_3$, 298 K) 8.27 (dd, 2H, J_1 = 4.6 Hz, J_2 = 1.3 Hz, NC-*H*), 7.68 (dd, 2H, J_1 = 4.6 Hz, J_2 = 1.3 Hz, ICC-*H*); δ_C (125 MHz, $CDCl_3$) 150.21, 133.11, 105.35; *m/z* (ToF MS ES+) 206.0 ([M+H]$^{\bullet+}$, C_5H_5NI, requires 206.0); Lit.[152] δ_H ($CDCl_3$, 300 MHz) 8.27 (2H, d, *J* = 5.0 Hz), 7.68 (2H, d, *J* = 5.0 Hz).

Tert-Butyl 3,4-bis(3-butoxy-4-(pyridin-4-ylethynyl)phenyl)-1H-pyrrole-2-carboxylate 15

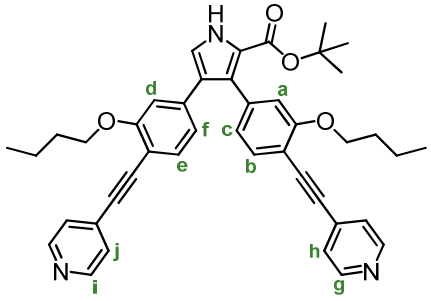

Tert-butyl 3,4-bis(3-butoxy-4-((trimethylsilyl)ethynyl)phenyl)-1H-pyrrole-2-carboxylate **45** (750 mg, 1.14 mmol), $Pd_2(dba)_3$ (52.3 mg, 57.2 μmol), triphenylphosphine (60.0 mg, 0.23 mmol) and copper(I) iodide (21.8 mg, 0.11 mmol) were dried under vacuum for 2 h. 4-iodopyridine **48** (2.34 g, 11.4 mmol) was added, and the flask purged with N_2. Dry, degassed toluene (26.0 mL), THF (26.0 mL) and triethylamine (26.0 mL) were added and the mixture was freeze-thaw degassed. Tetrabutylammonium fluoride (1.0 M in THF, 11.4 mL, 11.4 mmol) was added and the mixture heated to 50 °C and stirred for 3 h until TLC (EtOAc, R_f = 0.33) showed the reaction to be complete. The solvent was evaporated, and the crude purified by column chromatography (EtOAc) to yield a yellow solid (735 mg, 97%); δ_H (400 MHz, $CDCl_3$, 298 K) 8.60 (br s, 2H, g), 8.57 (br s, 2H, i), 7.46 (d, 1H, J = 7.8 Hz, b), 7.38–7.32 (m, 5H, e, h, j), 7.14 (s, 1H, C*H*), 6.88 (dd, 1H, J_1 = 7.9 Hz, J_2 = 1.2 Hz, c), 6.83 (dd, 1H, J_1 = 7.9 Hz, J_2 = 1.4 Hz, f), 6.77 (s, 1H, a), 6.48 (s, 1H, d), 3.94 (t, 2H, J = 6.3 Hz, OCH_2 adj. $CO_2{}^t$Bu), 3.62 (t, 2H, J = 6.5 Hz, OCH_2 opp. $CO_2{}^t$Bu), 1.78–1.67 (m, 4H, CH_2), 1.55–1.45 (m, 4H, CH_2), 1.26 (s, 9H, ^{t}Bu), 0.97 (t, 3H, J = 7.3 Hz, CH_3), 0.94 (t, 3H, J = 7.3 Hz, CH_3); δ_C (125 MHz, $CDCl_3$) 160.40, 159.68, 159.45, 149.66, 149.61, 137.99, 136.97, 133.29, 132.70, 132.13, 132.05, 131.93, 131.91, 128.54, 128.44, 127.52, 125.73, 123.14, 121.91, 119.69, 119.67, 114.70, 111.79, 110.11, 109.12, 91.13, 91.06, 90.80, 90.70, 81.46, 68.33, 68.09, 31.03, 30.98, 28.18, 19.18, 19.09, 13.79; *m/z* (TOF MS ES+) 666.3 ($[M+H]^{\bullet+}$, $C_{43}H_{44}N_3O_4$, requires 666.3); Lit.[131] δ_H (400 MHz, $CDCl_3$) 8.61 (br s, 4H),

7.46 (d, 1H, *J* = 7.8 Hz), 7.36 (br s, 4H), 7.34 (d, 1H, *J* = 7.8 Hz), 7.17 (d, 1H, *J* = 3.1 Hz), 6.94 (m, 1H), 6.84–6.82 (m, 2H), 6.53 (s, 1H), 3.93 (t, 2H, *J* = 6.4 Hz), 3.64 (t, 2H, *J* = 6.4 Hz), 1.79–1.65 (m, 4H), 1.56–1.43 (m, 4H), 1.37 (s, 9H), 0.98–0.90 (m, 6H).

2,3-diphenylacrylonitrile 52

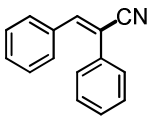

This compound was prepared by adaptation of a published procedure.[131]

Sodium metal (1.65 g, 71.6 mmol) was washed with 40/60 petroleum ether to remove any protective oil, then sonicated in ethanol (16.0 mL) under an inert atmosphere until homogeneous. The resulting solution was added dropwise to a solution of benzaldehyde (760 µL, 7.54 mmol) and phenylacetonitrile (870 µL, 7.54 mmol) in ethanol (1.6 mL) to effect immediate precipitation of crude solid. After stirring for 5 min, the mixture was dissolved into CH_2Cl_2 and extracted with water. Recrystallisation from ethanol gave a pale yellow solid (1.11 g, 72%); δ_H (400 MHz, $CDCl_3$, 298 K) 7.92–7.90 (m, 2H, Ar-H^{ortho} adj. CN), 7.69 (dd, 2H, J_1 = 8.5 Hz, J_2 = 1.4 Hz, Ar-H^{ortho} opp. CN), 7.56 (s, 1H, C=C*H*), 7.51–7.36 (m, 6H, Ar-*H*); Lit.[18] δ_H (400 MHz, $CDCl_3$) 7.89–7.91 (m, 2H), 7.68–7.70 (m, 2H), 7.55 (s, 1H), 7.40–7.50 (m, 6H).

Dipyrromethane 5

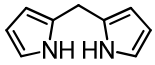

This compound was prepared according to published procedure.[320]

Freshly distilled pyrrole (150 mL, 2.16 mol) and formaldehyde (37% aqueous solution, 8.1 mL, 90.0 mmol) were pump degassed. While vigorously stirring, trifluroacetic acid (810 µL, 10.9

mmol) was added dropwise. After 5 min, CH_2Cl_2 (150 mL) and aqueous sodium carbonate (100 mL) were added. The organic layer was washed further with aqueous sodium carbonate, followed by water, and evaporated. Distillation of the crude product on a Kugelrohr (170–200 °C @ 260 Torr) gave a white crystalline solid (6.39 g, 49%); δ_H (400 MHz, $CDCl_3$, 298 K) 7.82 (br s, 2H, N*H*), 6.66 (m, 2H, *α-H*), 6.17 (m, 2H, *β-H*), 6.06 (m, 2H, *β-H*), 3.98 (s, 2H, CH_2); δ_C (62.5 MHz, $CDCl_3$, 298 K) 129.50, 117.74, 108.80, 106.84, 26.82; Lit.[321] δ_H (200 MHz, $CDCl_3$) 7.65 (br s, 2H), 6.60 (dd, 2H), 6.15 (dd, 2H), 6.05 (m, 2H), 3.95 (s, 2H).

Ethynyltrihexylsilane 98

This compound was prepared according to published procedure.[243]

Trihexylsilyl chloride (8.8 mL, 23.9 mmol) was added dropwise to a solution of ethynyl magnesium bromide (0.5 M solution in THF, 50.0 mL, 25.0 mmol) under argon. The reaction mixture was refluxed for 1 h, then quenched by addition of hydrochloric acid (10% aqueous solution, 40.0 mL). The organic layer was reduced under vacuum to yield a yellow oil (7.35 g, 99%); δ_H (400 MHz, $CDCl_3$, 298 K) 2.37 (s, 1H, Si–C≡C–*H*), 1.42–1.29 (m, 24H, CH_2), 0.89 (t, 9H, J = 7.0 Hz, CH_3); Lit.[145] δ_H ($CDCl_3$) 2.35 (s, 1H), 1.41–1.26 (m, 24H), 0.89–0.83 (m, 9H).

Free base 5,15-bis-(3,5-bis-*tert*-butyl-phenyl)-porphyrin 92

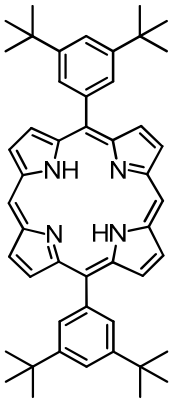

Dipyrromethane **5** (1.88 g, 12.8 mmol) and 3,5-di(*tert*-butyl)benzaldehyde **91** (2.80 g, 12.8 mmol) were dissolved in CH_2Cl_2 (2.5 L). The solution was protected from the light, and pump degassed. Trifluoroacetic acid (619 µL, 8.08 mmol) was added dropwise, and the mixture was stirred in the dark for 3 h. DDQ (3.73 g, 16.4 mmol) was added, and stirred for a further 30 min. Triethylamine (12.5 mL) was added to quench the acid. The reaction volume was reduced and passed through a short silica plug with CH_2Cl_2 to remove black tarry side products. Recrystallisation with CH_2Cl_2/MeOH gave a purple metallic solid (2.92 g, 66%); δ_H (400 MHz, $CDCl_3$, 298 K) 10.35 (s, 2H, *meso*-*H*), 9.44 (d, 4H, *J* = 4.6 Hz, *β*-*H*), 9.19 (d, 4H, *J* = 4.6 Hz, *β*-*H*), 8.20 (d, 4H, *J* = 1.7 Hz, Ar-H^{ortho}), 7.89 (t, 2H, *J* = 1.7 Hz, Ar-H^{para}), 1.62 (s, 36H, ^{t}Bu), –2.96 (s, 2H, N*H*); Lit.[75] δ_H (400 MHz, $CDCl_3$, 298 K) 10.33 (s, 2H), 9.42 (d, 4H, *J* = 4.5 Hz), 9.15 (d, 2H, *J* = 4.6 Hz, *β*-*H*), 8.16 (d, 4H, *J* = 2.0 Hz), 7.85 (t, 2H, *J* = 2.0 Hz), 1.58 (s, 36H), –3.10 (br s, 2H).

Zinc 5,15-bis-(3,5-bis-*tert*-butyl-phenyl)-porphyrin 93

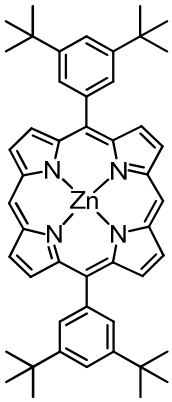

A methanolic solution (45.0 mL) of $Zn(OAc)_2.H_2O$ (4.86 g, 22.1 mmol) was added to a solution of free base 5,15-bis-(3,5-bis-*tert*-butyl-phenyl)-porphyrin **92** (2.92 g, 4.25 mmol) in $CHCl_3$ (341 mL). After stirring at 40 °C for 1 h, the reaction mixture volume was reduced and passed through a short silica plug with CH_2Cl_2. Precipitation with CH_2Cl_2/MeOH gave dark purple metallic crystals (2.28 g, 72%); δ_H (250 MHz, $CDCl_3$, 298 K) 10.20 (s, 2H, *meso*-*H*), 9.37 (d, 4H, *J* = 4.4 Hz, *β*-*H*), 9.12 (d, 4H, *J* = 4.4 Hz, *β*-*H*), 8.11 (d, 4H, *J* = 1.8 Hz, Ar-H^{ortho}), 7.81 (t, 2H, *J* = 1.8 Hz, Ar-H^{para}), 1.57 (s, 36H, ^{t}Bu); *m/z* (MALDI-ToF MS+, DCTB) 747.3 ($[M]^{\bullet+}$, $C_{48}H_{52}N_4Zn$, requires 750.4); Lit.[75] δ_H (400 MHz, $CDCl_3$, 298 K) 10.36 (s, 2H), 9.45 (d, 4H, *J* = 4.5 Hz), 9.23 (d, 4H, *J* = 4.5 Hz), 8.17 (d, 4H, *J* = 2.0 Hz), 7.86 (t, 2H, *J* = 2.0 Hz), 1.59 (s, 36H).

Zinc 5,15-bis-(3,5-bis-*tert*-butyl-phenyl)-10,20-dibromo-porphyrin 94

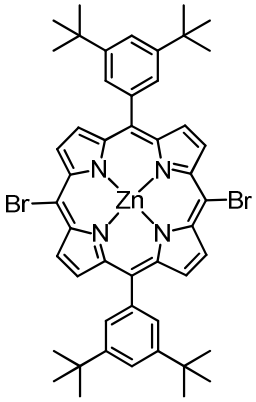

A solution of *N*-bromosuccinimide (237 mg, 1.33 mmol) in $CHCl_3$ (20.0 mL) was added dropwise over 1 h to a solution of zinc 5,15-bis-(3,5-bis-*tert*-butyl-phenyl)-porphyrin **93** (0.50 g, 0.67 mmol) in $CHCl_3$ (30.0 mL) and pyridine (315 µL), in a flask protected from the light. After 15 min, the reaction was quenched with acetone (1.0 mL). Recrystallisation in CH_2Cl_2/MeOH gave a dark purple solid (471 mg, 78%); δ_H (250 MHz, $CDCl_3$ / 1 % d_5-pyridine, 298 K) 9.66 (d, 4H, *J* = 4.7 Hz, *β-H*), 8.90 (d, 4H, *J* = 4.7 Hz, *β-H*), 7.98 (d, 4H, *J* = 1.8 Hz, Ar-H^{ortho}), 7.80 (t, 2H, *J* = 1.8 Hz, Ar-H^{para}), 1.54 (s, 36H, ^{t}Bu); *m/z* (MALDI-ToF MS+, dithranol) 908.2 ($[M]^{\bullet+}$, $C_{48}H_{50}N_4Br_2Zn$, requires 908.2); Lit.[75] δ_H (400 MHz, $CDCl_3$, 298 K) 9.66 (d, 4H, *J* = 4.5 Hz), 8.91 (d, 4H, *J* = 4.5 Hz), 7.99 (d, 4H, *J* = 2.0 Hz), 7.80 (t, 2H, *J* = 2.0 Hz), 1.50 (s, 36H).

Zinc 5,15-bis-(3,5-bis-*tert*-butyl-phenyl)-10,20-bis-trihexylsilanylethynyl-porphyrin monomer *l*-P1

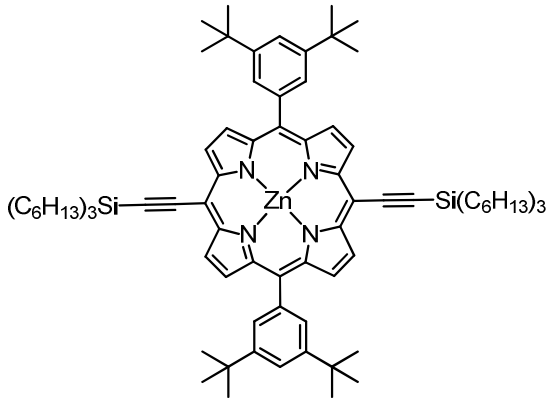

Zinc 5,15-bis-(3,5-bis-*tert*-butyl-phenyl)-10,20-dibromo-porphyrin **94** (1.00 g, 1.10 mmol), $Pd_2(dba)_3$ (101 mg, 0.11 mmol), copper(I) iodide (41.9 mg, 0.22 mmol), and triphenylphosphine (57.8 mg, 0.22 mmol) were dried in a Schlenk tube under vacuum for 30 min. The solids were dissolved in dry toluene (70.0 mL), pyridine (2.0 mL) and $^{i}Pr_2NH$ (3.8 mL) and the solution freeze-thaw degassed. Ethynyltrihexylsilane **98** (2.12 mL, 5.51 mmol) was added, the tube was sealed and the mixture was heated to 80 °C for 2 h. The mixture was passed through a silica plug with CH_2Cl_2, and the crude product recrystallised by layer addition of CH_2Cl_2/MeOH to yield a dark green solid (1.37 g, 91%); δ_H (400 MHz, $CDCl_3$, 298 K) 9.64 (d, 4H, *J* = 4.6 Hz, *β-H*), 8.87 (d, 4H, *J* = 4.4 Hz, *β-H*), 8.00 (d, 4H, *J* = 1.7 Hz, Ar-H^{ortho}), 7.78 (t, 2H, *J* = 1.8 Hz, Ar-H^{para}), 1.80–1.72 (m, 12H, CH_2), 1.56–1.49 (m, 48H, CH_2, ^{t}Bu) 1.41–1.33 (m, 24H, CH_2), 1.02–0.98 (m, 12H, CH_2), 0.89 (t, 4H, *J* = 7.0 Hz, Si-CH_2); *m/z* (MALDI-ToF MS+, dithranol) 1362 ([M]$^{\bullet+}$, $C_{88}H_{128}N_4Si_2Zn$, requires 1364); Lit.[75] δ_H (400 MHz, $CDCl_3$, 298 K) 9.74 (d, 4H, *J* = 4.5 Hz), 8.98 (d, 4H, *J* = 4.5 Hz), 8.06 (d, 4H, *J* = 1.5 Hz), 7.83 (t, 2H, *J* = 1.5 Hz), 1.77 (m, 12H), 1.58–1.51 (m, 48H) 1.39 (m, 24H), 1.02 (m, 12H), 0.90 (t, 4H, *J* = 7.0 Hz).

Zinc 5,15-bis-(3,5-bis-*tert*-butyl-phenyl)-10,20-bis-ethynyl-porphyrin monomer *l*-dP1

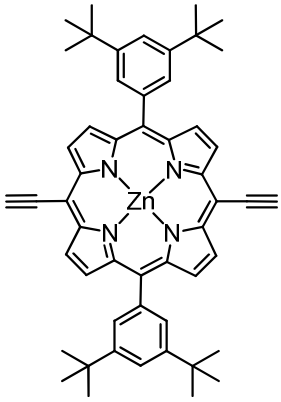

This compound was prepared according to published procedure.[75]

Tetrabutylammonium fluoride (1.0 M solution in THF, 293 μL, 0.29 mmol) was added to a stirring solution of zinc 5,15-bis-(3,5-bis-*tert*-butyl-phenyl)-10,20-bis-trihexylsilanylethynyl-porphyrin monomer ***l*-P1** (40.0 mg, 29.3 μmol) and pyridine (20 μL) in dry CH_2Cl_2 (10.0 mL). Once the reaction was shown to be complete by TLC (20:1:1 40/60 petroleum ether : EtOAc : pyridine), the mixture was passed through a short silica plug with CH_2Cl_2 to give a green solid (21.3 mg, 91%); δ_H (250 MHz, $CDCl_3$, 298 K) 9.68 (d, 4H, *J* = 4.6 Hz, *β-H*), 8.92 (d, 4H, *J* = 4.9 Hz, *β-H*), 8.02 (d, 4H, *J* = 1.8 Hz, Ar-H^{ortho}), 7.80 (m, 2H, Ar-H^{para}), 4.15 (s, 2H, C≡C–*H*), 1.55 (s, 36H, ^{t}Bu); *m/z* (MALDI-ToF MS+, dithranol) 799.5 ([M]$^{\bullet+}$, $C_{52}H_{52}N_4Zn$, requires 798.4); Lit.[75] δ_H (200 MHz, $CDCl_3$, 298 K) 9.79 (d, 4H), 8.89 (d, 4H), 7.99 (d, 4H, *J* = 1.5 Hz), 7.78 (br s, 2H), 4.12 (s, 2H), 1.52 (s, 36H).

Zinc 5,15-bis-(3,5-bis-*tert*-butyl-phenyl)-10,20-bis-trihexylsilanylethynyl-porphyrin dimer *l*-P2

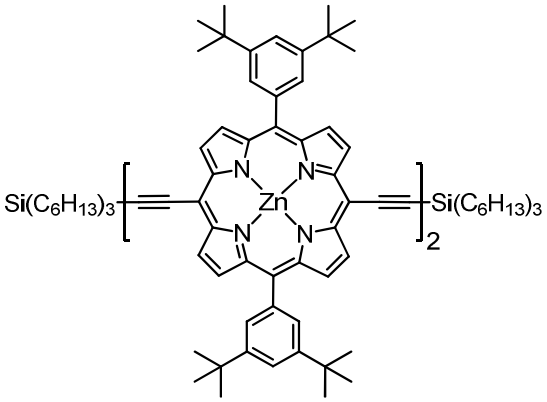

This compound was prepared according to published procedure.[75]

Tetrabutylammonium fluoride (1.0 M solution in THF, 3.75 mL, 3.75 mmol) was added to a solution of zinc 5,15-bis-(3,5-bis-*tert*-butyl-phenyl)-10,20-bis-trihexylsilanylethynyl-porphyrin monomer ***l*-P1** (3.41g, 2.50 mmol) and pyridine (50 µL) in $CHCl_3$ (634 mL) and CH_2Cl_2 (634 mL). The reaction mixture was stirred for 50 min at room temperature until TLC showed starting material and doubly-deprotected spots of roughly equal intensity (20:1:1 40/60 petroleum ether : EtOAc : pyridine). The mixture was immediately poured onto a short silica plug and eluted with CH_2Cl_2 to remove the TBAF. The mixture was columned on silica (20:1:1 → 5:1:1 40/60 petroleum ether : EtOAc : pyridine) to remove the mono-deprotected product.

The mono-deprotected product ***l*-mP1** and freshly prepared copper(I) chloride (7.37 g, 74.4 mmol) were added to a 3 L round bottom flask equipped with a calcium chloride drying tube and made into a solution with dry CH_2Cl_2 (400 mL). *N*,*N*,*N*',*N*'-tetramethylethylenediamine (10.4 mL, 69.4 mmol) was added, and the reaction mixture stirred vigorously under air. After approximately 30 min, TLC (10:1:1 40/60 petroleum ether : EtOAc : pyridine) showed

complete conversion to dimer, so the mixture was passed through a short silica plug with CH_2Cl_2. The crude product was purified by chromatography on silica (10:1:1 → 5:1:1 40/60 petroleum ether : EtOAc : pyridine) and precipitated with CH_2Cl_2/MeOH to give a olive green solid (1.15 g, 43% over two steps); δ_H (400 MHz, $CDCl_3$ / 1% d_5-pyridine, 298 K) 9.88 (d, 4H, *J* = 4.6 Hz, *β-H*), 9.66 (d, 4H, *J* = 4.6 Hz, *β-H*), 8.98 (d, 4H, *J* = 4.6 Hz, *β-H*), 8.88 (d, 4H, *J* = 4.4 Hz, *β-H*), 8.05 (d, 8H, *J* = 1.8 Hz, Ar-H^{ortho}), 7.81 (t, 4H, *J* = 1.8 Hz, Ar-H^{para}), 1.80–1.73 (m, 12H, CH_2), 1.57–1.51 (m, 84H, CH_2, ^{t}Bu) 1.42–1.34 (m, 24H, CH_2), 1.04–1.00 (m, 12H, CH_2), 0.90 (t, 18H, *J* = 7.1 Hz, CH_3); *m/z* (MALDI-ToF MS+, dithranol) 2159 ([M]$^{\bullet+}$, $C_{140}H_{178}N_8Si_2Zn_2$, requires 2160); Lit.[75] δ_H (400 MHz, $CDCl_3$ / 1% d_5-pyridine, 298 K) 9.89 (d, 4H, *J* = 4.5 Hz), 9.66 (d, 4H, *J* = 4.5 Hz), 8.99 (d, 4H, *J* = 4.5 Hz), 8.89 (d, 4H, *J* = 4.5 Hz), 8.05 (d, 8H, *J* = 1.5 Hz), 7.82–7.81 (m, 4H), 1.82–1.73 (m, 12H), 1.61–1.51 (m, 84H) 1.45–1.35 (m, 24H), 1.04–1.00 (m, 12H), 0.91 (t, 18H, *J* = 7.0 Hz).

Zinc 5,15-bis-(3,5-bis-*tert*-butyl-phenyl)-10,20-bis-ethynyl-porphyrin dimer *l*-dP2

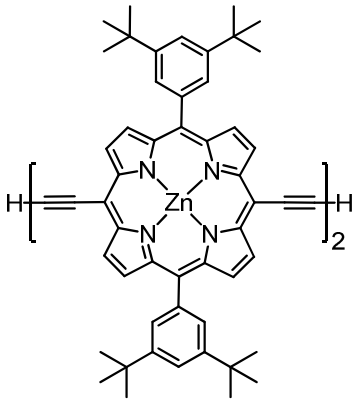

This compound was prepared by adaptation of a published procedure.[75]

Tetrabutylammonium fluoride (1.0 M solution in THF, 177 µL, 0.18 mmol) was added to a stirring solution of zinc 5,15-bis-(3,5-bis-*tert*-butyl-phenyl)-10,20-bis-trihexylsilanylethynyl-porphyrin dimer ***l*-P2** (19.1 mg, 8.84 µmol) and pyridine (10 µL) in dry CH_2Cl_2 (5.0 mL). Once

the reaction was shown to be complete by TLC (17:1:2 40/60 petroleum ether : THF : pyridine), the mixture was passed through a short silica plug with CH_2Cl_2/pyridine (10:1) to give a brown solid (13.9 mg, 99%); δ_H (250 MHz, $CDCl_3$ / 1% d_5-pyridine, 298 K) 9.91 (d, 4H, *J* = 4.6 Hz, *β-H*), 9.67 (d, 4H, *J* = 4.6 Hz, *β-H*), 9.00 (d, 4H, *J* = 4.6 Hz, *β-H*), 8.92 (d, 4H, *J* = 4.6 Hz, *β-H*), 8.06 (d, 8H, *J* = 1.7 Hz, Ar-H^{ortho}), 7.82 (m, 4H, Ar-H^{para}), 4.17 (s, 2H, C≡C–*H*), 1.65 (s, 72H, ^{t}Bu); *m/z* (MALDI-ToF MS+, dithranol) 1596 ($[M]^{\bullet+}$, $C_{104}H_{102}N_8Zn_2$, requires 1595); Lit.[69] δ_H (500 MHz, $CDCl_3$ / 1% d_5-pyridine, 328 K) 9.91 (d, 4H, *J* = 5.0 Hz), 9.68 (d, 4H, *J* = 5.0 Hz), 8.99 (d, 4H, *J* = 5.0 Hz), 8.91 (d, 4H, *J* = 5.0 Hz), 8.07 (d, 8H, *J* = 2.0 Hz), 7.86 (t, 4H, *J* = 2.0 Hz), 4.16 (s, 2H, C≡C–*H*), 1.60 (s, 72H).

Zinc 5,15-bis-(3,5-bis-*tert*-butyl-phenyl)-10,20-bis-trihexylsilanylethynyl-porphyrin tetramer *l*-P4

Zinc 5,15-bis-(3,5-bis-*tert*-butyl-phenyl)-10,20-bis-trihexylsilanylethynyl-porphyrin hexamer *l*-P6

Zinc 5,15-bis-(3,5-bis-*tert*-butyl-phenyl)-10,20-bis-trihexylsilanylethynyl-porphyrin octamer *l*-P8

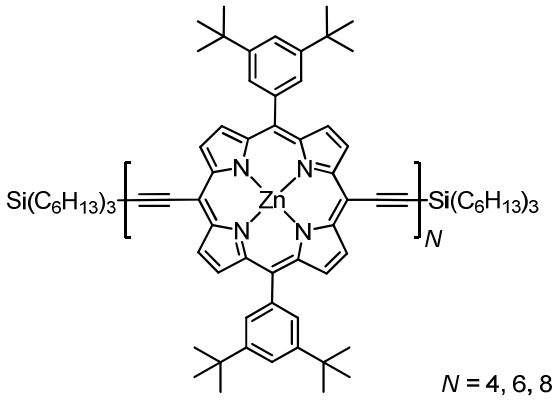

Tetrabutylammonium fluoride (1.0 M solution in THF, 1.37 mL, 1.37 mmol) was added to a solution of zinc 5,15-bis-(3,5-bis-*tert*-butyl-phenyl)-10,20-bis-trihexylsilanylethynyl-porphyrin dimer ***l*-P2** (1.15 g, 0.53 mmol) and pyridine (50 μL) in $CHCl_3$ (211 mL) and CH_2Cl_2

(211 mL). The reaction mixture was stirred for 50 min at room temperature until TLC showed starting material and doubly-deprotected spots of approximately equal intensity. The mixture was immediately poured onto a short silica plug and eluted with CH_2Cl_2/pyridine (10:1) to remove the TBAF. The mixture was columned on silica to remove the mono-deprotected product and fully deprotected products, ***l*-mP2** and ***l*-dP2**.

Mono-THS *tert*-butyl porphyrin dimer ***l*-mP2** (345 mg, 0.18 mmol), deprotected *tert*-butyl porphyrin dimer ***l*-dP2** (73.0 mg, 45.9 μmol) and freshly prepared copper(I) chloride (1.23 g, 12.4 mmol) were dissolved in dry CH_2Cl_2 (102 mL) in a large round bottom flask equipped with a drying tube. *N,N,N',N'*-Tetramethylethylenediamine (1.7 mL, 11.8 mmol) was added, and the reaction stirred vigorously under air for 1 h. The mixture was passed down a short silica column with $CHCl_3$/pyridine (10:1). Separation by preparative GPC (10% pyridine in toluene, 8.5 mL min^{-1}) yielded ***l*-P4** (R_t = 35.4 min), ***l*-P6** (R_t = 33.6 min) and ***l*-P8** (R_t = 32.4 min):

Zinc 5,15-bis-(3,5-bis-*tert*-butyl-phenyl)-10,20-bis-trihexylsilanylethynyl-porphyrin tetramer *l*-P4

(0.20 g, 30%); δ_H (250 MHz, $CDCl_3$ / 1% d_5-pyridine, 298 K) 9.93 (d, 4H, *J* = 4.6 Hz, *β-H*), 9.92 (d, 4H, *J* = 4.6 Hz, *β-H*), 9.91 (d, 4H, *J* = 4.6 Hz, *β-H*), 9.67 (d, 4H, *J* = 4.6 Hz, *β-H*), 9.02 (d, 4H, *J* = 4.3 Hz, *β-H*), 9.01 (d, 4H, *J* = 4.3 Hz, *β-H*), 9.00 (d, 4H, *J* = 4.3 Hz, *β-H*), 8.90 (d, 4H, *J* = 4.6 Hz, *β-H*), 8.12 (d, 8H, *J* = 1.8 Hz, Ar-H^{ortho}), 8.08 (d, 8H, *J* = 1.8 Hz, Ar-H^{ortho}), 7.86 (t, 4H, *J* = 1.8 Hz, Ar-H^{para}), 7.83 (t, 4H, *J* = 1.8 Hz, Ar-H^{para}), 1.86–1.72 (m, 12H, CH_2), 1.60 (s, 72H, ^{t}Bu), 1.58 (s, 72H, ^{t}Bu), 1.59–1.53 (m, 12H, CH_2), 1.43–1.34 (m, 24H, CH_2), 1.06–0.99 (m, 12H, CH_2), 0.92 (t, 18H, *J* = 7.0 Hz, CH_3); *m/z* (MALDI-ToF MS+, dithranol) 3751 ($[M]^{\bullet+}$, $C_{244}H_{278}N_{16}Si_2Zn_4$, requires 3753); Lit.[69] δ_H (500 MHz, $CDCl_3$ / 1% d_5-pyridine, 318 K) 9.92 (d, 4H, *J* = 5.0 Hz), 9.91 (d, 4H, *J* = 5.0 Hz), 9.90 (d, 4H, *J* = 5.0 Hz), 9.67 (d, 4H, *J* = 5.0 Hz), 9.00 (d, 4H, *J* = 5.0 Hz), 8.99 (d, 4H, *J* = 5.0 Hz), 8.98 (d, 4H, *J* = 5.0 Hz), 8.88 (d, 4H, *J* = 5.0 Hz), 8.11 (d, 8H, *J* = 2.0 Hz), 8.07 (d, 8H, *J* =

2.0 Hz), 7.87 (t, 4H, *J* = 2.0 Hz), 7.85 (t, 4H, *J* = 2.0 Hz), 1.81 (m, 12H), 1.61 (s, 72H), 1.59 (s, 72H), 1.56 (m, 12H), 1.42 (m, 24H), 1.05 (m, 12H), 0.92 (t, 18H, *J* = 7.0 Hz).

Zinc 5,15-bis-(3,5-bis-*tert*-butyl-phenyl)-10,20-bis-trihexylsilanylethynyl-porphyrin hexamer *l*-P6

(41.1 mg, 17%); δ_H (500 MHz, d_8-toluene/1% d_5-pyridine, 353 K) 10.14–10.11 (m, 20H, *β-H*), 10.06 (d, 4H, *J* = 4.3 Hz, *β-H*), 9.16–9.14 (m, 20H, *β-H*), 9.12 (d, 4H, *J* = 4.6 Hz, *β-H*), 8.31 (br d, 8H, Ar-H^{ortho}), 8.30 (br d, 8H, Ar-H^{ortho}), 8.26 (br d, 8H, Ar-H^{ortho}), 8.00 (br t, 8H, Ar-H^{para}), 7.97 (br t, 4H, Ar-H^{para}), 1.59 (s, 72H, ^{t}Bu), 1.58 (s, 72H, ^{t}Bu), 1.56 (s, 72H, ^{t}Bu); *m/z* (MALDI-ToF MS+, dithranol) 5349 ([M]$^{\bullet+}$, $C_{348}H_{378}N_{24}Si_2Zn_6$, requires 5347). Lit.[69] δ_H (500 MHz, $CDCl_3$/1% d_5-pyridine, 328 K) 9.90 (m, 20H), 9.67 (d, 4H, *J* = 5.0 Hz), 8.99 (m, 20H), 8.87 (d, 4H, *J* = 5.0 Hz), 8.12 (d, 8H, *J* = 2.0 Hz), 8.11 (d, 8H, *J* = 2.0 Hz), 8.06 (d, 8H, *J* = 2.0 Hz), 7.88 (t, 4H, *J* = 2.0 Hz), 7.87 (t, 4H, *J* = 2.0 Hz), 7.85 (d, 4H, *J* = 2.0 Hz), 1.81 (m, 12H), 1.62 (s, 72H), 1.61 (s, 144H), 1.58 (m, 12H), 1.41 (m, 24H), 1.05 (m, 12H), 0.92 (t, 18H, *J* = 7.0 Hz).

Zinc 5,15-bis-(3,5-bis-*tert*-butyl-phenyl)-10,20-bis-trihexylsilanylethynyl-porphyrin octamer *l*-P8

(8.8 mg, 5%); δ_H (500 MHz, d_8-toluene/10% d_5-pyridine, 353 K) 10.13–10.11 (m, 28H, *β-H*), 10.06 (d, 4H, *J* = 4.3 Hz, *β-H*), 9.16–9.14 (m, 28H, *β-H*), 9.12 (d, 4H, *J* = 4.6 Hz, *β-H*), 8.31–8.30 (m, 22H, Ar-H^{ortho}), 8.26 (d, 10H, *J* = 1.2 Hz, Ar-H^{ortho}), 8.01–8.00 (m, 10H, Ar-H^{para}), 7.97 (m, 6H, Ar-H^{para}), 1.59 (s, 108H, ^{t}Bu), 1.58 (s, 90H, ^{t}Bu), 1.55 (s, 90H, ^{t}Bu); *m/z* (MALDI-ToF MS+, dithranol) 6930 ([M]$^{\bullet+}$, $C_{452}H_{478}N_{32}Si_2Zn_8$, requires 6838); λ_{max} (toluene/10% pyridine) / nm (log ε) 466 (5.85), 811 (5.50).

Zinc 5,15-bis-(3,5-bis-*tert*-butyl-phenyl)-10,20-bis-ethynyl-porphyrin tetramer *l*-dP4

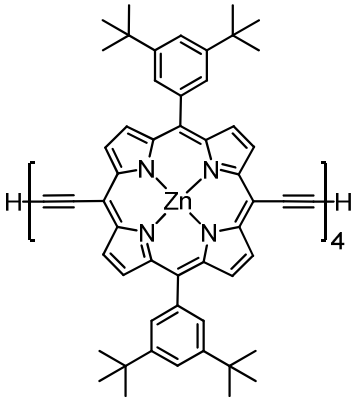

This compound was prepared by adaptation of a published procedure.[75]

Tetrabutylammonium fluoride (1.0 M solution in THF, 1.14 mL, 1.14 mmol) was added to a stirring solution of zinc 5,15-bis-(3,5-bis-*tert*-butyl-phenyl)-10,20-bis-trihexylsilanylethynyl-porphyrin tetramer ***l*-P4** (286 mg, 72.6 μmol) and pyridine (50 μL) in dry CH_2Cl_2 (71.5 mL). After 50 min, the mixture was passed through a short silica plug with CH_2Cl_2/pyridine (10:1) to give a brown solid (181 mg, 75%); δ_H (700 MHz, $CDCl_3$ / 5% d_5-pyridine, 298 K) 9.95–9.93 (m, 12H, *β-H*), 9.70 (d, 4H, *J* = 4.4 Hz, *β-H*), 9.03–9.02 (m, 12H, *β-H*), 8.95 (d, 4H, *J* = 4.4 Hz, *β-H*), 8.13 (d, 8H, *J* = 1.7 Hz, Ar-H^{ortho}), 8.08 (d, 8H, *J* = 1.4 Hz, Ar-H^{ortho}), 7.87 (br t, 4H, Ar-H^{para}), 7.85 (br t, 4H, Ar-H^{para}), 4.20 (s, 2H, C≡C–*H*), 1.62 (s, 72H, ^{t}Bu), 1.60 (s, 72H, ^{t}Bu). *m/z* (MALDI-ToF MS+, dithranol) 3186 ($[M]^{\bullet+}$, $C_{208}H_{202}N_{16}Zn_4$, requires 3187).

(3,5-Bis-octyloxy-phenyl)-methanol 99

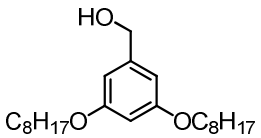

This compound was prepared by adaptation of a published procedure.[147]

A solution of methyl 3,5-bis(octyloxy)benzoate (20.0 g, 51.0 mmol) in freshly distilled THF (100 mL) was added dropwise to a solution of lithium aluminium hydride (2.32 g, 61.2 mmol) in dry THF (80.0 mL) under argon. The reaction mixture was stirred at 40 °C for 4 h. To quench, the mixture was cooled to 0 °C, and water (7.0 mL) was added dropwise, followed by aqueous sodium hydroxide (1.0 M, 2.0 mL). The mixture was passed through Celite, washed with CH_2Cl_2, and solvents removed under vacuum to give a yellow oil (15.8 g, 85%); δ_H (400 MHz, $CDCl_3$, 298 K) 6.51 (d, 2H, *J* = 1.9 Hz, Ar-*H*^{ortho}), 6.38 (t, 1H, *J* = 2.1 Hz, Ar-*H*^{para}), 4.62 (d, 2H, *J* = 5.6 Hz, C*H*$_2$OH), 3.94 (t, 4H, *J* = 6.6 Hz, OC*H*$_2$), 1.80–1.73 (m, 4H, C*H*$_2$), 1.48–1.29 (m, 20H, C*H*$_2$), 0.89 (t, 6H, *J* = 6.7 Hz, C*H*$_3$); Lit.[147] δ_H (300 MHz, $CDCl_3$) 6.48 (d, 2H, *J* = 2.2 Hz), 6.36 (t, 1H, *J* = 2.3 Hz), 4.59 (d, 2H, *J* = 5.8 Hz), 3.92 (t, 4H, *J* = 6.6 Hz), 1.98 (t, 1H, *J* = 6.0 Hz), 1.80–1.71 (m, 4H), 1.49–1.21 (m, 20H), 0.89 (t, 6H, *J* = 6.8 Hz).

3,5-Bis-octyloxy-benzaldehyde 100

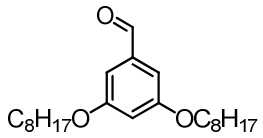

This compound was prepared by adaptation of a published procedure.[131]

Pyridinium chlorochromate (19.1 g, 88.6 mmol) was added to a solution of (3,5-bis-octyloxy-phenyl)-methanol **99** (15.8 g, 43.2 mmol) in CH_2Cl_2 (80.0 mL) and stirred for 2 h at room temperature. The solvent was removed, and the resulting tar-like substance was columned on silica (1:1 40/60 petroleum ether : CH_2Cl_2) to obtain a yellow oil (8.12 g, 52%); δ_H (250 MHz, $CDCl_3$, 298 K) 9.90 (s, 1H, C*H*O), 6.99 (d, 2H, *J* = 2.3 Hz, Ar-*H*^{ortho}), 6.70 (t, 1H, *J* = 2.3 Hz, Ar-*H*^{para}), 3.99 (t, 4H, *J* = 6.6 Hz, Ar-OC*H*$_2$), 1.85–1.74 (m, 4H, Ar-OCH$_2$C*H*$_2$), 1.51–1.30 (m, 20H, C*H*$_2$), 0.90 (t, 6H, *J* = 6.9 Hz, C*H*$_3$); Lit.[322] δ_H ($CDCl_3$) 9.90 (s, 1H), 6.98 (d, 2H, *J* = 2.0 Hz), 6.70 (t, 1H, *J* = 4.0 Hz), 3.99 (t, 4H, *J* = 7.0 Hz), 1.80 (tt, 4H, *J* = 7.0 Hz), 1.43 (m, 4H), 1.29 (m, 16H), and 0.89 (t, 6H, *J* = 7.0 Hz).

Free base 5,15-bis-(3,5-bis-octyloxy-phenyl)-porphyrin 101

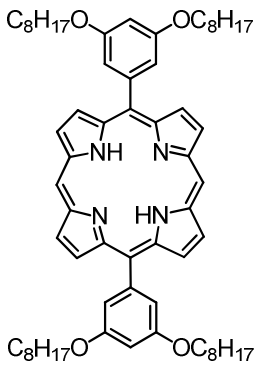

This compound was prepared according to published procedure.[145]

Dipyrromethane **5** (1.61 g, 11.0 mmol) and 3,5-bis-octyloxy-benzaldehyde **100** (3.99 g, 11.0 mmol) were dissolved in CH_2Cl_2 (2.0 L); the flask was covered in foil, and the solution was pump degassed. Trifluoroacetic acid (560 μL, 3.20 mmol) was added dropwise, and the mixture was stirred in the dark for 3 h. DDQ (4.04 g, 17.8 mmol) was added, and stirred for a further 30 min. Triethylamine (15.0 mL) was added to quench the acid. The reaction volume was reduced and passed through a short silica plug with CH_2Cl_2 to remove black tarry side products. Recrystallisation with CH_2Cl_2/MeOH gave a purple metallic solid (2.25 g, 42%); δ_H (400 MHz, $CDCl_3$, 298 K) 10.31 (s, 2H, *meso-H*), 9.39 (d, 4H, *J* = 4.4 Hz, *β-H*), 9.20 (d, 4H, *J* = 4.6 Hz, *β-H*), 7.43 (d, 4H, *J* = 2.2 Hz, Ar-H^{ortho}), 6.92 (t, 2H, *J* = 2.1 Hz, Ar-H^{para}), 4.16 (t, 8H, *J* = 6.6 Hz, OCH_2), 1.93–1.86 (m, 8H, OCH_2CH_2), 1.55–1.28 (m, 40H, CH_2), 0.87 (t, 12H, *J* = 6.7 Hz, CH_3); Lit.[145] δ_H (400 MHz, $CDCl_3$) 10.33 (s, 2H), 9.37 (d, 4H, *J* = 4.5 Hz), 9.18 (d, 4H, *J* = 4.5 Hz), 7.48 (d, 4H, *J* = 2.1 Hz), 6.97 (t, 2H, *J* = 2.1 Hz), 4.18 (t, 8H, *J* = 6.5 Hz), 1.95–1.88 (m, 8H), 1.63–1.33 (m, 40H), 0.91 (t, 12H, *J* = 6.5 Hz).

Zinc 5,15-bis-(3,5-bis-octyloxy-phenyl)-porphyrin 102

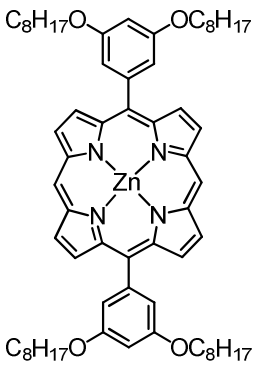

This compound was prepared according to published procedure.[145]

A methanolic solution (55.0 mL) of $Zn(OAc)_2.H_2O$ (2.68 g, 12.2 mmol) was added to a solution of free base 5,15-bis-(3,5-bis-octyloxy-phenyl)-porphyrin **101** (2.25 g, 2.31 mmol) in $CHCl_3$ (420 mL). After stirring at room temperature for 1 h, the reaction volume was reduced and passed through a short silica plug with CH_2Cl_2/ 40/60 petroleum ether (1:1). Precipitation with CH_2Cl_2/MeOH gave dark purple metallic crystals (2.19 g, 91%); δ_H (250 MHz, $CDCl_3$ / 5% d_5-pyridine, 298 K) 10.33 (s, 2H, *meso-H*), 9.44 (d, 4H, *J* = 4.5 Hz, *β-H*), 9.27 (d, 4H, *J* = 4.5 Hz, *β-H*), 7.44 (d, 4H, *J* = 2.3 Hz, Ar-H^{ortho}), 6.93 (t, 2H, *J* = 2.1 Hz, Ar-H^{para}), 4.16 (t, 8H, *J* = 6.6 Hz, OCH_2), 1.95–1.84 (m, 8H, OCH_2CH_2), 1.57–1.28 (m, 40H, CH_2), 0.87 (t, 12H, *J* = 6.8 Hz, CH_3); Lit.[145] δ_H (400 MHz, $CDCl_3$ / 5% d_5-pyridine) 10.23 (s, 2H), 9.40 (d, 4H, *J* = 4.4 Hz), 9.25 (d, 4H, *J* = 4.4 Hz), 7.46 (d, 4H, *J* = 2.1 Hz), 6.94 (t, 2H, *J* = 2.1 Hz), 4.18 (t, 8H, *J* = 6.5 Hz), 1.94–1.87 (m, 8H), 1.61–1.25 (m, 40H), 0.91 (t, 12H, *J* = 6.5 Hz).

Zinc 5,15-bis-(3,5-bis-octyloxy-phenyl)-10,20-dibromo-porphyrin 103

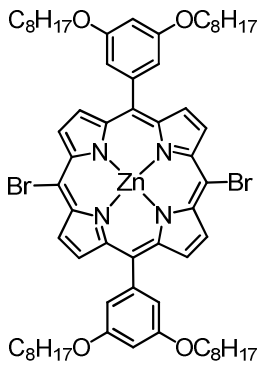

This compound was prepared according to published procedure.[145]

A solution of *N*-bromosuccinimide (0.17 g, 0.96 mmol) in $CHCl_3$ (11.0 mL) was added dropwise to a solution of zinc 5,15-bis-(3,5-bis-octyloxy-phenyl)-porphyrin **102** (0.50 g, 0.48 mmol) in $CHCl_3$ (16.0 mL) and pyridine (300 µL) under air. The reaction was quenched with acetone (1.0 mL). Recrystallisation in CH_2Cl_2/MeOH gave a dark purple solid (519 mg, 90%); δ_H (400 MHz, $CDCl_3$ / 5% d_5-pyridine, 298 K) 9.63 (d, 4H, *J* = 4.8 Hz, *β-H*), 8.98 (d, 4H, *J* = 4.8 Hz, *β-H*), 7.31 (d, 4H, *J* = 2.2 Hz, Ar-H^{ortho}), 6.88 (t, 2H, *J* = 2.2 Hz, Ar-H^{para}), 4.13 (t, 8H, *J* = 6.5 Hz, OCH_2), 1.91–1.84 (m, 8H, OCH_2CH_2), 1.51 (m, 8H, $OCH_2CH_2CH_2$), 1.41–1.26 (m, 32H, CH_2), 0.87 (t, 12H, *J* = 7.0 Hz, CH_3); *m/z* (MALDI-ToF MS+, dithranol) 1196 ($[M]^{\bullet+}$, $C_{64}H_{82}Br_2N_4O_4Zn$, requires 1196); Lit.[145] δ_H (400 MHz, $CDCl_3$ / 5% d_5-pyridine) 9.63 (m, 4H), 8.99 (m, 4H), 7.31 (d, 4H, *J* = 2.1 Hz), 6.89 (t, 2H, *J* = 2.1 Hz), 4.13 (t, 8H, *J* = 6.5 Hz), 1.91–1.84 (m, 8H), 1.63–1.28 (m, 40H), 0.87 (t, 12H, *J* = 6.6 Hz).

Zinc 5,15-bis-(3,5-bis-octyloxy-phenyl)-10,20-bis-trihexylsilanylethynyl-porphyrin monomer *l*-P1^{C8}

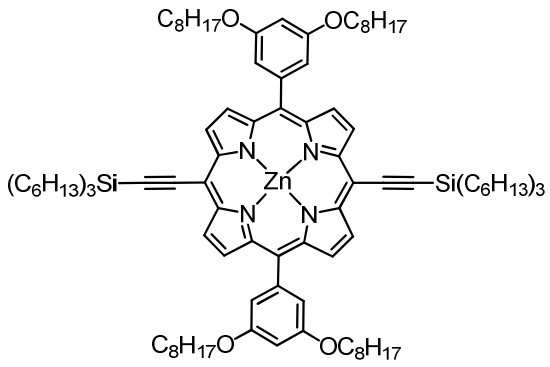

This compound was prepared according to published procedure.[145]

Zinc 5,15-bis-(3,5-bis-octyloxy-phenyl)-10,20-dibromo-porphyrin **103** (100 mg, 83.6 μmol), copper(I) iodide (3.8 mg, 20.1 μmol), $Pd_2(dba)_3$ (4.9 mg, 5.35 μmol) and triphenylphosphine (10.5 mg, 40.1 μmol) were placed under an argon atmosphere. Argon saturated toluene (3.3 mL) and triethylamine (3.3 mL) were added, and the solution freeze-thaw degassed. Ethynyltrihexylsilane **98** was added, and the reaction mixture was stirred at 40 °C for 2 h until TLC (10:1:1 40/60 petroleum ether : EtOAc : pyridine, R_f 0.80) showed the reaction to be complete. The reaction volume was reduced and passed through a short silica plug with 40/60 petroleum ether/pyridine (100:1). Recrystallisation with CH_2Cl_2/MeOH gave a metallic blue solid (0.56 g, 85%); δ_H (400 MHz, $CDCl_3$ / 5% d_5-pyridine, 298 K) 9.60 (d, 4H, J = 4.6 Hz, *β-H*), 8.93 (d, 4H, J = 4.6 Hz, *β-H*), 7.31 (d, 4H, J = 2.2 Hz, Ar-H^{ortho}), 6.86 (t, 2H, J = 2.1 Hz, Ar-H^{para}), 4.11 (t, 8H, J = 6.6 Hz, OCH_2), 1.89–1.70 (m, 20H, CH_2), 1.55–1.26 (m, 78H, CH_2), 1.01–0.83 (m, 40H, CH_2, CH_3); *m/z* (MALDI-ToF MS+, dithranol) 1652 ([M]$^{\bullet+}$, $C_{104}H_{160}N_4O_4Si_2Zn$, requires 1652); Lit.[145] δ_H (400 MHz, $CDCl_3$ / 5% d_5-pyridine) 9.76 (d, 4H, J = 4.5 Hz), 9.08 (d, 4H, J = 4.5 Hz), 7.32 (d, 4H, J = 2.1 Hz), 6.89 (t, 2H, J = 2.1 Hz), 4.15 (t, 8H, J = 6.6 Hz), 1.94–1.75 (m, 20H), 1.68–1.34 (m, 78H), 1.15–1.01 (m, 40H).

Zinc 5,15-bis-(3,5-bis-octyloxy-phenyl)-10,20-bis-trihexylsilanylethynyl-porphyrin dimer *l*-P2^{C8}

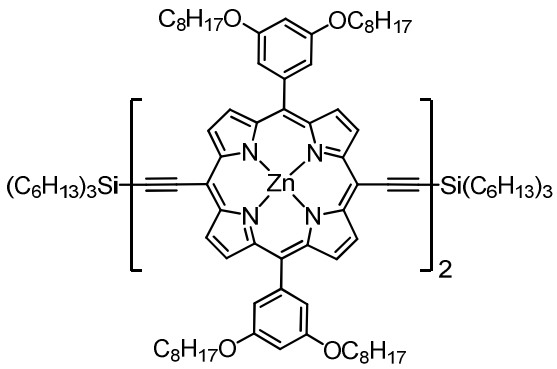

This compound was prepared by adaptation of a published procedure.[145]

Tetrabutylammonium fluoride (1.0 M solution in THF, 454 µL, 0.45 mmol) was added to a solution of zinc 5,15-bis-(3,5-bis-octyloxy-phenyl)-10,20-bis-trihexylsilanylethynyl-porphyrin monomer ***l*-P1^{C8}** (0.50 g, 0.30 mmol) and pyridine (15 µL) in $CHCl_3$ (32.0 mL) and CH_2Cl_2 (32.0 mL). The reaction mixture was stirred for 50 min at room temperature until TLC showed starting material and doubly-deprotected spots of approximately equal intensity (25:1:1 40/60 petroleum ether : EtOAc : pyridine; protected monomer ***l*-P1^{C8}** R_f 0.39; mono-deprotected ***l*-mP1^{C8}** R_f 0.21; doubly-deprotected ***l*-dP1^{C8}** R_f 0.03). The reaction mixture was immediately poured onto a short silica plug and eluted with CH_2Cl_2 to remove the TBAF. The mixture was columned on silica (25:1:1 → 18:1:1 40/60 petroleum ether : EtOAc : pyridine) to remove the mono-deprotected product.

The mono-deprotected product ***l*-mP1^{C8}** and freshly prepared copper(I) chloride (0.89 g, 9.00 mmol) were added to a 3 L round bottom flask equipped with a calcium chloride drying tube and made into a solution with dry CH_2Cl_2 (60.0 mL). *N*,*N*,*N*',*N*'-tetramethylethylenediamine (1.26 mL, 8.40 mmol) was added, and the reaction mixture stirred vigorously under air. After approximately 15 min, TLC (18:1:1 40/60 petroleum ether : EtOAc : pyridine, R_f 0.36) showed

complete conversion to dimer, so the mixture was passed through a short silica plug with CH_2Cl_2. The crude product was passed through a size-exclusion column with THF and precipitated with CH_2Cl_2/MeOH to give a olive green solid (0.28 g, 34%); δ_H (250 MHz, $CDCl_3$ / 5% d_5-pyridine, 298 K) 9.86 (d, 4H, *J* = 4.6 Hz, *β-H*), 9.64 (d, 4H, *J* = 4.6 Hz, *β-H*), 9.06 (d, 4H, *J* = 4.6 Hz, *β-H*), 8.96 (d, 4H, *J* = 4.6 Hz, *β-H*), 7.37 (s, 8H, Ar-H^{ortho}), 6.91 (s, 4H, Ar-H^{para}), 4.17 (t, 16H, *J* = 6.0 Hz, OCH_2), 1.92–1.72 (m, 28H, CH_2), 1.55–1.29 (m, 116H, CH_2), 1.06–0.99 (m, 12H, CH_2), 0.94–0.85 (m, 42H, CH_3); *m/z* (MALDI-ToF MS+, dithranol) 2734 ([M]$^{\bullet+}$, $C_{172}H_{242}N_8O_8Si_2Zn_2$, requires 2737); Lit.[145] δ_H (400 MHz, $CDCl_3$ / 5% d_5-pyridine) 9.98 (d, 4H, *J* = 4.4 Hz), 9.74 (d, 4H, *J* = 4.4 Hz), 9.17 (d, 4H, *J* = 4.5 Hz), 9.06 (d, 4H, *J* = 4.5 Hz), 7.43 (d, 8H, *J* = 1.9 Hz), 6.93 (t, 4H, *J* = 1.9 Hz), 4.20 (t, 16H, *J* = 6.4 Hz), 1.98–1.82 (m, 28H), 1.67–1.35 (m, 116H), 1.17–1.03 (m, 12H), 1.01–0.93 (m, 42H).

Zinc 5,15-bis-(3,5-bis-octyloxy-phenyl)-10,20-bis-trihexylsilanylethynyl-porphyrin tetramer *l*-P4^{C8}

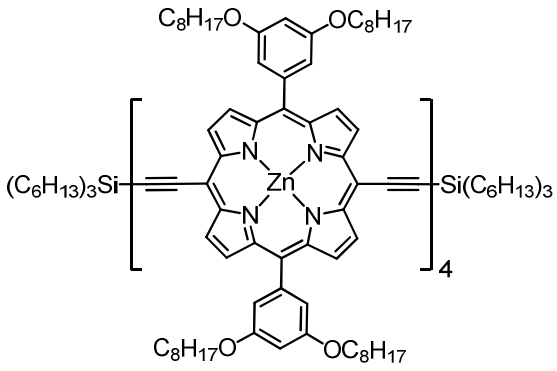

This compound was prepared by adaptation of a published procedure.[145]

Tetrabutylammonium fluoride (1.0 M solution in THF, 56 µL, 55.9 mmol) was added to a solution of zinc 5,15-bis-(3,5-bis-octyloxy-phenyl)-10,20-bis-trihexylsilanylethynyl-porphyrin dimer ***l*-P2^{C8}** (0.10 g, 37 µmol) and pyridine (15 µL) in $CHCl_3$ (3.5 mL) and CH_2Cl_2 (3.5 mL). The reaction mixture was stirred for 50 min at room temperature until TLC (18:1:1 40/60

petroleum ether : EtOAc : pyridine) showed starting material and doubly-deprotected spots of approximately equal intensity. The reaction mixture was immediately poured onto a short silica plug and eluted with CH_2Cl_2 to remove the TBAF. The mixture was then columned on silica (12:1:1 40/60 petroleum ether : EtOAc : pyridine) to remove the mono-deprotected product ***l*-mP2^{C8}**.

The mono-deprotected product ***l*-mP2^{C8}** and freshly prepared copper(I) chloride (54.3 mg, 0.55 mmol) were added to a 3 L round bottom flask equipped with a calcium chloride drying tube and made into a solution with dry CH_2Cl_2 (7.0 mL). *N*,*N*,*N*',*N*'-tetramethylethylenediamine (83 μL, 0.55 mmol) was added, and the reaction mixture stirred vigorously under air. After 15 min, the mixture was passed through a short silica plug with CH_2Cl_2. The crude product was passed through a size-exclusion column with THF and precipitated with CH_2Cl_2/MeOH to give a brown solid (17.3 mg, 77%); δ_H (250 MHz, $CDCl_3$ / 5% d_5-pyridine, 298 K) 9.87 (dt, 12H, J_1 = 4.4 Hz, J_2 = 2.1 Hz, *β-H*), 9.63 (d, 4H, *J* = 4.6 Hz, *β-H*), 9.06 (dd, 12H, J_1 = 4.6 Hz, J_2 = 2.0 Hz, *β-H*), 8.96 (d, 4H, *J* = 4.6 Hz, *β-H*), 7.41 (d, 8H, *J* = 2.1 Hz, Ar-H^{ortho}), 7.37 (d, 8H, *J* = 2.1 Hz, Ar-H^{ortho}), 6.93–6.89 (m, 8H, Ar-H^{para}), 4.21–4.13 (m, 32H, OCH_2), 1.96–1.72 (m, 44H, CH_2), 1.54–1.28 (m, 196H, CH_2), 1.05–0.83 (m, 78H, CH_2, CH_3); *m/z* (MALDI-ToF MS+, dithranol) 4904 ([M]$^{\bullet+}$, $C_{308}H_{406}N_{16}O_{16}Si_2Zn_4$, requires 4907); Lit.[145] δ_H (400 MHz, $CDCl_3$ / 5% d_5-pyridine) 9.90 (m, 12H), 9.65 (d, 4H, *J* = 4.6 Hz), 9.08 (m, 12H), 8.98 (d, 4H, *J* = 4.6 Hz), 7.44 (d, 8H, *J* = 2.0 Hz), 7.39 (d, 8H, *J* = 2.0 Hz), 6.93 (m, 8H), 4.20 (m, 32H), 1.93–1.72 (m, 44H), 1.56–1.30 (m, 196H), 1.08–0.85 (m, 78H).

Zinc 5,15-bis-(3,5-bis-octyloxy-phenyl)-10,20-bis-ethynyl-porphyrin tetramer *I*-dP4^{C8}

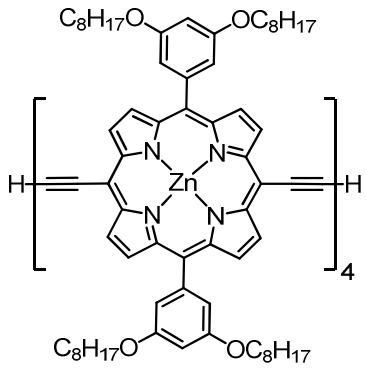

This compound was prepared according to published procedure.[75]

Tetrabutylammonium fluoride (1.0 M solution in THF, 12 µL, 12.3 µmol) was added to a stirring solution of zinc 5,15-bis-(3,5-bis-octyloxy-phenyl)-10,20-bis-ethynyl-porphyrin tetramer ***I*-P4^{C8}** (12.1 mg, 2.5 µmol) and pyridine (10 µL) in dry CH_2Cl_2 (3.0 mL). Once the reaction was shown to be complete by TLC (85:5:10 40/60 petroleum ether : THF : pyridine, R_f 0.15), the mixture was passed through a short silica plug with CH_2Cl_2 to give a green brown solid (10.6 mg, 99%); δ_H (500 MHz, $CDCl_3$ / 5% d_5-pyridine, 298 K) 9.90-9.88 (m, 12H, *β-H*), 9.66 (d, 4H, *J* = 4.4 Hz, *β-H*), 9.09–9.07 (m, 12H, *β-H*), 8.99 (d, 4H, *J* = 4.4 Hz, *β-H*), 7.42 (d, 8H, *J* = 1.9 Hz, Ar-H^{ortho}), 7.38 (d, 8H, *J* = 2.0 Hz, Ar-H^{ortho}), 6.93 (d, 8H, *J* = 9.6 Hz, Ar-H^{para}), 4.21–4.16 (m, 32H, OCH_2), 1.54 (dq, J_1 = 14.7 Hz, J_2 = 7.2 Hz, OCH_2CH_2), 1.42–1.26 (m, 160H, CH_2), 0.90–0.86 (m, 48H, CH_3); *m/z* (MALDI-ToF MS+, dithranol) 4340 ($[M]^{\bullet+}$, $C_{272}H_{330}N_{16}O_{16}Zn_4$, requires 4341); Lit.[75] δ_H (400 MHz, $CDCl_3$ / 5% d_5-pyridine) 9.89 (m, 12H), 9.63 (d, 4H, *J* = 4.4 Hz), 9.08 (m, 12H), 8.98 (d, 4H, *J* = 4.4 Hz), 7.42 (d, 8H, *J* = 2.0 Hz), 7.38 (d, 4H, *J* = 2.0 Hz), 6.92 (m, 8H), 4.18 (m, 32H), 1.90 (m, 32H), 1.53–1.29 (m, 160H), 0.87 (m, 48H).

Zinc 5,15-bis-(3,5-bis-octyloxy-phenyl)-10,20-bis-trihexylsilanylethynyl-porphyrin octamer *l*-P8^{C8}

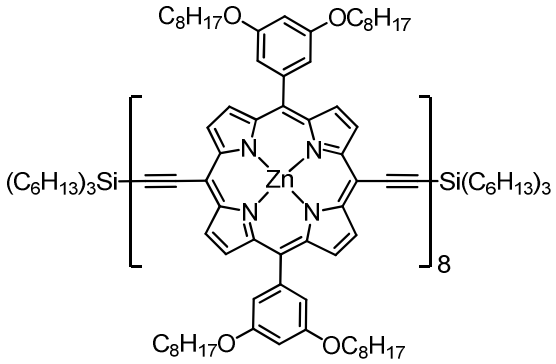

Tetrabutylammonium fluoride (1.0 M solution in THF, 19 µL, 18.5 µmol) was added to a solution of zinc 5,15-bis-(3,5-bis-octyloxy-phenyl)-10,20-bis-trihexylsilanylethynyl-porphyrin tetramer ***l*-P4^{C8}** (60.4 mg, 12.3 µmol) and pyridine (15 µL) in $CHCl_3$ (4.0 mL) and CH_2Cl_2 (4.0 mL). The reaction mixture was stirred for 50 min at room temperature until TLC (16:2:1 40/60 petroleum ether : THF : pyridine) showed starting material and doubly-deprotected spots of roughly equal intensity. The reaction mixture was immediately poured onto a short silica plug and eluted with CH_2Cl_2/pyridine (10:1) to remove the TBAF. The mixture was then purified by preparative GPC (10% pyridine in toluene, 8.5 mL min^{-1}) to remove the mono-deprotected product ***l*-mP4^{C8}**.

The mono-deprotected product ***l*-mP4^{C8}** and freshly prepared copper(I) chloride (13.3 mg, 0.14 mmol) were added to a 500 mL round bottom flask equipped with a calcium chloride drying tube and made into a solution with dry CH_2Cl_2 (3.0 mL). *N*,*N*,*N*',*N*'-tetramethylethylenediamine (19 µL, 0.13 mmol) was added, and the reaction mixture stirred vigorously under air. After 30 min, the mixture was passed through a short silica plug with CH_2Cl_2/pyridine (10:1). The crude product was passed through a size-exclusion column with THF and precipitated with CH_2Cl_2/MeOH to give a brown solid (6.4 mg, 11% over two steps);

δ_H (250 MHz, $CDCl_3$ / 5% d_5-pyridine, 298 K) 9.90 (m, 28H, *β-H*), 9.64 (d, 4H, *J* = 4.6 Hz, *β-H*), 9.09 (m, 28H, *β-H*), 8.97 (d, 4H, *J* = 4.6 Hz, *β-H*), 7.43-7.38 (m, 32H, Ar-H^{ortho}), 6.95–6.92 (m, 32H, Ar-H^{para}), 4.19 (m, 64H, OCH_2), 1.96–1.86 (m, 60H, CH_2), 1.81–1.75 (m, 6H, CH_2), 1.61–1.25 (m, 372H, CH_2), 1.06–1.00 (m, 6H, CH_2), 0.94–0.81 (m, 114H, CH_3); Lit.[145] δ_H (250 MHz, $CDCl_3$ / 5% d_5-pyridine, 298 K) 9.89 (m, 28H), 9.64 (d, 4H, *J* = 4.5 Hz), 9.08 (m, 28H), 8.97 (d, 4H, *J* = 4.5 Hz), 7.44–7.38 (m, 32H), 6.95–6.91 (m, 32H), 4.21 (m, 64H), 1.96–1.87 (m, 60H), 1.82–1.75 (m, 6H), 1.61–1.25 (m, 372H), 1.07–1.00 (m, 6H), 0.94–0.86 (m, 114H).

Hexakis(4-bromophenyl)benzene 96

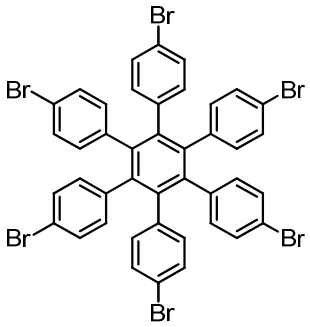

This compound was prepared according to published procedure.[128]

Neat bromine (1.30 mL, 26.2 mmol) was added dropwise to hexaphenylbenzene (1.00 g, 1.87 mmol), capturing the evolved HBr gas with an aqueous sodium hydroxide trap. The resulting slurry was stirred at room temperature for 1 h. To quench, the reaction mixture was cooled to –78 °C and ethanol (20.0 mL) was added slowly. The resulting precipitate was filtered and washed with aqueous sodium thiosulfate. Recrystallisation with CH_2Cl_2/MeOH gave a white powder (1.88 g, 99%); δ_H (250 MHz, $CDCl_3$, 298 K) 7.06 (d, 12H, *J* = 8.5 Hz, Ar-*H*), 6.62 (d, 12H, *J* = 8.5 Hz, Ar-*H*); Lit.[128] δ_H (400 MHz, $CDCl_3$) 7.07 (d, 12H, *J* = 8.5 Hz), 6.61 (d, 12H, *J* = 8.5 Hz).

Hexadentate template T6

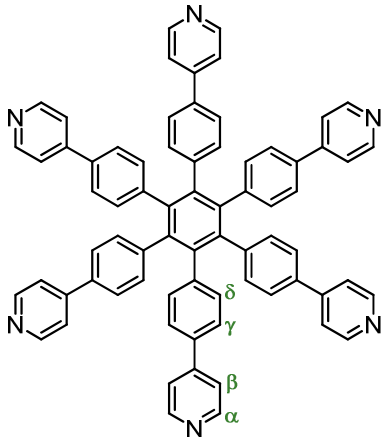

This compound was prepared according to published procedure.[128]

Hexakis(4-bromophenyl)benzene **96** (0.30 g, 0.30 mmol), 4-pyridine boronic acid (0.88 g, 7.14 mmol), $Pd(PPh_3)_2Cl_2$ (40.0 mg, 59.5 μmol) and sodium hydrogencarbonate (0.45 g, 5.36 mmol) were placed under an argon atmosphere. Argon saturated dimethoxyethane (9.0 mL), THF (21.0 mL) and water (12.0 mL) were added and the solution freeze-thaw degassed. The reaction mixture was stirred at 70 °C for 3 d. Additional 4-pyridine boronic acid (0.28 g, 1.79 mmol) and palladium catalyst (20.9 mg, 29.8 μmol) were added, and the mixture stirred at 70 °C for a further 2 d. The mixture was dissolved in CH_2Cl_2, and washed with brine. The organic layer was columned on silica (10:1:0.05 CH_2Cl_2: MeOH : Et_3N), and the resulting yellow solid was dissolved in hot pyridine, and precipitated with triethylamine to give a white powder (0.11 g, 35%); δ_H (400 MHz, $CDCl_3$, 298 K) 8.54 (br d, 12H, J = 3.8 Hz, α), 7.33 (d, 12H, J = 5.3 Hz, β), 7.26 (d, 12H, J = 8.2 Hz, γ), 7.03 (d, 12H, J = 8.2 Hz, δ); Lit.[128] δ_H (400 MHz, $CDCl_3$) 8.36 (d, 12H, J = 5.5 Hz), 7.29 (d, 12H, J = 5.5 Hz), 7.18 (d, 12H, J = 8.5 Hz), 6.96 (d, 12H, J = 8.5 Hz).

***Tert*-butyl cyclic hexamer complex *c*-P6·T6**

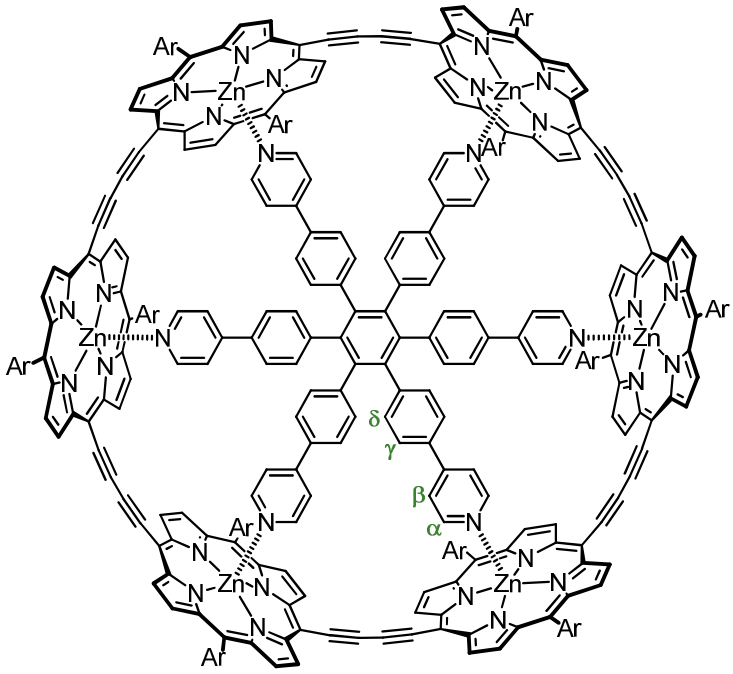

This compound was prepared by modification of a published procedure.[135]

Deprotected *tert*-butyl porphyrin dimer ***l*-dP2** (26.5 mg, 16.6 μmol) and hexadentate template **T6** (5.5 mg, 5.52 μmol) were sonicated in CH_2Cl_2 (5.0 mL) for 1 h. A catalyst solution of $Pd(PPh_3)_2Cl_2$ (5.1 mg, 7.27 μmol), copper(I) iodide (7.2 mg, 37.7 μmol), 1,4-benzoquinone (16.3 mg, 0.14 mmol), and $^{i}Pr_2NH$ (265 μL) was made in $CHCl_3$ (38.0 mL), and added to the solution of the dimer-template complex. The mixture was stirred at room temperature for 1 h and then 50 °C for 1.5 h until no further change was observed by UV-vis. The crude was passed over a 10 cm alumina plug in $CHCl_3$, and then purified by preparatory GPC with toluene at 8.5 mL min^{-1}, isolating the major peak. Recrystallisation by layer addition (CH_2Cl_2/MeOH) yielded a brown solid (6.8 mg, 21%); δ_H (400 MHz, $CDCl_3$, 298 K) 9.58 (d, 24H, *J* = 4.5 Hz, *β-H*), 8.81 (d, 24H, *J* = 4.5 Hz, *β-H*), 8.05 (m, 12H, Ar-H^{ortho}), 7.86 (m, 12H, Ar-H^{ortho}), 7.80 (d, 12H, *J* = 1.6 Hz, Ar-H^{para}), 5.51 (d, 12H, *J* = 9.0 Hz, δ), 5.45 (d, 12H, *J* = 9.0 Hz, γ), 5.00 (m, 12H, β), 2.42 (m, 12H, α), 1.57 (s, 108H, ^{t}Bu), 1.53 (s, 108H, ^{t}Bu); *m/z* (MALDI-ToF MS+, dithranol) 5775 ($[M]^{\bullet+}$,

$C_{384}H_{348}N_{30}Zn_6$, requires 5775); Lit.[128] δ_H (400 MHz, $CDCl_3$, 298 K) 9.59 (d, 24H, *J* = 4.5 Hz), 8.81 (d, 24H, *J* = 4.5 Hz), 8.05 (s, 12H), 7.86 (s, 12H), 7.81 (s, 12H), 5.52 (d, 12H, *J* = 9.0 Hz), 5.48 (d, 12H, *J* = 9.0 Hz), 5.00 (d, 12H, *J* = 7.0 Hz), 2.33 (d, 12H, *J* = 7.0 Hz), 1.58 (s, 108H), 1.54 (s, 108H).

Free base *tert*-butyl cyclic hexamer 2H.*c*-P6

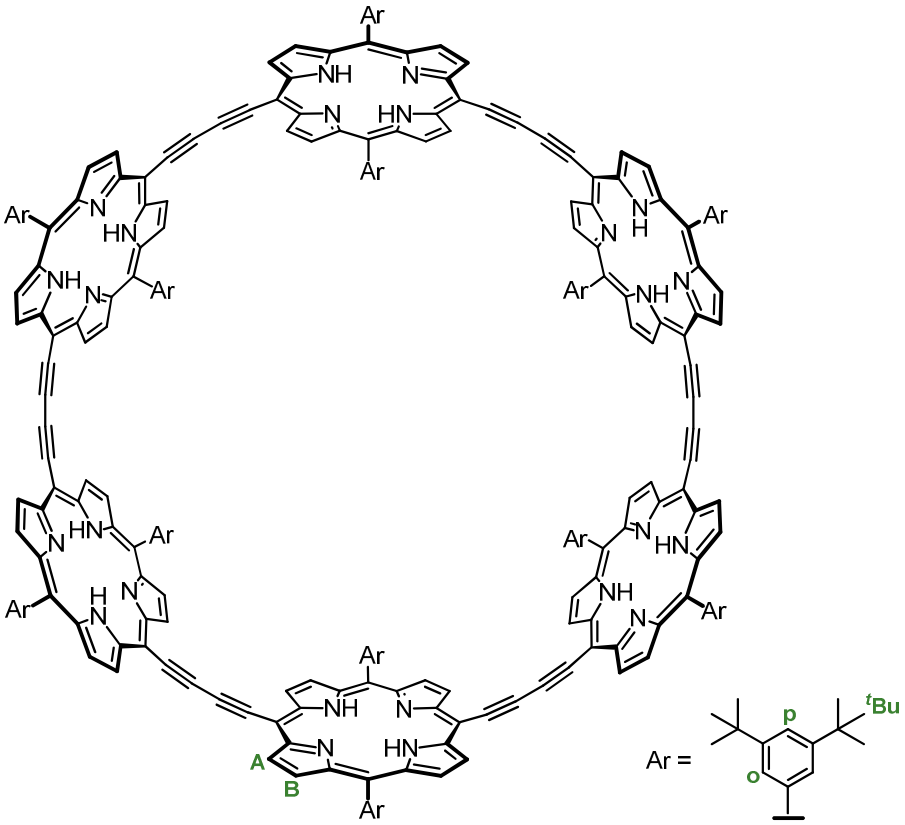

This compound was prepared according to published procedure.[308]

Trifluoroacetic acid in $CHCl_3$ (1.3 M, 410 µL, 53.7 mmol) was added to a solution of *tert*-butyl cyclic hexamer complex ***c*-P6.T6** (3.1 mg, 0.54 µmol) in $CHCl_3$ (2.5 mL) and stirred for 15 min. An excess of pyridine (500 µL) was added, and the solution stirred for a further 15 min, before being passed down a short silica plug with $CHCl_3$. The solvent was removed to yield a dark green solid (2.3 mg, 97%); δ_H (250 MHz, $CDCl_3$/1% d_5-pyridine, 298 K) 9.62 (d, 24H, *J* = 4.7 Hz,

A), 8.79 (d, 24H, *J* = 4.7 Hz, B), 7.91 (d, 24H, *J* = 1.8 Hz, o), 7.75 (br t, 12H, p), 1.49 (s, 216H, ^{t}Bu), –1.33 (br s, 12H, N*H*). Lit.[308] δ_H (400 MHz, $CDCl_3$, 298 K) 9.62 (d, 24H, *J* = 4.5 Hz), 8.80 (d, 24H, *J* = 4.5Hz), 7.96 (d, 24H, *J* = 1.3 Hz), 7.83 (t, 12H, *J* = 1.3 Hz), 1.51 (s, 216H), 1.33 (s, 12H).

***Tert*-butyl cyclic hexamer *c*-P6**

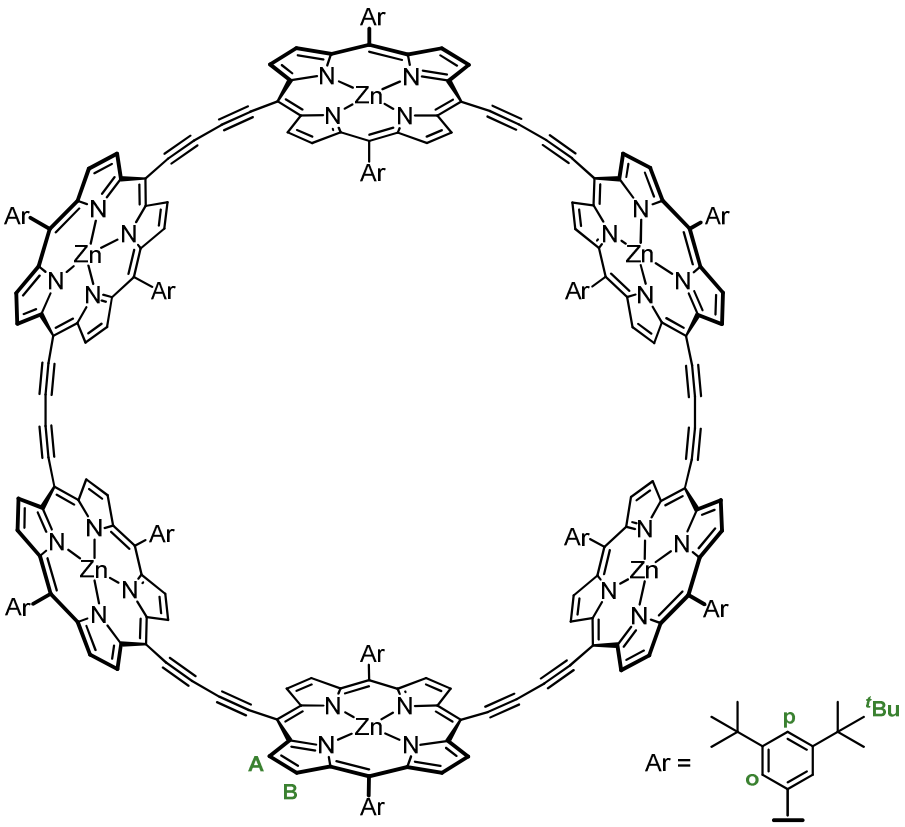

This compound was prepared according to published procedure.[308]

A methanolic solution (100 µL) of $Zn(OAc)_2.2H_2O$ (4.0 mg, 18.2 µmol) was added to a solution of free base *tert*-butyl cyclic hexamer **2H.*c*-P6** (2.3 mg, 0.52 µmol) in CH_2Cl_2 (3.0 mL), and the mixture was stirred at 36 °C for 2 h until no further change was observed by UV-Vis. The solution was passed down a short silica column with CH_2Cl_2. Recrystallisation by layer addition (CH_2Cl_2/MeOH) gave a brown solid (1.5 mg, 58%); δ_H (250 MHz, $CDCl_3$/1% d_5-pyridine, 298 K) 9.62 (d, 24H, *J* = 4.6 Hz, A), 8.79 (d, 24H, *J* = 4.6 Hz, B), 7.91 (d, 24H, *J* = 1.8 Hz, o), 7.75 (t, 12H, *J*

= 1.7 Hz, p), 1.49 (s, 216H, ^{t}Bu); *m/z* (MALDI-ToF MS+, dithranol) 4777 ([M]$^{\bullet+}$, $C_{312}H_{300}N_{24}Zn_6$, requires 4778); Lit.[128] δ_H (400 MHz, $CDCl_3$, 298 K) 9.62 (d, 24 H, *J* = 4.5 Hz), 8.79 (d, 24H, *J* = 4.5 Hz), 7.90 (d, 24H, *J* = 1.5 Hz), 7.75 (d, 12H, *J* = 1.5 Hz), 1.49 (s, 216H).

Octadentate template T8

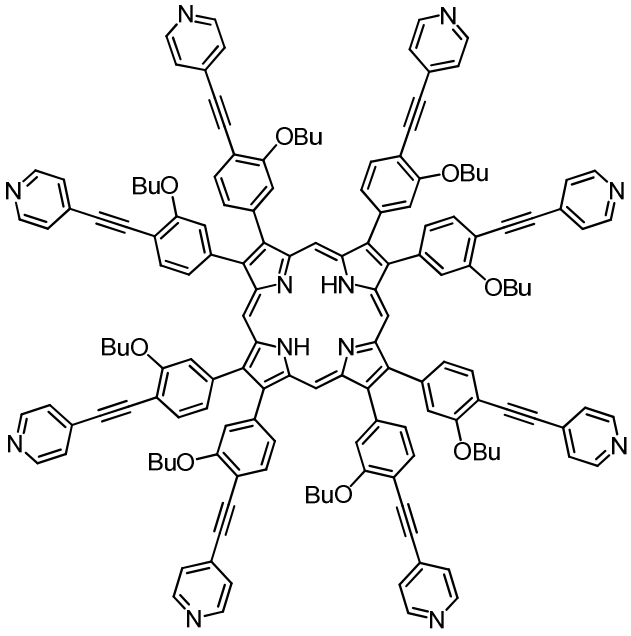

This compound was prepared according to published procedure.[131]

Lithium aluminium hydride (1.0 M in THF, 1.5 mL, 1.50 mmol) was added dropwise to a solution of *tert*-butyl 3,4-bis(3-butoxy-4-(pyridin-4-ylethynyl)phenyl)-1H-pyrrole-2-carboxylate **15** (500 mg, 0.75 mmol) in dry THF (20.0 mL) cooled in an ice bath. The reaction mixture was stirred at 0 °C for 30 min, then quenched by dropwise addition of aqueous sodium hydroxide (1.0 M, 30.0 mL). The mixture was extracted with CH_2Cl_2 and washed with brine. The organic layer was dried over magnesium sulfate and the solvents removed.

The crude product was dissolved in CH_2Cl_2 (100 mL), and dimethoxymethane (200 µL, 2.25 mmol) was added and the solution degassed. The mixture was protected from the light, and *p*-

toluene sulfonic acid monohydrate (570 mg, 3.00 mmol) was added. The mixture was degassed again and stirred overnight in the dark. DDQ (170 mg, 0.75 mmol) was added and the reaction mixture stirred for 30 min before quenching by addition of triethylamine (1.0 mL). The solvents were removed, and the crude product was purified by column chromatography on silica (100:1:1 → 40:1:1 CH_2Cl_2 : MeOH : NEt_3). Recrystallisation by layer addition (CH_2Cl_2/MeOH) gave a purple solid (39.0 mg, 9%); δ_H (400 MHz, $CDCl_3$, 298 K) 10.57 (s, 4H, *meso-H*), 8.66 (br s, 16H, py-*H*), 7.81 (d, 8H, *J* = 8.0 Hz, Ar-*H*), 7.61 (d, 8H, *J* = 8.0 Hz, Ar-*H*), 7.53 (s, 8H, Ar-*H*), 7.45 (d, 16H, *J* = 5.5 Hz, py-*H*), 3.91 (t, 8H, *J* = 6.5 Hz, OCH_2), 1.83 (m, 16H, CH_2), 1.57 (m, 16H, CH_2), 0.99 (t, 24H, *J* = 7.5 Hz, CH_3), –2.87 (s, 2H, N*H*); *m/z* (MALDI-ToF MS+, dithranol) 2308 ($[M]^{\bullet+}$, $C_{156}H_{134}N_{12}O_8$, requires 2305); Lit.[131] δ_H (400 MHz, $CDCl_3$, 298 K) 10.57 (s, 4H), 8.66 (d, 16H, *J* = 5.5 Hz), 7.81 (d, 8H, *J* = 7.8 Hz), 7.61 (m, 8H), 7.54 (d, 8H, *J* = 2.1 Hz), 7.45 (d, 16H, *J* = 5.0 Hz), 3.92 (t, 16H, *J* = 6.3 Hz), 1.90–1.77 (m, 16H), 1.67–1.49 (m, 16H), 1.00 (t, 24H, *J* = 7.3 Hz), –2.88 (s, 2H).

6.3 Synthesis of novel compounds

Tert-butyl 3,4-diphenyl-1H-pyrrole-2-carboxylate 53

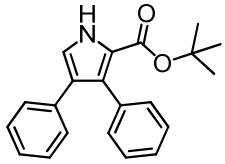

This compound was prepared by adaptation of a published procedure.[131]

WARNING: KCN IS PRODUCED AS A SIDEPRODUCT. KCN IS HIGHLY TOXIC. DISPOSAL: ALL CONTAMINATED MATERIALS AND RESIDUES WERE TREATED WITH SODIUM HYPOCHLORITE FOR 24 HOURS BEFORE DILUTING AND DISPOSING DOWN THE DRAIN.

A solution of 2,3-diphenylacrylonitrile **52** (1.11 g, 5.39 mmol) and *tert*-butyl isocyanoacetate (1.2 mL, 8.09 mmol) in dry THF (7.5 mL) was added dropwise to a suspension of potassium *tert*-butoxide (2.18 g, 19.4 mmol) in THF (7.5 mL) at 0 °C under N_2. The mixture was stirred at 50 °C for 1 h. The reaction solvent was removed under reduced pressure and resulting solid passed through a silica column (CH_2Cl_2, R_f 0.50). The resulting yellow solid was recrystallised in ethanol to give pale yellow crystals (0.74 g, 63%); δ_H (400 MHz, CD_2Cl_2, 298 K) 9.41 (br s, 1H, N*H*), 7.32–7.23 (m, 5H, Ar-*H* adj. $CO_2{}^t$Bu), 7.19–7.12 (m, 3H, Ar-H^{meta}, C-*H*), 7.11–7.09 (m, 3H, Ar-H^{ortho}, Ar-H^{para}), 1.35 (s, 9H, ^{t}Bu); δ_C (125 MHz, CD_2Cl_2) 160.95, 135.54, 135.24, 131.25, 128.72, 128.61, 128.46, 127.84, 126.96, 126.73, 126.31, 121.93, 120.04, 81.25, 28.27; *m/z* (ESI MS+) 342.1456 ($[M+Na]^{\bullet+}$, $C_{21}H_{21}NNaO_2$, requires 342.1465); Found: C 78.44, H 6.65, N 4.33 %, Calc. for $C_{21}H_{21}NO_2$: C 78.97, H 6.63, N 4.39 %; m.p. 169–172 °C.

***Tert*-butyl 1,3,4-triphenyl-1H-pyrrole-2-carboxylate 54**

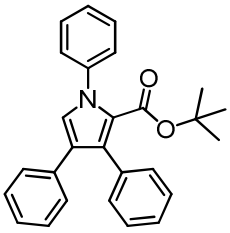

This compound was prepared by adaptation of a published procedure.[141]

To a mixture of *tert*-butyl 3,4-diphenyl-1H-pyrrole-2-carboxylate **53** (50.0 mg, 0.29 mmol), copper(I) iodide (2.2 mg, 0.11 μmol) and potassium phosphate (0.10 g, 0.48 mmol) under argon, phenyl iodide (30 μL, 0.27 mmol), *N,N'*-dimethylethylenediamine (5 μL, 0.46 μmol) and degassed toluene (1.0 mL) were added, and the mixture heated to 110 °C for 1 d until TLC (CH_2Cl_2, R_f 0.67) showed complete consumption of starting material. The reaction mixture was diluted with $CHCl_3$, washed with saturated aqueous ammonium chloride and concentrated under reduced pressure. Precipitation with pentane gave a white solid (41.2 mg, 46%); δ_H (500 MHz, $CDCl_3$, 298 K) 7.49–7.46 (m, 2H, Ar-*H*), 7.42–7.39 (m, 3H, Ar-*H*), 7.31 (s, 5H, Ar-*H*), 7.20–7.17 (m, 2H, Ar-*H*), 7.16–7.11 (m, 3H, Ar-*H*), 7.07 (s, 1H, C-*H*), 1.14 (s, 9H, ^{t}Bu); δ_C (125 MHz, $CDCl_3$) 160.22, 140.94, 135.26, 134.31, 130.84, 130.70, 128.79, 128.13, 128.10, 127.61, 127.53, 126.65, 125.97, 125.73, 125.39, 125.18, 123.23, 80.72, 27.61; *m/z* (ESI MS+) 418.1777 ($[M+Na]^{\bullet+}$, $C_{27}H_{25}NNaO_2$, requires 418.1778); m.p. 128–129 °C.

***Tert*-butyl 1-[4-(4-{2,3,4,5,6-pentakis[4-(4-{2-[(*tert*-butoxy)carbonyl]-3,4-diphenyl-1H-pyrrol-1-yl}phenyl)phenyl]phenyl}phenyl)phenyl]-3,4-diphenyl-1H-pyrrole-2-carboxylate 55**

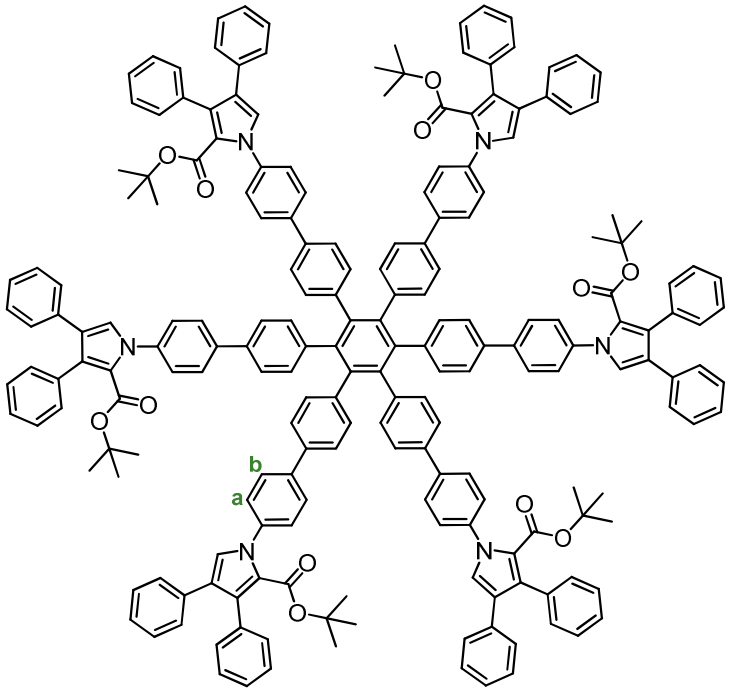

This compound was prepared by adaptation of a published procedure.[141]

1,2,3,4,5,6-hexakis[4-(4-iodophenyl)phenyl]benzene **27** (25.0 mg, 14.3 μmol), *tert*-butyl 3,4-diphenyl-1H-pyrrole-2-carboxylate **53** (91.4 mg, 0.29 mmol), copper(I) iodide (16.4 mg, 85.9 μmol) and potassium phosphate (79.0 mg, 0.37 mmol) were ground to a fine powder using a mortar and pestle, then put under an argon atmosphere. *N,N'*-dimethylethylenediamine (37 μL, 0.34 mmol) and argon-saturated toluene (1.5 mL) were added, and the solution freeze-thaw degassed. After stirring at 110 °C for 2 d, the crude was columned on silica (1:4 EtOAc : 40/60 petroleum ether). The solvent was removed to give a brown oil. Precipitation by slow addition of ethyl acetate afforded the pure product as a white powder (14.9 mg, 37%); δ_H (400 MHz, CD_2Cl_2, 298 K) 7.57 (d, 12H, *J* = 8.5 Hz, b), 7.36 (d, 12H, *J* = 8.5 Hz, a), 7.32–7.24 (m, 42H,

Ar-*H*), 7.14–7.07 (m, 42H, Ar-*H*), 7.04 (s, 6H, C-*H*), 1.07 (s, 54H, ^{t}Bu); δ_C (125 MHz, CD_2Cl_2) 160.45, 140.75, 140.55, 140.37, 140.22, 137.36, 136.03, 134.81, 132.54, 131.25, 131.14, 128.54, 128.47, 127.96, 127.40, 127.02, 126.41, 126.30, 125.83, 125.76, 125.58, 123.55, 81.00, 78.01, 77.75, 77.50, 27.84; *m/z* (MALDI-ToF MS+, DCTB) 2894 ($[M]^{\bullet+}$, $C_{204}H_{168}N_6O_{12}$, requires 2894); Found: C 84.58, H 5.76, N 2.82 %, Calc. for $C_{204}H_{168}N_6O_{12}$: C 84.62, H 5.85, N 2.90 %; m.p. 251–256 °C.

[12]template T12

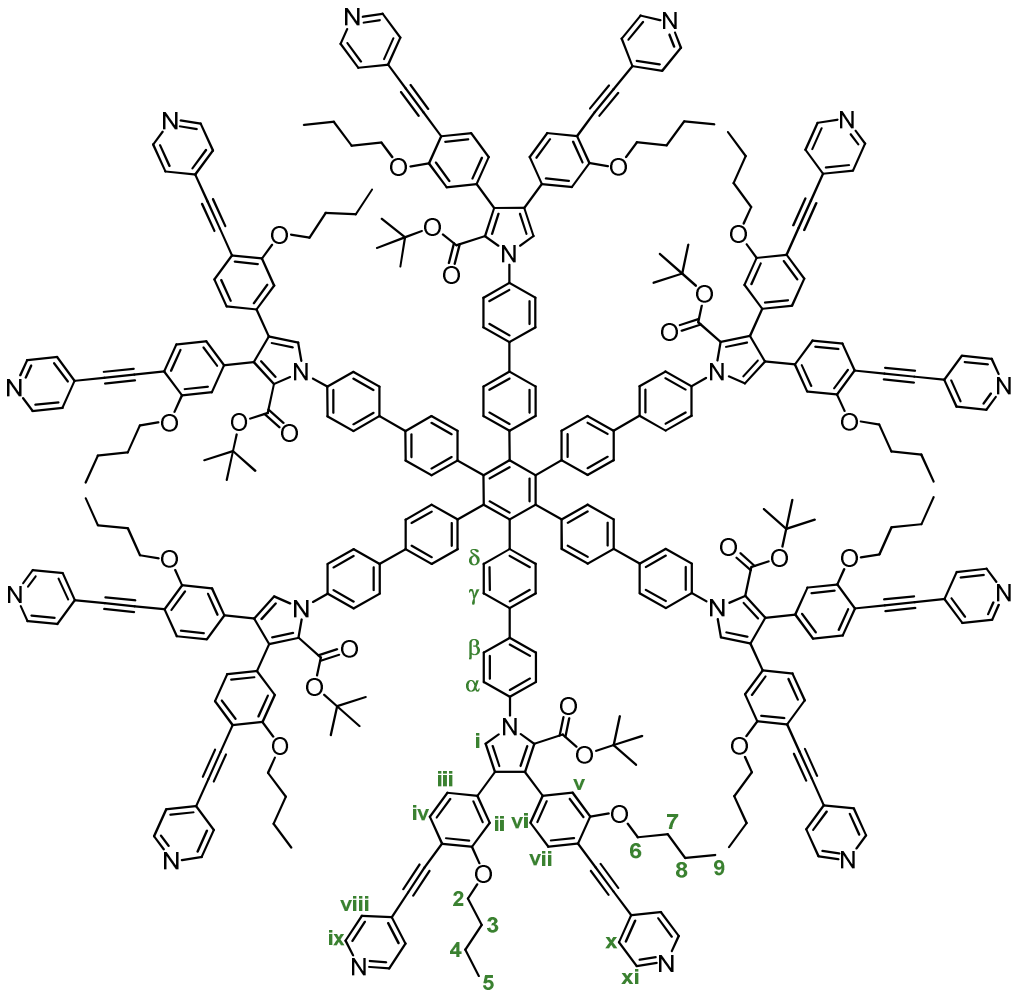

1,2,3,4,5,6-Hexakis[4-(4-iodophenyl)phenyl]benzene **27** (50.0 mg, 28.6 μmol), *tert*-butyl 3,4-bis(3-butoxy-4-(pyridin-4-ylethynyl)phenyl)-1H-pyrrole-2-carboxylate **15** (381 mg, 0.57 mmol), copper(I) iodide (98.2 mg, 0.52 mmol) and potassium phosphate (474 mg, 2.23 mmol) were put under an argon atmosphere. *N,N'*-Dimethylethylenediamine (222 μL, 2.06 mmol) and argon-saturated dry toluene (3.0 mL) were added, and solution degassed using the freeze-thaw method. After 3 d of stirring at 110 °C, the solvent was removed and resulting residue dissolved in CH_2Cl_2 and washed with saturated aqueous ammonium chloride. The organic layer was dried with magnesium sulfate and solvent removed. The yellow oil was passed down a

short size-exclusion column (Biobeads SX-1) in THF to remove excess starting material and low molecular weight side products. Fractions containing compound at R_f = 0 (20:1 ethyl acetate/pyridine) were collected, dissolved in CH_2Cl_2 and purified by HPLC (ACE 5 μm CN 150 × 10 mm id column, heptane/ CH_2Cl_2 /pyridine ramp, 3.5 mL min^{-1} flow rate, 313 K) to give the pure template as a pale yellow solid (4.2 mg, 4%); δ_H (500 MHz, $CDCl_3$, 298 K) 8.61 (br s, 24H, ix, xi), 7.62 (d, 12H, *J* = 8.2 Hz, β), 7.48 (d, 6H, *J* = 8.0 Hz, vii), 7.39 (d, 12H, *J* = 8.2 Hz, α), 7.38 (br s, 24H, viii, x), 7.33 (d, 6H, *J* = 8.0 Hz, iv), 7.30 (d, 12H, *J* = 8.2 Hz, γ), 7.12 (s, 6H, i), 7.07 (d, 12H, *J* = 8.0 Hz, δ), 6.93 (d, 6H, *J* = 8.0 Hz, vi), 6.83 (s, 6H, v), 6.81 (d, 6H, *J* = 8.0 Hz, iii), 6.51 (s, 6H, ii), 3.94 (t, 12H, *J* = 6.3 Hz, 6), 3.63 (t, 12H, *J* = 6.5 Hz, 2), 1.78–1.74 (m, 12H, 7), 1.71–1.67 (m, 12H, 3), 1.57–1.44 (m, 24H, 8, 4), 1.17 (s, 9H, 1), 0.98–0.92 (m, 36H, 5, 9); *m/z* (MALDI-ToF MS+, DCTB) 4974 ($[M]^{\bullet+}$, $C_{336}H_{300}N_{18}O_{24}$ requires 4974).

***Tert*-butyl cyclic dodecamer complex *c*-P12·T12**

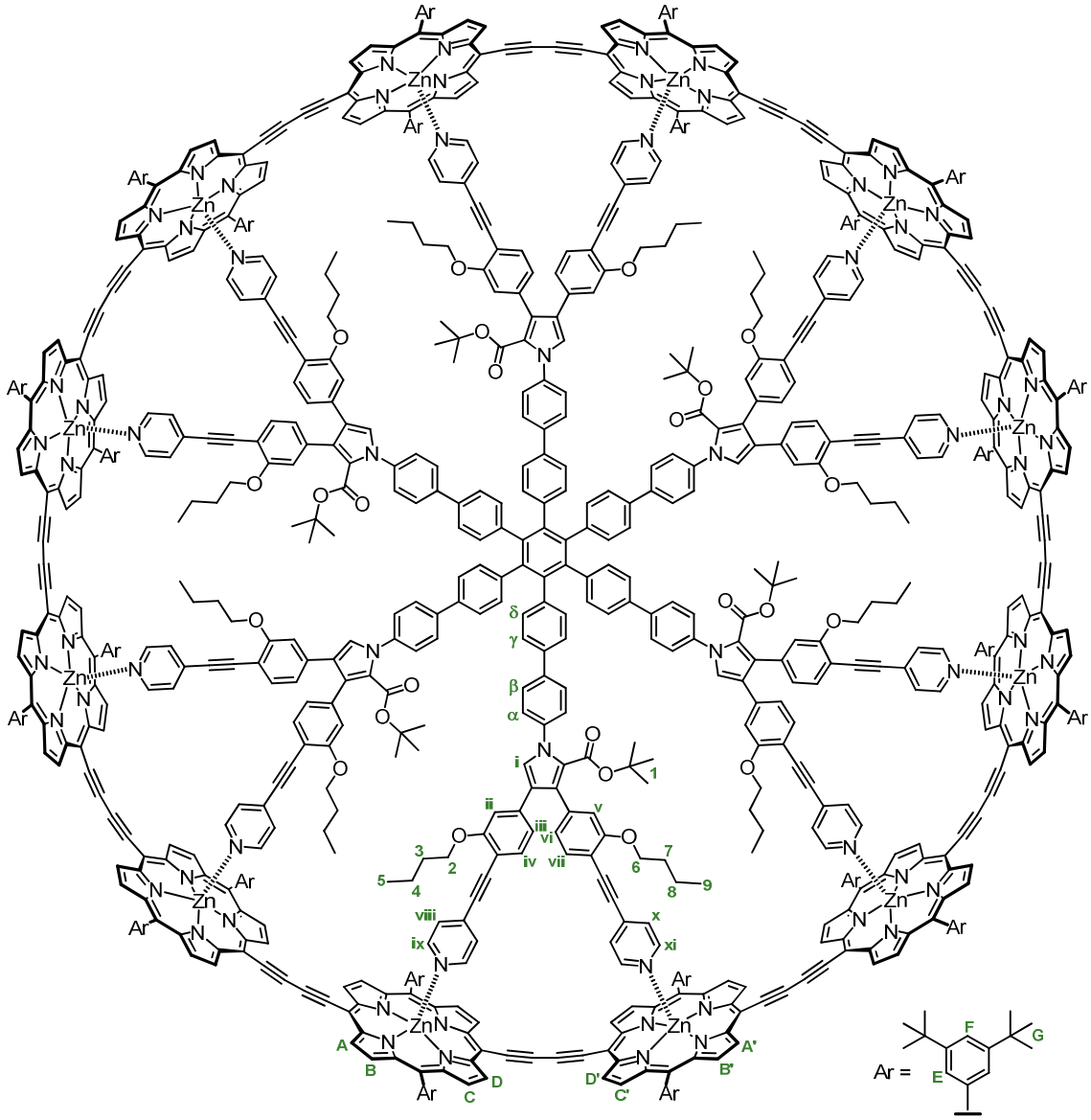

Zinc 5,15-bis-(3,5-bis-*tert*-butyl-phenyl)-10,20-bis-ethynyl-porphyrin tetramer ***l*-dP4** (7.9 mg, 2.47 µmol) and dodecadentate template **T12** (4.1 mg, 0.82 µmol) were dissolved in $CHCl_3$ (6.0 mL) and sonicated for 1 h. A solution of $Pd(PPh_3)_2Cl_2$ (1.1 mg, 1.64 µmol), copper(I) iodide (1.6 mg, 8.22 µmol) and 1,4-benzoquinone (3.6 mg, 32.9 µmol) in $CHCl_3$ (1.6 mL) and distilled $^{i}Pr_2NH$ (80.0 µL) was added to the complex solution and stirred at room temperature for 1 h.

The reaction mixture was heated to 50 °C for 1.5 h until no further change was observed by UV-vis absorption. The mixture was cooled, and the solvent removed under reduced pressure. The resulting solid was redissolved in toluene, filtered over glass wool, then passed down a size-exclusion column to give complex ***c*-P12·T12** as a brown solid (12.0 mg, 35%); δ_H (700 MHz, CD_2Cl_2/0.4% d_5-pyridine, 298 K) 9.87 (d, 48H, *J* = 3.6 Hz, A,A',D,D'), 8.99 (d, 48H, *J* = 3.5 Hz, B,B',C,C'), 8.12 (s, 48H, E), 7.91 (s, 24H, F), 7.26 (d, 12H, *J* = 9.0 Hz, β), 7.02 (d, 12H, *J* = 7.3 Hz, γ), 6.98 (d, 12H, *J* = 8.0 Hz, α), 6.85 (d, 12 H, *J* = 8.0 Hz, δ), 6.81 (d, 6H, *J* = 9.2 Hz, vii), 6.68 (s, 6H, i), 6.64 (d, 6H, *J* = 8.5 Hz, iv), 6.36 (d, 6H, *J* = 8.5 Hz, vi), 6.27-6.26 (m, 12H, iii, v), 5.87 (s, 6H, ii), 5.84 (d, 12H, *J* = 4.9 Hz, viii, x), 5.65 (d, 12H, *J* = 6.1 Hz, viii, x), 3.35 (br t, 12H, *J* = 6.2 Hz, 6), 2.94 (br t, 12H, *J* = 5.5 Hz, 2), 1.60 (s, 432H, G), 1.15–1.13 (m, 12H, 7), 1.01–0.99 (m, 12H, 3), 0.89–0.87 (m, 12H, 8), 0.76–0.74 (m, 12H, 4), 0.70 (s, 54H, 1), 0.42 (t, 18H, *J* = 7.2 Hz, 9), 0.27 (t, 18H, *J* = 7.4 Hz, 5); λ_{max} (CH_2Cl_2) / nm (log ε) 494 (5.67), 801 (5.23), 866 (5.80).

***Tert*-butyl dipyridyl pyrrole complex *l*-P2·15**

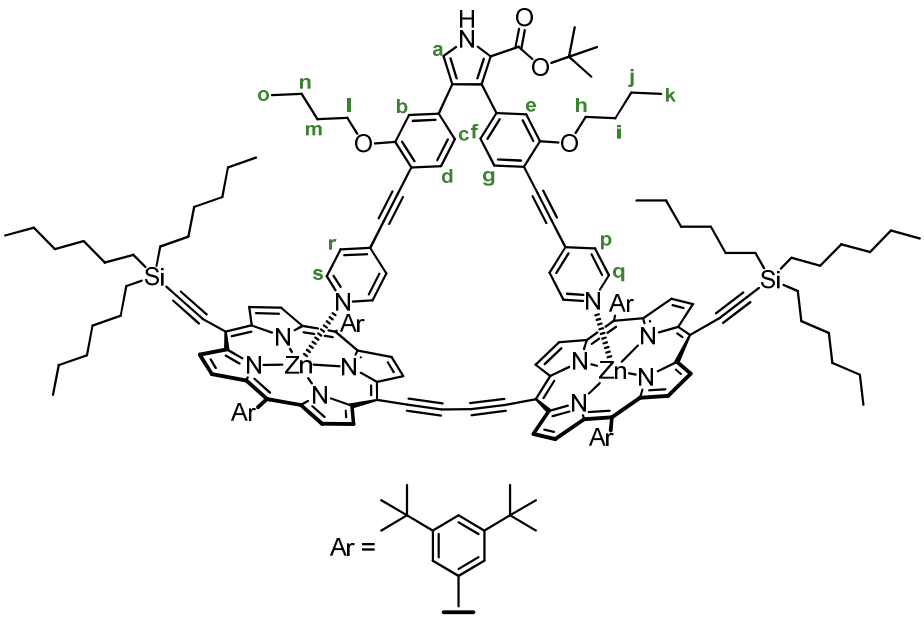

A stock solution of *tert*-butyl 3,4-bis(3-butoxy-4-(pyridin-4-ylethynyl)phenyl)-1H-pyrrole-2-carboxylate **15** in $CDCl_3$ (3.8×10^{-3} M) was titrated into a solution of zinc 5,15-bis-(3,5-bis-*tert*-butyl-phenyl)-10,20-bis-trihexylsilanylethynyl-porphyrin dimer ***l*-P2** (2.20 mg, 1.02 μmol) in $CDCl_3$ (500 μL) until a 1:1 complex was formed, measured by ^{1}H NMR peak integration. The solvent was removed and resulting green-brown residue was recrystallised by layer addition (CH_2Cl_2/MeOH) to yield a green/brown solid (2.6 mg, 92%); δ_H (500 MHz, $CDCl_3$, 298 K) 9.95 (br s, 4H, *β-H*), 9.72 (br s, 4H, *β-H*), 9.06 (br s, 4H, *β-H*), 8.96 (br s, 4H, *β-H*), 8.77 (br s, 1H, N*H*), 8.10 (s, 8H, Ar-H^{ortho}), 7.85 (s, 4H, Ar-H^{para}), 6.88 (d, 1H, *J* = 2.8 Hz, a), 6.84 (d, 1H, *J* = 8.2 Hz, g), 6.76 (d, 1H, *J* = 8.2 Hz, d), 6.47 (d, 1H, *J* = 7.9 Hz, f), 6.37 (d, 1H, *J* = 8.5 Hz, c), 6.31 (s, 1H, e), 5.92 (s, 1H, b), 5.55 (d, 2H, *J* = 6.6 Hz, p), 5.53 (d, 2H, *J* = 6.3 Hz, r), 3.42 (t, 2H, *J* = 6.5 Hz, h), 3.06 (t, 2H, *J* = 6.8 Hz, l), 2.66 (d, 2H, *J* = 6.3 Hz, q), 2.64 (d, 2H, *J* = 6.3 Hz, s), 1.82–1.75 (m, 12H, CH_2), 1.59 (s, 72H, Ar-^{t}Bu), 1.59–1.52 (m, 12H, CH_2), 1.46–1.34 (m, 24H, CH_2CH_2), 1.26 (m, 2H, i), 1.15 (t, 2H, *J* = 7.3 Hz, m), 1.09 (s, 9H, ^{t}Bu), 1.05–1.02 (m, 14H, CH_2, j), 0.91 (t, 18H, *J* = 7.1 Hz, CH_3), 0.87–0.85 (m, 2H, n), 0.55 (t, 3H, *J* = 7.4 Hz, k), 0.40 (t, 3H, *J* = 7.4 Hz, o).

***Tert*-butyl figure-of-eight complex *c*-P12·(T6)$_2$**

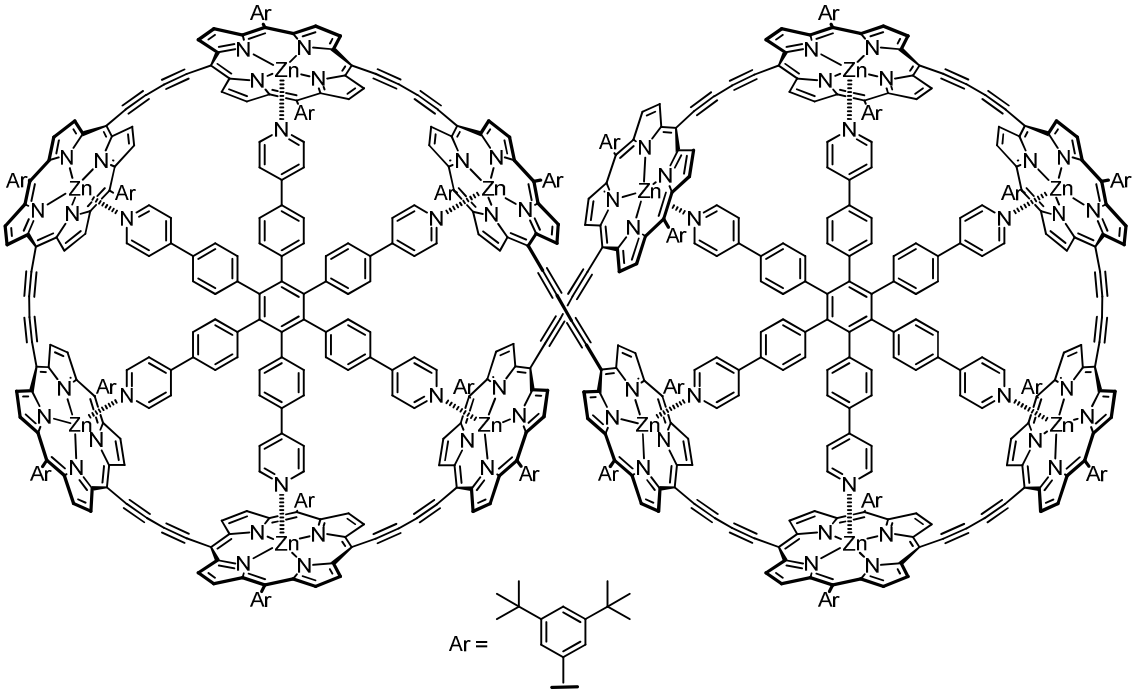

Hexadentate template **T6** (19.5 mg, 19.6 μmol) and zinc 5,15-bis-(3,5-bis-*tert*-butyl-phenyl)-10,20-bis-ethynyl-porphyrin tetramer ***l*-dP4** (61.0 mg, 19.1 μmol) were dissolved in $CHCl_3$ (88 mL) and sonicated for 1 h. A catalyst solution was prepared by dissolving $Pd(PPh_3)_2Cl_2$ (17.7 mg, 25.2 μmol), copper(I) iodide (24.2 mg, 0.13 mmol) and 1,4-benzoquinone (56.1 mg, 0.52 mmol) in $CHCl_3$ (12.0 mL) and freshly distilled $^{i}Pr_2NH$ (610 μL). The catalyst solution was added to the template and porphyrin tetramer mixture. The reaction mixture was stirred at room temperature for 1 h and then for 1.5 h at 50 °C under air. The solution was passed through a plug of alumina using $CHCl_3$ as eluent. The crude was further purified by size-exclusion chromatography on Biobeads SX-1 in toluene. Recrystallisation by layer addition (CH_2Cl_2/MeOH) gave the product as a dark brown solid (29.0 mg, 39%); δ_H (700 MHz, $CDCl_3$, 298 K) 10.92 (d, 4H, *J* = 4.4 Hz, *β-H*), 10.16 (d, 4H, *J* = 3.4 Hz, *β-H*), 9.57–9.53 (m, 32H, *β-H*), 9.48 (d, 4H, *J* = 4.3 Hz, *β-H*), 9.30 (d, 4H, *J* = 3.6 Hz, *β-H*), 9.03 (d, 4H, *J* = 2.9 Hz, *β-H*), 8.86 (d, 4H, *J* = 4.4 Hz, *β-H*), 8.80–8.75 (m, 28H, *β-H*), 8.72 (d, 4H, *J* = 3.9 Hz, *β-H*), 8.32 (d, 4H, *J* = 3.4 Hz, *β-H*),

8.11 (s, 4H, Ar-*H*), 8.08 (d, 4H, *J* = 4.3 Hz, *β*-*H*), 8.06–8.02 (m, 16H, Ar-*H*), 7.89 (s, 4H, Ar-*H*), 7.83–7.74 (m, 36H, Ar-*H*), 7.37 (s, 4H, Ar-*H*), 6.98 (s, 4H, Ar-*H*), 6.40 (s, 4H, Ar-*H*), 5.53 (d, 4H, *J* = 9.7 Hz, -C_6H_4-), 5.49–5.42 (m, 32H, -C_6H_4-), 5.39 (d, 4H, *J* = 9.2 Hz, -C_6H_4-), 5.27 (d, 4H, *J* = 9.9 Hz, -C_6H_4-), 5.22 (d, 4H, *J* = 9.4 Hz, -C_6H_4-), 4.97–4.94 (m, 16H, *β*-pyridyl), 4.81 (d, 8H, *J* = 9.4 Hz, *β*-py), 2.22–2.19 (m, 24H, *α*-py), 1.70 (s, 36H, ^{t}Bu), 1.58 (m, 72H, ^{t}Bu), 1.55–1.54 (m, 72H, ^{t}Bu), 1.53–1.51 (m, 144H, ^{t}Bu), 1.46 (s, 36H, ^{t}Bu), 1.14 (s, 36H, ^{t}Bu), –0.64 (s, 36H, ^{t}Bu); *m/z* (MALDI-ToF MS+, DCTB) 11554 ($[M]^{\bullet+}$, $C_{768}H_{696}N_{60}Zn_{12}$ requires 11551); λ_{max} ($CHCl_3$) / nm (log ε) 497 (5.88), 766 (5.45), 803 (5.54), 882 (5.85), 840 (5.59).

***Tert*-butyl cyclic porphyrin dodecamer *c*-P12**

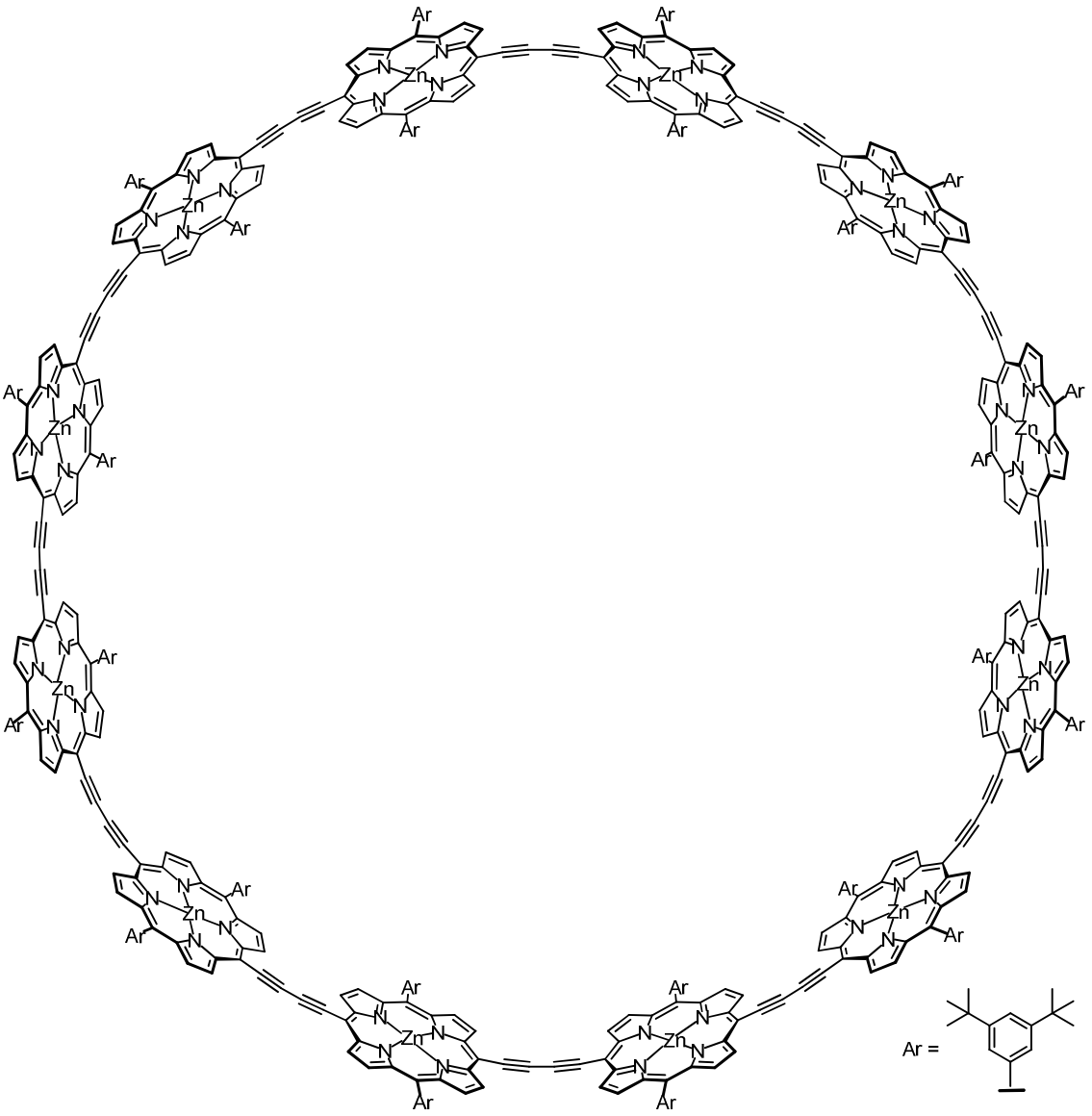

Figure-of-eight complex ***c*-P12·(T6)$_2$** (3.0 mg, 0.26 mmol) was passed over a size-exclusion column (Biobeads SX-1) using a mixture of toluene and pyridine (10:1 *v/v*) as eluent. Recrystallisation by layer addition ($CHCl_3$/MeOH) gave the product as a dark brown solid (2.4 mg, 96%); δ_H (500 MHz, $CDCl_3$/1% d_5-pyridine, 298 K) 9.84 (d, 48H, *J* = 4.5 Hz, *β-H*), 8.95 (d, 48H, *J* = 4.6 Hz, *β-H*), 8.05 (d, 48H, *J* = 1.5 Hz, Ar-*H*), 7.81 (s, 24H, Ar-*H*), 1.56 (s, 432H, ^{t}Bu); δ_C (125 MHz, $CDCl_3$/1% d_5-pyridine): 153.0, 150.8, 150.0, 148.9, 141.8, 136.3, 133.6, 131.0, 129.4,

128.6, 125.3, 124.0, 121.3, 100.5, 84.3, 35.4, 32.1; *m/z* (MALDI-ToF MS+, DCTB) 9563 ($[M]^{\bullet+}$, $C_{624}H_{600}N_{48}Zn_{12}$ requires 9556); λ_{max} (toluene/1% pyridine) / nm (log ε) 472 (5.86), 488 (shoulder, 5.83), 816 (5.66).

***Tert*-butyl cyclic octamer complex *c*-P8·T8**

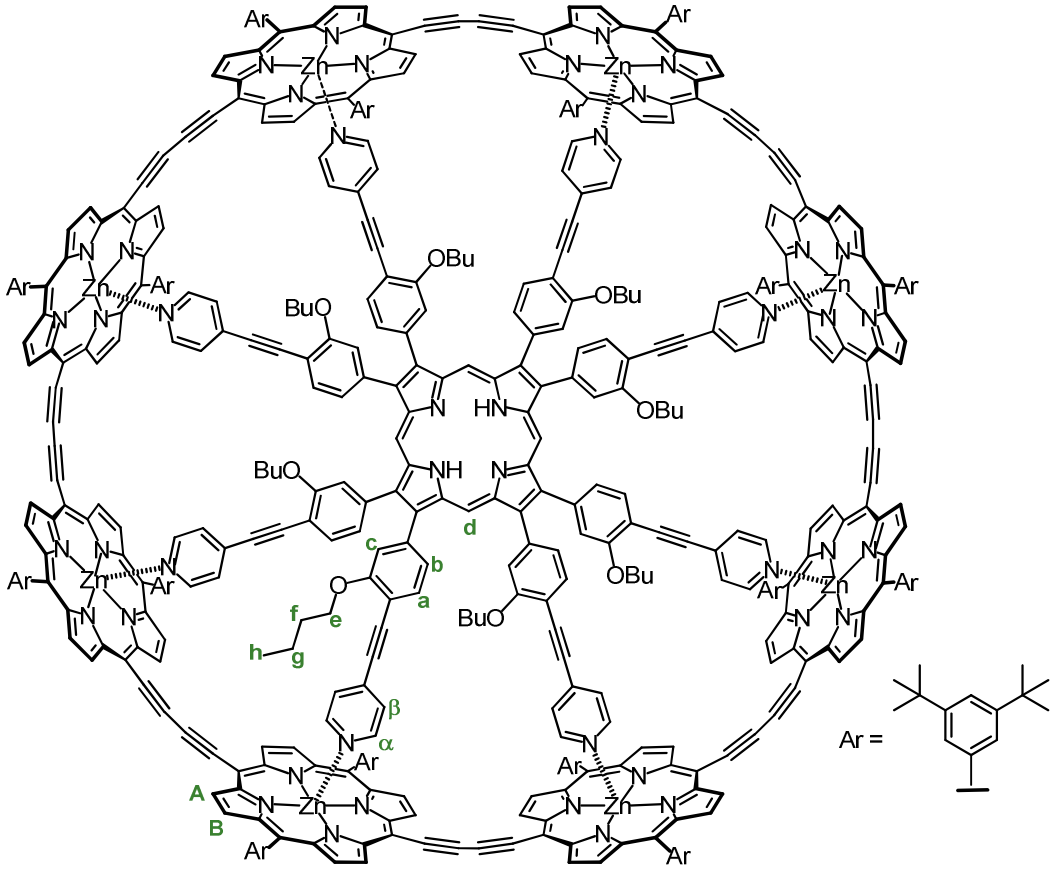

Zinc 5,15-bis-(3,5-bis-*tert*-butyl-phenyl)-10,20-bis-ethynyl-porphyrin dimer ***l*-dP2** (8.4 mg, 5.27 μmol) and octadentate template **T8** (3.0 mg, 1.30 μmol) were sonicated in $CHCl_3$ (5.0 mL) for 1 h. A solution of $Pd(PPh_3)_2Cl_2$ (1.8 mg, 2.56 μmol), copper(I) iodide (2.4 mg, 13.0 μmol), 1,4-benzoquinone (5.6 mg, 52.0 μmol) and freshly distilled $^{i}Pr_2NH$ (114 μL) in $CHCl_3$ (2.0 mL) was added and the reaction mixture was stirred at room temperature for 1 h. The reaction mixture was then heated to 50 °C and stirred for a further 1.5 h. The mixture was cooled, and passed down an alumina column with $CHCl_3$. The mixture was further purified using

preparative GPC with toluene at 8.5 mL min^{-1}, and the peak at 35.0 min was isolated. Recrystallisation by layer addition (CH_2Cl_2/MeOH) gave a brown solid (2.9 mg, 25%); δ_H (500 MHz, $CDCl_3$, 298 K) 9.88 (br s, 4H, d), 9.80 (br s, 32H, A), 8.94 (br s, 32H, B), 8.21 (br s, 16H, Ar-H^{ortho}), 7.89 (br s, 16H, Ar-H^{ortho*}), 7.84 (br s, 16H, Ar-H^{para}), 6.78 (br s, 8H, b), 6.47 (br s, 8H, c), 5.41 (br s, 16H, β-py), 5.32 (br s, 8H, a), 2.90 (br s, 16H, e), 2.58 (br s, 16H, α-py), 1.61 (s, 144H, Ar-^{t}Bu), 1.56 (s, 144H, Ar-^{t}Bu*), 0.84 (br s, 16H, f), 0.60 (br s, 16H, g), 0.12 (br s, 24H, h); *m/z* (MALDI-ToF MS+, dithranol) 8670 ([M]$^{\bullet+}$, $C_{572}H_{534}N_{44}O_8Zn_8$ requires 8676); λ_{max} ($CHCl_3$) / nm (log ε) 439 (6.00), 499 (5.94), 766 (5.43), 808 (5.61), 861 (6.03).

***Tert*-butyl cyclic octamer *c*-P8**

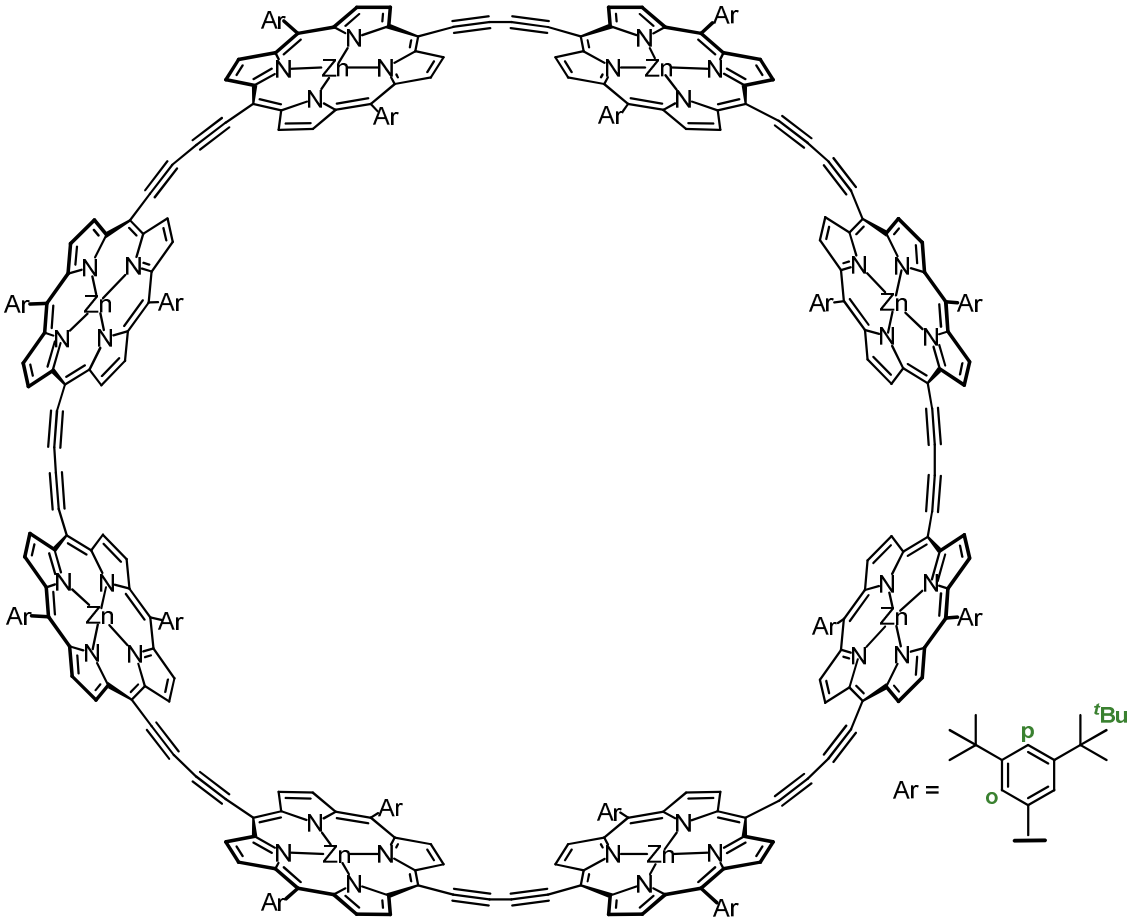

Tert-butyl cyclic octamer complex ***c*-P8·T8** (1.0 mg, 0.12 μmol) was dissolved in toluene/pyridine (10:1, 1.0 mL) and sonicated for 15 min. The brown solution was passed down a size-exclusion column with toluene/pyridine (10:1) and the porphyrin fraction taken. Recrystallisation by layer addition (CH_2Cl_2/MeOH) gave a brown solid (0.7 mg, 98%); ^{1}H NMR (250 MHz, $CDCl_3$/1% d_5-pyridine, 298 K): δ_H 9.75 (d, 32H, J = 4.6 Hz, *β-H*), 8.88 (d, 32H, J = 4.6 Hz, *β-H*), 7.99 (d, 32H, J = 1.8 Hz, Ar-H^{ortho}), 7.79 (d, 16H, J = 1.8 Hz, Ar-H^{para}), 1.77 (s, 288H, ^{t}Bu); *m/z* (MALDI-ToF MS+, dithranol) 6367 ([M]$^{\bullet+}$, $C_{416}H_{400}N_{32}Zn_8$ requires 6371); λ_{max} ($CHCl_3$/1% pyridine) / nm (log ε) 467 (5.43), 492 (5.40), 817 (5.18).

6.4 Experimental procedure for DOSY experiments

DOSY NMR experiments were performed on a Bruker AVII 500 spectrometer equipped with a $^{1}H/^{13}C/^{19}F$ probe with sample temperatures regulated to 298 K. Samples were prepared in d_8-toluene at a concentration of 10^{-4} M. A longitudinal eddy-current delay with bipolar pulsed field gradients (LED-BPP sequence) was used. The high molecular weight of the samples in a low viscosity solvent meant that convection artefacts would be significant: these were minimised by using a double stimulated echo response (DSTE). The gradient pulse durations δ and total diffusion times Δ used are tabulated in Table 6.1.

Complex	Gradient pulse duration δ /ms	Total diffusion time Δ /ms	Gradient /%
***c*-P6·T6**	4	100	2–85
***c*-P8·T8**	4	100	2–85
***c*-P12·(T6)$_2$**	1.6	800	2–85
***c*-P24·(T8)$_3$**	1.6	800	2–85

Table 6.1 Gradient pulse duration and total diffusion times used in the *FW*-determining ^{1}H DOSY experiments.

Diffusion constants were obtained by fitting the intensity decays to

$$I = I_0 \exp(-D\gamma^2\delta^2 g^2 \left(\Delta - \frac{\delta}{3}\right)) \qquad \text{Eq. 35}$$

where I and I_0 are the signal intensities in the presence and the absence of the field gradient respectively.[265] D is the diffusion constant to be determined, g is the gradient strength, $\gamma$is the ^{1}H magnetogyric ratio, δ is the gradient pulse duration, and Δ is the total diffusion time. Data fitting was carried out using Bruker software and DOSY toolbox.[323]

References

[1] E. Vogel, W. Haas, B. Knipp, J. Lex, H. Schmickler, *Angew. Chem. Int. Ed. Engl.* **1988**, *27*, 406-409.

[2] L. R. Milgrom, in *The Colours of Life*, Oxford University Press, **1997**.

[3] J. W. Buchler, *The Porphyrins, Structure and Synthesis Part A*, Academic Press, New York, **1978**.

[4] H. L. Anderson, *Inorg. Chem.* **1994**, *33*, 972-981.

[5] A. D. Adler, F. R. Longo, J. D. Finarelli, J. Goldmacher, J. Assour, L. Korsakoff, *J. Org. Chem.* **1967**, *32*, 476-476.

[6] J. Lindsey, *Tetrahedron Lett.* **1986**, *27*, 4969-4970.

[7] M. J. Gunter, L. N. Mander, *J. Org. Chem.* **1981**, *46*, 4792-4795.

[8] J. Manka, *Tetrahedron Lett.* **1989**, *30*, 6989-6992.

[9] B. J. Littler, M. A. Miller, C.-H. Hung, R. W. Wagner, D. F. O'Shea, P. D. Boyle, J. S. Lindsey, *J. Org. Chem.* **1999**, *64*, 1391-1396.

[10] R. Schlözer, J.-H. Fuhrhop, *Angew. Chem. Int. Ed. Engl.* **1975**, *14*, 363-363.

[11] D. E. Chumakov, A. V. Khoroshutin, A. V. Anisimov, K. I. Kobrakov, *Chem. Heterocycl. Comp.* **2009**, *45*, 259-283.

[12] M. Gouterman, *The Porphyrins, Physical Chemistry Part A*, Academic Press, New York, **1978**.

[13] M. Gouterman, *J. Chem. Phys.* **1959**, *30*, 1139-1161.

[14] M. Gouterman, *J. Mol. Spectrosc.* **1961**, *6*, 138-163.

[15] A. Rosa, E. J. Baerends, *Inorg. Chem.* **1994**, *33*, 584-595.

[16] L. Edwards, M. Gouterman, *J. Mol. Spectrosc.* **1970**, *33*, 292-310.

[17] N. Allen S., Ed., *Handbook of Photochemistry and Photophysics of Polymer Materials*, J. Wiley, Hoboken N.J., **2010**.

[18] P. D. Harvey, in *The Porphyrin Handbook* (Eds.: K.M. Kadish, K.M. Smith, R. Guilard), Academic Press, **2000**, pp. 63-243.

[19] T. Förster, *Ann. Phys.* **1948**, *437*, 55-75.

[20] K. F. Wong, B. Bagchi, P. J. Rossky, *J. Phys. Chem. A* **2004**, *108*, 5752-5763.

[21] J. Guillet, *Polymer Photophysics and Photochemistry: An Introduction to the Study of Photoprocesses in Macromolecules*, Cambridge University Press, Cambridge [Cambridgeshire]; New York, **1985**.

[22] D. L. Dexter, *J. Chem. Phys.* **1953**, *21*, 836-850.

[23] P. L. Burn, A. B. Holmes, A. Kraft, D. D. C. Bradley, A. R. Brown, R. H. Friend, R. W. Gymer, *Nature* **1992**, *356*, 47-49.

[24] H. Sirringhaus, *Science* **2000**, *290*, 2123-2126.

[25] H. E. Katz, A. J. Lovinger, J. Johnson, C. Kloc, T. Siegrist, W. Li, Y.-Y. Lin, A. Dodabalapur, *Nature* **2000**, *404*, 478-481.

[26] H. Sirringhaus, P. J. Brown, R. H. Friend, M. M. Nielsen, K. Bechgaard, B. M. W. Langeveld-Voss, A. J. H. Spiering, R. A. J. Janssen, E. W. Meijer, P. Herwig, et al., *Nature* **1999**, *401*, 685-688.

[27] R. H. Friend, R. W. Gymer, A. B. Holmes, J. H. Burroughes, R. N. Marks, C. Taliani, D. D. C. Bradley, D. A. D. Santos, J. L. Bredas, M. Logdlund, et al., *Nature* **1999**, *397*, 121-128.

[28] J. H. Burroughes, D. D. C. Bradley, A. R. Brown, R. N. Marks, K. Mackay, R. H. Friend, P. L. Burns, A. B. Holmes, *Nature* **1990**, *347*, 539-541.

[29] D. Braun, A. J. Heeger, *Appl. Phys. Lett.* **1991**, *58*, 1982-1984.

[30] S. Chen, L. Deng, J. Xie, L. Peng, L. Xie, Q. Fan, W. Huang, *Adv. Mater.* **2010**, *22*, 5227-5239.

[31] F. Garnier, R. Hajlaoui, A. Yassar, P. Srivastava, *Science* **1994**, *265*, 1684-1686.

[32] L. Torsi, A. Dodabalapur, L. J. Rothberg, A. W. P. Fung, H. E. Katz, *Science* **1996**, *272*, 1462-1464.

[33] A. Facchetti, *Chem. Mater.* **2011**, *23*, 733-758.

[34] M. Gratzel, *Nature* **2001**, *414*, 338-344.

[35] J. J. M. Halls, C. A. Walsh, N. C. Greenham, E. A. Marseglia, R. H. Friend, S. C. Moratti, A. B. Holmes, *Nature* **1995**, *376*, 498-500.

[36] D. P. Arnold, A. W. Johnson, M. Mahendran, *J. Chem. Soc., Perkin Trans. 1* **1978**, 366-370.

[37] D. Arnold, L. J. Nitschinsk, *Tetrahedron* **1992**, *48*, 8781-8792.

[38] V. S. Lin, S. G. DiMagno, M. J. Therien, *Science* **1994**, *264*, 1105-1111.

[39] P. N. Taylor, A. P. Wylie, J. Huuskonen, H. L. Anderson, *Angew. Chem. Int. Ed.* **1998**, *37*, 986-989.

[40] K. Susumu, T. V. Duncan, M. J. Therien, *J. Am. Chem. Soc.* **2005**, *127*, 5186-5195.

[41] A. Osuka, N. Tanabe, S. Nakajima, K. Maruyama, *J. Chem. Soc., Perkin Trans. 2* **1996**, 199-203.

[42] T. Nagata, A. Osuka, K. Maruyama, *J. Am. Chem. Soc.* **1990**, *112*, 3054-3059.

[43] A. Helms, D. Heiler, G. McLendon, *J. Am. Chem. Soc.* **1991**, *113*, 4325-4327.

[44] D. Heiler, G. McLendon, P. Rogalskyj, *J. Am. Chem. Soc.* **1987**, *109*, 604-606.

[45] A. Osuka, K. Maruyama, *J. Am. Chem. Soc.* **1988**, *110*, 4454-4456.

[46] I. Abdalmuhdi, C. K. Chang, *J. Org. Chem.* **1985**, *50*, 411-413.

[47] D. A. Fletcher, R. F. McMeeking, D. Parkin, *J. Chem. Inf. Model.* **1996**, *36*, 746-749.

[48] R. E. Martin, F. Diederich, *Angew. Chem. Int. Ed.* **1999**, *38*, 1350-1377.

[49] L. T. Cheng, W. Tam, S. R. Marder, A. E. Stiegman, G. Rikken, C. W. Spangler, *J. Phys. Chem.* **1991**, *95*, 10643-10652.

[50] M. J. Frampton, H. Akdas, A. R. Cowley, J. E. Rogers, J. E. Slagle, P. A. Fleitz, M. Drobizhev, A. Rebane, H. L. Anderson, *Org. Lett.* **2005**, *7*, 5365-5368.

[51] T. E. O. Screen, I. M. Blake, L. H. Rees, W. Clegg, S. J. Borwick, H. L. Anderson, *J. Chem. Soc., Perkin Trans. 1* **2002**, 320-329.

[52] L. J. Esdaile, P. Jensen, J. C. McMurtrie, D. P. Arnold, *Angew. Chem. Int. Ed.* **2007**, *46*, 2090-2093.

[53] A. Osuka, H. Shimidzu, *Angew. Chem. Int. Ed. Engl.* **1997**, *36*, 135-137.

[54] T. Ogawa, Y. Nishimoto, N. Yoshida, N. Ono, A. Osuka, *Angew. Chem. Int. Ed.* **1999**, *38*, 176-179.

[55] N. Aratani, A. Osuka, Y. H. Kim, D. H. Jeong, D. Kim, *Angew. Chem. Int. Ed.* **2000**, *39*, 1458-1462.

[56] A. Tsuda, A. Osuka, *Science* **2001**, *293*, 79-82.

[57] A. Tsuda, H. Furuta, A. Osuka, *J. Am. Chem. Soc.* **2001**, *123*, 10304-10321.

[58] P. N. Taylor, J. Huuskonen, R. T. Aplin, H. L. Anderson, G. Rumbles, E. Williams, *Chem. Commun.* **1998**, 909-910.

[59] M. Kasha, H. R. Rawls, M. Ashraf El-Bayoumi, *Pure Appl. Chem.* **1965**, *11*, 371-392.

[60] H. L. Anderson, *Adv. Mater.* **1994**, *6*, 834-836.

[61] N. Turro, *Modern Molecular Photochemistry*, University Science Books, Mill Valley Calif., **1991**.

[62] M. U. Winters, J. Kärnbratt, M. Eng, C. J. Wilson, H. L. Anderson, B. Albinsson, *J. Phys. Chem. C* **2007**, *111*, 7192-7199.

[63] R. Stranger, J. E. McGrady, D. P. Arnold, I. Lane, G. A. Heath, *Inorg. Chem.* **1996**, *35*, 7791-7797.

[64] A. A. Bothner-By, J. Dadok, T. E. Johnson, J. S. Lindsey, *J. Phys. Chem.* **1996**, *100*, 17551-17557.

[65] V. S.-Y. Lin, M. J. Therien, *Chem. Eur. J.* **1995**, *1*, 645-651.

[66] R. Kumble, S. Palese, V. S.-Y. Lin, M. J. Therien, R. M. Hochstrasser, *J. Am. Chem. Soc.* **1998**, *120*, 11489-11498.

[67] R. D. McCullough, P. C. Ewbank, R. S. Loewe, *J. Am. Chem. Soc.* **1997**, *119*, 633-634.

[68] S. Yue, G. C. Berry, R. D. McCullough, *Macromolecules* **1996**, *29*, 933-939.

[69] P. N. Taylor, H. L. Anderson, *J. Am. Chem. Soc.* **1999**, *121*, 11538-11545.

[70] B. L. Crawford, *J. Chem. Phys.* **1939**, *7*, 555-562.

[71] L. K. Montgomery, L. E. Applegate, *J. Am. Chem. Soc.* **1967**, *89*, 2952-2960.

[72] M. Trætteberg, W. Luttke, R. Machinek, A. Krebs, H. J. Hohlt, *J. Mol. Struct.* **1985**, *128*, 217-232.

[73] G. N. Lewis, M. Calvin, *Chem. Rev.* **1939**, *25*, 273-328.

[74] J. Gierschner, J. Cornil, H.-J. Egelhaaf, *Adv. Mater.* **2007**, *19*, 173-191.

[75] M. Hoffmann, Nanosized Porphyrin Molecular Wires and Rings, DPhil Thesis, University of Oxford, **2008**.

[76] L. Milgrom, *The Colours of Life: An Introduction to the Chemistry of Porphyrins and Related Compounds*, Oxford University Press, New York, **1997**.

[77] S. Scheuring, J. N. Sturgis, *Science* **2005**, *309*, 484-487.

[78] G. Drews, *Microbiol. Rev.* **1985**, *49*, 59-70.

[79] G. McDermott, S. M. Prince, A. A. Freer, A. M. Hawthornthwaite-Lawless, M. Z. Papiz, R. J. Cogdell, N. W. Isaacs, *Nature* **1995**, *374*, 517-521.

[80] R. J. Cogdell, T. D. Howard, N. W. Isaacs, K. McLuskey, A. T. Gardiner, *Photosynth. Res.* **2002**, *74*, 135-141.

[81] K. Sauer, R. J. Cogdell, S. M. Prince, A. Freer, N. W. Isaacs, H. Scheer, *Photochem. Photobiol.* **1996**, *64*, 564-576.

[82] A. W. Roszak, T. D. Howard, J. Southall, A. T. Gardiner, C. J. Law, N. W. Isaacs, R. J. Cogdell, *Science* **2003**, *302*, 1969-1972.

[83] C. J. Law, A. W. Roszak, J. Southall, A. T. Gardiner, N. W. Isaacs, R. J. Cogdell, *Mol. Membr. Biol.* **2009**, *21*, 183-191.

[84] J. P. Allen, G. Feher, T. O. Yeates, H. Komiya, D. C. Rees, *Proc. Natl. Acad. Sci. USA* **1987**, *84*, 5730-5734.

[85] J. D. Watson, F. H. C. Crick, *Nature* **1953**, *171*, 737-738.

[86] D. H. Busch, *J. Incl. Phenom. Macrocycl. Chem.* **1992**, *12*, 389-395.

[87] J. P. Sauvage, *Acc. Chem. Res.* **1990**, *23*, 319-327.

[88] B. Odell, M. V. Reddington, A. M. Z. Slawin, N. Spencer, J. F. Stoddart, D. J. Williams, *Angew. Chem. Int. Ed. Engl.* **1988**, *27*, 1547-1550.

[89] W. L. Mock, T. A. Irra, J. P. Wepsiec, M. Adhya, *J. Org. Chem.* **1989**, *54*, 5302-5308.

[90] T. R. Kelly, G. J. Bridger, C. Zhao, *J. Am. Chem. Soc.* **1990**, *112*, 8024-8034.

[91] D. Mössinger, D. Chaudhuri, T. Kudernac, S. Lei, S. De Feyter, J. M. Lupton, S. Höger, *J. Am. Chem. Soc.* **2010**, *132*, 1410-1423.

[92] F. Diederich, *Templated Organic Synthesis*, Wiley-vch, Weinheim; Chichester, **2000**.

[93] S. Anderson, H. L. Anderson, J. K. M. Sanders, *Acc. Chem. Res.* **1993**, *26*, 469-475.

[94] R. Hoss, F. Vögtle, *Angew. Chem. Int. Ed. Engl.* **1994**, *33*, 375-384.

[95] B. Hasenknopf, J.-M. Lehn, N. Boumediene, A. Dupont-Gervais, A. Van Dorsselaer, B. Kneisel, D. Fenske, *J. Am. Chem. Soc.* **1997**, *119*, 10956-10962.

[96] F. H. Moser, A. L. Thomas, *Phthalocyanine Compounds*, Reinhold Pub. Co., New York, **1963**.

[97] T. J. Marks, D. R. Stojakovic, *J. Am. Chem. Soc.* **1978**, *100*, 1695-1705.

[98] A. Meller, A. Ossko, *Monatsh. Chem.* **1972**, *103*, 150-155.

[99] N. Kobayashi, R. Kondo, S. Nakajima, T. Osa, *J. Am. Chem. Soc.* **1990**, *112*, 9640-9641.

[100] R. N. Greene, *Tetrahedron Lett.* **1972**, *13*, 1793-1796.

[101] H. L. Anderson, J. K. M. Sanders, *Angew. Chem. Int. Ed. Engl.* **1990**, *29*, 1400-1403.

[102] W. R. Scheidt, C. W. Eigenbrot, M. Ogiso, K. Hatano, *Bull. Chem. Soc. Jpn.* **1987**, *60*, 3529-3533.

[103] H. Imai, S. Nakagawa, E. Kyuno, *J. Am. Chem. Soc.* **1992**, *114*, 6719-6723.

[104] P. N. Taylor, A. P. Wylie, J. Huuskonen, H. L. Anderson, *Angew. Chem. Int. Ed.* **1998**, *37*, 986-989.

[105] E. Alessio, Ed., *Non-Covalent Multi-Porphyrin Assemblies*, Springer-verlag Berlin Heidelberg, [New York], **2006**.

[106] F. A. Walker, M. Benson, *J. Am. Chem. Soc.* **1980**, *102*, 5530-5538.

[107] C. H. Kirksey, P. Hambright, *Inorg. Chem.* **1970**, *9*, 958-960.

[108] M. Tabata, J. Nishimoto, in *The Porphyrin Handbook* (Eds.: K.M. Kadish, K.M. Smith, R. Guilard), Academic Press, **2000**, pp. 221-417.

[109] S. J. Cole, G. C. Curthoys, E. A. Magnusson, J. N. Phillips, *Inorg. Chem.* **1972**, *11*, 1024-1028.

[110] D. M. Rudkevich, W. Verboom, D. N. Reinhoudt, *J. Org. Chem.* **1995**, *60*, 6585-6587.

[111] M. Sakuragi, K. Ichimura, H. Sakuragi, *Bull. Chem. Soc. Jpn.* **1992**, *65*, 1944-1949.

[112] J. K. M. Sanders, N. Bampos, Z. Clyde-Watson, S. L. Darling, J. C. Hawley, H.-J. Kim, C. C. Mak, S. J. Webb, in *The Porphyrin Handbook* (Eds.: K.M. Kadish, K.M. Smith, R. Guilard), Academic Press, **2000**, pp. 1-48.

[113] H. L. Anderson, S. Anderson, J. K. M. Sanders, *J. Chem. Soc., Perkin Trans. 1* **1995**, 2231-2245.

[114] G. Ercolani, L. Schiaffino, *Angew. Chem. Int. Ed.* **2011**, *50*, 1762-1768.

[115] G. Ercolani, C. Piguet, M. Borkovec, J. Hamacek, *J. Phys. Chem. B* **2007**, *111*, 12195-12203.

[116] C. A. Hunter, H. L. Anderson, *Angew. Chem. Int. Ed.* **2009**, *48*, 7488-7499.

[117] M. F. Perutz, *Quart. Rev. Biophys.* **1989**, *22*, 139-237.

[118] D. H. Williams, A. J. Maguire, W. Tsuzuki, M. S. Westwell, *Science* **1998**, *280*, 711-714.

[119] A. P. Bisson, C. A. Hunter, J. C. Morales, K. Young, *Chem. Eur. J.* **1998**, *4*, 845-851.

[120] C. Galli, L. Mandolini, *Eur. J. Org. Chem.* **2000**, *2000*, 3117-3125.

[121] V. M. Krishnamurthy, V. Semetey, P. J. Bracher, N. Shen, G. M. Whitesides, *J. Am. Chem. Soc.* **2007**, *129*, 1312-1320.

[122] M. I. Page, W. P. Jencks, *P. Natl. Acad. Sci. USA* **1971**, *68*, 1678-1683.

[123] M. C. Misuraca, T. Grecu, Z. Freixa, V. Garavini, C. A. Hunter, P. W. N. M. van Leeuwen, M. D. Segarra-Maset, S. M. Turega, *J. Org. Chem.* **2011**, *76*, 2723-2732.

[124] M. I. Page, *Chem. Soc. Rev.* **1973**, *2*, 295-323.

[125] G. Ercolani, *Struct. Bond.* **2006**, *121*, 167-215.

[126] C. B. Storm, A. H. Turner, M. B. Swann, *Inorg. Chem.* **1984**, *23*, 2743-2746.

[127] H. Hogben, Understanding Cooperativity of Binding to Porphyrin Oligomers, Part II Thesis, University of Oxford, **2008**.

[128] M. Hoffmann, J. Kärnbratt, M.-H. Chang, L. M. Herz, B. Albinsson, H. L. Anderson, *Angew. Chem. Int. Ed.* **2008**, *47*, 4993-4996.

[129] Q. Liu, D. J. Burton, *Tetrahedron Lett.* **1997**, *38*, 4371-4374.

[130] D. M. Collins, J. L. Hoard, *J. Am. Chem. Soc.* **1970**, *92*, 3761-3771.

[131] M. Hoffmann, C. J. Wilson, B. Odell, H. L. Anderson, *Angew. Chem. Int. Ed.* **2007**, *46*, 3122-3125.

[132] A. Hocquet, M. Langgard, *J. Mol. Model.* **1998**, *4*, 94-112.

[133] R. M. Gomila, D. Quiñonero, A. Frontera, P. Ballester, P. M. Deyà, *J. Mol. Struc. Theochem* **2000**, *531*, 381-386.

[134] D. L. Cullen, E. F. Meyer Jnr, *Acta Crystallogr. B* **1976**, *32*, 2259-2269.

[135] J. K. Sprafke, D. V. Kondratuk, M. Wykes, A. L. Thompson, M. Hoffmann, R. Drevinskas, W.-H. Chen, C. K. Yong, J. Kärnbratt, J. E. Bullock, et al., *manuscript submitted* **n.d.**

[136] F. Y. Kwong, A. Klapars, S. L. Buchwald, *Org. Lett.* **2002**, *4*, 581-584.

[137] J. Wu, M. D. Watson, K. Müllen, *Angew. Chem. Int. Ed.* **2003**, *42*, 5329-5333.

[138] X. Shen, D. M. Ho, R. A. Pascal, *J. Am. Chem. Soc.* **2004**, *126*, 5798-5805.

[139] L. Zhu, L. Cheng, Y. Zhang, R. Xie, J. You, *J. Org. Chem.* **2007**, *72*, 2737-2743.

[140] H. Zhang, Q. Cai, D. Ma, *J. Org. Chem.* **2005**, *70*, 5164-5173.

[141] J. C. Antilla, J. M. Baskin, T. E. Barder, S. L. Buchwald, *J. Org. Chem.* **2004**, *69*, 5578-5587.

[142] J. W. W. Chang, X. Xu, P. W. H. Chan, *Tetrahedron Lett.* **2007**, *48*, 245-248.

[143] F. Dotz, J. D. Brand, S. Ito, L. Gherghel, K. Mullen, *J. Am. Chem. Soc.* **2000**, *122*, 7707-7717.

[144] H. J. Barber, R. Slack, *J. Chem. Soc.* **1944**, 612-615.

[145] C. J. Wilson, Large Porphyrin-based π-Systems, DPhil Thesis, University of Oxford, **2006**.

[146] R. J. Pilling, D. A. Whiting, *J. Chem. Soc., Perkin Trans. 1* **1999**, 2077-2086.

[147] P. B. Rheiner, D. Seebach, *Chem. Eur. J.* **1999**, *5*, 3221-3236.

[148] L. Friedman, H. Shechter, *J. Org. Chem.* **1960**, *25*, 877-879.

[149] S. Wawzonek, E. M. Smolin, *Org. Syn.* **1953**, *Collective Volume 3*, 715-716.

[150] J. L. Bullington, R. R. Wolff, P. F. Jackson, *J. Org. Chem.* **2002**, *67*, 9439-9442.

[151] C. Coudret, *Synthetic Commun.* **1996**, *26*, 3543-3547.

[152] A. C. Spivey, L. Shukla, J. F. Hayler, *Org. Lett.* **2007**, *9*, 891-894.

[153] L. J. Esdaile, Unpublished Results, **n.d.**

[154] Z. Wang, H. Fu, Y. Jiang, Y. Zhao, *Synlett* **2008**, *2008*, 2540-2546.

[155] A. Correa, C. Bolm, *Adv. Synth. Catal.* **2007**, *349*, 2673-2676.

[156] R. Zhu, L. Xing, X. Wang, C. Cheng, D. Su, Y. Hu, *Adv. Synth. Catal.* **2008**, *350*, 1253-1257.

[157] D. Marchand, K. Croes, J. Dolan, L. Snyder, *J. Chromatogr. A* **2005**, *1062*, 57-64.

[158] A. Kalk, H. J. C. Berendsen, *J. Magn. Reson.* **1976**, *24*, 343-366.

[159] T. Wagenknecht, V. A. Bloomfield, *Biopolymers* **1975**, *14*, 2297-2309.

[160] E. Kellenberger, in *Symmetry and Function of Biological Systems at the Macromolecular Level* (Eds.: A. Engstrom, B. Strandberg), Wiley-interscience, New York, **1969**, pp. 349-366.

[161] D. Caspar, *Biophys. J.* **1980**, *32*, 103-138.

[162] E. M. Levy, *J. Theor. Biol.* **1974**, *43*, 133-149.

[163] A. Klug, *Angew. Chem. Int. Ed. Engl.* **1983**, *22*, 565-582.

[164] K. Namba, R. Pattanayek, G. Stubbs, *J. Mol. Biol.* **1989**, *208*, 307-325.

[165] J. King, *J. Mol. Biol.* **1971**, *58*, 693-698.

[166] P. Vernier, *La Construction, L'usage, Et Les Propriétés Du Quadrant Nouveau De Mathématiques*, **1631**.

[167] J. A. Petruska, A. J. Hodge, *P. Natl. Acad. Sci. USA* **1964**, *51*, 871-876.

[168] H. E. Huxley, W. Brown, *J. Mol. Biol.* **1967**, *30*, 383-434.

[169] T. F. Anderson, R. Stephens, *Virology* **1964**, *23*, 113-117.

[170] J. S. Lindsey, *New J. Chem.* **1991**, *15*, 153-180.

[171] T. R. Kelly, R. L. Xie, C. K. Weinreb, T. Bregant, *Tetrahedron Lett.* **1998**, *39*, 3675-3678.

[172] T. Hill, *Linear Aggregation Theory in Cell Biology*, Springer-verlag, Berlin, **1987**.

[173] C. A. Hunter, S. Tomas, *J. Am. Chem. Soc.* **2006**, *128*, 8975-8979.

[174] K. Tahara, Y. Tobe, *Chem. Rev.* **2006**, *106*, 5274-5290.

[175] H. W. Kroto, J. R. Heath, S. C. O'Brien, R. F. Curl, R. E. Smalley, *Nature* **1985**, *318*, 162-163.

[176] W. Krätschmer, L. D. Lamb, K. Fostiropoulos, D. R. Huffman, *Nature* **1990**, *347*, 354-358.

[177] S. Iijima, *Nature* **1991**, *354*, 56-58.

[178] L. T. Scott, *Angew. Chem. Int. Ed.* **2003**, *42*, 4133-4135.

[179] H. S. Choi, K. S. Kim, *Angew. Chem. Int. Ed.* **1999**, *38*, 2256-2258.

[180] V. Elser, R. C. Haddon, *Nature* **1987**, *325*, 792-794.

[181] R. C. Haddon, L. F. Schneemeyer, J. V. Waszczak, S. H. Glarum, R. Tycko, G. Dabbagh, A. R. Kortan, A. J. Muller, A. M. Mujsce, M. J. Rosseinsky, et al., *Nature* **1991**, *350*, 46-47.

[182] R. S. Ruoff, D. Beach, J. Cuomo, T. McGuire, R. L. Whetten, F. Diederich, *J. Phys. Chem.* **1991**, *95*, 3457-3459.

[183] J. W. Bausch, G. K. S. Prakash, G. A. Olah, D. S. Tse, D. C. Lorents, Y. K. Bae, R. Malhotra, *J. Am. Chem. Soc.* **1991**, *113*, 3205-3206.

[184] E. Jariwala, P. Mohanty, M. Ketchen, R. Webb, *Phys. Rev. Lett.* **2001**, *86*, 1594-1597.

[185] V. Chandrasekhar, R. Webb, M. Brady, M. Ketchen, W. Gallagher, A. Kleinsasser, *Phys. Rev. Lett.* **1991**, *67*, 3578-3581.

[186] D. Mailly, C. Chapelier, A. Benoit, *Phys. Rev. Lett.* **1993**, *70*, 2020-2023.

[187] M. Mayor, C. Didschies, *Angew. Chem. Int. Ed.* **2003**, *42*, 3176-3179.

[188] D. Eisenberg, R. Shenhar, M. Rabinovitz, *Chem. Soc. Rev.* **2010**, *39*, 2879-2890.

[189] R. Hoffmann, *Tetrahedron* **1966**, *22*, 521-538.

[190] J. Bernholc, J. C. Phillips, *J. Chem. Phys.* **1986**, *85*, 3258-3267.

[191] K. S. Pitzer, E. Clementi, *J. Am. Chem. Soc.* **1959**, *81*, 4477-4485.

[192] F. Diederich, Y. Rubin, C. B. Knobler, R. L. Whetten, K. E. Schriver, K. N. Houk, Y. Li, *Science* **1989**, *245*, 1088-1090.

[193] Y. Rubin, S. S. Lin, C. B. Knobler, J. Anthony, A. M. Boldi, F. Diederich, *J. Am. Chem. Soc.* **1991**, *113*, 6943-6949.

[194] F. Diederich, Y. Rubin, O. L. Chapman, N. S. Goroff, *Helv. Chim. Acta* **1994**, *77*, 1441-1457.

[195] Y. Rubin, C. B. Knobler, F. Diederich, *J. Am. Chem. Soc.* **1990**, *112*, 4966-4968.

[196] F. Diederich, *Nature* **1994**, *369*, 199-207.

[197] Y. Rubin, M. Kahr, C. B. Knobler, F. Diederich, C. L. Wilkins, *J. Am. Chem. Soc.* **1991**, *113*, 495-500.

[198] Y. Tobe, T. Fujii, H. Matsumoto, K. Naemura, *Pure Appl. Chem.* **1996**, *68*, 239-242.

[199] Y. Tobe, R. Umeda, N. Iwasa, M. Sonoda, *Chem. Eur. J.* **2003**, *9*, 5549-5559.

[200] S. W. McElvany, M. M. Ross, N. S. Goroff, F. Diederich, *Science* **1993**, *259*, 1594-1596.

[201] H. Darabi, T. Kawase, M. Oda, *Tetrahedron Lett.* **1995**, *36*, 9525-9526.

[202] T. Kawase, H. R. Darabi, M. Oda, *Angew. Chem. Int. Ed. Engl.* **1996**, *35*, 2664-2666.

[203] T. Kawase, K. Tanaka, N. Fujiwara, H. R. Darabi, M. Oda, *Angew. Chem. Int. Ed.* **2003**, *42*, 1624-1628.

[204] T. Kawase, K. Tanaka, Y. Seirai, N. Shiono, M. Oda, *Angew. Chem. Int. Ed.* **2003**, *42*, 5597-5600.

[205] T. Kawase, Y. Nishiyama, T. Nakamura, T. Ebi, K. Matsumoto, H. Kurata, M. Oda, *Angew. Chem. Int. Ed.* **2007**, *46*, 1086-1088.

[206] T. Kawase, N. Ueda, K. Tanaka, Y. Seirai, M. Oda, *Tetrahedron Lett.* **2001**, *42*, 5509-5511.

[207] M. Ohkita, K. Ando, T. Tsuji, *Chem. Commun.* **2001**, 2570-2571.

[208] R. Jasti, J. Bhattacharjee, J. B. Neaton, C. R. Bertozzi, *J. Am. Chem. Soc.* **2008**, *130*, 17646-17647.

[209] T. Hiroko, O. Haruka, Y. Yosuke, B. Jean, I. Kenichiro, *Angew. Chem. Int. Ed.* **2009**, *48*, 6112-6116.

[210] H. Omachi, S. Matsuura, Y. Segawa, K. Itami, *Angew. Chem. Int. Ed.* **2010**, *49*, 10202-10205.

[211] T. Iwamoto, Y. Watanabe, Y. Sakamoto, T. Suzuki, S. Yamago, *J. Am. Chem. Soc.* **2011**, *133*, 8354-8361.

[212] S. Yamago, Y. Watanabe, T. Iwamoto, *Angew. Chem. Int. Ed.* **2009**, *49*, 757-759.

[213] B. M. Wong, *J. Phys. Chem. C* **2009**, *113*, 21921-21927.

[214] Y. Segawa, S. Miyamoto, H. Omachi, S. Matsuura, P. Šenel, T. Sasamori, N. Tokitoh, K. Itami, *Angew. Chem. Int. Ed.* **2011**, *50*, 3244-3248.

[215] J. Krömer, I. Rios-Carreras, G. Fuhrmann, C. Musch, M. Wunderlin, T. Debaerdemaeker, E. Mena-Osteritz, P. Bäuerle, *Angew. Chem. Int. Ed.* **2000**, *39*, 3481-3486.

[216] G. Fuhrmann, J. Krömer, P. Bäurele, *Synth. Met.* **2001**, *119*, 125-126.

[217] D. O'Krongly, S. R. Denmeade, M. Y. Chiang, R. Breslow, *J. Am. Chem. Soc.* **1985**, *107*, 5544-5545.

[218] G. Fuhrmann, T. Debaerdemaeker, P. Bäuerle, *Chem. Commun.* **2003**, 948-949.

[219] F. Zhang, G. Götz, H. D. F. Winkler, C. A. Schalley, P. Bäuerle, *Angew. Chem. Int. Ed.* **2009**, *48*, 6632-6635.

[220] M. Iyoda, P. Huang, T. Nishiuchi, M. Takase, T. Nishinaga, *Heterocycles* **2011**, *82*, 1143-1149.

[221] M. Williams-Harry, A. Bhaskar, G. Ramakrishna, T. Goodson, M. Imamura, A. Mawatari, K. Nakao, H. Enozawa, T. Nishinaga, M. Iyoda, *J. Am. Chem. Soc.* **2008**, *130*, 3252-3253.

[222] K. Nakao, M. Nishimura, T. Tamachi, Y. Kuwatani, H. Miyasaka, T. Nishinaga, M. Iyoda, *J. Am. Chem. Soc.* **2006**, *128*, 16740-16747.

[223] D. L. Pearson, J. M. Tour, *J. Org. Chem.* **1997**, *62*, 1376-1387.

[224] W. L. Driessen, T. X. Neenan, *Acta Crystallogr. C* **1996**, *52*, 59-61.

[225] A. Hay, *J. Org. Chem.* **1960**, *25*, 1275-1276.

[226] Y. Kobuke, H. Miyaji, *J. Am. Chem. Soc.* **1994**, *116*, 4111-4112.

[227] R. Takahashi, Y. Kobuke, *J. Am. Chem. Soc.* **2003**, *125*, 2372-2373.

[228] R. Takahashi, Y. Kobuke, *J. Org. Chem.* **2005**, *70*, 2745-2753.

[229] K. Ogawa, Y. Kobuke, *Angew. Chem. Int. Ed.* **2000**, *39*, 4070-4073.

[230] T. M. Trnka, R. H. Grubbs, *Acc. Chem. Res.* **2001**, *34*, 18-29.

[231] A. Ohashi, A. Satake, Y. Kobuke, *Bull. Chem. Soc. Jpn.* **2004**, *77*, 365-374.

[232] C. Ikeda, A. Satake, Y. Kobuke, *Org. Lett.* **2003**, *5*, 4935-4938.

[233] M. C. Chang, P. M. Callahan, P. S. Parkes-Loach, T. M. Cotton, P. A. Loach, *Biochemistry* **1990**, *29*, 421-429.

[234] T. Hori, N. Aratani, A. Takagi, T. Matsumoto, T. Kawai, M.-C. Yoon, Z. S. Yoon, S. Cho, D. Kim, A. Osuka, *Chem. Eur. J.* **2006**, *12*, 1319-1327.

[235] T. Hori, X. Peng, N. Aratani, A. Takagi, T. Matsumoto, T. Kawai, Z. S. Yoon, M.-C. Yoon, J. Yang, D. Kim, et al., *Chem. Eur. J.* **2008**, *14*, 582-595.

[236] Y. Nakamura, I. Hwang, N. Aratani, T. K. Ahn, D. M. Ko, A. Takagi, T. Kawai, T. Matsumoto, D. Kim, A. Osuka, *J. Am. Chem. Soc.* **2005**, *127*, 236-246.

[237] S. Rucareanu, A. Schuwey, A. Gossauer, *J. Am. Chem. Soc.* **2006**, *128*, 3396-3413.

[238] O. Mongin, A. Schuwey, M.-A. Vallot, A. Gossauer, *Tetrahedron Lett.* **1999**, *40*, 8347-8350.

[239] K. Sugiura, Y. Fujimoto, Y. Sakata, *Chem. Commun.* **2000**, 1105-1106.

[240] A. Kato, K. Sugiura, H. Miyasaka, H. Tanaka, T. Kawai, M. Sugimoto, M. Yamashita, *Chem. Lett.* **2004**, *33*, 578-579.

[241] C. Houarner-Rassin, Unpublished Results, **n.d.**

[242] M. S. Newman, L. F. Lee, *J. Org. Chem.* **1972**, *37*, 4468-4469.

[243] D. Lehnherr, J. Gao, F. A. Hegmann, R. R. Tykwinski, *Org. Lett.* **2008**, *10*, 4779-4782.

[244] J. K. Sprafke, Supramolecular Control of Synthesis and Electronic Structure of Porphyrin Oligomers, DPhil Thesis, University of Oxford, **2011**.

[245] V. E. Williams, T. M. Swager, *J. Polym. Sci. A Polym. Chem.* **2000**, *38*, 4669-4676.

[246] F. C. Grozema, C. Houarner-Rassin, P. Prins, L. D. A. Siebbeles, H. L. Anderson, *J. Am. Chem. Soc.* **2007**, *129*, 13370-13371.

[247] D. W. J. McCallien, J. K. M. Sanders, *J. Am. Chem. Soc.* **1995**, *117*, 6611-6612.

[248] R. F. Kelley, S. J. Lee, T. M. Wilson, Y. Nakamura, D. M. Tiede, A. Osuka, J. T. Hupp, M. R. Wasielewski, *J. Am. Chem. Soc.* **2008**, *130*, 4277-4284.

[249] D. I. Svergun, M. H. J. Koch, *Rep. Prog. Phys.* **2003**, *66*, 1735-1782.

[250] A. Guinier, G. Fournet, *Small-angle Scattering of X-rays*, Wiley, New York, **1955**.

[251] D. Svergun, C. Barberato, M. H. J. Koch, *J. Appl. Crystallogr.* **1995**, *28*, 768-773.

[252] D. I. Svergun, *J. Appl. Crystallogr.* **1992**, *25*, 495-503.

[253] E. Mylonas, D. I. Svergun, *J. Appl. Crystallogr.* **2007**, *40*, s245-s249.

[254] P. V. Konarev, V. V. Volkov, A. V. Sokolova, M. H. J. Koch, D. I. Svergun, *J. Appl. Crystallogr.* **2003**, *36*, 1277-1282.

[255] R. Rathore, C. L. Burns, M. I. Deselnicu, *Org. Lett.* **2001**, *3*, 2887-2890.

[256] M. C. O'Sullivan, J. K. Sprafke, D. V. Kondratuk, C. Rinfray, T. D. W. Claridge, A. Saywell, M. O. Blunt, J. N. O'Shea, P. H. Beton, M. Malfois, et al., *Nature* **2011**, *469*, 72-75.

[257] K. L. Mardis, H. M. Sutton, X. Zuo, J. S. Lindsey, D. M. Tiede, *J. Phys. Chem. A* **2009**, *113*, 2516-2523.

[258] A. Saywell, J. K. Sprafke, L. J. Esdaile, A. J. Britton, A. Rienzo, H. L. Anderson, J. N. O'Shea, P. H. Beton, *Angew. Chem. Int. Ed.* **2010**, *49*, 9136-9139.

[259] D. V. Kondratuk, Unpublished Results, **n.d.**

[260] D. Kondratiuk, Synthesis, Structure and Electronic Properties of Porphyrin-based Single-molecule Junctions, Wires and Rings, PRS Transfer Report, University of Oxford, **2010**.

[261] J. K. Sprafke, B. Odell, T. D. W. Claridge, H. L. Anderson, *Angew. Chem. Int. Ed.* **2011**, *50*, 5572-5575.

[262] A. Chen, D. Wu, C. S. Johnson, *J. Am. Chem. Soc.* **1995**, *117*, 7965-7970.

[263] A. J. Simpson, *Magn. Reson. Chem.* **2002**, *40*, S72-S82.

[264] A. R. Waldeck, P. W. Kuchel, A. J. Lennon, B. E. Chapman, *Prog. Nucl. Magn. Reson. Spectrosc.* **1997**, *30*, 39-68.

[265] Y. Cohen, L. Avram, L. Frish, *Angew. Chem. Int. Ed.* **2005**, *44*, 520-554.

[266] A. Macchioni, G. Ciancaleoni, C. Zuccaccia, D. Zuccaccia, *Chem. Soc. Rev.* **2008**, *37*, 479-489.

[267] D. Li, G. Kagan, R. Hopson, P. G. Williard, *J. Am. Chem. Soc.* **2009**, *131*, 5627-5634.

[268] B. Valeur, *Molecular Fluorescence: Principles and Applications*, Wiley-vch, Weinheim; New York, **2002**.

[269] I. Hwang, G. D. Scholes, *Chem. Mater.* **2011**, *23*, 610-620.

[270] I. Gryczynski, H. Malak, J. R. Lakowicz, *Chem. Phys. Lett.* **1995**, *245*, 30-35.

[271] S. E. Bradforth, R. Jimenez, F. van Mourik, R. van Grondelle, G. R. Fleming, *J. Phys. Chem.* **1995**, *99*, 16179-16191.

[272] S. Karrasch, P. A. Bullough, R. Ghosh, *EMBO J.* **1995**, *14*, 631-638.

[273] T. Joo, Y. Jia, J.-Y. Yu, D. M. Jonas, G. R. Fleming, *J. Phys. Chem.* **1996**, *100*, 2399-2409.

[274] S. Savikhin, W. Struve, *Biophys. J.* **1994**, *67*, 2002-2007.

[275] M. H. Vos, M. R. Jones, C. N. Hunter, J. Breton, J.-C. Lambry, J.-L. Martin, *Biochemistry* **1994**, *33*, 6750-6757.

[276] R. J. Stanley, S. G. Boxer, *J. Phys. Chem.* **1995**, *99*, 859-863.

[277] R. Jimenez, S. N. Dikshit, S. E. Bradforth, G. R. Fleming, *J. Phys. Chem.* **1996**, *100*, 6825-6834.

[278] S. Volker, *Annu. Rev. Phys. Chem.* **1989**, *40*, 499-530.

[279] C. De Caro, R. W. Visschers, R. van Grondelle, S. Voelker, *J. Phys. Chem.* **1994**, *98*, 10584-10590.

[280] R. Monshouwer, *Chem. Phys. Lett.* **1995**, *246*, 341-346.

[281] S. Hess, E. Akesson, R. Cogdell, T. Pullerits, V. Sundstrom, *Biophys. J.* **1995**, *69*, 2211-2225.

[282] H. Amerongen, L. Valkunas, R. van Grondelle, *Photosynthetic Excitons*, World Scientific, Singapore; River Edge N.J., **2000**.

[283] J. Strümpfer, K. Schulten, *J. Chem. Phys.* **2009**, *131*, 225101.

[284] V. Nagarajan, W. W. Parson, *Biochemistry* **1997**, *36*, 2300-2306.

[285] S. Hess, M. Chachisvilis, K. Timpmann, M. R. Jones, G. J. Fowler, C. N. Hunter, V. Sundström, *Proc. Natl. Acad. Sci. USA* **1995**, *92*, 12333-12337.

[286] U. Finkele, C. Lauterwasser, W. Zinth, K. A. Gray, D. Oesterhelt, *Biochemistry* **1990**, *29*, 8517-8521.

[287] V. Nagarajan, W. W. Parson, D. Gaul, C. Schenck, *Proc. Natl. Acad. Sci. USA* **1990**, *87*, 7888-7892.

[288] L. M. P. Beekman, F. van Mourik, M. R. Jones, H. M. Visser, C. N. Hunter, R. van Grondelle, *Biochemistry* **1994**, *33*, 3143-3147.

[289] G. R. Fleming, R. van Grondelle, *Curr. Opinion Struct. Biol.* **1997**, *7*, 738-748.

[290] J. Larsen, J. Andersson, T. Polívka, J. Sly, M. J. Crossley, V. Sundström, E. Åkesson, *Chem. Phys. Lett.* **2005**, *403*, 205-210.

[291] N. Aratani, D. Kim, A. Osuka, *Acc. Chem. Res.* **2009**, *42*, 1922-1934.

[292] X. Peng, N. Aratani, A. Takagi, T. Matsumoto, T. Kawai, I.-W. Hwang, T. K. Ahn, D. Kim, A. Osuka, *J. Am. Chem. Soc.* **2004**, *126*, 4468-4469.

[293] I.-W. Hwang, D. M. Ko, T. K. Ahn, Z. S. Yoon, D. Kim, X. Peng, N. Aratani, A. Osuka, *J. Phys. Chem. B* **2005**, *109*, 8643-8651.

[294] S. Hintschich, F. Dias, A. Monkman, *Phys. Rev. B* **2006**, *74*, 045210.

[295] W. Rettig, B. Strehmel, S. Schrader, H. Seifert, *Applied Fluorescence in Chemistry, Biology, and Medicine*, Springer, Berlin; New York, **1999**.

[296] K. F. Wong, M. S. Skaf, C.-Y. Yang, P. J. Rossky, B. Bagchi, D. Hu, J. Yu, P. F. Barbara, *J. Phys. Chem. B* **2001**, *105*, 6103-6107.

[297] R. Kersting, U. Lemmer, R. Mahrt, K. Leo, H. Kurz, H. Bässler, E. Göbel, *Phys. Rev. Lett.* **1993**, *70*, 3820-3823.

[298] G. Hayes, I. Samuel, R. Phillips, *Phys. Rev. B* **1995**, *52*, R11569-R11572.

[299] I. Samuel, B. Crystall, G. Rumbles, P. Burn, A. Holmes, R. Friend, *Synth. Met.* **1993**, *54*, 281-288.

[300] A. Ruseckas, P. Wood, I. Samuel, G. Webster, W. Mitchell, P. Burn, V. Sundström, *Phys. Rev. B* **2005**, *72*, 115214.

[301] S. Tretiak, A. Saxena, R. Martin, A. Bishop, *Phys. Rev. Lett.* **2002**, *89*, 097402.

[302] K. Wong, H. Wang, G. Lanzani, *Chem. Phys. Lett.* **1998**, *288*, 59-64.

[303] G. Lanzani, M. Nisoli, V. Magni, S. De Silvestri, G. Barbarella, M. Zambianchi, R. Tubino, *Phys. Rev. B* **1995**, *51*, 13770-13773.

[304] M.-H. Chang, M. Hoffmann, H. L. Anderson, L. M. Herz, *J. Am. Chem. Soc.* **2008**, *130*, 10171-10178.

[305] I. V. Rubtsov, K. Susumu, G. I. Rubtsov, M. J. Therien, *J. Am. Chem. Soc.* **2003**, *125*, 2687-2696.

[306] T. E. O. Screen, J. R. G. Thorne, R. G. Denning, D. G. Bucknall, H. L. Anderson, *J. Am. Chem. Soc.* **2002**, *124*, 9712-9713.

[307] T. E. O. Screen, J. R. G. Thorne, R. G. Denning, D. G. Bucknall, H. L. Anderson, *J. Mater. Chem.* **2003**, *13*, 2796-2808.

[308] W. J. R. Peveler, Porphyrin Nanorings, Part II Thesis, University of Oxford, **2011**.

[309] T. E. O. Screen, K. B. Lawton, G. S. Wilson, N. Dolney, R. Ispasoiu, T. Goodson III, S. J. Martin, D. D. C. Bradley, H. L. Anderson, *J. Mater. Chem.* **2001**, *11*, 312-320.

[310] H. L. Anderson, J. K. M. Sanders, *J. Chem. Soc., Perkin Trans. 1* **1995**, 2223-2229.

[311] D. Marsh, L. Mink, *J. Chem. Educ.* **1996**, *73*, 1188-1190.

[312] P. N. Day, K. A. Nguyen, R. Pachter, *J. Chem. Theory Comput.* **2008**, *4*, 1094-1106.

[313] G. Herzberg, E. Teiler, *Z. Phys. Chem. B* **1933**, *21*, 410.

[314] J. Shah, T. C. Damen, B. Deveaud, D. Block, *Appl. Phys. Lett.* **1987**, *50*, 1307-1309.

[315] D. N. Nikogosyan, *Appl. Phys. A* **1991**, *52*, 359-368.

[316] M. Dahlbom, T. Pullerits, S. Mukamel, V. Sundström, *J. Phys. Chem. B* **2001**, *105*, 5515-5524.

[317] D. R. Coulson, L. C. Satek, S. O. Grim, *Inorg. Synth.* **1972**, *13*, 121-124.

[318] R. N. Keller, H. D. Wycoff, *Inorg. Synth.* **1946**, *2*, 1-4.

[319] S. M. Waybright, K. McAlpine, M. Laskoski, M. D. Smith, U. H. F. Bunz, *J. Am. Chem. Soc.* **2002**, *124*, 8661-8666.

[320] H. Collins, Porphyrin Dimers for Two-Photon Photodynamic Therapy, DPhil Thesis, University of Oxford, **2008**.

[321] C. Bruckner, J. J. Posakony, C. K. Johnson, R. W. Boyle, B. R. James, D. Dolphin, *Porphyrins and Phthalocyanines* **1998**, *2*, 455-465.

[322] N. Aratani, A. Takagi, Y. Yanagawa, T. Matsumoto, T. Kawai, Z. S. Yoon, D. Kim, A. Osuka, *Chem. Eur. J.* **2005**, *11*, 3389-3404.

[323] M. Nilsson, *J. Magn. Reson.* **2009**, *200*, 296-302.

Appendix

7.1 Characterisation

7.1.1 Derivation of the 1:1 binding equation

The binding of an *N*-dentate ligand **L** with an *N*-site porphyrin receptor **P** can be described by the following equilibrium:

$$P + L \underset{}{\overset{K_f}{\rightleftharpoons}} LP$$

where K_f is the binding constant of ligand to the receptor, and can be characterised:

$$K_f = \frac{[LP]}{[P][L]} \quad \text{Eq. 36}$$

which can be rewritten as:

$$K_f[L][P] - [LP] = 0 \quad \text{Eq. 37}$$

The concentration of unbound ligand [L], and the concentration of unbound porphyrin [P], can be described in terms of the concentration of porphyrin-ligand complex [LP] and the total concentration of ligand or porphyrin, $[L]_0$ and $[P]_0$, respectively:

$$[L] = [L]_0 - [LP] \quad \text{Eq. 38}$$

$$[P] = [P]_0 - [LP] \quad \text{Eq. 39}$$

Substituting Equations 38 and 39 into Equation 37 gives:

$$K_f([L]_0 - [LP])([P]_0 - [LP]) - [LP] = 0 \quad \text{Eq. 40}$$

This expands into the form $ax^2 + bx + c = 0$:

$$K_f[LP]^2 - \left(K_f([L]_0 + [P]_0) + 1\right)[LP] + K_f[L]_0[P]_0 = 0 \quad \text{Eq. 41}$$

which can be solved for x:

$$[LP] = \frac{(K_f([L]_0 + [P]_0) + 1) \pm \sqrt{\left(K_f([L]_0 + [P]_0) + 1\right)^2 - 4{K_f}^2[L]_0[P]_0}}{2K_f} \quad \text{Eq. 42}$$

which can also be expressed as the ratio:

$$\frac{[LP]}{[P]_0} = \frac{(K_f([L]_0 + [P]_0) + 1) \pm \sqrt{\left(K_f([L]_0 + [P]_0) + 1\right)^2 - 4{K_f}^2[L]_0[P]_0}}{2K_f[P]_0} \quad \text{Eq. 43}$$

The absorption of the porphyrin during the titration follows the Beer Lambert Law, such that:

$$A_{ini} = \varepsilon_P[P]_0 l \quad \text{Eq. 44}$$

$$A_\infty = \varepsilon_{LP}[P]_0 l \quad \text{Eq. 45}$$

$$A = \varepsilon_P[P]l + \varepsilon_{LP}[LP]l \quad \text{Eq. 46}$$

where ε is the extinction coefficient and l is the pathlength. Substituting Equations 44–46 with Equation 39 allows the ratio $[LP]/[P]_0$ to be expressed in terms of absorption:

$$\frac{A - A_{ini}}{A_{\infty} - A_{ini}} = \frac{[LP]}{[P]_0} \qquad \text{Eq. 47}$$

This can be substituted into Equation 43 to give:

$$\frac{A - A_{ini}}{A_{\infty} - A_{ini}} = \frac{(K_f([L]_0 + [P]_0) + 1) \pm \sqrt{\left(K_f([L]_0 + [P]_0) + 1\right)^2 - 4{K_f}^2[L]_0[P]_0}}{2K_f[P]_0} \qquad \text{Eq. 48}$$

It was found out experimentally that the negative solution to Equation 48 was correct:[127]

$$\frac{A - A_{ini}}{A_{\infty} - A_{ini}} = \frac{\left(K_f([L]_0 + [P]_0) + 1\right) - \sqrt{\left(K_f([L]_0 + [P]_0) + 1\right)^2 - 4{K_f}^2[L]_0[P]_0}}{2K_f[P]_0} \qquad \text{Eq. 49}$$

Equation 49 was used to fit the UV-vis binding data using a non-linear curve fitting algorithm in OriginPro.

7.1.2 Crystal structure of model pyrrole **53**

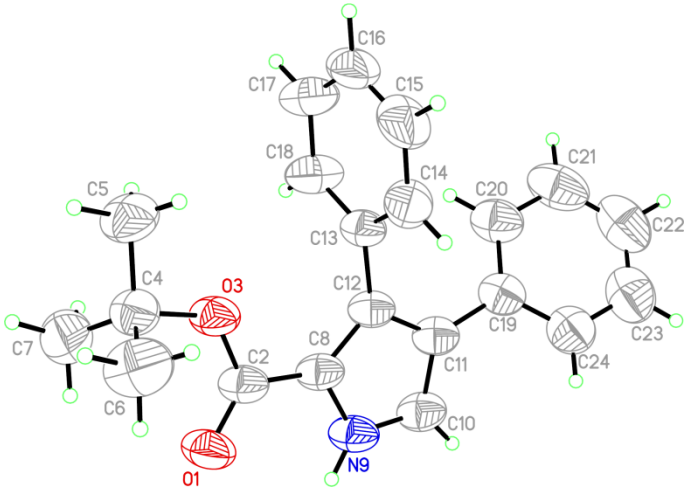

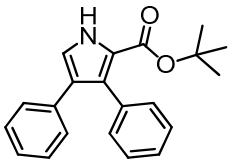

53

Figure A.1 ORTEP drawing of pyrrole **53**.

***Tert*-butyl 3,4-diphenyl-1H-pyrrole-2-carboxylate**	
Formula	$C_{21}H_{21}NO_2$
Formula weight	319.40
Crystal system	Monoclinic
Space group	$P\ 1\ 2_1/c\ 1$
a /Å	10.2486 (4)
b /Å	8.8394 (4)
c /Å	18.2359 (8)
α /°	90
β /°	94.9457 (19)
γ /°	90
V /Å^3	1832.06 (13)
Z	4
T /K	250
Crystal size /mm^3	$0.32 \times 0.20 \times 0.18$
Reflections measured	13147
Unique reflections	4051
R_1	0.0497
Rw_2	0.1078

Table A.1 X-ray crystallographic data for pyrrole **53**.

Selected bond lengths /Å			
O1–C2	1.221 (2)	C12–C13	1.488 (2)
C2–O3	1.329 (2)	C13–C14	1.375 (3)
C2–C8	1.443 (3)	C13–C18	1.380 (3)
O3–C4	1.472 (2)	C14–C15	1.384 (3)
C4–C5	1.524 (3)	C15–C16	1.360 (4)
C4–C6	1.515 (3)	C16–C17	1.361 (4)
C4–C7	1.513 (3)	C17–C18	1.378 (3)
C8–N9	1.376 (2)	C19–C20	1.387 (3)
C8–C12	1.388 (3)	C19–C24	1.385 (3)
N9–C10	1.343 (2)	C20–C21	1.392 (3)
C10–C11	1.384 (3)	C21–C22	1.374 (4)
C11–C12	1.420 (3)	C22–C23	1.359 (4)
C11-C19	1.472 (3)	C23–C24	1.370 (3)

Table A.2 Selected bond lengths from the crystal structure of pyrrole **53**.

Selected bond angles /°			
O1–C2–O3	124.31 (18)	C11–C12–C13	125.43 (17)
O1–C2–C8	123.61 (16)	C8–C12–C13	127.24 (16)
O3–C2–C8	112.07 (16)	C12–C13–C14	120.04 (18)
C2–O3–C4	122.81 (15)	C12–C13–C18	121.87 (17)
O3–C4–C5	101.35 (16)	C14–C13–C18	118.08 (18)
O3–C4–C6	109.37 (19)	C13–C14–C15	120.5 (2)
C5–C4–C6	110.97 (18)	C14–C15–C16	120.7 (2)
O3–C4–C7	110.04 (16)	C15–C16–C17	119.4 (2)
C5–C4–C7	110.89 (19)	C16–C17–C18	120.5 (3)
C6–C4–C7	113.5 (2)	C13–C18–C17	120.8 (2)
C2–C8–N9	118.39 (16)	C11–C19–C20	122.2 (2)
C2–C8–C12	133.71 (16)	C11–C19–C24	120.23 (19)
N9–C8–C12	107.75 (16)	C20–C19–C24	117.5 (2)
C8–N9–C10	109.28 (15)	C19–C20–C21	120.1 (3)
N9–C10–C11	109.55 (16)	C20–C21–C22	120.5 (3)
C10–C11–C12	106.25 (17)	C21–C22–C23	119.8 (3)
C10–C11–C19	124.45 (17)	C22–C23–C24	119.9 (3)
C12–C11–C19	129.28 (16)	C19–C24–C23	122.2 (3)
C11–C12–C8	107.17 (15)		

Table A.3 Selected bond angles from the crystal structure of pyrrole **53**.

7.1.3 ^{1}H NMR characterisation of ***l*-P2·15**

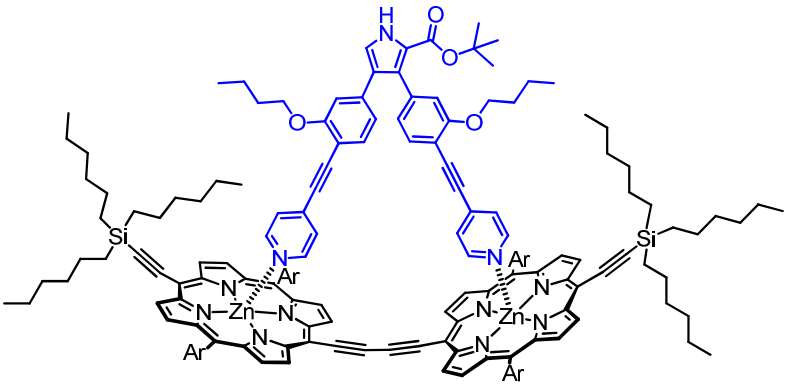

Figure A.2 Structural formula of ***l*-P2·15**.

As with previous porphyrin-pyridyl systems, the ^{1}H NMR of the porphyrin-ligand complex ***l*-P2·15** can be split into distinct regions. Peaks from porphyrin *β*-pyrrole protons occur at lowest field, followed by the porphyrin *meso*-aryl side chains. The dipyridyl pyrrole protons are shifted to higher field, between δ 2.5 and δ 7.0 ppm, due to the shielding effect of the porphyrin π-system on binding. In the aliphatic region of the spectrum, the alkyl protons from the trihexylsilyl (THS) groups, porphyrin *tert*-butyl protons and alkyl functionality on the pyrrole ligand can be found (Figure A.3).

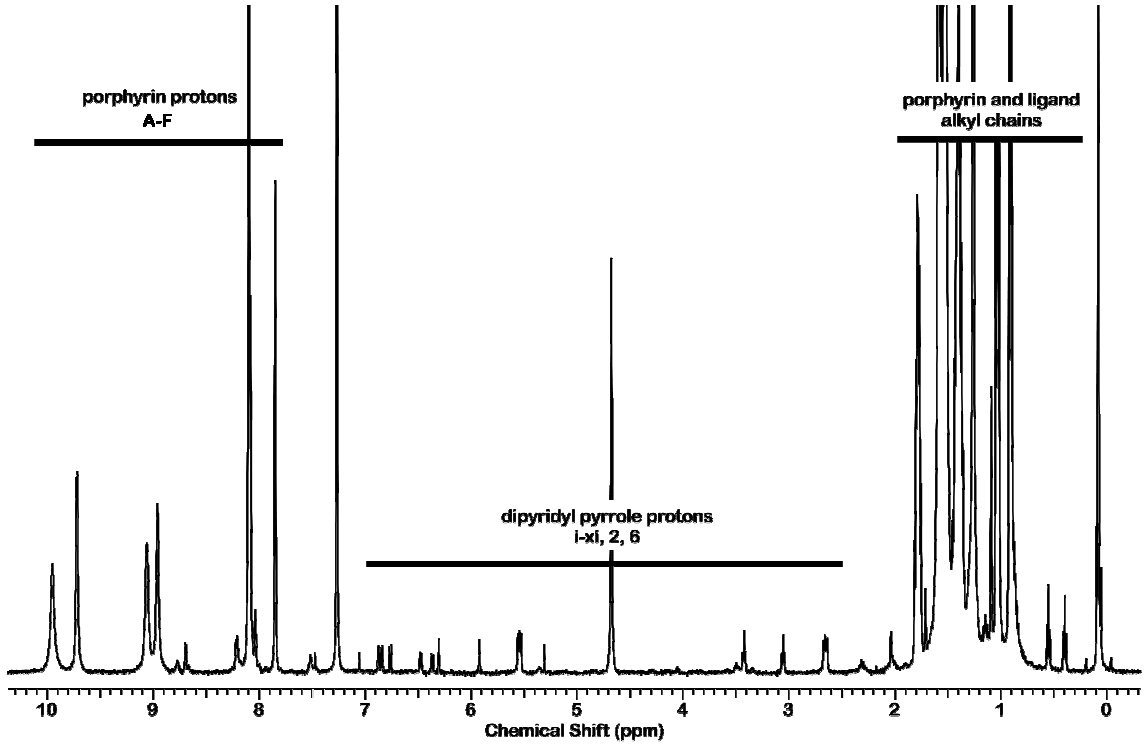

Figure A.3 ^{1}H NMR (500 MHz, $CDCl_3$, 298 K) of dipyridyl pyrrole-porphyrin complex ***l*-P2·15**, showing the full spectral region.

The presence of the *tert*-butyl ester at the 2-pyrrolic position desymmetrises the ligand, making each "leg" of the ligand spectroscopically distinct, with the chemical shift differences lessening with distance from the pyrrole. For this reason, we expect to see eight signals arising from the pyrrole *n*-butyl chains, which is what we find when examining the COSY (Figure A.4).

The triplets at δ 0.40 and δ 0.55 correlate to peaks hidden under the large signals arising from the protecting group alkyl chains. The COSY peaks can be traced, with the next methylene protons along the chain situated under the singlet at δ 1.26, and the other set as a triplet at δ 1.15. The final butoxy protons, 2 and 6, give triplets at δ 3.06 and δ 3.42, integrating at two protons each.

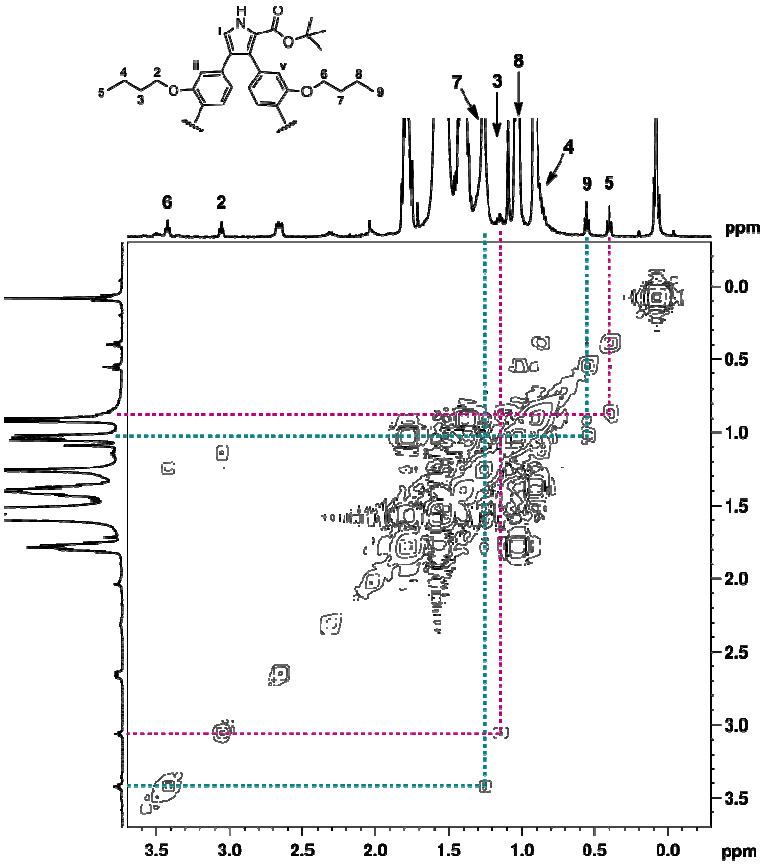

Figure A.4 ^{1}H COSY (500 MHz, $CDCl_3$, 298 K) of ***l*-P2·15** showing assignment of pyrrole *n*-butyl crosspeaks.

NOE crosspeaks would be expected to occur between butoxy protons 2 and 6 with their respective neighbouring aryl protons ii and v. 2 and 6 can be seen to correlate to two singlets downfield, and can thus be assigned (Figure A.5). Distinguishing which singlet corresponds to ii and which to v, was determined by the NOE that arises between pyrrole proton i and aryl proton ii. Figure A.6 shows a very weak NOE between the singlet at δ 5.92 and a doublet with a very small coupling constant at δ 6.87, corresponding to ii and i, respectively. A stronger NOE between i and a doublet at δ6.37 corresponds to an interaction with adjacent aryl proton iii.

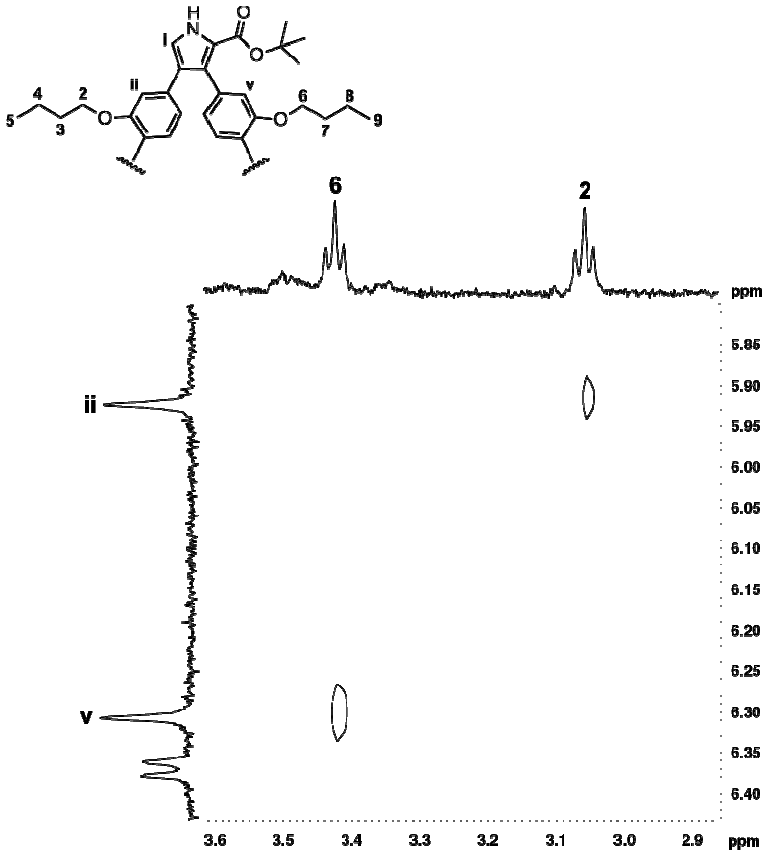

Figure A.5 ^{1}H 2D NOESY spectrum (500 MHz, $CDCl_3$, 298 K) of ***l*-P2·15** showing coupling between butoxy-peaks 2 and 6 with aryl protons ii and v, respectively. A mixing time of 400 ms was used (applied as a phase-alternating spin-lock pulse).

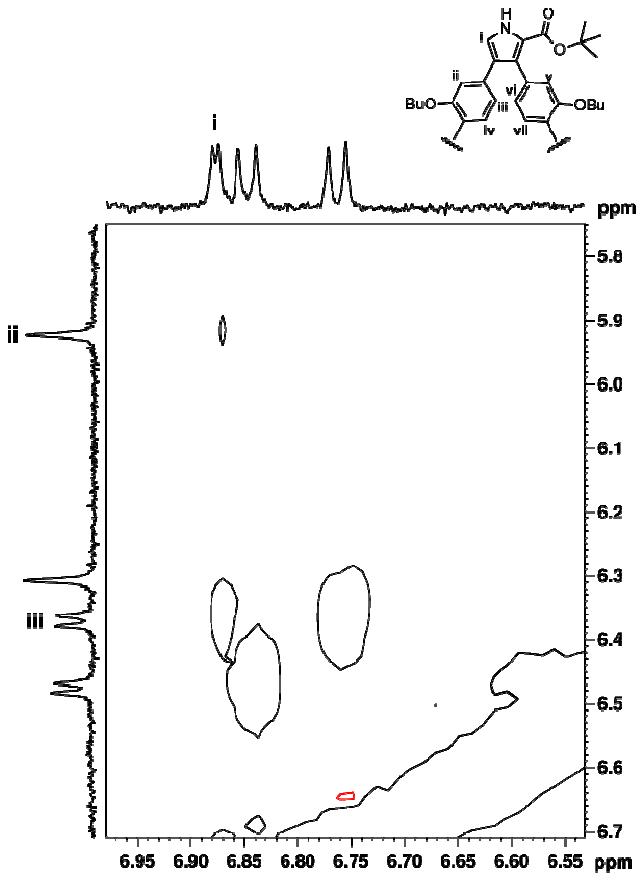

Figure A.6 ^{1}H 2D NOESY spectrum (500 MHz, $CDCl_3$, 298 K) of ***l*-P2·15** showing NOE crosspeaks between pyrrolic proton i, and aryl protons ii and iii. A mixing time of 400 ms was used (applied as a phase-alternating spin-lock pulse).

The COSY in Figure A.7 shows aryl proton iii coupling to a doublet at δ 6.76, which can be assigned as iv. All protons on the "leg" adjacent to the *tert*-butyl ester are deshielded and are downfield to the analogous protons on the opposite "leg". It can therefore be assumed that the two remaining doublets that are coupling to one another correspond to protons vi and vii.

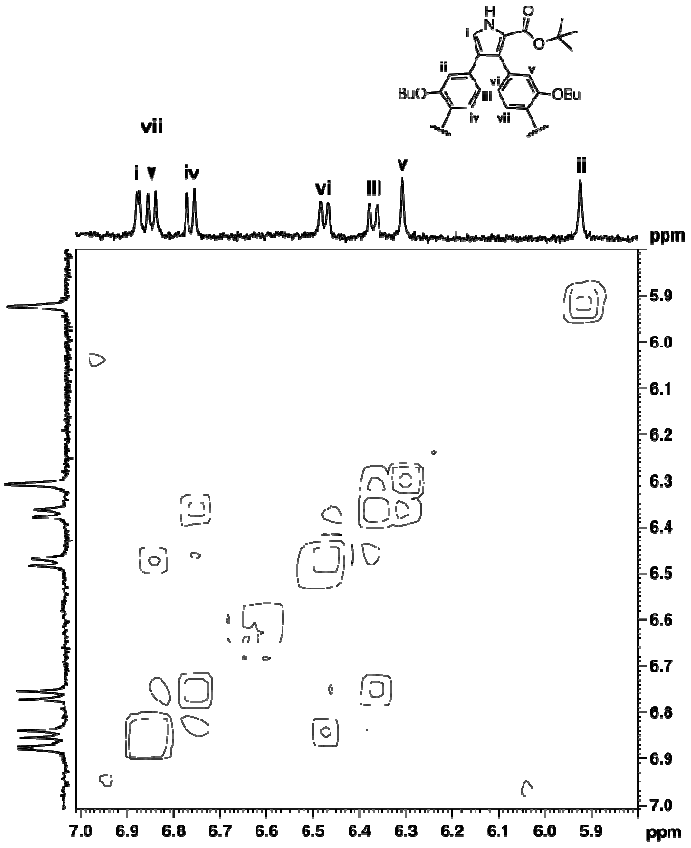

Figure A.7 ^{1}H COSY (500 MHz, $CDCl_3$, 298 K) of ***l*-P2·15** showing correlations between iii and iv, vi and vii.

The NOESY shows a very weak NOE between one of the porphyrin *β*-pyrrole protons, and what appears to be a double doublet at *δ* 2.66 (Figure A.8). Comparison with other ^{1}H NMR studies of pyridine-porphyrin complexes shows this is consistent with *α*-pyridyl protons ix and xi. The strong upfield shift of these protons is due to shielding by the porphyrin π-system. At a far distance from the *tert*-butyl ester, the shift difference between the two "legs" is much smaller, yet is still sufficient to split the pyridyl protons into two distinct doublets.

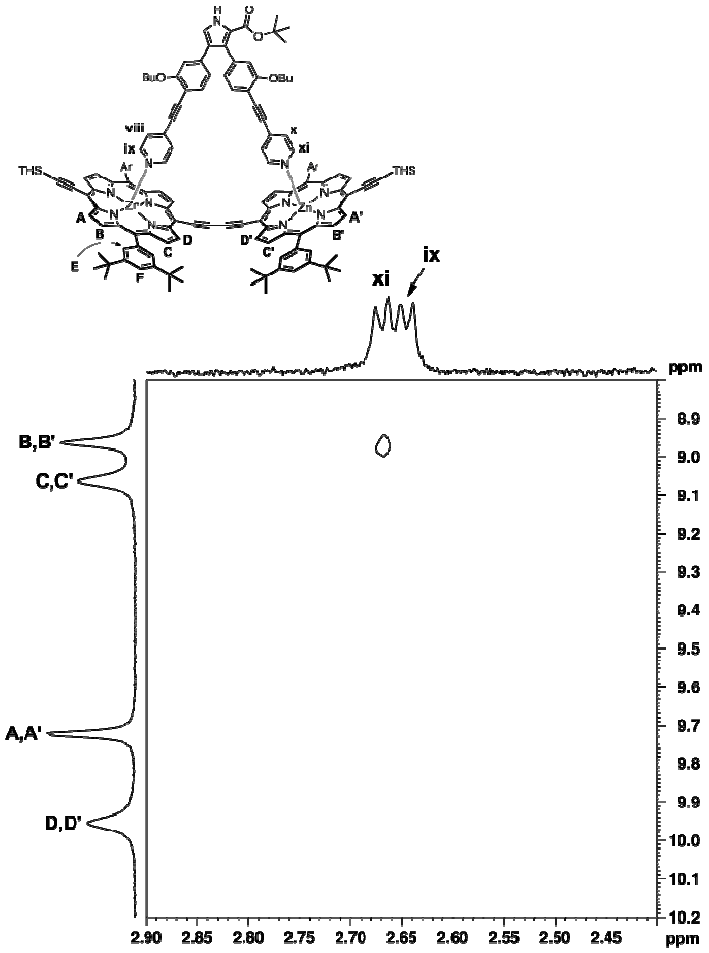

Figure A.8 ^{1}H 2D NOESY (500 MHz, $CDCl_3$, 298 K) of ***l*-P2·15** showing an NOE between porphyrin β-pyrrole protons B/B' and α-pyridyl protons ix and xi. A mixing time of 400 ms was used (applied as a phase-alternating spin-lock pulse).

Protons ix and xi give a strong COSY correlation with a second pair of doublets at δ 5.55, which can be assigned to the β-pyridyl protons viii and x (Figure A.9).

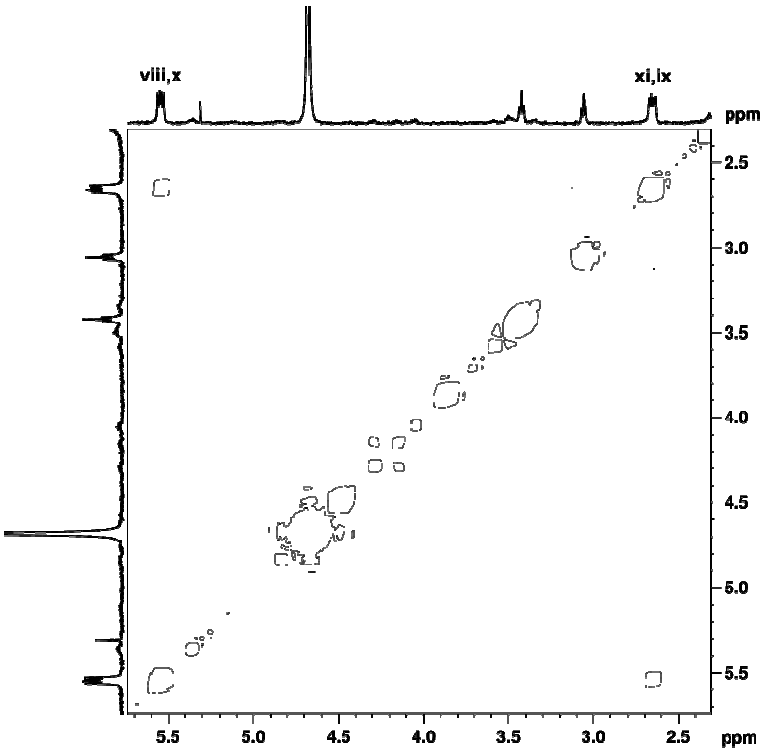

Figure A.9 ^{1}H COSY (500 MHz, $CDCl_3$, 298 K) of ***l*-P2·15** showing correlation between the pyridyl proton sets ix xi, and viii x.

The 2D NOESY of the porphyrin spectral region allows the porphyrin and aryl sidechain protons to be assigned (Figure A.10).

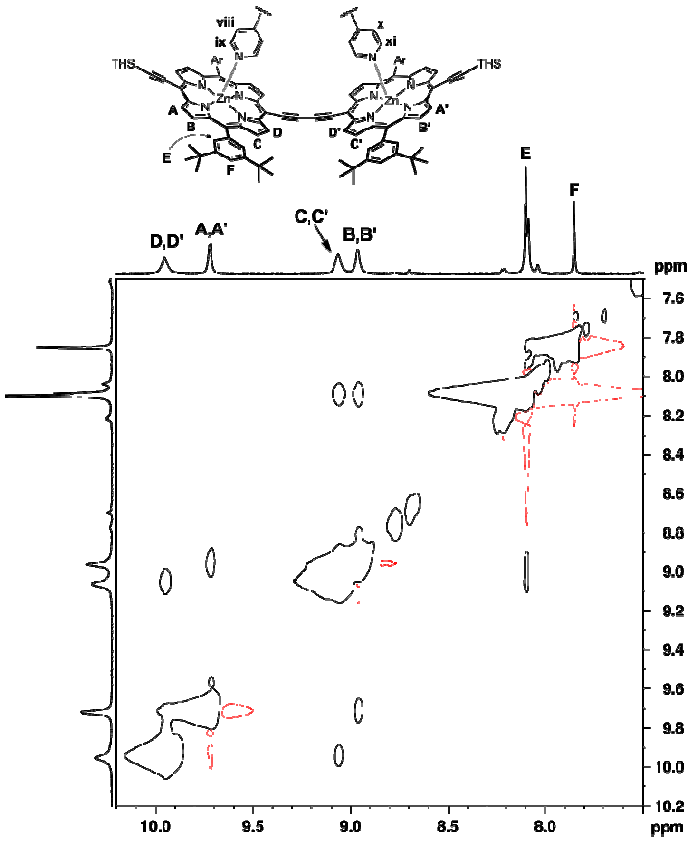

Figure A.10 ^{1}H 2D NOESY (500 MHz, $CDCl_3$, 298 K) of ***l*-P2·15** showing the porphyrin region of the spectrum. A mixing time of 400 ms was used (applied as a phase-alternating spin-lock pulse).

The two high field porphyrin peaks at δ 8.96 and δ 9.06 are seen to correlate to a singlet at δ 8.10. Integration shows the ratio of these peaks to be 1:2, showing the sharp singlet is due to the eight *ortho* protons on the aryl sidechains, E. The two porphyrin peaks are the β-pyrrole protons B and C, adjacent to the *meso*-aryl sidegroups. The singlet at δ 7.85 couples to E in the COSY, thus can be assigned to *para*- protons F.

The remaining two porphyrin peaks, can be assigned to the β-pyrrole protons A and D. Due to the greater deshielding effects of the inner butadiyne moiety relative to the single alkyne, protons towards the centre of the dimer, B and C, are shifted to higher field. Although the

dipyridyl pyrrole ligand breaks the molecular symmetry of the porphyrin dimer, by ^{1}H NMR the effects of the *tert*-butyl ester are negligible and protons A/A', B/B'…etc. are equivalent.

7.1.4 Cyclic octamer complex ***c*-P8·T8** ^{1}H NMR data

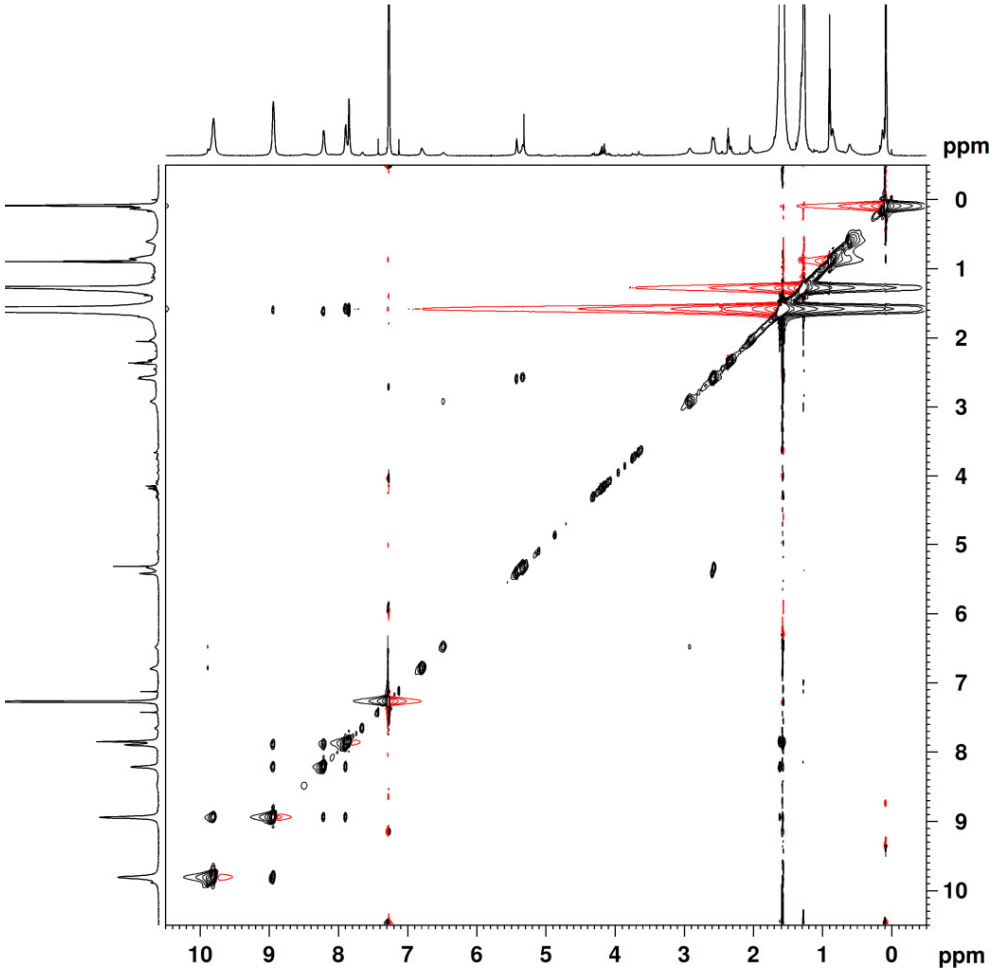

Figure A.11 ^{1}H 2D NOESY (700 MHz, $CDCl_3$, 298 K) of ***c*-P8·T8**. A mixing time of 200 ms was used (applied as a phase-alternating spin-lock pulse).

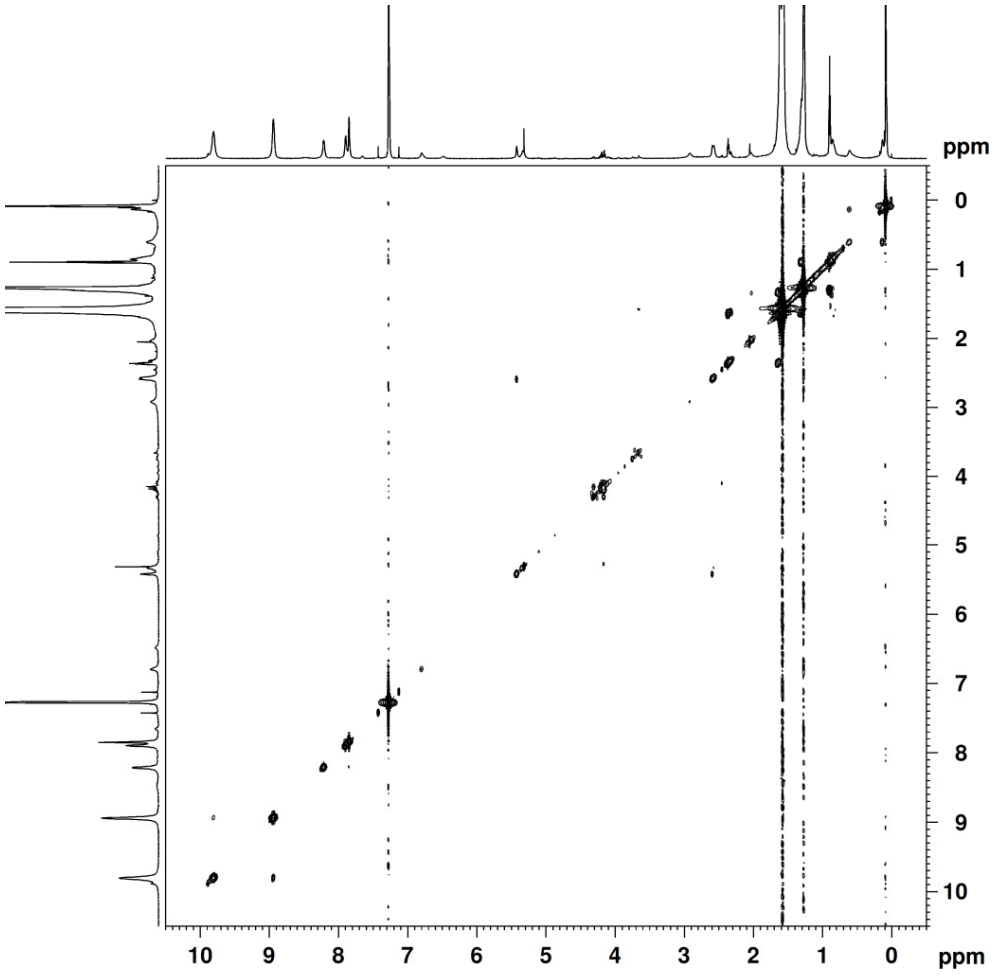

Figure A.12 ^{1}H COSY (700 MHz, $CDCl_3$, 298 K) of ***c*-P8·T8**.

7.2 Artwork

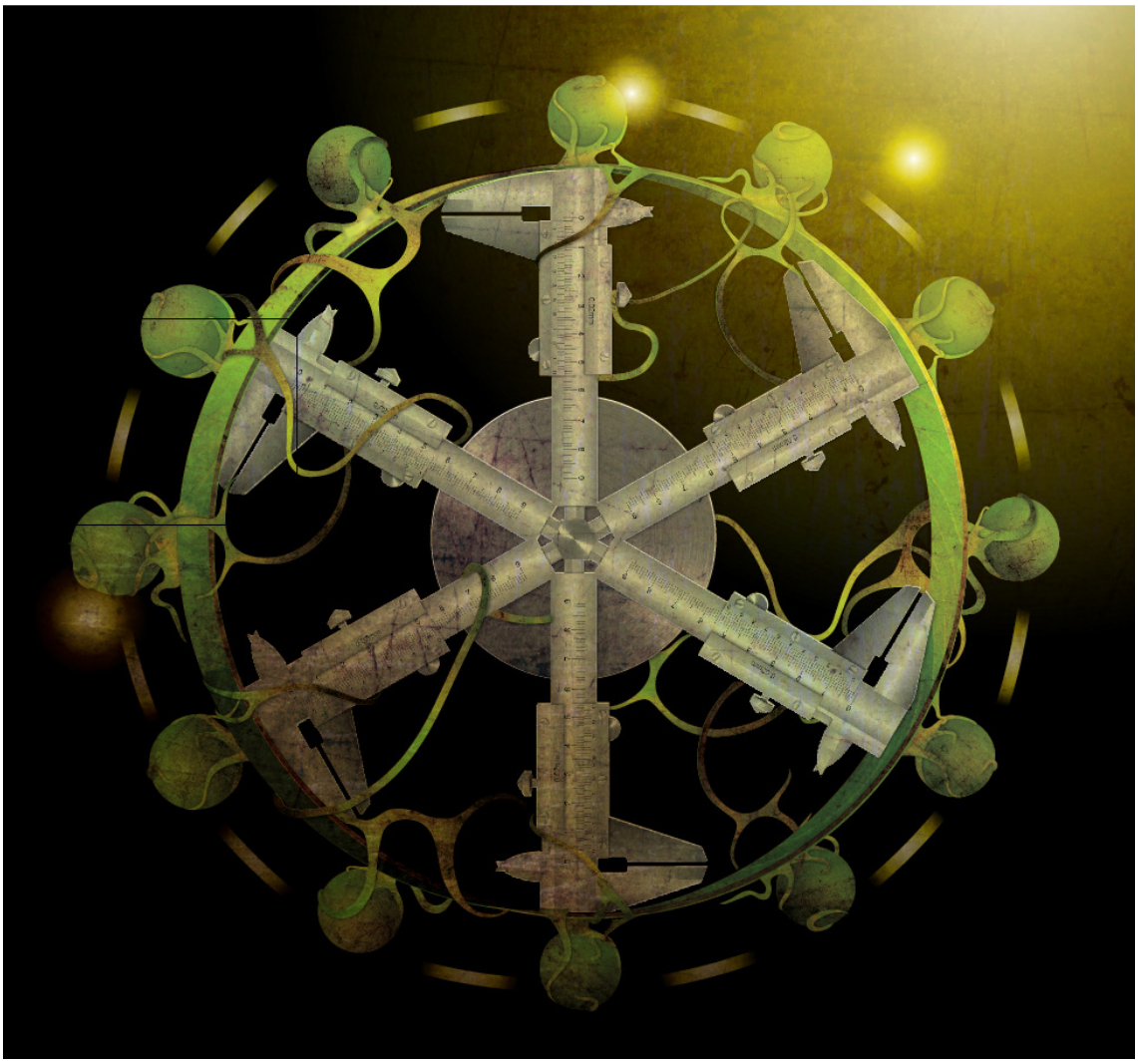

Figure A.13 Cover picture submitted to *Nature*. Cyclic dodecamer ***c*-P12** can be constructed by Vernier templating and is of interest due to its resemblance to natural light harvesting systems. Designed by Karis Flavell (DoodleKaz).

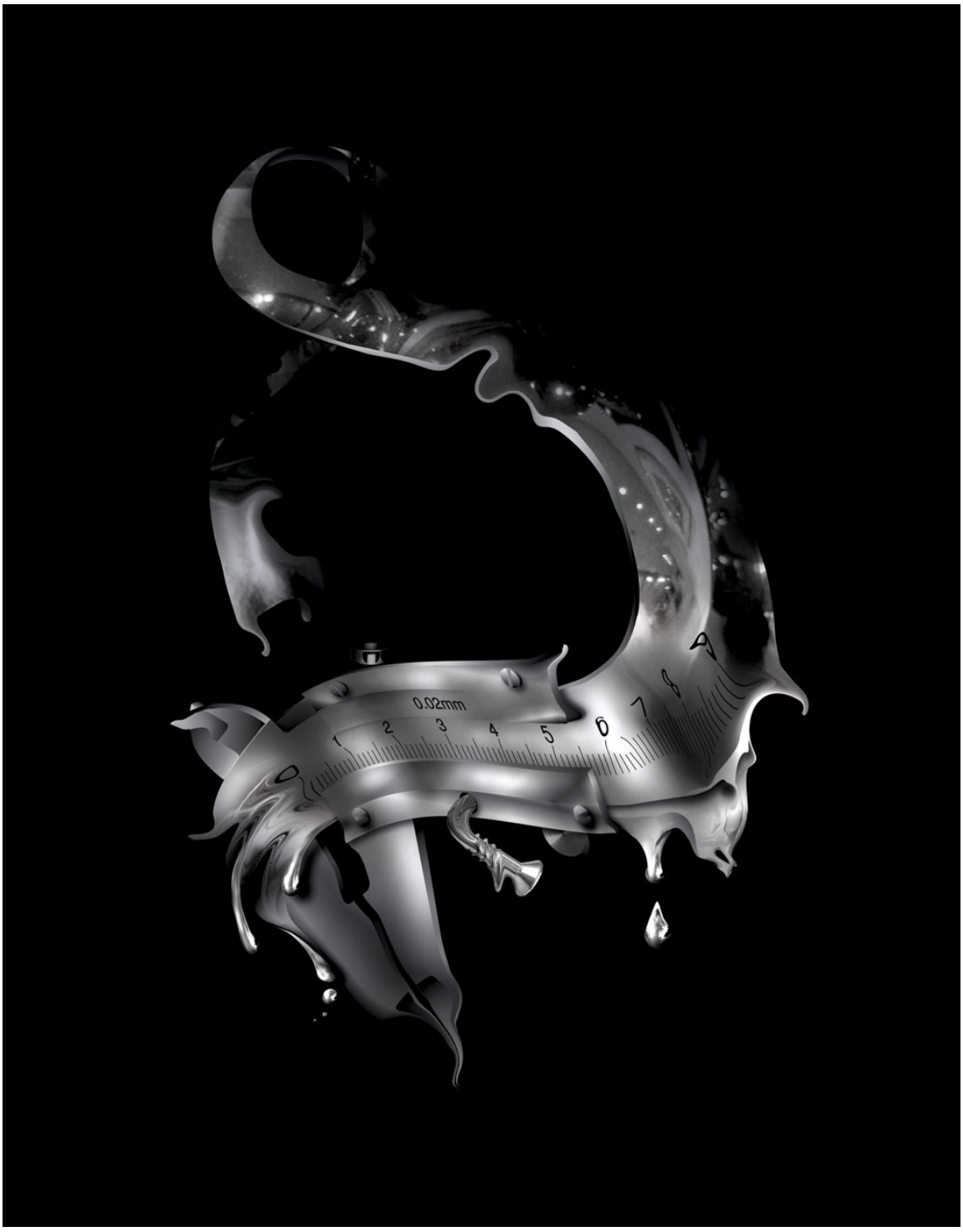

Figure A.14 Cover picture submitted to *Nature*. Melting calipers: Vernier templating, based on the same principle as Pierre Vernier's scale, gives a figure-of-eight structure. Designed by Karis Flavell (DoodleKaz).